Science

24 February 2012 | $10

Science in India

AAAS

CONTENTS

Volume 335 Issue 6071

CONTENTS continued >>

page 907

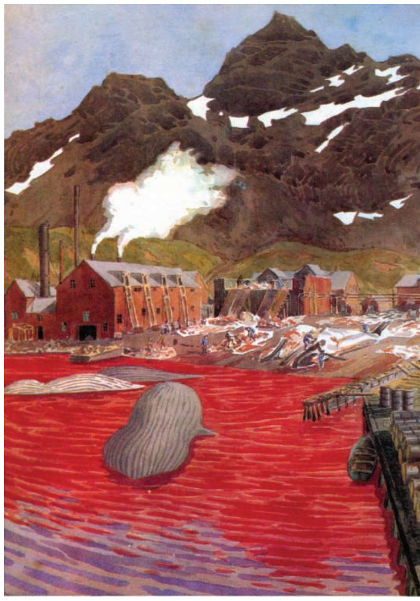

page 920

COVER

An agricultural outreach educator visits a village in rural Andhra Pradesh, India. India aims to double the research and development share of its economy and engage a broader swathe of its 1.2 billion citizens in science and technology. See an interview with Prime Minister Manmohan Singh (page 907), an Editorial by Raghunath Mashelkar (page 891), and a special News package (beginning on page 904).

Photo: Pallava Bagla

DEPARTMENTS

page 932

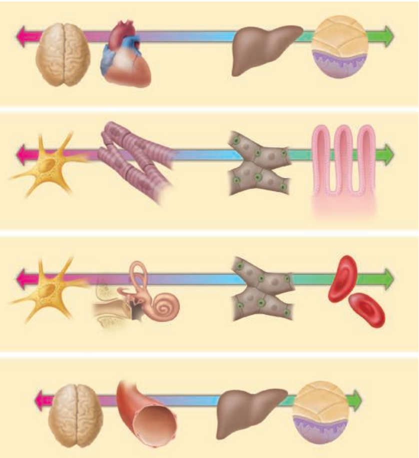

page 936

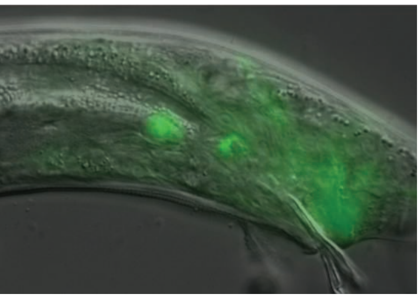

pages 926 & 970

Published by AAAS

SCIENCEONLINE

SCIENCEXPRESS

www.sciencexpress.org

Seroevidence for H5N1 Influenza Infections in Humans: Meta-Analysis
T. T. Wang et al.
One to two percent of 14,000 people tested in 20 studies showed evidence of prior H5N1 infection.
10.1126/science.1218888
>> See all H5N1 coverage online at http://scim.ag/_h5n1

Glucocorticoids Can Induce PTSD-Like Memory Impairments in Mice
N. Kaouane et al.
The infusion of a stress hormone produces fear responses to cues that were not associated with the traumatic event itself.
10.1126/science.1207615

A Bruce Effect in Wild Geladas
E. K. Roberts et al.
Long-term field studies show that female monkeys improve their fitness by terminating their pregnancies when a new male becomes dominant.
10.1126/science.1213600

Coherent Sensing of a Mechanical Resonator with a Single-Spin Qubit
S. Kolkowitz et al.
The spin of a nitrogen vacancy defect in diamond is used to sense the motion of a magnetized microresonator.
10.1126/science.1216821

The Role of Driving Energy and Delocalized States for Charge Separation in Organic Semiconductors
A. A. Bakulin et al.
Bound excited charge carriers achieve long-range separation by promotion to delocalized band states.
10.1126/science.1217745

TECHNICALCOMMENTS

Comment on "Lévy Walks Evolve Through Interaction Between Movement and Environmental Complexity"
V. A. A. Jansen et al.
Full text at www.sciencemag.org/cgi/content/full/335/6071/918-c

Response to Comment on "Lévy Walks Evolve Through Interaction Between Movement and Environmental Complexity"
M. de Jager et al.
Full text at www.sciencemag.org/cgi/content/full/335/6071/918-d

SCIENCENOW

www.sciencenow.org
Highlights From Our Daily News Coverage

A Practical Blueprint for a Low-Carbon Electric World?
'Transformative' technologies may wean the world from fossil fuel–based electricity.
http://scim.ag/Electric_World

Nuclear Reactors Not Needed to Make the Most Common Medical Isotope
A new technique uses a medical cyclotron to produce radioisotopes.
http://scim.ag/Medical_Isotope

Global Fisheries Deals: What's the Catch?
Some fishing agreements are not what they seem.
http://scim.ag/Global_Fisheries

SCIENCESIGNALING

www.sciencesignaling.org
The Signal Transduction Knowledge Environment
21 February issue: http://scim.ag/ss022112

RESEARCH ARTICLE: RGS Proteins Maintain Robustness of GPCR-GIRK Coupling by Selective Stimulation of the G Protein Subunit Gα_o
H. Chuang and A. Y. Chuang
Opposing actions of RGS proteins both stimulate and inhibit G proteins to modulate the amplitude and kinetics of the downstream response.

RESEARCH ARTICLE: Inhibition of Autophagy Ameliorates Acute Lung Injury Caused by Avian Influenza A H5N1 Infection
Y. Sun et al.
Blocking autophagy reduces the extent of lung damage and decreases mortality in mice infected with the H5N1 strain of avian influenza.

PERSPECTIVE: Semaphorin Signaling Meets Rap
J. L. Bos and W.-J. Pannekoek
Semaphorin binding stimulates the ability of plexin receptors to inhibit the GTPase Rap1, thereby enabling neurite retraction.

PRESENTATION: TGF-β Signaling in Endothelial-to-Mesenchymal Transition—The Role of Shear Stress and Primary Cilia
P. ten Dijke et al.
The loss of primary cilia is a prerequisite for flow-induced endothelial-to-mesenchymal transition in heart development.

GLOSSARY
Find out what 4E-BP, DEAD, and eIF4E mean in the world of cell signaling.

SCIENCETRANSLATIONAL MEDICINE

www.sciencetranslationalmedicine.org
Integrating Medicine and Science
22 February issue: http://scim.ag/stm022212

RESEARCH ARTICLE: First-in-Human Testing of a Wirelessly Controlled Drug Delivery Microchip
R. Farra et al.
A wireless microchip-based device implanted in humans delivers a drug for treating osteoporosis.

EDITORIAL: Reengineering Device Translation Timelines
J. Watson
Innovative engineering will shorten the translational timeline from concept to clinical application for medical devices.

RESEARCH ARTICLE: MicroRNA-21 Blocks Abdominal Aortic Aneurysm Development and Nicotine-Augmented Expansion
L. Maegdefessel et al.
miR-21 modulates abdominal aortic aneurysm development by regulating cell proliferation and apoptosis.

RESEARCH ARTICLE: Breast Cancer–Associated *Abraxas* Mutation Disrupts Nuclear Localization and DNA Damage Response Functions
S. Solyom et al.
A germline mutation in the *Abraxas* gene impairs the BRCA1 DNA damage response in familial breast cancer.

COMMENTARY: Recalibrating Intellectual Property Rights to Enhance Translational Research Collaborations
T. Bubela et al.
New collaborative models of therapeutic research and development require active governance of intellectual property rights to enable sharing.

SCIENCECAREERS

www.sciencecareers.org/career_magazine
Free Career Resources for Scientists

Experimental Error: I've Got Your Impact Factor Right Here
A. Ruben
The *Journal of Negative Results* is only the beginning.
http://scim.ag/EE_NewJournals

Stepping Out of Big Pharma's Shadow
M. Price
As big-pharma jobs disappear, pharma scientists are landing at start-ups, launching their own, or joining academia.
http://scim.ag/SteppingOutBigPharma

Q&A: Outsourcing Himself
E. Pain
Chemist Andrew McElroy got the idea for his company the day he was told he would likely lose his job at Pfizer.
http://scim.ag/OutsourcingHimself

SCIENCEPODCAST

www.sciencemag.org/multimedia/podcast
Free Weekly Show

On the 24 February *Science* Podcast: restoring ecological "networks of networks,"climate change and early horse evolution, the state of science in India, and more.

SCIENCE (ISSN 0036-8075) is published weekly on Friday, except the last week in December, by the American Association for the Advancement of Science, 1200 New York Avenue, NW, Washington, DC 20005. Periodicals Mail postage (publication No. 484460) paid at Washington, DC, and additional mailing offices. Domestic individual membership and subscription (51 issues): $149 ($74 allocated to subscription). Domestic institutional subscription (51 issues): $990; Foreign postage extra: Mexico, Caribbean (surface mail) $55; other countries (air assist delivery) $85. First class, airmail, student, and emeritus rates on request. Canadian rates with GST available upon request, GST #1254 88122. Publications Mail Agreement Number 1069624. **Printed in the U.S.A**.

Change of address: Allow 4 weeks, giving old and new addresses and 8-digit account number. **Postmaster:** Send change of address to AAAS, P.O. Box 96178, Washington, DC 20090–6178. **Single-copy sales:** $10.00 current issue, $15.00 back issue prepaid includes surface postage; bulk rates on request. **Authorization to photocopy** material for internal or personal use under circumstances not falling within the fair use provisions of the Copyright Act is granted by AAAS to libraries and other users registered with the Copyright Clearance Center (CCC) Transactional Reporting Service, provided that $30.00 per article is paid directly to CCC, 222 Rosewood Drive, Danvers, MA 01923. The identification code for *Science* is 0036-8075. *Science* is indexed in the *Reader's Guide to Periodical Literature* and in several specialized indexes.

AAAS
ADVANCING SCIENCE, SERVING SOCIETY

EDITED BY CAROLINE ASH

Enduring Tolerance

During an infection, the host organism deploys multiple defense strategies. Disease resistance, the process by which the immune system decreases pathogen burden is perhaps the most well-known, and certainly the mechanism that is best studied and understood. Other defense strategies range from pathogen avoidance, through tolerance of pathogen-induced tissue damage, and endurance of the overall pathogen burden. **Medzhitov *et al.*** (p. 936) review the concept of disease tolerance and suggest that particularly in animals, it is an overlooked mechanism of host defense.

Tunnel Barriers for Graphene Transistors

Transistor operation for integrated circuits not only requires that the gate material has high-charge carrier mobility, but that there is also an effective way of creating a barrier to current flow so that the device can be switched off and not waste power. Graphene offers high carrier mobility, but the shape of its conduction and valence bands enables electron tunneling and makes it difficult to achieve low currents in an "off" state. **Britnell *et al.*** (p. 947, published online 2 February) have fabricated field-effect transistors in which a thin tunneling barrier created from a layered material—either hexagonal boron nitride or molybdenum disulfide—is sandwiched between graphene sheets. These devices exhibit on-off switching ratios of ≈50 and ≈10,000, respectively, at room temperature.

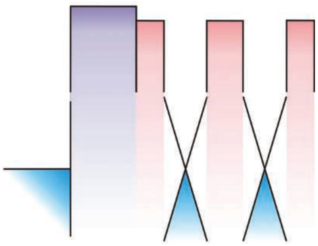

Paracrystalline

Amorphous silicon has traditionally been represented by a continuous random network model in which there is no long-range ordering for the atoms, and some have less than fourfold coordination, which form dangling bonds—a type of defect. **Treacy and Borisenko** (p. 950; see the Perspective by **Gibson**) used fluctuation electron microscopy to explain that models including regions of crystalline order are needed to fit the observed local variations in structure. Thus, on the 1- to 2-nanometer-length scale, this material should be thought of as having a paracrystalline structure containing localized crystalline regions.

Warming and Shrinking

In most mammals, individual body sizes tend to be smaller in warmer regions and larger in cooler regions. **Secord *et al.*** (p. 959; see the Perspective by **Smith**) examined a high-resolution 175,000-year record of equid fossils deposited over a past climate shift—the Paleocene-Eocene Thermal Maximum—for changes in body size. Using oxygen isotopes collected from the teeth of co-occurring mammal species to track prevailing environmental temperature, a clear decrease in equid body size was seen during 130,000 years of warming, followed by a distinct increase as the climate cooled at the end of the period. These results indicate that temperature directly influenced body size in the past and may continue to have an influence as our current climate changes.

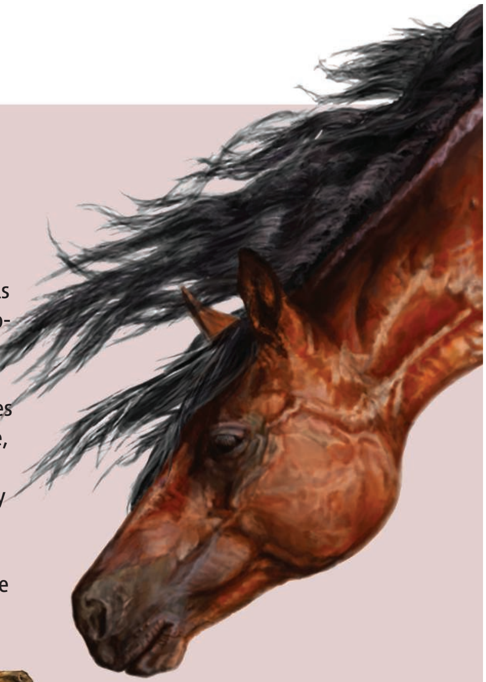

How Dry They Were

How much rainfall failure contributed to the disintegration of classical Maya civilization? **Medina-Elizalde and Rohling** (p. 956) analyzed records from three lakes and a stalagmite from the Yucatán Peninsula to quantify the change in precipitation that the region experienced between 800 to 1000 years A.D. Precipitation decreased episodically for up to a decade at a time and in total by as much as 40% during the 200 years of the civilization's fall, probably as a result of a reduction in summer tropical storm rainfall. This finding highlights the sensitivity of this region to modest reductions of rainfall that are projected by some climate model.

Cashing Up

Do small businesses in developing economies benefit from an infusion of cash or of capital, such as inventory or materials, and is the effect a momentary blip or a sustained expansion? **De Mel *et al*.** (p. 962) have extended their study of one-time cash or capital transfers to a group of randomized business owners in Sri Lanka to look at the status of the businesses 5 years later and find an increased likelihood of survival and higher profits for male-owned enterprises, but no significant effects on female-owned businesses. The authors suggest that capital transfers are more likely to be used by male-owned firms to grow the business, but more likely to be "cashed-out" from female-owned firms and diverted to household uses.

Distinguishing Ciliopathy

Cilia were once thought to be evolutionary remnants, but structural defects reveal their importance in signaling pathways and human disease, such as Joubert syndrome. Either of the genes *TMEM138* and *TMEM216* can be found mutated in phenotypically indistinguishable ciliopathy patients. Interestingly, despite their lack of sequence homology, these genes have always been aligned in head-to-tail configuration during vertebrate evolution. The proteins expressed by these genes mark distinct tethered vesicles, which differentially carry ciliary proteins for assembly. **Lee *et al.*** (p. 966, published online 26 January; see the Perspective by **Chakravarti and Kapoor**) show that the coordinated expression of these adjacent genes depends upon a coevolved regulatory element in the noncoding intergenic region, which thus integrates the roles of both gene products. This discovery explains not only the indistinguishable pathogenesis of the patients' genotypes but also how the evolutionary clustering of genes unrelated in sequence may correlate with coordinated control of expression and function.

CREDITS (TOP TO BOTTOM): FLORIDA MUSEUM OF NATURAL HISTORY, ILLUSTRATION BY DANIELLE BYERLEY; BRITNELL *ET AL.*

Published by AAAS

Death for Development

Cell death is critical for animal development and for the promotion of gastrulation, as well as for sculpting tissues. Although cell death by apoptosis is essential in some invertebrates, genes promoting apoptosis in the mouse are not required for viability. This surprising observation prompted investigations by **Blum *et al.*** (p. 970; see the Perspective by **Link and Saldi**), who have discovered a nonapoptotic developmental cell death process mediated by a polyglutamine-repeat protein in the nematode worm *Caenorhabditis elegans*. This form of cell death is morphologically similar to cell death occurring during vertebrate development, particularly cell death accompanying polyglutamine-dependent neurodegeneration.

Networks of Networks

Quantitative networks, such as those represented by food webs, have become an important way of investigating the structure of ecological communities, but thus far only encompass a small subset of species. **Pocock *et al.*** (p. 973) have linked seven different types of ecological networks to form a network of networks. They found that although networks varied in their robustness to species loss, they did not strongly co-vary; that is, what happens to one network is unrelated to what happens to another. The networks studied were identified from an agroecosystem in the southwestern UK, a habitat in which biodiversity has suffered substantially. This study succeeded in revealing which species are potential targets for restoration of ecological function in this and other systems.

Winging It

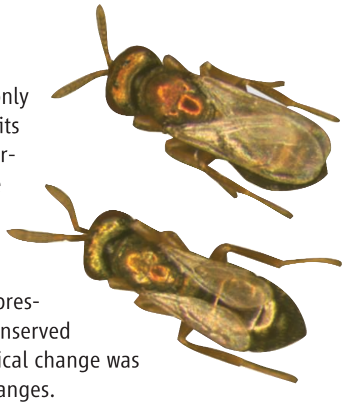

Genes that explain phenotypic variation between species have only been identified within a handful of model organisms, which limits the scope and understanding of the genetics of phenotypic diversification. On investigating the phenotypic diversity in wing size among wasps of the genus *Nasonia*, **Loehlin and Werren** (p. 943) have identified the genetic basis of a morphological difference between two closely related species and showed how changes in regulatory elements have evolved to change expression of a single gene, *unpaired-like* (*upd-like*), a functionally conserved signaling gene. Overall, it appeared that significant morphological change was achieved through a series of relatively rapid, but small-scale changes.

A Fraction of Folding

An energy barrier has to be crossed as a protein transforms between folded and unfolded states. Molecular dynamic simulations have observed sharp transitions, with barrier crossing times of less than a microsecond, a fraction of the total folding time; however, this time range has been inaccessible to single-molecule experiments. **Chung *et al.*** (p. 981) described single-molecule fluorescence experiments that allowed measurement of the transition-path time for a fast-folding protein and to reduce the upper bound for a slow-folding protein. Although the folding rates differed by a factor of 10,000, the transition-path times differ by less than a factor of 5, pointing to energy landscape theory for the explanation.

Sound the Alarm

When small protein fragments or nucleic acids derived from an invading pathogen are detected by pattern recognition receptors on immune cells, the innate immune response is triggered. This event activates cells of the adaptive immune system, and together, both responses clear the infection. Infections also induce the release of "danger-associated molecular patterns," or alarmins, from the host as a result of tissue damage. Whether these are also important for the ensuing immune response is less clear. **Bonilla *et al.*** (p. 984, published online 2 February) report that the alarmin, interleukin-33, is required for optimal cytotoxic $CD8^+$ T cells responses and antiviral immunity in mice. In virus-infected mice deficient in IL-33 or its receptor, IL-33 is essential for signaling $CD8^+$ T cells to expand, produce multiple cytokines and acquire cytotoxic capabilities. These results showed that endogenous material, independently of pathogen-derived molecules, are also required for antiviral immunity.

CREDIT: LOEHLIN AND WERREN

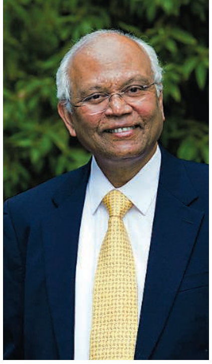

Raghunath Mashelkar is National Research Professor at the National Chemical Laboratory, Pune, India. E-mail: ram@ncl.res.in.

India's "Science for All" Academy

IN 1905, SIR WILLIAM OSLER, THE MOST INFLUENTIAL PHYSICIAN OF HIS TIME, STEPPED DOWN from the medical faculty of Johns Hopkins University at the age of 55. At his farewell, he emphasized that the "effective, moving, vitalizing work of the world is done between the ages of 25 and 40—these 15 golden years of plenty." Many of us, who are old but still active like myself, may like to strongly disagree. But the power of the creative prime in this age group is irrefutable. Therefore, when the Global Young Academy was established in 2010 to catalyze the formation of national Young Academies that promote leadership by a country's most outstanding scientists aged 30 to 40 (www.globalyoungacademy.org), it was enthusiastically applauded by the international science community. One country that urgently needs a Young Academy is India, a nation of 1.2 billion people, 55% of whom are under 25 years old. What would be a good design for a Young Academy of India?

After experiencing stagnation over the past decade, Indian science is showing signs of a great recovery. But it continues to deal with its frustrating contradictions. India's Moon mission Chandrayan-1 led to the detection of water on the Moon, yet rural Indian women continue to walk kilometers each day in search of water. To achieve her quest for growth and innovation that include the entire population, India does not need yet another science academy. She needs a "science for all" academy. By this I mean an academy that simultaneously pursues a quest for both excellence and relevance. Indian science should not be judged only by the "H index," which aims at a global measure of excellence, but also by an "I index," which should measure the ability to provide Indian solutions to the specifically Indian problems of 800 million resource-poor people.

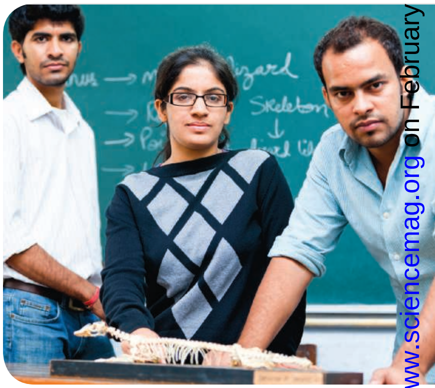

Are young Indian scientists ready to accept this challenge? The answer is a resounding yes. India's Council of Scientific and Industrial Research launched its Open Source Drug Discovery challenge in 2008. Since then, the 3000 young graduate student participants have made some breathtakingly creative contributions, ranging from increasing our understanding of *Mycobacterium tuberculosis* to the synthesis of novel compounds that could lead to drugs for tuberculosis treatment. Techpedia (www.techpedia.in/) has posted over 100,000 undergraduate projects by students in their early 20's, the majority of which reflect their impatience with crippling societal problems. I witnessed this impatience in rural Maharashtra last month: Vidarbha has the highest incidence of farmer suicides, and the young scientists there asked me only one question: What can scientists do to stop these suicides? So there is a community of energetic and compassionate young Indian scientists with great passion in their bellies. And this community is set to grow exponentially, as India's Innovation in Science Pursuit for Inspired Research (INSPIRE) scheme aims to support a whopping 1 million science students by the end of 2013.

India should be listening seriously to its future scientific leaders. Yet, disappointingly, young scientists have no venue in which to express their views on the big questions facing India—from the huge recent controversy about genetically modified eggplant, to the public protests at Jaitapur regarding new nuclear power plants. Nor have young researchers been involved in the design of the Indian Planning Commission's 12th 5-year (2012–2017) plan on science and technology. A new Young Academy should, therefore, provide an influential voice for the next generation of Indian scientists. This Young Academy should be borderless, taking the disciplines of the natural sciences, engineering, social sciences, arts, and humanities into its fold; and dynamic, harnessing the power of technology and social media. And it should have a mind of its own, with a constantly questioning, "yes, we can" mindset. The youth of India are ready for a Young Academy. It's time to get to work to form it.

– Raghunath Mashelkar

10.1126/science.1220166

CREDITS: (TOP) PETER FIRUS; (RIGHT) ISTOCKPHOTO.COM

EDITED BY KRISTEN MUELLER AND JAKE YESTON

POLICY

Assessing the Assessments

Though a modern-day Galileo may still woo an occasional Medici patron to support his research, a vast number of scientists depend on much more bureaucratic means to keep their labs running. Since 1986, when the UK Research Assessment Exercise was launched, at least 14 countries have implemented systems to distribute research funding to universities based on evaluation of research output. These have been motivated by the increasing importance of research to economic growth, as well as broader interests in improving public management. Hicks analyzes the systems' rationale, design, and impact. There is a range of assessments (e.g., citation analysis, peer review), across a range of scales (e.g., university, department, individual), that affect a range of funding outcomes (e.g., 25% of UK research support, 2% of Italian block grants). Although distribution of research funding is the putative purpose, direct financial impacts appear small compared to incentives to compete for public prestige. Some values widely associated with universities, such as diversity and equity, may suffer under systems focused solely on excellence and international competition. Though touted as critical to economic success, the systems do not appear to be well designed to meet that goal. — BW

Res. Policy **41**, 251 (2012).

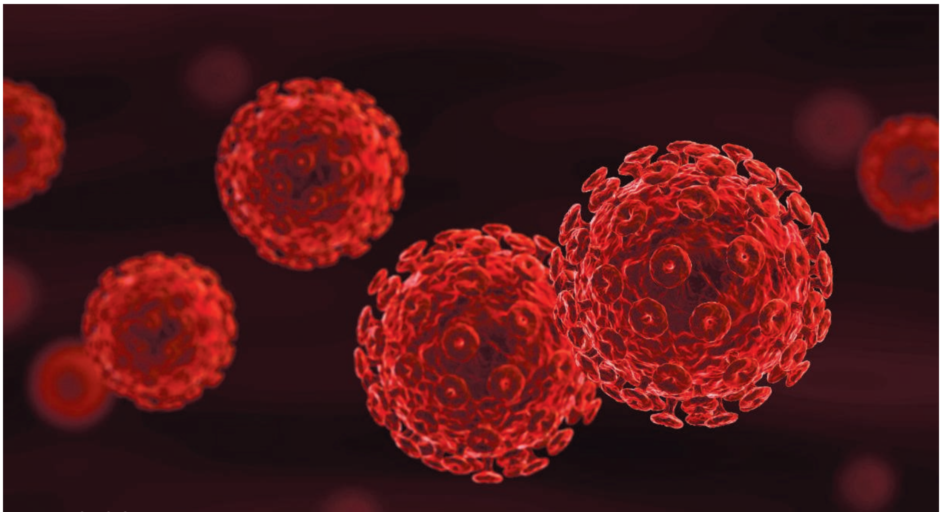

VIROLOGY

Replication Restricted

Despite its deadly nature, HIV-1 is quite limited in the types of cells that it can infect. HIV-1 primarily infects $CD4^+$ T cells but not many myloid-derived immune cells. This is because most myeloid-derived cells express the viral restriction factor SAMHD1. Although this may seem like an advantage to the host, the virus actually gains the upper hand because it can escape detection by the innate immune system. In support of this, HIV-2 and some SIV strains that do not cause such severe pathology express Vpx, which counteracts the effects of SAMHD1. Little is known, however, about how SAMHD1 prevents HIV-1 infections from taking hold. Lahouassa *et al.* noted that SAMHD1 shares homology with a protein from *Enterococcus fecalis* that has nucleotide metabolism activity. Using a variety of in vitro analyses, they found that SAMHD1 exhibited phosphohydrolase activity for dNTPs and regulated the pool of dNTPs in myeloid-derived cells. SAMHD1 expression lowered the concentration of dNTPs below what is required for productive reverse transcription by HIV-1, thereby blocking infection. Thus, regulation of nucleotide pools may be a means by which cells regulate their susceptibility to viral infection, but hidden benefits for the virus may be lurking, too. — KLM

Nat. Immunol. **13**, 10.1038/ni.2236 (2012).

BIOTECHNOLOGY

Small Sources of Sweetness

The sucrose sourced from sugarcane to sweeten our tea and cake—and more recently, to foster ethanol as a transportation fuel—is the same molecule produced by many microorganisms that potentially face fewer cultivation constraints. The trouble is that the microbes don't release their sugar easily. Ducat *et al.* noted that heterotrophic and autotrophic bacteria induce oppositely directed transmembrane proton gradients, and as such, a gradient-dependent native transporter that pulls sucrose into the former might expel it from the latter. They therefore expressed this sucrose permease in *Synechococcus elongatus* cyanobacteria—known to produce sucrose under osmotic stress—and indeed collected the sugar in the medium. Furthermore, strains incorporating the transporter manifested enhanced photosynthetic productivity, as assessed by measuring oxygen evolution rates and fixation of ^{14}C-labeled tracers. Though scale-up presents a range of challenges, extrapolation of the laboratory results suggests prospective sucrose productivities on par with or even exceeding that of sugarcane. — JSY

Appl. Environ. Microbiol. **78**, 10.1128/AEM.07901-11 (2012).

PHYSIOLOGY

Fructose Sweetens the Deal

Glucose, a metabolic product of dietary sucrose, triggers pancreatic beta cells to release insulin, which in turn allows many different cells types to take up glucose to store or use as energy. The other breakdown product of sucrose is fructose, and Kyriazis *et al.* report that it too plays a role in controlling insulin release. Fructose activates a sweet taste receptor (the TIR2-TIR3 heterodimer) expressed by mouse and human beta cells. This enhances the effect of glucose on insulin release. Mice injected with fructose (or saccharine, another taste receptor ligand) showed a rapid increase in circulating insulin, but only if functional taste receptors were present and only if glucose stimulated beta cells as well.

Fructose-activated sweet taste receptors signal through a phosphoinositide pathway, which elevates cytoplasmic Ca^{2+} concentration

CREDITS (TOP TO BOTTOM): ISTOCKPHOTO.COM

Published by AAAS

and depolarizes the membrane via a cation channel, TRPM5. Functional interaction between these two pathways is not yet clear, but because TRPM5 has been implicated in glucose-stimulated insulin secretion, it may be a convergence point. Whatever the mechanism, these findings may have implications for the link between high fructose consumption and the development of metabolic diseases such as obesity and diabetes. — LC

Proc. Natl. Acad. Sci. U.S.A. **109**, 10.1073/pnas.1200797109 (2012).

NEUROSCIENCE

The Reading Brain

Developmental dyslexia, which manifests as difficulty with reading, can have long-lasting and detrimental effects on a child's experience with education, with echoes that persist long into adulthood. Raschle *et al.* have leveraged the indications of familial risk for dyslexia to distinguish differences in brain structure present before reading from those that arise after the battle with reading difficulties is well engaged. The authors studied a total of 36 5-year-old children, all pre-literate, characterized by whether or not their family had a history of dyslexia. Even at these pre-reading ages, functional brain imaging revealed an aberrant signal similar to that found in older children with a confirmed diagnosis of dyslexia. Development of the brain network supporting phonological processing appeared to be delayed. On the other hand, the two groups of children showed no difference in other networks that are hyperactivated when persons with dyslexia are reading. Those networks may instead represent compensation brought into play in the struggle to defeat reading difficulties. — PJH

Proc. Natl. Acad. Sci. U.S.A. **109**, 2156 (2012).

EDUCATION

Getting the Rubric Right

Despite the growing popularity of online learning, how to grade online discussions remains a challenge. Simply modifying existing grading rubrics can be problematic, because the format of online learning discussions differs from that of traditional classroom work. To evaluate the value of a clearly defined online learning grading rubric, or scoring tool, Solan and Linardopoulos developed a rubric that took into account the quantity and quality of posts, timeliness of participation, and communication proficiency, and then surveyed undergraduate and graduate student perceptions. Results indicated that although students are appreciative that a rubric is available, most did not consult it while contributing to online discussions. Teachers therefore may need to emphasize, review, and clearly link the rubric to grades assigned throughout the duration of the course. Students also reported that such a tool needs to be dynamic, because despite attempts to be comprehensive, unexpected scenarios will probably occur. Whether such a tool led to increased student learning is unknown, and, along with faculty perceptions of the rubric's value, should be a topic of future research. — MM

J. Online Learn. Teach. **7**, 452 (2011).

ASTROPHYSICS

Swifter than the Sun

Stars form from the gravitational collapse of clouds of gas and dust. Before they attain a stable radius, they spin faster and faster as they contract, much like a spinning ice skater does as she folds her arms to her body. After gravitational collapse stops, stars start slowing down because of magnetic braking—the loss of stellar angular momentum as material gets removed from the star because of a magnetized stellar wind. Stars thus start as fast rotators and then slow down as they age. Current theories of angular momentum evolution reproduce the rotation data for Sun-like stars, but fail to account for those with masses lower than half that of the Sun. These very low-mass stars don't seem to slow down with age as much as expected, and the lower their masses, the faster they rotate at a given age. Reiners and Mohanty reexamined the theories of angular momentum evolution for low-mass stars, and show that angular momentum evolution must depend on stellar radius if the rotation of a star is related to its magnetic field strength. Stars with lower masses have smaller radii and lower magnetic braking efficiencies, meaning that they will take longer to slow down. — MJC

Astrophys. J. **746**, 43 (2012).

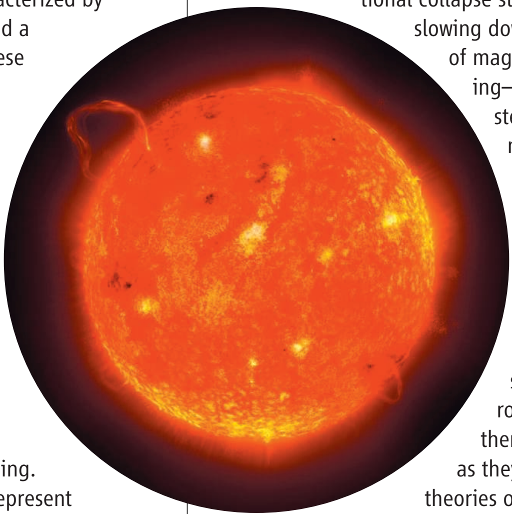

CREDIT: ISTOCKPHOTO.COM

Published by AAAS

AROUND THE WORLD

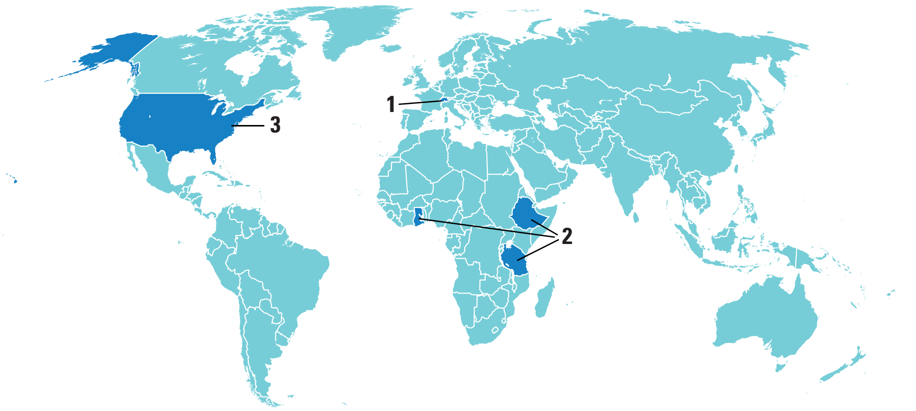

Lausanne, Switzerland **1**

Swiss Satellite Would Clean Up Space Debris

Space researchers in Switzerland are seeking funding to build a spacecraft, dubbed CleanSpaceOne, that would help reduce space debris in orbit around Earth. The spacecraft would home in on a redundant satellite, grab it, and drag it down to burn up when reentering the atmosphere.

Researchers at the Swiss Space Center at the École Polytechnique Fédérale de Lausanne have been working on the necessary technology for 3 years, says Swiss Space Center Director Volker Gass. He also says the spacecraft would cost an estimated $11 million to build and launch and could be ready between 2015 and 2017.


Clean air. CleanSpaceOne zeroes in on space debris.

Using cameras, the semiautomatic probe would identify the target satellite and use ion microthrusters to move next to it and capture it. The combined object will have a new center of gravity, so the probe has to stabilize the trajectory and then guide itself onto a curve toward the atmosphere.

The probe's potential first target would be a picosatellite called SwissCube, launched in 2009. "Switzerland is a country that likes to keep things clean," Gass says. "So we decided to first get our own satellite down."
http://scim.ag/cleanspace

Ethiopia, Ghana, and Tanzania **2**

Gates Foundation Funds African Agricultural Impact Monitoring

By boosting farm yields, Asia's green revolution of the 1960s and 1970s prevented millions of people from starving. But it also created social and environmental problems, such as contamination of ground water, in some places. To help Africans avoid making the same mistakes, the Gates Foundation today announced a $10 million grant over 3 years to monitor the effects of agriculture on people and the environment.

Conservation International (CI) will set up computer infrastructure to handle data collected in Tanzania, Ethiopia, Ghana, and two other African countries that are not yet determined. With Columbia University and the Council for Scientific and Industrial Research in South Africa, CI will give money to local universities, museums, and other institutions to gather information—on the ground and via remote sensing—about agriculture, ecosystems, and human well-being in five regions each roughly the size of Oregon. All of these data will be synthesized into a half-dozen indicators that will be relevant to policymakers. "We want to move forward quickly in implementing this," says Sandy Andelman, director of the Tropical Ecology, Assessment and Monitoring Network at Conservation International.

Washington, D.C. **3**

Journals Warned Not to Publish Diesel Exhaust Studies

At least four journals have been warned by an attorney this month to hold off distributing health data they may have under review. The admonition—which concerns a large U.S. study of the effect of diesel exhaust on miners' lungs—came from Henry Chajet, an attorney at the Patton Boggs firm in Washington, D.C., and lobbyist for the Mining Awareness Resource Group, an industry coalition. Editors at two U.K.-based publications—*Occupational and Environmental Medicine* and *The Annals of Occupational Hygiene*—say they and others received a letter from Chajet advising against "publication or other distribution" of the Diesel Exhaust in Miners Study (DEMS) until it is vetted by Chajet's industry clients and a U.S. House committee.

Chajet and others involved in the DEMS fracas, including researchers, declined to comment, as a court decision is pending. DEMS has been entangled in litigation almost from its start in 1992. The mining coalition has argued that DEMS is flawed, and it won a court order enforcing their right to preview data for 90 days before publication. DEMS leaders have argued against the restrictions in the U.S. Court of Appeals in New Orleans, Louisiana. A ruling is expected soon.
http://scim.ag/dieselstudies

NEWSMAKERS

MIT President Stepping Down

The first woman and first biologist to run the Massachusetts Institute of Technology (MIT) announced last week that she is stepping down as president after 7 years. **Susan Hockfield**, who turns 61 next month, said in a statement that this is "an opportune moment for a leadership transition," in part because the university is planning a new fundraising campaign that will require the "full focus" of MIT's president for years. Hockfield will stay on until the next president takes office.


Hockfield

Hockfield came to MIT from Yale University, where she spent 20 years studying brain development and brain tumors and served as provost. MIT recruited her after a damning internal report, publicly released in 1999, charged that women at MIT often faced career roadblocks. Hockfield's appointment was also noteworthy because the engineering powerhouse had traditionally looked to engineers to lead it.

During her MIT tenure, Hockfield helped raise almost $3 billion. She also worked to get engineers and life scientists to collabo-

Published by AAAS

rate, and helped launch the MIT Energy Initiative in 2006. It conducts research into alternative energy sources and better ways to use existing ones. She also focused on boosting diversity at MIT, from undergraduates to faculty.

FINDINGS

Elephant Footsteps Reveal Ancient Herd Behavior

When a herd of elephant ancestors walked through mud in the Arabian Desert about 7 million years ago, they unwittingly left their footprints—and clues about their behavior—behind. Those prints now expose how the herd behaved: Just like modern elephants, they followed a female leader.

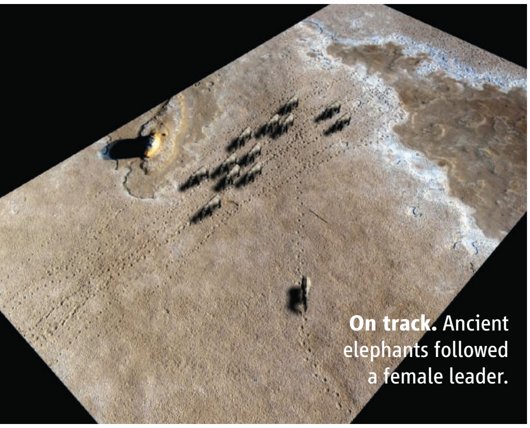

On track. Ancient elephants followed a female leader.

The remarkable 260-meter-long trackway, made by at least 13 proboscideans of different sizes, is at the site of Mleisa 1 in the Al Gharbia region of Abu Dhabi Emirate. Using a kite-mounted camera to take aerial photographs of the footprints, an international team of researchers, with the support of the Abu Dhabi Authority for Tourism and Culture, analyzed the prints' stride lengths and patterns. One solitary trackway was made by a large male traveling in a totally different direction from the other, smaller animals, according to a study in this week's *Biology Letters*. This "fossilized behavior" suggests that 7 million years ago, females and young elephant ancestors followed a matriarchal female but males dispersed when they reached sexual maturity, just as modern elephants behave today, says primary author Faysal Bibi of the Museum für Naturkunde in Germany.
http://scm.ag/oldtracks

Random Sample

Road Scholars Solve Pothole Problem

The streets of Boston have met their match. This week, Massachusetts-based InnoCentive announced the winners of its latest Web-based challenge: to use smartphones to detect potholes. Building on a city of Boston app called Street Bump, which uses GPS and accelerometer data from a smartphone to record a car's location and sudden bounces, contestants vied to find ways to pool this data from many vehicles while distinguishing potholes from jolt-inducing features like railroad crossings.

Winning strategies varied widely. Undergraduates Nathan Marculis and SaraJane Parsons chose mathematical techniques called wavelets and Kruskal clustering. The challenge "involves detecting spikes or jumps in data," says their advisor, mathematician Ed Aboufadel of Grand Valley State University in Allendale, Michigan. "That's something wavelets are good at." Kruskal's algorithm helps identify related reports from different vehicles. Somerville, Massachusetts–based researchers headed by Massachusetts Institute of Technology grad Michael Nagle took a different approach. Using a tennis ball for scale, they measured the size of the potholes. They also used common-sense insights, such as realizing that a pothole jolt has a horizontal component to it (unlike that of a railroad crossing).

"We were impressed with the quality of the solutions," says Nigel Jacob, co-chief of the city's New Urban Mechanics Office, which co-sponsored the competition with InnoCentive and Liberty Mutual. "The challenge format allows us to focus on quality rather than the size of the vendor." The two teams and a third winner, Elizabeth Yip of Washington, will each receive a $9000 prize. Before making the pothole-detecting apps available to the public, the city plans to merge the best features of the three algorithms into a single program.

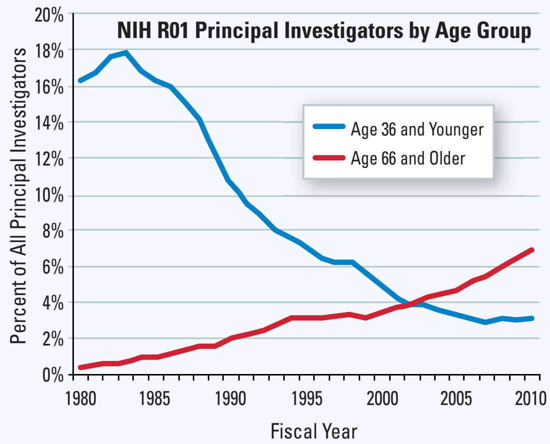

Older Scientists Still Get the Grants

A graph posted by the National Institutes of Health (NIH) this month highlights the growing imbalance between the youngest and oldest researchers. In 1980, almost 18% of principal investigators (PIs) holding NIH's basic research grant, called an R01 grant, were 36 and younger, and less than 1% were 66 and older. But by 2012, those 66 and older made up almost 7% of grantees and the youngsters were at only 3%. "These are big changes," wrote NIH extramural grants chief Sally Rockey on her Rock Talk blog.

The average age of a PI, now around 51, tracks the aging of medical school faculty, Rockey reports. Faculty over 65 may be staying on because of an end to mandatory retirement, a longer U.S. average life span, and slumping retirement portfolios, she suggests. The data offer a new slant on NIH's worry that the average investigator doesn't get his or her first grant until age 42 (*Science*, 7 November 2008, p. 834). NIH policies since 2007 that give an edge to proposals from young investigators have not yet lowered that number, Rockey reports.

CREDITS (FROM TOP): COURTESY OF ED ABOUFADEL; SVARIOPHOTO/ISTOCKPHOTO.COM; © MAURICIO ANTÓN; NIH

Published by AAAS

AAAS MEETING

The AAAS annual meeting attracted more than 11,000 attendees overall to Vancouver, Canada, from 16 to 20 February. For more on these meeting snapshots, plus additional stories, Q&As, online chats, and podcasts, go to **http://scim.ag/aaas2012.**

Fracking Acquitted of Contaminating Groundwater

A major review of fracking—the controversial practice of pumping fluids into tight shale formations to release natural gas—uncovered no direct evidence that it is contaminating groundwater. The review, released at the meeting, suggests that problems that have been attributed to fracking tend to occur closer to the surface, when gas and drilling fluid escape from poorly lined wells or storage ponds. Charles Groat, a former director of the U.S. Geological Survey who led the study, said that the $380,000 report was conducted only with university funds. Groat, now at the University of Texas, Austin, and four UT colleagues found no evidence of drilling fluids leaking deep underground and concluded that methane in water wells in some areas probably comes from natural sources.


A natural gas drilling tower.

The review acknowledges that gaps remain in understanding fracking, including whether pumping wastewater into the ground causes small earthquakes. In addition, the cumulative and long-term impacts of the technique remain unclear, especially in areas where some gas naturally escapes from below ground. **http://scim.ag/aaas-frack**

Eat or Be Eaten

For most of the past 5000 years, hunter-gatherers called the Aleuts lived on Sanak Island off of Alaska, surviving on fish, sea otters, clams, mussels, and more. According to ecologist Jennifer Dunne of the Santa Fe Institute in New Mexico, who with colleagues has created a food web for the island's intertidal zone from a variety of data, those Aleuts were "super-generalists", consuming the greatest variety of different intertidal prey—50 of 171 species—of any predator. In a broader marine food web for Sanak Island, which includes birds and additional animals, Pacific cod took the top spot, munching on 124 of the 513 species, although the Aleuts were not far behind with a diet of 122 species. "This is our first detailed picture of how humans fit into food webs," Dunne says. "It is the first time that the roles of humans as predators are explicitly compared to the roles of other predators in food webs." **http://scim.ag/aaas-foodweb**

Intertidal Food Web

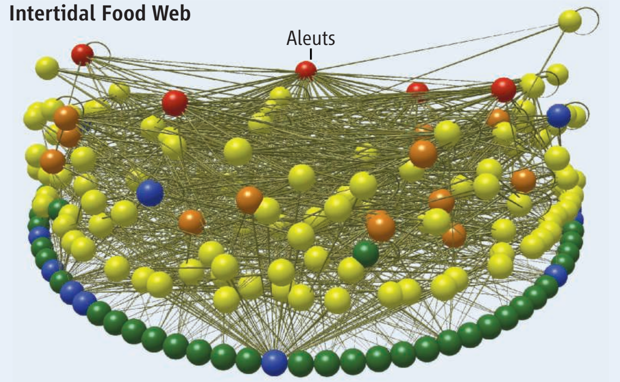

Ocean Changes Dried Out East Africa

The development of large differences in the temperatures of the Indian and Pacific oceans 2 million years ago shifted rainfall patterns and dried out East Africa, replacing woodland with grassland and leading to an explosion in the number of species that grazed the region, results presented at the meeting suggest.

Peter deMenocal, a marine geologist and geochemist at Columbia University, and colleagues examined sea-surface temperature records from the western and eastern Indian Ocean and previously published temperature records from sea-floor sediment cores for the Pacific Ocean. Temperatures across the Indian Ocean were fairly uniform, hovering around 27° to 28°C, until about 2 million years ago. The western Indian Ocean near the Arabian Sea then cooled to 25°C, while the eastern Indian Ocean near northwestern Australia warmed to 28° to 29°C. At the same time, the western Pacific Ocean warmed and the eastern Pacific cooled. These changes coincided with less rain over East Africa. When deMenocal and his colleagues ran climate models that erased those temperature differences, they found that rainfall increased in eastern Africa, reflecting its once wetter past.

"It was a lovely study," says Andrew Weaver, a climate scientist at the University of Victoria in Canada. "Something's going on 2 million years ago," he says, "and the question is, 'What's the big driver?' " **http://scim.ag/aaas-dryafrica**

Reactor-Free Recipe for Isotope

In recent years, hospitals worldwide have faced short supplies of technetium-99 (Tc-99), the most commonly used radioisotope in medical imaging scans. But a team of Canadian researchers now suggests Tc-99 can be efficiently made with a common medical cyclotron rather than via the current technique, which depends on nuclear reactors fueled with highly enriched uranium.

At the meeting, Paul Schaffer, head of nuclear medicine at TRIUMF, a nuclear and particle physics laboratory in Vancouver, Canada, described how his group used a popular GE cyclotron to fire protons at a stable isotope of molybdenum, generating Tc-99. The demonstration holds out the hope that existing medical cyclotrons, which hospitals already use to make other radioisotopes, could generate enough Tc-99 to fulfill Canada's entire demand, Schaffer says.

"This is wonderful for Canada," says Robert Atcher, director of the National Isotope Development Center at the Los Alamos National Laboratory in New Mexico, although he questions whether the approach will work in the United States, where the population is more diffuse, and many outlying hospitals don't have access to an appropriate cyclotron. Tc-99 decays within 6 hours, so those hospitals would need to be continuously resupplied, he suggests. **http://scim.ag/aaas-tc99**

CREDITS (TOP TO BOTTOM): JENNIFER DUNNE; RUHRFISCH/WIKIMEDIA COMMONS; WIKIMEDIA COMMONS

AVIAN INFLUENZA

WHO Group: H5N1 Papers Should Be Published in Full

An elite group of 22 influenza scientists, public health officials, and journal editors from 11 countries recommended last week that the details of how a highly pathogenic bird flu virus was rendered capable of being transmitted easily among mammals be published in full. The recommendation, agreed to at a meeting at the World Health Organization (WHO) in Geneva, flies in the face of advice from an influential U.S. committee that key details of the experiments be confined only to those who have a need to know.

H5N1 is highly lethal to humans but does not spread easily from person to person. Two teams working with ferrets, which many researchers consider the best animal model for humans, manipulated H5N1 to introduce genetic changes that made it easily spread through the air between these weasel-like animals. In December, the National Science Advisory Board for Biosecurity (NSABB), a U.S. government committee, recommended that *Science* and *Nature*, which have reviewed papers about the work, not publish key details. NSABB feared that in the wrong hands, the information could provide a recipe for triggering a devastating human pandemic. An impassioned international debate ensued, pitting scientific freedom against public safety. The journals, heeding NSABB's advice, had planned to publish manuscripts stripped of critical details in mid-March, provided an as-yet-undetermined mechanism is established to make the entire manuscripts available to flu investigators and public health officials who need to know all the data.

In Geneva, the researchers who led the work—Ron Fouchier of the Erasmus University Medical Center in Rotterdam, the Netherlands, and Yoshiro Kawaoka of the University of Wisconsin, Madison—passed out copies of the papers they submitted to the journals. To demonstrate what the papers would look like if the journals followed NSABB's advice, the researchers also distributed redacted versions at the closed-door meeting. The drafts of each paper were numbered, participants had to sign for them upon receipt and return, and in the end, the authors shredded all the papers in front of everyone in the room. "That certainly was a surreal touch," says Barbara Jasny, a deputy editor at *Science*, who represented the journal at the meeting, held 16–17 February.

The group recommended that the journals publish the papers without deleting details. Keiji Fukuda, WHO's assistant director-general for Health Security and Environment, said the complexity of distributing the full manuscripts to a select few, combined with the public health and scientific value of widely sharing the data, led to a "quite strong"—but not unanimous—agreement among the Geneva group to go against NSABB's recommendations. "Who would hold on to the sensitive information?" Fukuda asked at a WHO press conference. "Under what conditions would that information be released? What are the other complicating factors? It was recognized that coming up with such a mechanism would be very difficult to do overnight, if not impossible."

Peer review. WHO's Keiji Fukuda led an expert group that said papers on transmissible bird flu viruses should not be redacted.

Paul Keim, the acting chair of NSABB, who attended the Geneva meeting, disagrees with the consensus opinion. Keim, a geneticist and anthrax specialist at the University of Northern Arizona in Flagstaff, praises the international makeup of the WHO group but stresses that it mainly consisted of influenza researchers. "I believe that the redacted versions were so obvious to them that they held them in little value," Keim said. "This type of policy decision can't be made by the flu research community alone." The U.S. government's top representative at the meeting, Anthony Fauci, also dissented from the consensus. "I stand by the NSABB recommendations," says Fauci, who heads the U.S. National Institute of Allergy and Infectious Diseases (NIAID).

In many ways, the WHO meeting gave a stamp of validation to NIAID, which funded both of the studies, and the researchers themselves, whom some have criticized for conducting the work in the first place. Summing up the consensus of the WHO group, Fauci said, "being able to pursue openly this type of research by the public health and scientific community outweighs the issues of a terrorist getting enough information to do something nefarious."

Fouchier, Kawaoka, and their co-workers say their studies reveal critical factors that lead to transmission of H5N1 in mammals. They contend that their data can also potentially help surveillance efforts detect dangerous mutations in birds or other species before these variants make the jump into humans (*Science*, 17 February, p. 785).

Albert Osterhaus, a meeting participant who works with Fouchier, says the WHO group received information about recently detected H5N1 variants in nature that underscores the value of their ferret work. "Quite a number of data, which are not yet in the public domain, have been shown that actually indicated that the H5N1 viruses are developing very fast," says Osterhaus, who did not want to discuss specifics. These new details, which he noted were not available to NSABB, mean their experiments could aid surveillance today. "That's a very important thing to realize," he says.

Although it endorsed full publication,

CREDIT: CHRISTOPHER BLACK/WHO

the WHO group urged the journals to delay publishing the manuscripts and asked the research community to continue a voluntary 60-day moratorium set to expire on 20 March to allow time to increase "public awareness" about the importance of the work. "This was a most important step for making sure anxieties will not be unnecessarily increased," Fukuda said. The WHO group also hopes that extending the moratorium will allow for a fuller discussion about the safety conditions needed by labs that work with these viruses.

Like NSABB, the WHO group influences but does not control the fate of these papers. *Science* Editor-in-Chief Bruce Alberts, who was not at the WHO meeting, said he is "not completely clear about what the decision means because it's qualified," but said *Science* has scuttled plans to publish the redacted papers next month. *Nature* Editor-in-Chief Philip Campbell, who attended the Geneva gathering, issued a statement that *Nature* supports the group's decisions about the benefits of full publication. "Discussions at the WHO meeting made it clear how ineffective redaction and restricted distribution would be for the *Nature* paper," Campbell's statement said. Neither journal offered a timeline for publication. **–JON COHEN**

U.S. SCIENCE BUDGET

Scientists Decry Cuts That Would Doom ExoMars Missions

Next week, planetary scientists building instruments for a 2016 Mars mission called Trace Gas Orbiter will update a committee advising NASA on its Mars exploration program. But they'll also be grilling NASA officials attending the meeting on the Obama Administration's decision last week to kill the mission, one of two joint efforts with the European Space Agency (ESA) dubbed ExoMars (*Science*, 17 February, p. 783).

The president's 2013 budget request eliminates funding for the 2016 mission, which received $27 million this year, as part of a 20% cut to NASA's planetary science division. The division's proposed $1.2 billion budget also terminates NASA's participation in an ESA-led 2018 mission to Mars, for which the two space agencies were planning to build a rover. NASA had planned to spend up to $1.2 billion on ExoMars.

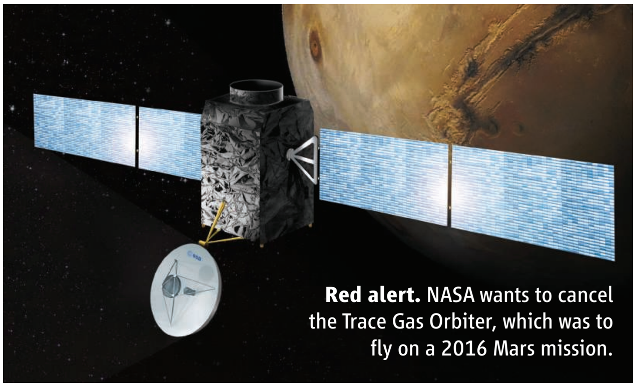

Red alert. NASA wants to cancel the Trace Gas Orbiter, which was to fly on a 2016 Mars mission.

Planetary scientists say that NASA's decision to withdraw from ExoMars is a devastating blow that will end U.S. leadership in Mars exploration after five successful missions to the Red Planet. "The Mars community cannot understand why they have been targeted when they have been so successful," says G. Scott Hubbard, who served as the first Mars program director at NASA and is now a professor at Stanford University in Palo Alto, California.

NASA Administrator Charles Bolden says the agency pulled the plug on ExoMars because "it was another multibillion-dollar flagship mission. Flagships are expensive. We just could not afford to do another one." But he says NASA isn't walking away from Mars. In August, a rover called Curiosity is scheduled to land and begin exploring the Red Planet, and next year NASA hopes to launch the Mars Atmosphere and Volatile Evolution Mission.

In lieu of ExoMars, officials are discussing a small 2018 mission that would still advance NASA's goal of sending humans to Mars by the mid-2030s. John Grunsfeld, the new head of the $5 billion Science Mission Directorate, wants scientists to provide ideas that NASA can use to plan a "basic mission" that "both answers scientific questions and supports future human exploration of Mars."

That approach puzzles planetary scientists. "You cut the budget by a significant amount, and you're going to send humans to Mars, which would be several times more expensive than a robotic mission," Hubbard says. "It doesn't make any sense." Jim Bell, an astronomer at Arizona State University in Tempe and head of the Planetary Society, says the Administration's decision to cancel ExoMars is all the more painful because the community "brought Mars back into the ball park" by scaling back the cost of the 2016 and the 2018 missions.

Bell and others believe the White House Office of Management and Budget (OMB) feared backing yet another project that would end up with massive cost overruns like so many NASA missions before it. "Some part of me can't fault OMB. It's up to NASA to demonstrate that we can estimate costs correctly and then stick to those estimates," Bell says. At the same time, he says, "it is the nature of complex, big projects that they end up costing more than anticipated."

The proposed cuts in the Planetary Science Division affect more than just ExoMars, notes Mark Sykes, head of the Planetary Science Institute in Tucson, Arizona. Designated funding to continue operating and analyzing data from Mars Reconnaissance Orbiter (MRO) would be eliminated. MRO's "HiRISE instrument only recently found evidence for seasonal water flow just below the surface of Mars," Sykes says. Funding for a program to prepare for a return to the moon would drop from $140 million to $61 million in 2013, and the outer planets program, which supports the ongoing Cassini mission to Saturn, would decline from $122 million to $84 million.

The flagship instrument on the Trace Gas Orbiter, much of which was being built at NASA's Jet Propulsion Laboratory (JPL) in Pasadena, California, would have measured the distribution of trace gases that could signal the presence of life on the planet. JPL's John Schofield is principal investigator on another instrument that aims to measure the global distribution of atmospheric temperature, dust, ices, and water vapor on a daily basis. Together, the instruments would have helped NASA prepare for future landings and human missions. Schofield says he and others "have been instructed to close out the 2016 mission in the next several months."

The elimination of ExoMars in the president's budget does not mean game over, says John Mustard, a planetary astronomer at Brown University and a member of the Mars advisory panel. "The Mars exploration community is a resilient one," he says. "We'll be thinking very hard on how to get these cuts reversed." **–YUDHIJIT BHATTACHARJEE**

CREDIT: ESA

Published by AAAS

U.S. SCIENCE BUDGET

Bigger Contribution to ITER Erodes Domestic Fusion Program

The U.S. fusion program is in a bind. To remain at the cutting edge, U.S. fusion researchers must participate in the huge international experiment called ITER being built in Cadarache, France. But to pay for ITER—which aims to produce a self-sustaining fusion reaction, or "burning plasma," and prove that fusion is a viable energy source—the United States may have to sacrifice the very community of researchers who would use the machine when it is ready.

That paradox hit home last week, when President Barack Obama submitted a 2013 budget request to Congress that would slash the nation's already beleaguered domestic fusion program while boosting the U.S. contribution to ITER. Contributing to ITER "is reasonable only in the context of a domestic program," says Martin Greenwald, a physicist at the Massachusetts Institute of Technology (MIT) in Cambridge and chair of the Department of Energy's (DOE's) Fusion Energy Sciences Advisory Committee (FESAC). "Otherwise, you're just building a piece of equipment for other people to use."

At first blush, the proposed 2013 budget for the fusion energy sciences program at DOE doesn't look so bad. It would dip by less than 1% to $398 million. However, within that flat budget, spending on ITER construction would increase by 43% next year, from $105 million to $150 million. As a result, spending on fusion research at home would fall 16%, to $248 million.

The effects of the cut would be dramatic. DOE supports three large experimental devices called tokamaks—doughnut-shaped chambers in which ionized gas, or "plasma," is confined by magnetic fields and heated and squeezed to the point at which atomic nuclei fuse and release energy. In the biggest blow, the tokamak at MIT, called the Alcator C-Mod, would shut down.

"I was shocked," says Miklos Porkolab, director of MIT's Plasma Science and Fusion Center. "I didn't have the vaguest idea of what was coming." C-Mod is the only U.S. tokamak that operates at magnetic fields as strong as ITER's will be, Porkolab says. It supports 100 staff members and 30 graduate students.

The budget of the United States's sole dedicated fusion lab, the Princeton Plasma Physics Laboratory (PPPL) in New Jersey, would drop by 16%, to $61.8 million. "If all the cuts go through, we would have to lay off about 100 of 435 staff," says PPPL Director Stewart Prager, who notes that the lab has already shrunk by two-thirds since the 1990s. The proposed cut for 2013 would stretch by 6 months an ongoing upgrade of the lab's National Spherical Torus Experiment, delaying the tokamak's restart until 2015.

Obama's budget request, if adopted by Congress, would leave the United States with only one tokamak operating next year, the DIII-D at General Atomics in San Diego, California. But its running time would be reduced to 10 weeks—3 weeks less than this year and a far cry from the 25 weeks that would constitute full utilization, says Tony Taylor, vice president of the magnetic fusion energy division at General Atomics. The cuts would also require axing 30 of 180 DIII-D staff and postponing key upgrades.

Even the proposed $150 million contribution to ITER in 2013 won't keep the United States on pace to meet its commitment to the project, says Stephen Dean, a physicist and president of Fusion Power Associates, a nonprofit research and education foundation in Gaithersburg, Maryland. That would require about $200 million, he says.

The budgetary train wreck is exactly what some researchers have long feared. When the United States signed on to ITER in 2003—as a junior partner alongside the European Union, China, India, Japan, Russia, and South Korea—its projected cost was $5 billion, making the U.S. share roughly $500 million. Now the price tag tops $20 billion, and the U.S. share has ballooned to $2.2 billion or more. At the same time, DOE's fusion budget has been flat for the past decade when adjusted for inflation.

Oddly, although the proposed budget would provide just $40 million for running facilities, it still provides $154 million for research. A typical operations-to-research ratio for a DOE program is 1:1. Why the imbalance? One reason is that much of that research might be done overseas. Last summer William Brinkman, director of DOE's Office of Science, asked FESAC to study the idea of sending legions of researchers to South Korea and China to work on new tokamaks that those countries have built. Its report is due this month, but scientists already have misgivings about that approach.

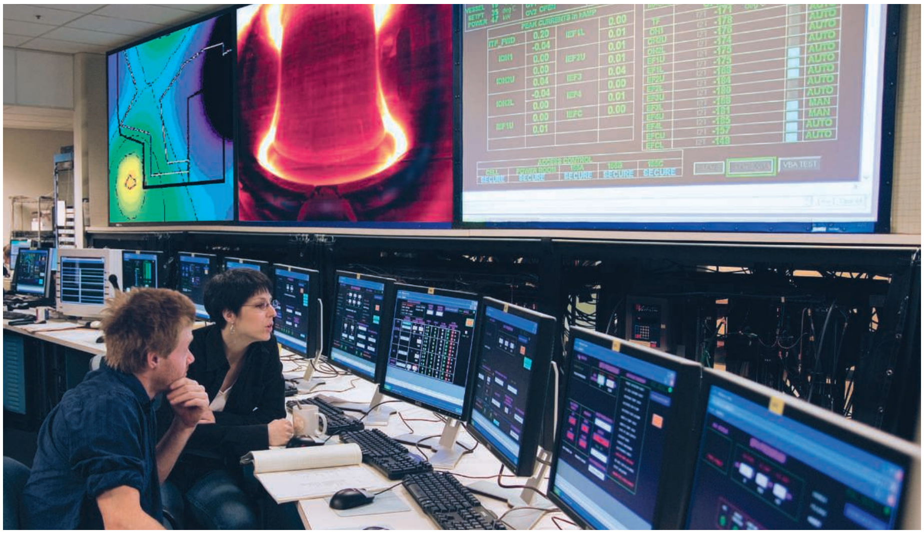

Lights out? With the device's glowing heart showing on the screen above them, students control MIT's tokamak, which could shut down next year.

CREDIT: PAUL RIVENBERG/M. P. MCNALLY

If nothing else, it will make it harder to attract younger scientists, researchers say. (Already, the 2013 budget would slash the number of student positions from 325 to 263.) The scheme also exports the country's most valuable resource: knowledge. "It makes no sense for the United States to pay to ship our intellectual capital overseas and make ourselves less competitive," Taylor says.

The proposed budget isn't a done deal. "I can tell you that the community does not support this plan, does not support this budget, and is going to try to get Congress to overturn it," Dean says. Brinkman agrees that "it makes no sense to invest in ITER if there isn't a base program" and suggests that the department may also be looking for help from Congress.

Published by AAAS

"This [budget] has to go to the Hill, and we'll see what the Hill does with it," he says.

Even if Congress kicks in the $50 million needed to shore up the domestic program next year, 2014 could be far worse. The United States will have to pony up $2 billion for ITER over 8 years, so its annual contribution will likely shoot up to $300 million, potentially consuming the whole domestic program.

Restructuring those payments may be the best short-term solution. Brinkman says that Office of Science staff members have begun talking to other Administration officials and ITER partners about such changes. "One thing you learn in this government town is you take it one year at a time," he says. But fusion physicists worry that such a tactical approach will only delay the demise of their research program.

Greenwald and other fusion scientists would like greater support from the Obama Administration. But presidential science adviser John Holdren says the Administration is doing what it can. "The cutting edge of fusion is determining whether we can create a burning plasma, and the only machine in the world that has a prospect of doing that is [ITER]," Holdren said last week during a rollout of the new budget when asked if ITER was being favored over the domestic program. But he added that "we are going to maintain a strong plasma science program and invest in ITER." **–ADRIAN CHO**

U.S. SCIENCE BUDGET

Advocates Win 'Exceptional' Boost for Alzheimer's Research

The 2013 budget proposed by President Barack Obama last week would give the National Institutes of Health (NIH) not a penny more than it received this year. But the Administration found a way to give special attention to one disease: Alzheimer's, which will receive $80 million in new research funding from a source outside NIH's budget. This month, the Administration also announced, to the surprise of many at NIH, that the agency will reprogram $50 million in its current budget for the disease.

Jackpot. HHS Secretary Kathleen Sebelius announces $156 million for Alzheimer's.

Alzheimer's research advocates credit the new focus to several years of organized lobbying. "It's persistence," says Harvard University's Rudolph Tanzi, who like many researchers in the Alzheimer's field has taken part in this effort to boost the roughly $450 million NIH already spends on the disease. Advocates say they've finally hammered home the message that the growing costs to Medicaid and Medicare of caring for Alzheimer's patients could eventually swamp the federal budget. "We kept pushing and saying, 'You guys are asleep here. You need to wake up,' " Tanzi says.

But in addition to such "compelling facts," says Robert Egge, vice president of public policy and advocacy for the Alzheimer's Association, this month's victory also reflects a series of steps that built bipartisan support in Congress and the Administration. "Congress is a stimulus-response organization," says Representative Edward Markey (D–MA), an Alzheimer's champion. Compared with cancer and AIDS, advocacy was hampered because the disease doesn't leave survivors, and families were reluctant to discuss it. "Recently, the Alzheimer's advocacy community has risen to overcome this unique challenge," Markey says.

Momentum began to build 5 years ago when current Republican presidential candidate Newt Gingrich, who has an interest in brain diseases, and George Vradenburg, a former television and AOL executive who became an Alzheimer's fundraiser, began working with Markey and a nonpartisan panel. Deliberately "independent," Vradenburg says, the Alzheimer's Study Group was co-chaired by Gingrich and Senator John Kerry (D–MA), and included former NIH Director Harold Varmus and former U.S. Supreme Court Justice Sandra Day O'Connor. Its 2009 report called for $1 billion in annual research funding.

Relentless lobbying led to the National Alzheimer's Project Act. It passed in December 2010 "in a very divided Congress" with strong White House support, notes Daniel Perry, president of the Alliance for Aging Research. The Department of Health and Human Services (HHS) has since formed a federal advisory committee; it recently set a deadline of 2025 for preventing and treating the disease. Last December, advocates met with White House officials, who said they were trying to find new funding for Alzheimer's in the 2013 budget, Perry says.

On 7 February, HHS Secretary Kathleen Sebelius announced that HHS had found $50 million in 2012 and $80 million in 2013 (and $26 million for related programs). Last week, HHS officials explained that the 2013 funding will come from the HHS Public Health and Prevention Fund, created by the 2010 health care law. "It took real budget legerdemain" to find the money, Perry says. It may run into opposition; some say the fund wasn't meant for this use.

NIH officials, meanwhile, are still working out the details of redirecting $50 million this year to Alzheimer's. About half of that sum—possibly from large DNA sequencing centers—will go for genetics. The other $25 million or so will likely fund high-quality grant proposals across institutes that fund Alzheimer's, says National Institute on Aging Director Richard Hodes. That will mean less money to fund research in other areas, Hodes says. He said that although $50 million out of NIH's $31 billion budget "is not very large" (it's 0.16%), at a time of record-low grant success rates, "there will undoubtedly be people who will be concerned." He added: "This is something that should happen only in the most exceptional of circumstances, and in this case the Administration has determined this urgency of Alzheimer's and its demographics to be such a circumstance."

Tanzi acknowledges that squeezing other areas is a "downside" to the 2012 funding. And he admits that the wildly ambitious 2025 goal is "not scientific." (The Alzheimer's advisory panel plans to release its plan for getting there in time for an Alzheimer's summit at NIH in May.) But to mobilize advocates and policymakers, "you have to do things like this," Tanzi says. **–JOCELYN KAISER**

CREDIT: CHRIS SMITH/HHS PHOTO

Published by AAAS

U.S. SCIENCE BUDGET

Kansas Veterinary Biosecurity Lab Trampled in Spending Plan

Home on the range. NBAF's Manhattan, Kansas, site is ready for construction, but funding is in doubt.

It's an irony as thick as a T-bone steak: A flagship government biodefense laboratory set to be built in Kansas is facing critical funding troubles—in part because of fierce opposition from cattle ranchers the facility is supposed to help.

Last week, the Obama Administration announced that it is requesting no new money in its 2013 budget plan for the National Bio and Agro-Defense Facility (NBAF), a highly secure veterinary research center that is supposed to study viruses and other agents that could threaten livestock and human health. In addition, officials at the U.S. Department of Homeland Security (DHS), which is funding NBAF, said they were convening a special task force to reassess "whether and for what purpose a Bio-Safety Level 4 (BSL-4) facility should be stood up." BSL-4 labs are designed to contain the most dangerous pathogens.

The announcement delighted NBAF opponents, including livestock interests who fear a devastating disease could escape from the facility into the heart of cattle country. "This was an irresponsible, unsafe plan from the beginning, and we're pleased to see that the tide is turning against it," said Bill Bullard, the head of the Ranchers-Cattlemen Action Legal Fund, United Stockgrowers of America (R-CALF USA) of Billings, Montana. The group, which represents thousands of livestock growers, has worked closely with Montana Senator Jon Tester (D) and other members of Congress to block funding for the facility.

Kansas lawmakers, however, are vowing to save NBAF. "It's going to be a fight," predicted Governor Sam Brownback (R), who has committed $150 million in state funds to the facility, scheduled to be built near Kansas State University in Manhattan. In Congress, NBAF allies spent much of last week attempting to extract promises to move ahead with NBAF from senior Obama Administration officials, with mixed results. "This nation needs a BSL Level 4 facility" for studies related to agriculture, DHS Secretary Janet Napolitano told the House Appropriations Committee during a 15 February hearing. But "this is one of those issues that I think requires serious conversations with the Congress," she added, noting that "we have had trouble getting the money for the NBAF the last few years." Last year, for instance, the Administration requested $150 million for NBAF, but Congress provided just $50 million—part of a compromise after the Senate voted to provide no funds.

Such lukewarm congressional support stems, in large part, from continuing controversy surrounding the safety and cost of the proposed lab, which is supposed to replace the aging Plum Island Animal Disease Center in New York. The BSL-3 center, located on an isolated shoal off the coast of Long Island, is the only place in the United States where researchers can work with certain pathogens, such as the virus that causes foot-and-mouth disease, which has caused extensive livestock losses in other nations. In the wake of 9/11, some scientists argued that the United States needed a more modern, secure, and better-situated facility, and in 2008, DHS awarded the new NBAF to Kansas after a competition (*Science*, 12 December 2008, p. 1620). Less than a year later, however, Congress requested a study by the Government Accountability Office that ultimately slammed DHS's safety studies (*Science*, 7 August 2009, p. 661), and a 2010 assessment by a National Academies panel raised similar concerns. Meanwhile, an accounting scandal enveloped the state-funded group that had managed Kansas's winning bid, and NBAF's projected cost began to escalate, from about $450 million to up to $1 billion by some estimates.

These developments gave NBAF opponents, such as R-CALF USA and Representative Tim Bishop (D–NY), whose district includes Plum Island, plenty of political ammunition and apparently persuaded the Administration to abandon NBAF for now. "Even in the best fiscal situation, NBAF as currently proposed would be difficult to justify; in our current climate it is simply unaffordable," Bishop said in a statement. Instead, the government should fix up Plum Island, he says—but not to BSL-4 standards (which locals oppose). He also wants the government to suspend plans to sell the island; in the past, DHS officials had said the sale might help pay for NBAF.

In the meantime, DHS officials are organizing an interagency task force to take a fresh look. "We are going to ask the question, do we need to build a BSL-4 lab to tackle these threats—yes or no?" says Tara O'Toole, the head of the department's Science and Technology Directorate. If the answer is yes, O'Toole says, DHS could make the case to the White House for reinstating the plan in next year's budget.

–DAVID MALAKOFF

With reporting by Yudhijit Bhattacharjee.

CREDITS (TOP TO BOTTOM): NBAF DESIGN PARTNERSHIP; ERIC DURBAN/HARVEST PUBLIC MEDIA

Published by AAAS

INDIA RISING

India excels in rocketry and nuclear science but has produced few breakthroughs in other fields. Now, free of sanctions and swimming in cash, the world's largest democracy is gunning for status as a scientific powerhouse

BANGALORE, INDIA—When A. P. J. Abdul Kalam, the father of India's missile program, inaugurated a center of excellence in aerodynamics here last November, he emphasized how the new facility would boost the nation's defenses. Indo-Russian missilemaker BrahMos Aerospace helped bankroll the center at the Indian Institute of Science (IISc) Bangalore as a testing ground for its next-generation BrahMos-II missiles and hypersonic space vehicles. Indeed, after the ceremony, Kalam, the octogenarian former president of India, urged BrahMos to think grander and pioneer a reusable hypersonic cruise missile that would return after dropping a payload—a feat that could rival technology under development in the United States.

In a hangar here on the IISc Bangalore campus, BrahMos projects and other sensitive ventures are hidden behind black curtains. The military R&D is the center of excellence's raison d'être and a jewel in the crown of India's vaunted defense R&D establishment. But what's out in the open in the cavernous laboratory is far more revealing about the rapid development and entrepreneurial spirit of Indian science.

"I want to show you our latest invention," says aerospace engineer K. P. J. Reddy, head of IISc's Laboratory for Hypersonic and Shock Wave Research. He walks past a 16-meter-long steel shock tunnel, stops at a lab bench, and picks up what looks like an ordinary medical syringe. It's outfitted with a "Reddy tube": a shock tunnel writ small that's capable of generating shock waves traveling at twice the speed of sound. Applications abound. One Reddy tube called "Super Bull" boosts the success of livestock artificial insemination by slinging sperm deep into the uterus. A micro–Reddy tube delivers DNA through a nuclear membrane for cell transformation. Another is a juicer: Aim it at an apple, and shock waves disintegrate pulp while leaving the skin intact. "Juice doesn't get any fresher," Reddy says.

Such bench-top derring-do may seem incongruent with India's reputation as a champion of Big Science. After the nation's first atomic bomb test in 1974, the United States and other countries slapped sanctions on India that squeezed its supply of high-tech equipment and materials. Over the next 3 decades, India grew an indigenous civilian nuclear power industry and a space program on par with those of leading nations. In 2008, a landmark civilian nuclear pact between India and the United States beckoned Indian scientists in strategic sectors to come in from the cold; access to imported precision instruments is allowing India to make up ground in areas such as nanotechnology and supercomputing.

Now the government intends to lift all disciplines on a rising tide. At the Indian Science Congress in Bhubaneswar last month, Prime Minister Manmohan Singh pledged to hike R&D expenditures during the 5-year plan that begins this spring, from around \$3 billion last year to \$8 billion in 2017. In an exclusive interview with *Science* (see p. 907), Singh explained how his government plans to "increase gradually the proportion of money that is spent on R&D and at the same time create a system of incentives which will induce the private sector to increase their spending on science and technology."

The windfall is meant to turbocharge initiatives under way to create elite research institutions, bring expatriate Indian scientists home, enrich science education, and equip smart new laboratories. Included in this push

Online
sciencemag.org
Podcast interview (http://scim.ag/pod_6071) with co-author Pallava Bagla.

CREDITS: ALL PALLAVA BAGLA EXCEPT BUTTERFLY: LAKSHMI NARAYANAN K./WIKIMEDIA COMMONS; RICE FIELDS: ISTOCKPHOTO.COM; FLAG: WIKIMEDIA COMMONS; JANTAR MANTAR ASTRONOMICAL OBSERVATORY: JOERG HACKEMANN/FOTOSEARCH

is South Asia's first biosafety level–4 lab for handling the most dangerous pathogens, slated to be up and running at the National Institute of Virology in Pune this spring. "Funding is no longer a constraint. What we once had to do abroad we can now do here," says Govindaraju Thimmaiah, a chemist at the Jawaharlal Nehru Centre for Advanced Scientific Research here. Over the next 5 years, an estimated $1.2 billion in public funds will be funneled to a new National Science and Engineering Research Board. Modeled after the U.S. National Science Foundation, the board is just now getting off the ground and is expected to fund its first competitive grants this year. "It's critical to our future, because it's run by scientists for scientists," says Raghunath "Ramesh" Mashelkar, former director general of the Council of Scientific and Industrial Research (CSIR), a national network of 37 laboratories.

Researchers will have to clear some daunting hurdles, though. India's legendary bureaucracy can snarl grant proposals and expenditures in red tape for months. The anticipated R&D budget boost "will be useless if structural reform is not undertaken," warns vaccine specialist Maharaj Kishan Bhan, secretary of the Department of Biotechnology, the central government's main conduit for supporting applied biology in India. Another woe is that scores of universities are deteriorating or riddled with corruption. They nurture few stars and are overburdened with dead wood. "On a day-to-day basis, people are discouraged from doing breakthrough research," says Raghavendra Gadagkar, a sociobiologist at IISc Bangalore. "Our system creates followers, not leaders. That's our biggest problem."

Still, the scientific outlook is brightening rapidly. From 2000 to 2010, India's peer-reviewed publications more than doubled to 40,000 a year, its world share rose from 2.2% to 3.4%, and citation impact improved from 40% to nearly 60% of the world average, according to the Thomson Reuters Web of Knowledge database. Moreover, Indian scientists are keenly aware of the need for research that raises living standards in the world's largest democracy, home to 1.2 billion people. "We are promoting what we call 'inclusive innovation,'" says Mashelkar, who like other top scientists here believes that a new day is dawning for Indian science.

Big bang theory

For many Indian researchers, a long night preceded the dawn. When Mashelkar, a chemist, returned to India in 1976 after a postdoc stint in the United States, he says it was a struggle to keep pace with his field. Scientific journals took 4 months to arrive by mail. "We were out of competition before we started," he says. Everything was difficult and slow. Mashelkar waited 6 years for installation of a phone line because he refused to pay an exorbitant fee for

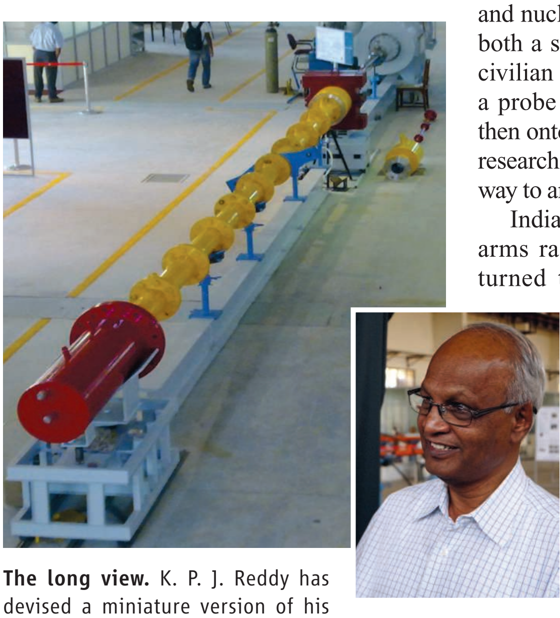

The long view. K. P. J. Reddy has devised a miniature version of his lab's shock tunnel (*above*) for applications as diverse as artificial insemination and cell transformation. Over the past 20 years, Indian scientists have expanded their reach in the literature.

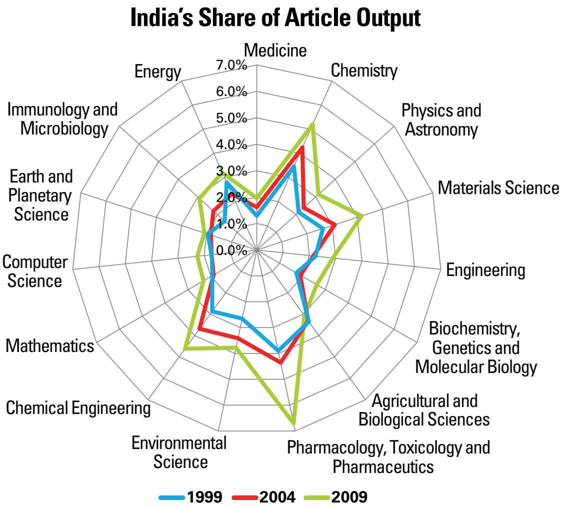

faster service. C. N. R. Rao, Singh's science adviser and a chemist at the Jawaharlal Nehru Centre for Advanced Scientific Research here, recalls that as a young professor decades ago he would receive the equivalent of about $60 per year for research. "I got my first spectrometer 17 years into my career and first electron microscope 30 years into my career," he says. Rao—éminence grise and India's most-cited scientist—was exceptionally productive. In the sprawling field of biology, "I don't think there were any breakthroughs in India" for decades, says L. S. Shashidhara, a geneticist at the Indian Institute of Science Education and Research (IISER) in Pune.

While basic research and living standards languished, India was pouring massive resources into two strategic areas: rocketry and nuclear science. The former gave rise to both a sophisticated missile program and a civilian space program that intends to send a probe to Mars and astronauts into space then onto the moon (see p. 906). India's early research on nuclear power, meanwhile, led the way to an atomic arsenal.

India's first atomic test ignited a nuclear arms race with China and Pakistan—and turned the nation into a nuclear pariah: Western countries banned most high-tech exports to India. Self-reliance promoted technological ingenuity, as India's nuclear and space programs have demonstrated on numerous occasions. India's research on using thorium as fuel for nuclear power reactors is nonpareil, and this year it will bring online a homemade prototype fast breeder plutonium reactor. Denied access to radiation-hardened computer chips and lightweight silica tiles for satellites, Indian space researchers developed their own.

The demise in 1991 of the Soviet Union, then India's main ally, was a turning point. India narrowly averted a financial meltdown. "CSIR had a tough time even to pay its electricity bills," recalls biophysicist Samir Brahmachari, CSIR's director general. Singh, as finance minister in the early '90s, engineered radical reforms that steered India from socialism to a free market economy. A few years later, the country's information technology industry took off—and "started taking away all the bright students," says chemical biologist Krishna Ganesh, director of IISER Pune.

Another signature Singh accomplishment was the Indo-U.S. nuclear agreement, which paved the way for the export of high-tech instruments and sensitive materials to India. Institutes across the country have since gone on a spending spree.

Muscling up

In a corner of IISc Bangalore down the road from the aerospace hangar, workers are putting the finishing touches on a

CREDITS (TOP TO BOTTOM): COURTESY OF K. P. J. REDDY; R. STONE/*SCIENCE*; ELSEVIER SCOPUS

Published by AAAS

$30 million, 1300-square-meter clean lab for nanotechnology. It's instrumented to the hilt. "Money is not much of a problem," says materials scientist Srinivasan Raghavan, one of four IISc Bangalore researchers who are helping midwife the new lab. All is not flawless: Raghavan and his colleagues suffer "supply-chain" delays due to Indian import regulations, he says, and a sanctions hangover. It took several months, for instance, to import a 2-centimeter-square piece of ultrathin zirconia foil for experiments with nanoporous zirconium. That foil is used in the nuclear industry, and despite the easing of restrictions, some countries still hesitate to export high-tech equipment and materials to India, says IISc Bangalore's S. A. Shivashankar, who got the ball rolling on the nanotech lab a decade ago. It will be fully operational next month and is expected to churn out 50 Ph.D. scientists a year.

State-of-the-art facilities are popping up far and wide. Ensuring their smooth operation is a challenge, however. "We readily can purchase expensive equipment," Shashidhara says. But he and others are frustrated over Indian regulations that limit spending on reagents and other research materials. "The government tells us to cut down consumables. It's considered waste."

The main impediment, scientists often say, is the bureaucracy. "Even the best of intentions can disappear without a trace in the quicksands of officialdom," IISc Bangalore Director Padmanabhan Balaram penned in an editorial last month in India's premier journal, *Current Science*. There's a lack of transparency. And bureaucrats sometimes demand that researchers give a regular accounting of progress on their grants. According to IISc Bangalore's Gadagkar, who studies social behavior of wasps, "I will be evaluated as if I was building a road. They want a report every 3 kilometers."

On the bright side, Indian researchers will have more opportunities to explain how they are spending their money. Major directions in the next 5-year plan include a $350 million Neutrino Observatory in Theni—India's single largest investment to date in basic

Continued on page 909

Dreaming small. IISc Bangalore's Srinivasan Raghavan and S. A. Shivashankar will roll out their nanotechnology clean lab next month.

Ad Astra, With a 'Uniquely Indian Flavor'

BANGALORE, INDIA—India's space program has a bold agenda this year: It aims to launch five rockets and four satellites, all built at home. The Indian Space Research Organisation (ISRO) already has 11 remote-sensing satellites in orbit—the largest constellation of civilian eyes in the sky. This record puts India securely in the global space club.

Part of India's achievement is to have joined at a modest cost. ISRO's $1.5 billion annual budget is almost 10 times smaller than NASA's. But its dreams are not modest. In the coming years, ISRO plans planetary exploration missions, a reusable launch vehicle, and a program to send astronauts into space. "In a very tough economic environment, India remains one of the few countries in the world which maintains and even reinforces its space program," says Jean-Yves Le Gall, chair and CEO of Arianespace in Paris. "This is absolutely remarkable."

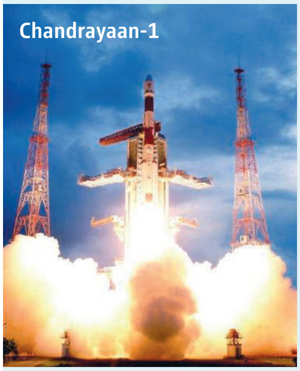

In its 5-year plan submitted last month, ISRO sets some concrete goals. One is to see that its big rocket—the Geosynchronous Satellite Launch Vehicle (GSLV)—becomes "a reliable vehicle." The GSLV can put a 2-ton communications satellite in orbit; a new version is designed to launch 4-ton satellites. But GSLV's record is spotty. Only two of seven launches have been fully successful. One of the liquid cryogenic upper stages—designed in India—packed up within seconds after ignition in an April 2010 launch. Retooling it is a top priority.

On the scientific front, last October, India launched Megha-Tropiques, an Indo-French satellite to collect data on water and energy balance over the tropics. This mission marked the 19th consecutive successful launch of India's smaller rocket, the Polar Satellite Launch Vehicle. After lengthy delays, ISRO plans to use that rocket in 2013 to orbit its first dedicated astronomy satellite, Astrosat, which will be equipped with a suite of telescopes to view the sky in optical, infrared, ultraviolet, and gamma wavelengths.

ISRO's greatest claim to fame is the scintillating finding of water on the moon. Instruments aboard the 2008–09 Chandrayaan-1 probe, a bargain at about $100 million, uncovered water molecules on the lunar surface. The finding demonstrates that "the moon can support long-term human presence, a discovery of vital significance to man's future in space," says Paul D. Spudis, a lunar scientist at the Lunar and Planetary Institute in Houston, Texas, who ran a radar experiment aboard Chandrayaan-1 that detected traces of water. India is planning a return trip to the moon with a lander and rover in 2014. Also in the works is a solar mission in 2014 called Aditya and, in the next 5 years, an asteroid flyby. And while NASA earlier this month revealed that it has canceled a pair of upcoming Mars missions, ISRO is sketching out a robotic mission to Mars within a decade.

Whereas the United States has given up on shuttles, India now wants to build its own. Recyclable technology would sharply reduce launch costs, ISRO says. A first-generation vehicle would lift off vertically and land in the sea; later models would glide to a runway. A prototype is housed at a secret facility in Kerala, says ISRO Chair K. Radhakrishnan.

The defining moment for India's space program will come when India sends humans into space, Radhakrishnan says. ISRO has proposed a massive $2.5 billion project. Within 7 years of receiving government approval, India could orbit a few astronauts for a week, then later send them to the moon, Radhakrishnan says.

The government has approved about $25 million for preliminary studies "to wet our hands" with technology involved in human space flight, Radhakrishnan says. The big project may run into resistance. Asked whether this is the right thrust for Indian science, C. N. R. Rao, science adviser to Indian Prime Minister Manmohan Singh, said, "I have nothing against man going anywhere, but I am more worried about people on this earth." In an interview with *Science*, Singh declined to endorse the human space flight program (see p. 907).

Radhakrishnan is confident that ISRO's vision will prevail. "India is poised to soar higher in space," he says. "But it will be done with a uniquely Indian flavor." **–P.B.**

CREDITS (*TOP TO BOTTOM*): ISRO; R. STONE/*SCIENCE*

Published by AAAS

Continued from page 906

research—a novel open-source drug discovery program (see sidebar below), a $1 billion supercomputing initiative, and an effort to improve forecasts of the summer monsoon (see p. 910). At the science congress last month, Singh also vowed to double public and private R&D spending as a percentage of GDP to 2% by 2017. That will require much higher expenditures from the private sector, which currently contributes a mere 33% of total R&D spending.

Some observers wonder whether India's scientific community can make good use of the windfall. By Western standards, few disciplines or institutes have built up a critical mass. "The entire biology community of India is smaller than that of Boston," Shashidhara says. In genetics and development, he says, "many people are just doing gap-filling work." Researchers in other disciplines voice similar complaints. "In any given area of science or engineering, the number of experts is rather small in India," says Rao, who says that nationwide only five or six researchers are studying graphene—one of the hottest areas of materials science.

To build capacity, the government is wooing overseas talent through fellowship programs. "There's a concerted movement to bring people back," says Savita Ayyar, head of the research development office at the National Centre for Biological Sciences (NCBS) here. And scientists on their own have organized "Young Investigator Meetings" in U.S. cities meant to entice newly minted Ph.D.s and postdocs.

Feeling caged in. The Indian system discourages breakthrough research, says sociobiologist Raghavendra Gadagkar, who studies wasp behavior.

Science for the masses

The flip side of the shortage of well-trained researchers is the inadequacy of labs and institutes. Most of the 350-odd state universities "are terribly run," Ganesh says. Few can brag of world-class research. "They're broken down," says physical chemist Sourav Pal, director of the National Chemical Laboratory in Pune. This is a legacy of the Cold War years. After independence in 1947, India adopted a Soviet-style academic system in which "undergraduate teaching was decoupled from research," Ganesh says. Then a decade ago came a "great awakening," he says: "We realized we needed to merge teaching and research."

One obstacle to reform is India's employment laws. Researchers of any caliber can easily gain tenure. At the same time, scientific stars have limited opportunities to advance in salary or rank. "Administrations must follow the policy of benign neglect with respect to high performers, even while turning a blind eye to the significant dead wood accumulating in our institutions," Balaram noted in his editorial.

As a cure, the government has opted to spawn new institutions. In the past 5 years, Singh has presided over an expansion of

Crowd-Sourcing Drug Discovery

NEW DELHI—Each year, India tallies an astounding 1.7 million cases of tuberculosis (TB). Some 400,000 people succumb to the disease, making it the leading cause of death in India for those in the prime of life, from 15 to 45 years old. Most victims are poor, and pharmaceutical companies have little incentive to develop new drugs against the bug that causes TB, *Mycobacterium tuberculosis*. But the Indian government has a big incentive to reduce the disease burden.

Faced with this conundrum, Samir Brahmachari had a brainstorm a few years ago: crowd-sourcing. "That means looking for experts you don't know exist," he says. "I wanted to do something very different." So in 2008, Brahmachari, a biophysicist and director general of the Council of Scientific and Industrial Research (CSIR), India's largest network of scientific laboratories, launched the Open Source Drug Discovery (OSDD) network. Modeled after the open-source software community, OSDD's army of volunteers is building a kind of Wikipedia on TB. Some 5500 participants in 130 countries respond to "work packages" posted by OSDD: questions on everything from the biology of *M. tuberculosis* to leads on drugs; answers are tagged and credited.

"OSDD is an exciting new approach to drug discovery," says Melvin Spigelman, president of the TB Alliance in New York City. "It provides the opportunity for virtually a limitless number of scientists to contribute to the solution of any given problem." The Indian government gave OSDD $12 million in seed money; CSIR has requested $200 million over the next 5 years as the program ramps up for clinical trials and expands to other neglected diseases such as malaria and leishmaniasis, and possibly even cancer. "Drug discovery," Brahmachari says, "is too serious a business to be left solely in the hands of pharmaceutical companies."

The first challenge that OSDD's cyber-community assigned itself was to glean more information from the *M. tuberculosis* genome. It was sequenced in 1998, but researchers had clues to the functions of only a quarter of its 4000 genes. In December 2009, OSDD set out to reannotate all possible genes. Some 500 volunteers got the job done in a mere 4 months. Now OSDD is trying to exploit these data. "The more people you put to work on the problem, the more chances you will have to identify the set of compounds that will likely make it through compound optimization, animal models, preclinical, and, eventually, clinical trials. If you increase your success chances, then your overall costs decrease," says Marc Marti-Renom of the National Center for Genomic Analysis in Barcelona, Spain.

Open-source guru. CSIR's Samir Brahmachari.

OSDD's iterative approach has identified two drug candidates that it has contracted for testing. Under OSDD rules, data from program-sponsored clinical trials must be open for all to see—"a clear alternative," OSDD states, "to expensive clinical trials conducted in secrecy at high costs." OSDD drugs will be available in the developing world as generics, Brahmachari says. "When it comes to health, we need to have a balanced view between health as a right and health as business," he says. For TB and other neglected diseases, drug companies might embrace that philosophy. For cancer, all bets are off. **–P.B.**

CREDITS (TOP TO BOTTOM): R. STONE/SCIENCE; PALLAVA BAGLA

Published by AAAS

Drawing a Bead on India's Enigmatic Monsoon

NEW DELHI—India's booming economy is still a gamble on the monsoon. In any given year, if rainfall climbs more than 10% above a long-term monsoon average, floods ensue. If it declines more than 10% below average, a drought is declared. Slippage in either direction brings misery. For example, a drought in 2002 shrank India's GDP by an estimated 5.8%. Every meteorologist's dream here is to accurately predict the monsoon's arrival, distribution, and departure. Toward that end, this year the Ministry of Earth Sciences is launching a 5-year, $75 million "monsoon mission" to improve the study of complex ocean-atmosphere interactions.

India receives 105 cm of rainfall on average per year, 80% carried on southwest winds that sweep in from the Indian Ocean from June to September. A winter monsoon also brings moisture from the northeast. Farming is heavily dependent on the exact timing of the rain, especially where it is needed to germinate seed. Since official record-keeping began 137 years ago, the monsoon has never failed to arrive, and it has never delivered less than 75 cm of rain. But the spatial and temporal variations are vast—and this is what befuddles scientists. "Every year, the monsoon is peculiar in its own way," says atmospheric scientist Jayaraman Srinivasan of the Indian Institute of Science in Bangalore.

Extreme misfortune. A farmer in Orissa examines his parched field in 2003.

The India Meteorological Department here issues monsoon forecasts but has not been able to accurately predict when the worst floods and droughts will occur. "Extremes are really difficult to forecast," says Ajit Tyagi, the department's former director general. Everything needs closer study: how clouds form, develop, and die—and, crucially, how global warming will change the monsoon.

India's "current prediction capabilities are inadequate," concedes geologist Shailesh Nayak, secretary for the Earth Sciences Ministry. A big bottleneck, he says, is a shortage of trained scientists. By Nayak's estimate, over the next 5 years India will need about 1200 skilled meteorologists, but today has only about 350. The ministry has just launched a recruitment campaign.

In the new initiative, Indian scientists and overseas colleagues will try to adapt computer models developed by the U.K. Met Office and the U.S. National Centers for Environmental Prediction for long-range forecasting in India. The mission will also make use of data pouring in from Megha-Tropiques, an Indo-French satellite launched in October to monitor water and energy balance over the tropics. The Indian Institute of Tropical Meteorology in Pune will take the lead in seasonal forecasts and prediction of active and break periods of the monsoon. A key aim is to produce a prediction model that uses open-source software such as Linux.

The collaborative effort, Tyagi hopes, may at last "unravel the enigma that surrounds the Indian monsoon."

–P.B.

the education and research system not witnessed since the 1940s. Back then, the country's first prime minister, Jawaharlal Nehru, saw research labs as the "temples of modern India" and set in motion the creation of the elite Indian Institutes of Technology.

An impressive new phenomenon is the Indian Institutes of Scientific Education and Research, of which there are now five. The decision to establish them was controversial. "A lot of people were against the IISERs. They thought, 'Why not upgrade existing universities?' " Pal says. Skeptics warned that there wouldn't be enough skilled instructors to go around. The rapid buildup in fact has meant uneven faculties at some institutes. "If you can't get teachers who are qualified, you start compromising," Mashelkar says. Critics also say that the IISERs will skim off talented high school science grads, leaving impoverished universities in worse condition.

"We need to find ways to attract intelligent students into science," Ganesh says. Toward that end, the government's Department of Science and Technology hopes to hook youngsters on science through INSPIRE—Innovation in Science Pursuit for Inspired Research—a 5-year, $500 million program that hands out $125 grants to top science students at every high school in the nation. "We hope to catch them young and build a cadre of top-quality researchers," says T. Ramaswami, secretary of the Department of Science and Technology in New Delhi. He spearheads this ambitious scheme, which aims to have supported 1 million students by the end of next year.

Institutes, meanwhile, are striving to close the gap between education and research. IISER Pune, for instance, encourages its undergraduates to join labs and author publications. And CSIR is venturing into the teaching business. Last year, it established an accredited institution that's gunning for 6000 students. "It's a very important break from the Soviet model," Pal says.

One long-standing problem for science faculties is that many top graduates turn up their noses at academic careers. They flock to information technology, where companies offer large entry-level salaries. Meanwhile, those who stick with science tend to go overseas for postdocs, depriving Indian labs of the creative sparks that are the hallmark of labs in Europe and the United States. Stints in overseas labs are seen as a ticket to a decent position back in India. "People think you need to go abroad to get a job here," says NCBS neuroscientist Sumantra Chattarji.

Hoping to show that's not necessarily the case, the Department of Biotechnology and the U.K.'s Wellcome Trust teamed up in 2008 to create a 5-year, $140 million fellowship program for up to 375 young investigators in India. "Now we're able to create an environment and mechanisms for postdocs to stay here," Ayyar says. "You might think this is a small step. But it's about changing the way people think."

As India's economy roars and Western nations limp along, the trickle of talented expatriates returning home may turn into a flood. "You can be richer in India as an assistant professor than in the United States," says Ganesh, who says that new recruits to IISER Pune receive royal treatment. "We give them whatever they want to start up a lab." His institute may be a new kid on the block. But considering the climate for science in India these days, Ganesh says, "I have no excuse to fail."

Minding the gap. Krishna Ganesh is melding teaching and research.

–RICHARD STONE

With reporting by Pallava Bagla.

CREDITS (TOP TO BOTTOM): PALLAVA BAGLA; R. STONE/SCIENCE

$30 million, 1300-square-meter clean lab for nanotechnology. It's instrumented to the hilt. "Money is not much of a problem," says materials scientist Srinivasan Raghavan, one of four IISc Bangalore researchers who are helping midwife the new lab. All is not flawless: Raghavan and his colleagues suffer "supply-chain" delays due to Indian import regulations, he says, and a sanctions hangover. It took several months, for instance, to import a 2-centimeter-square piece of ultrathin zirconia foil for experiments with nanoporous zirconium. That foil is used in the nuclear industry, and despite the easing of restrictions, some countries still hesitate to export high-tech equipment and materials to India, says IISc Bangalore's S. A. Shivashankar, who got the ball rolling on the nanotech lab a decade ago. It will be fully operational next month and is expected to churn out 50 Ph.D. scientists a year.

State-of-the-art facilities are popping up far and wide. Ensuring their smooth operation is a challenge, however. "We readily can purchase expensive equipment," Shashidhara says. But he and others are frustrated over Indian regulations that limit spending on reagents and other research materials. "The government tells us to cut down consumables. It's considered waste."

The main impediment, scientists often say, is the bureaucracy. "Even the best of intentions can disappear without a trace in the quicksands of officialdom," IISc Bangalore Director Padmanabhan Balaram penned in an editorial last month in India's premier journal, *Current Science*. There's a lack of transparency. And bureaucrats sometimes demand that researchers give a regular accounting of progress on their grants. According to IISc Bangalore's Gadagkar, who studies social behavior of wasps, "I will be evaluated as if I was building a road. They want a report every 3 kilometers."

On the bright side, Indian researchers will have more opportunities to explain how they are spending their money. Major directions in the next 5-year plan include a $350 million Neutrino Observatory in Theni—India's single largest investment to date in basic

Continued on page 909

Dreaming small. IISc Bangalore's Srinivasan Raghavan and S. A. Shivashankar will roll out their nanotechnology clean lab next month.

Ad Astra, With a 'Uniquely Indian Flavor'

BANGALORE, INDIA—India's space program has a bold agenda this year: It aims to launch five rockets and four satellites, all built at home. The Indian Space Research Organisation (ISRO) already has 11 remote-sensing satellites in orbit—the largest constellation of civilian eyes in the sky. This record puts India securely in the global space club.

Part of India's achievement is to have joined at a modest cost. ISRO's $1.5 billion annual budget is almost 10 times smaller than NASA's. But its dreams are not modest. In the coming years, ISRO plans planetary exploration missions, a reusable launch vehicle, and a program to send astronauts into space. "In a very tough economic environment, India remains one of the few countries in the world which maintains and even reinforces its space program," says Jean-Yves Le Gall, chair and CEO of Arianespace in Paris. "This is absolutely remarkable."

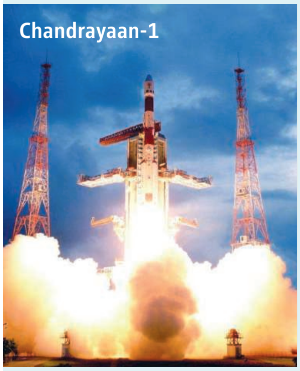

Chandrayaan-1

In its 5-year plan submitted last month, ISRO sets some concrete goals. One is to see that its big rocket—the Geosynchronous Satellite Launch Vehicle (GSLV)—becomes "a reliable vehicle." The GSLV can put a 2-ton communications satellite in orbit; a new version is designed to launch 4-ton satellites. But GSLV's record is spotty. Only two of seven launches have been fully successful. One of the liquid cryogenic upper stages—designed in India—packed up within seconds after ignition in an April 2010 launch. Retooling it is a top priority.

On the scientific front, last October, India launched Megha-Tropiques, an Indo-French satellite to collect data on water and energy balance over the tropics. This mission marked the 19th consecutive successful launch of India's smaller rocket, the Polar Satellite Launch Vehicle. After lengthy delays, ISRO plans to use that rocket in 2013 to orbit its first dedicated astronomy satellite, Astrosat, which will be equipped with a suite of telescopes to view the sky in optical, infrared, ultraviolet, and gamma wavelengths.

ISRO's greatest claim to fame is the scintillating finding of water on the moon. Instruments aboard the 2008–09 Chandrayaan-1 probe, a bargain at about $100 million, uncovered water molecules on the lunar surface. The finding demonstrates that "the moon can support long-term human presence, a discovery of vital significance to man's future in space," says Paul D. Spudis, a lunar scientist at the Lunar and Planetary Institute in Houston, Texas, who ran a radar experiment aboard Chandrayaan-1 that detected traces of water. India is planning a return trip to the moon with a lander and rover in 2014. Also in the works is a solar mission in 2014 called Aditya and, in the next 5 years, an asteroid flyby. And while NASA earlier this month revealed that it has canceled a pair of upcoming Mars missions, ISRO is sketching out a robotic mission to Mars within a decade.

Whereas the United States has given up on shuttles, India now wants to build its own. Recyclable technology would sharply reduce launch costs, ISRO says. A first-generation vehicle would lift off vertically and land in the sea; later models would glide to a runway. A prototype is housed at a secret facility in Kerala, says ISRO Chair K. Radhakrishnan.

The defining moment for India's space program will come when India sends humans into space, Radhakrishnan says. ISRO has proposed a massive $2.5 billion project. Within 7 years of receiving government approval, India could orbit a few astronauts for a week, then later send them to the moon, Radhakrishnan says.

The government has approved about $25 million for preliminary studies "to wet our hands" with technology involved in human space flight, Radhakrishnan says. The big project may run into resistance. Asked whether this is the right thrust for Indian science, C. N. R. Rao, science adviser to Indian Prime Minister Manmohan Singh, said, "I have nothing against man going anywhere, but I am more worried about people on this earth." In an interview with *Science*, Singh declined to endorse the human space flight program (see p. 907).

Radhakrishnan is confident that ISRO's vision will prevail. "India is poised to soar higher in space," he says. "But it will be done with a uniquely Indian flavor." **–P.B.**

CREDITS (TOP TO BOTTOM): ISRO; R. STONE/*SCIENCE*

Academic to the core. Manmohan Singh is reshaping the higher education landscape.

CREDIT: CHANNI ANAND/AP PHOTO

Q&A: MANMOHAN SINGH

India's Scholar–Prime Minister Aims For Inclusive Development

NEW DELHI—Indian Prime Minister Manmohan Singh vowed last month to more than double the nation's R&D spending to $8 billion a year by 2017. The pledge was no bolt from the blue. Since taking office in May 2004, Singh has launched initiatives to entice overseas scientists to return home, create elite universities, and establish a grants agency modeled after the U.S. National Science Foundation (see p. 891).

But the largesse announced at the Indian Science Congress comes with a sobering assessment. "Over the past few decades, India's relative position in the world of science had been declining, and we have been overtaken by countries like China," Singh declared. In an exclusive interview with *Science*, Singh reiterated that concern, observing that "China is in many ways far ahead of India."

In academic circles, Singh enjoys a form of street cred. "He's a scholar, a thinker," says Raghunath "Ramesh" Mashelkar, former director general of India's Council of Scientific and Industrial Research. Born in 1932 in Gah, now part of Pakistan, Singh walked to school and studied by the light of a kerosene lantern as a boy in his unelectrified village before becoming a professor at the Delhi School of Economics. As finance minister from 1991 to 1996, Singh presided over reforms that have transformed India into one of the world's fastest growing economies.

Gentle and modest, Singh's soft-spoken demeanor belies the grit he has shown on some issues of importance to scientists. He staked his government's future on nuclear power when, overriding fierce opposition, he inked a controversial deal with the United States in 2008 that opened India's civilian nuclear industry to the outside world. He has struck a cautious stance on genetically modified (GM) foods; in 2009, he did not intervene when his former environment minister rejected a scientific panel's advice and banned commercial planting of GM eggplant, or brinjal, until additional safety trials are completed.

On balance, Indian scientists give Singh high marks for his tenure as prime minister. Last month, they elected him general president of the Indian Science Congress Association during its centenary year—the first prime minister to receive that honor. In an interview at his residence here with Editor-in-Chief Bruce Alberts, Asia news editor Richard Stone, and India correspondent Pallava Bagla, Singh shared his thoughts about competing with China, foreign interference in the GM food debate, and how to tightly harness R&D to development in a country in which 42% of children are malnourished. The following transcript is edited for clarity and brevity.

–PALLAVA BAGLA AND RICHARD STONE

Q: At the Indian Science Congress last month, you said that "we need to do much more to change the face of Indian science." Please elaborate.

M.S.: Well, we need to spend a lot more on research and development. Our share of GDP which we spend on R&D is about 1%, and I said that we should raise it to about 2% of GDP. We need to spend a lot more money on the areas where our development needs are actively served by developments in science, technology, and innovation. So in our country today we have a situation where as far as the public sector is concerned, our proportion of GDP going into R&D in science and technology is roughly the same as the other developing countries, but it is the private sector in our country which has to do a lot more.

Q: What kind of incentives might work for industry?

M.S.: These matters cannot be decided upon merely in a short period. It is a medium-term process. We have a plan which will be launched from April for the next 5 years. Our effort will be to increase gradually the proportion of money spent on R&D and at the same time create a system of incentives which will induce the private sector to increase their spending on science and technology.

Q: In the United States, 17% of total research and development spending is spent in higher education systems, whereas in India the number is about 4%. It is the lowest percentage of any of your peers. Is this a problem that needs to be fixed?

M.S.: Well, we need to spend a lot more money on education, more so on higher education. We have increased the number of IITs [Indian Institutes of Technology]. We have increased the number of Indian Institutes for Information Technology in a massive way. We are going to increase the number of what we call innovation universities. So I am confident that the landscape of higher education in India will change enormously in the next 5 to 10 years.

Our real problem is quality teaching staff. We are trying to induce more people to go for Ph.D. degrees in science and technology. I

Published by AAAS

think we are making some impact, but not as fast as we need in order to meet the needs of our higher education system. Therefore, we must also find innovative means to draw upon the Indians working in the universities abroad, particularly in the United States, to find some time to spend teaching in our country.

Q: You also mentioned in your speech at the science congress about the need to do more to address the developmental needs of India through research. A good example is [agricultural scientist] M. S. Swaminathan's efforts to bring the benefits of science to Indian villages. Does India need to do more to invest in that kind of science and if so, how might it be done?

M.S.: We need to pay a lot more attention to the development of our agriculture. That will accelerate the tempo of rural development, which will help to increase the opportunities for our scientists to work in rural areas in development of water-management technologies, in development of environment-friendly technologies, and also communicable diseases. We have to pay a lot more attention to R&D, tackling the problems of communicable diseases. We are victims of a double whammy. There are diseases which are peculiar to developing countries, but there are also diseases, which I think know no level of development, and in both these areas we have opportunities.

The Indian agricultural research system could also be made much more productive in tackling problems of what I have often described as ushering in a second green revolution. We have difficulties in increasing the productivity of dry land agriculture. That means technologies which will save water and technologies which will conserve energy also should get a lot more attention.

Candid exchange. In an interview with *Science* Editor-in-Chief Bruce Alberts and colleagues, Manmohan Singh shared his concerns about GM foods, nuclear activists, and China.

Q: Why did your government put a moratorium on the release of Bt brinjal?

M.S.: Biotechnology has enormous potential, and in due course of time we must make use of genetic engineering technologies to increase the productivity of our agriculture. But there are controversies. There are NGOs, often funded from the United States and the Scandinavian countries, which are not fully appreciative of the development challenges that our country faces. But we are a democracy, we are not like China.

You know, for example, what's happening in Kudankulam [in southern India, where local NGO-led protests have stalled commissioning of two 1000-megawatt nuclear reactors]. The atomic energy program has got into difficulties because these NGOs, mostly I think based in the United States, don't appreciate the need for our country to increase the energy supply.

Q: After the Fukushima disaster in Japan, do you still think that nuclear energy has a role in India?

M.S.: Yes, where India is concerned, yes. The thinking segment of our population certainly is supportive of nuclear energy.

Q: At the science congress, you mentioned your feeling that China has overtaken India in science. Are you competing with China?

M.S.: Well, we are competing, yes and no. India and China are engaged in a stage of development where we have both to compete and cooperate. We are the two largest developing countries and the two fastest growing countries. China is our great neighbor. Now, we've had in the past problems way back in the 1960s, but we are finding pathways to promote cooperation.

Q: India has invested very large amounts of money in space.

M.S.: And it has paid off.

Q: The country wants to put astronauts in space. Indian astronauts from Indian soil using Indian rockets. Is that something you support?

M.S.: We supported the Chandrayaan lunar missions. And satellite technologies, rocket technologies—those are, I think, highly favorable outcomes of the Indian space program, and we need to do more.

Q: But what about the astronaut program? The Indian Space Research Organisation is asking for $2.5 billion. You talk of inclusive growth. In that inclusive growth, how does human space flight fit in?

M.S.: Well, ultimately science and technology must be viewed as an instrument of raising the standard of living of our people. Now, if information technology can be seen to promote the development of our country, particularly in the inclusive style of development, I think people will see space technology also as a new way of dealing with the ancient scourges of poverty, ignorance, and disease. Science and technology are the ultimate salvation for finding meaningful new pathways of developing our economy.

> *"Science and technology are the ultimate salvation for finding meaningful new pathways for developing our economy."*
> —MANMOHAN SINGH

Q: Where do you see the future of Indian science in 20 years?

M.S.: Indian science has a very bright future. I have no doubt that we will scale new heights, we will explore new frontiers, and more and more young people will take to science as a career. Things are already changing for the better.

One has to be optimistic. In poor countries, unless one is optimistic, one is overwhelmed by the dimension of the development task that we have to accomplish.

CREDIT: PALLAVA BAGLA

Published by AAAS

Continued from page 906

research—a novel open-source drug discovery program (see sidebar below), a $1 billion supercomputing initiative, and an effort to improve forecasts of the summer monsoon (see p. 910). At the science congress last month, Singh also vowed to double public and private R&D spending as a percentage of GDP to 2% by 2017. That will require much higher expenditures from the private sector, which currently contributes a mere 33% of total R&D spending.

Some observers wonder whether India's scientific community can make good use of the windfall. By Western standards, few disciplines or institutes have built up a critical mass. "The entire biology community of India is smaller than that of Boston," Shashidhara says. In genetics and development, he says, "many people are just doing gap-filling work." Researchers in other disciplines voice similar complaints. "In any given area of science or engineering, the number of experts is rather small in India," says Rao, who says that nationwide only five or six researchers are studying graphene—one of the hottest areas of materials science.

To build capacity, the government is wooing overseas talent through fellowship programs. "There's a concerted movement to bring people back," says Savita Ayyar, head of the research development office at the National Centre for Biological Sciences (NCBS) here. And scientists on their own have organized "Young Investigator Meetings" in U.S. cities meant to entice newly minted Ph.D.s and postdocs.

Feeling caged in. The Indian system discourages breakthrough research, says sociobiologist Raghavendra Gadagkar, who studies wasp behavior.

Science for the masses

The flip side of the shortage of well-trained researchers is the inadequacy of labs and institutes. Most of the 350-odd state universities "are terribly run," Ganesh says. Few can brag of world-class research. "They're broken down," says physical chemist Sourav Pal, director of the National Chemical Laboratory in Pune. This is a legacy of the Cold War years. After independence in 1947, India adopted a Soviet-style academic system in which "undergraduate teaching was decoupled from research," Ganesh says. Then a decade ago came a "great awakening," he says: "We realized we needed to merge teaching and research."

One obstacle to reform is India's employment laws. Researchers of any caliber can easily gain tenure. At the same time, scientific stars have limited opportunities to advance in salary or rank. "Administrations must follow the policy of benign neglect with respect to high performers, even while turning a blind eye to the significant dead wood accumulating in our institutions," Balaram noted in his editorial.

As a cure, the government has opted to spawn new institutions. In the past 5 years, Singh has presided over an expansion of

Crowd-Sourcing Drug Discovery

NEW DELHI—Each year, India tallies an astounding 1.7 million cases of tuberculosis (TB). Some 400,000 people succumb to the disease, making it the leading cause of death in India for those in the prime of life, from 15 to 45 years old. Most victims are poor, and pharmaceutical companies have little incentive to develop new drugs against the bug that causes TB, *Mycobacterium tuberculosis*. But the Indian government has a big incentive to reduce the disease burden.

Faced with this conundrum, Samir Brahmachari had a brainstorm a few years ago: crowd-sourcing. "That means looking for experts you don't know exist," he says. "I wanted to do something very different." So in 2008, Brahmachari, a biophysicist and director general of the Council of Scientific and Industrial Research (CSIR), India's largest network of scientific laboratories, launched the Open Source Drug Discovery (OSDD) network. Modeled after the open-source software community, OSDD's army of volunteers is building a kind of Wikipedia on TB. Some 5500 participants in 130 countries respond to "work packages" posted by OSDD: questions on everything from the biology of *M. tuberculosis* to leads on drugs; answers are tagged and credited.

"OSDD is an exciting new approach to drug discovery," says Melvin Spigelman, president of the TB Alliance in New York City. "It provides the opportunity for virtually a limitless number of scientists to contribute to the solution of any given problem." The Indian government gave OSDD $12 million in seed money; CSIR has requested $200 million over the next 5 years as the program ramps up for clinical trials and expands to other neglected diseases such as malaria and leishmaniasis, and possibly even cancer. "Drug discovery," Brahmachari says, "is too serious a business to be left solely in the hands of pharmaceutical companies."

The first challenge that OSDD's cyber-community assigned itself was to glean more information from the *M. tuberculosis* genome. It was sequenced in 1998, but researchers had clues to the functions of only a quarter of its 4000 genes. In December 2009, OSDD set out to reannotate all possible genes. Some 500 volunteers got the job done in a mere 4 months. Now OSDD is trying to exploit these data. "The more people you put to work on the problem, the more chances you will have to identify the set of compounds that will likely make it through compound optimization, animal models, preclinical, and, eventually, clinical trials. If you increase your success chances, then your overall costs decrease," says Marc Marti-Renom of the National Center for Genomic Analysis in Barcelona, Spain.

Open-source guru. CSIR's Samir Brahmachari.

OSDD's iterative approach has identified two drug candidates that it has contracted for testing. Under OSDD rules, data from program-sponsored clinical trials must be open for all to see—"a clear alternative," OSDD states, "to expensive clinical trials conducted in secrecy at high costs." OSDD drugs will be available in the developing world as generics, Brahmachari says. "When it comes to health, we need to have a balanced view between health as a right and health as business," he says. For TB and other neglected diseases, drug companies might embrace that philosophy. For cancer, all bets are off. **–P.B.**

CREDITS (TOP TO BOTTOM): R. STONE/SCIENCE; PALLAVA BAGLA

Drawing a Bead on India's Enigmatic Monsoon

NEW DELHI—India's booming economy is still a gamble on the monsoon. In any given year, if rainfall climbs more than 10% above a long-term monsoon average, floods ensue. If it declines more than 10% below average, a drought is declared. Slippage in either direction brings misery. For example, a drought in 2002 shrank India's GDP by an estimated 5.8%. Every meteorologist's dream here is to accurately predict the monsoon's arrival, distribution, and departure. Toward that end, this year the Ministry of Earth Sciences is launching a 5-year, $75 million "monsoon mission" to improve the study of complex ocean-atmosphere interactions.

India receives 105 cm of rainfall on average per year, 80% carried on southwest winds that sweep in from the Indian Ocean from June to September. A winter monsoon also brings moisture from the northeast. Farming is heavily dependent on the exact timing of the rain, especially where it is needed to germinate seed. Since official record-keeping began 137 years ago, the monsoon has never failed to arrive, and it has never delivered less than 75 cm of rain. But the spatial and temporal variations are vast—and this is what befuddles scientists. "Every year, the monsoon is peculiar in its own way," says atmospheric scientist Jayaraman Srinivasan of the Indian Institute of Science in Bangalore.

Extreme misfortune. A farmer in Orissa examines his parched field in 2003.

The India Meteorological Department here issues monsoon forecasts but has not been able to accurately predict when the worst floods and droughts will occur. "Extremes are really difficult to forecast," says Ajit Tyagi, the department's former director general. Everything needs closer study: how clouds form, develop, and die—and, crucially, how global warming will change the monsoon.

India's "current prediction capabilities are inadequate," concedes geologist Shailesh Nayak, secretary for the Earth Sciences Ministry. A big bottleneck, he says, is a shortage of trained scientists. By Nayak's estimate, over the next 5 years India will need about 1200 skilled meteorologists, but today has only about 350. The ministry has just launched a recruitment campaign.

In the new initiative, Indian scientists and overseas colleagues will try to adapt computer models developed by the U.K. Met Office and the U.S. National Centers for Environmental Prediction for long-range forecasting in India. The mission will also make use of data pouring in from Megha-Tropiques, an Indo-French satellite launched in October to monitor water and energy balance over the tropics. The Indian Institute of Tropical Meteorology in Pune will take the lead in seasonal forecasts and prediction of active and break periods of the monsoon. A key aim is to produce a prediction model that uses open-source software such as Linux.

The collaborative effort, Tyagi hopes, may at last "unravel the enigma that surrounds the Indian monsoon."

–P.B.

the education and research system not witnessed since the 1940s. Back then, the country's first prime minister, Jawaharlal Nehru, saw research labs as the "temples of modern India" and set in motion the creation of the elite Indian Institutes of Technology.

An impressive new phenomenon is the Indian Institutes of Scientific Education and Research, of which there are now five. The decision to establish them was controversial. "A lot of people were against the IISERs. They thought, 'Why not upgrade existing universities?' " Pal says. Skeptics warned that there wouldn't be enough skilled instructors to go around. The rapid buildup in fact has meant uneven faculties at some institutes. "If you can't get teachers who are qualified, you start compromising," Mashelkar says. Critics also say that the IISERs will skim off talented high school science grads, leaving impoverished universities in worse condition.

"We need to find ways to attract intelligent students into science," Ganesh says. Toward that end, the government's Department of Science and Technology hopes to hook youngsters on science through INSPIRE—Innovation in Science Pursuit for Inspired Research—a 5-year, $500 million program that hands out $125 grants to top science students at every high school in the nation. "We hope to catch them young and build a cadre of top-quality researchers," says T. Ramaswami, secretary of the Department of Science and Technology in New Delhi. He spearheads this ambitious scheme, which aims to have supported 1 million students by the end of next year.

Institutes, meanwhile, are striving to close the gap between education and research. IISER Pune, for instance, encourages its undergraduates to join labs and author publications. And CSIR is venturing into the teaching business. Last year, it established an accredited institution that's gunning for 6000 students. "It's a very important break from the Soviet model," Pal says.

One long-standing problem for science faculties is that many top graduates turn up their noses at academic careers. They flock to information technology, where companies offer large entry-level salaries. Meanwhile, those who stick with science tend to go overseas for postdocs, depriving Indian labs of the creative sparks that are the hallmark of labs in Europe and the United States. Stints in overseas labs are seen as a ticket to a decent position back in India. "People think you need to go abroad to get a job here," says NCBS neuroscientist Sumantra Chattarji.

Hoping to show that's not necessarily the case, the Department of Biotechnology and the U.K.'s Wellcome Trust teamed up in 2008 to create a 5-year, $140 million fellowship program for up to 375 young investigators in India. "Now we're able to create an environment and mechanisms for postdocs to stay here," Ayyar says. "You might think this is a small step. But it's about changing the way people think."

As India's economy roars and Western nations limp along, the trickle of talented expatriates returning home may turn into a flood. "You can be richer in India as an assistant professor than in the United States," says Ganesh, who says that new recruits to IISER Pune receive royal treatment. "We give them whatever they want to start up a lab." His institute may be a new kid on the block. But considering the climate for science in India these days, Ganesh says, "I have no excuse to fail."

Minding the gap. Krishna Ganesh is melding teaching and research.

–RICHARD STONE

With reporting by Pallava Bagla.

CREDITS (TOP TO BOTTOM): PALLAVA BAGLA; R. STONE/SCIENCE

COMMENTARY

IBI Prize essay

932

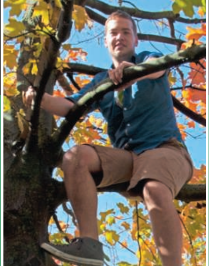

LETTERS

edited by Jennifer Sills

Uniting Church and Science for Conservation

HUMANS HAVE BEEN CUTTING ETHIOPIAN FORESTS FOR FUEL AND AGRICULTURE FOR CENTURIES (*1*). Only about 35,000 fragments remain in the northern highlands, ranging in size from 3 to 300 hectares. These fragments escaped deforestation because of their religious and spiritual importance; they are protected by, and are an integral part of, the Ethiopian Orthodox Tewahido Church (*2*). Within each forest, an Orthodox priest and his disciples live, conduct services, and oversee its use. These forests are both a religious and a biodiversity sanctuary (*3*–*6*), and they provide local people with essential ecosystem services such as fresh water, shade, honey, pollinators, and spiritual value.

The church leadership views biodiversity conservation as one of its primary stewardships, but the lack of perimeter delineation of these forest fragments threatens their future. Presently, less than 4% of the original forest cover remains in the region (*7*, *8*), and the remaining forests continue to be encroached upon (*9*), in part because of population increases—Ethiopia had a population of 43 million in 1984 but almost 80 million by 2000 (*10*). These church forests are also threatened by foraging livestock that increase soil compaction, hindering seed germination and forest regeneration. Sadly, when a forest disappears, the priest, his disciples and others living in the area also leave.

Valued. A church forest stands out against barren surroundings.

With such precious few fragments remaining, Ethiopia faces a conservation crisis. Understanding the role that church forests play in the provision of ecosystem services is critical, particularly for soil conservation, fresh water protection, and carbon sequestration. To preserve these forests, and perhaps even expand them, we must take an immediate, aggressive, and multidisciplinary approach that includes all stakeholders. For example, biologists, social scientists, ethnographers, religious leaders, and local people must collaborate. We must work to understand the relationship between local peoples and the forest and empower them to protect it. More immediately, we must establish perimeters to prevent grazing and encourage the planting of local trees in the forest areas (*8*). By taking these steps, we can protect Ethiopia's forests from further decline.

CATHERINE L. CARDELÚS,[1]* MARGARET D. LOWMAN,[2] ALEMAHEYU WASSIE ESHETE[3]

[1]Department of Biology, Colgate University, Hamilton, NY 13346, USA. [2]Nature Research Center, North Carolina Museum of Natural Sciences, Raleigh, NC 27601, USA. [3]College of Agriculture, Bahir Dar University, Bahir Dar, Ethiopia.

*To whom correspondence should be addressed. E-mail: ccardelus@colgate.edu

References

1. J. C. McCann, *Env. History* **2**, 138 (1997).
2. A. Wassie, "Opportunities, constraints and prospects of the Ethiopian Orthodox Tewahido Churches in conserving forest resources: The case of church forests in South Gonder, Northern Ethiopia," thesis (Swedish University of Agricultural Sciences, Uppsala, Sweden, 2002).
3. F. Bongers, A. Wassie, F. J. Sterck, T. Bekele, D. Teketay, *J. Drylands* **1**, 35 (2006).
4. M. D. Lowman, *Explorers J.* **88**, 26 (2010).
5. M. Tolera, Z. Asfaw, M. Lemenih, E. Karltun, *Agric. Ecosys. Env.* **128**, 52 (2008).
6. A. Wassie, D. Teketay, *Flora-Morphol. Distribut. Funct. Ecol. Plants* **201**, 32 (2006).

CREDIT: GOOGLE EARTH/2112GEOEYE

7. F. W. Gatzweiler, "Deforestation of Ethiopia's Afromontane rainforests; reasons for concern" (ZEF Policy Brief no. 7, Center for Development Research, Bonn, 2007).
8. A. Wassie, F. Sterck, D. Teketay, F. Bongers, *Biotropica* **41**, 110 (2009).
9. A. Wassie, D. Teketay, N. Powell, *Forests Trees Livelihoods* **15**, 349 (2005).
10. E. Feoli, L. G. Vuerich, W. Zerihun, *Agric. Ecosys. Env.* **91**, 313 (2002).

Growing Need for Agriculture Experts

ISSUES RELATED TO THE SAFETY AND SECURITY of our food supply top the news on a regular basis [e.g., (*1*, *2*)]. Yet the news media continue to undermine the entry of students into the study of agriculture (*3*, *4*).

Statistical data from the U.S. Department of Labor (*5*) and U.S. Department of Agriculture (*6*) indicate an expected growth in most agriculture-related fields, including inspectors, scientists, and veterinarians. The Bureau of Labor Statistics projects that over the next five years, there will be a 5% increase in the need for graduates in these disciplines, but a 10% decline in the number of students choosing these important programs as their career path (*7*). This means a shortfall of qualified workers in the areas where we need them most—horticulture, animal husbandry, food science, and climate change or environmental analysis. There are also growing opportunities in industries with activities linked to agriculture, such as transporting food, specialty processing (e.g., coffee brewing), addressing dietetic concerns, protecting animal welfare, and producing pet foods. The Bureau of Labor Statistics also suggests an 8% increase in the need for qualified, well-educated agriculture managers to keep pace with quickly advancing technological methods of farming across the United States and abroad, along with changes in regulations at all government levels (*7*).

The bottom line: Agriculture isn't dead. In fact, no other industry feeds the world's population, which could hit 9 billion by 2050 (*8*). The need for graduates in agriculture, horticulture, and animal science programs will be critical to finding ways of safely doubling food production in order to meet the demand of a growing population.

JEFFREY VOLENEC,[1] KENNETH BARBARICK,[2] GARY PIERZYNSKI,[3] ELLEN BERGFELD[4]*

[1]Department of Agronomy, Purdue University, West Lafayette, IN 47907–2054, USA. [2]Department of Soil and Crop Sciences, Colorado State University, Fort Collins, CO 80523, USA. [3]Kansas State University, Manhattan, KS 66506, USA. [4]Alliance of Crop, Soil, and Environmental Science Societies, Madison, WI 53711, USA.

*To whom correspondence should be addressed. E-mail: ebergfeld@sciencesocieties.org

References

1. Food and Drug Administration, Orange Juice Products and Carbendazim: Addendum to FDA Letter to the Juice Products Association (January 9, 2012) (www.fda.gov/Food/FoodSafety/Product-SpecificInformation/FruitsVegetablesJuices/ucm287783.htm).
2. Fresno County, Department of Environmental Health, Consumer Food Product Recalls (www.co.fresno.ca.us/DepartmentPage.aspx?id=908).
3. T. Loose, "College majors that are useless," Yahoo Education (http://education.yahoo.net/articles/most_useless_degrees.htm?kid=1KWNU).
4. "20 most useless degrees," The Daily Beast Blog (www.thedailybeast.com/galleries/2011/04/27/20-most-useless-degrees.slide3.html).
5. U.S. Department of Labor, Statistical Information (www.dol.gov/dol/audience/aud-workers.htm#stats).
6. U.S. Department of Agriculture, USDA Agricultural Projections to 2019 (www.usda.gov/oce/commodity/archive_projections/USDAAgriculturalProjections2019.pdf).
7. Bureau of Labor Statistics, *Occupational Outlook Handbook, 2010-11 Edition* (www.bls.gov/oco/ocos046.htm).
8. Feedstuffs FoodLink, "Ag must 'freeze food footprint,'" *Feedstuffs*, 4 April 2010.

CREDIT: BART COENDERS/ISTOCKPHOTO.COM

Demography's Role in Sustainable Development

IN PREPARING FOR THE RIO+20 EARTH Summit, the world community must acknowledge that population trends interact strongly with economic development and environmental change at local and global levels. The International Institute for Applied Systems Analysis (IIASA) recently convened leading experts to consider how demographic factors promote or impede sustainable development. The panel concluded that human beings—their numbers, distribution, and characteristics—are at the center of concern for sustainable development (*1*). The evidence is clear that demographic differences fundamentally affect people's contribution to environmental burdens, their ability to participate in sustainable development, and their adaptability to a changing environment. The developmental challenges are by far the most significant where population growth and poverty are the highest, education is the lowest, and vulnerabilities to environmental change are the greatest. Within families, women and children are most vulnerable.

As members of this panel, we put forward five action implications: (i) Recognize that the numbers, characteristics, and behaviors of people are at the heart of sustainable development challenges and of their solutions. (ii) Identify subpopulations that contribute most to environmental degradation and those that are most vulnerable to its consequences. In poor countries especially, these subpopulations are readily identifiable according to age, gender, level of education, place of residence, and standard of living. (iii) Devise sustainable development policies to treat these subpopulations differently and appropriately, according to their demographic and behavioral characteristics. (iv) Facilitate the inevitable trend of increasing urbanization in ways that ensure that environmental hazards and vulnerabilities are under control. (v) Invest in human capital—people's education and health, including reproductive health—to slow population growth, accelerate the transition to green technologies, and improve people's adaptive capacity to environmental change.

WOLFGANG LUTZ,[1]* WILLIAM P. BUTZ,[1] MARCIA CASTRO,[2] PARTHA DASGUPTA,[3] PAUL G. DEMENY,[4] ISAAC EHRLICH,[5] SILVIA GIORGULI,[6] DEMISSIE HABTE,[7] WERNER HAUG,[8] ADRIAN HAYES,[9] MICHAEL HERRMANN,[10] LEIWEN JIANG,[11] DAVID KING,[12] DETLEF KOTTE,[13] MARTIN LEES,[14] PAULINA K. MAKINWA-ADEBUSOYE,[15] GORDON MCGRANAHAN,[16] VINOD MISHRA,[17] MARK R. MONTGOMERY,[18] KEYWAN RIAHI,[19] SERGEI SCHERBOV,[1] XIZHE PENG,[20] BRENDA YEOH[21]

[1]World Population Program, International Institute for Applied Systems Analysis, Laxenburg, A-2361, Austria. [2]Department of Global Health and Population, Harvard School of Public Health, Cambridge, MA 02115, USA. [3]Faculty of Economics, Cambridge University, Cambridge, CB3 9DD, UK. [4]Population Council, New York, NY 10017, USA. [5]Department of Economics, State University of New York, Buffalo, NY 14260, USA. [6]Center for Demographic, Urban, and Environmental Studies, El Colegio del Mexico, Mexico City, Mexico. [7]Ethiopian Academy of Sciences, Addis Ababa, Ethiopia. [8]Technical Division, UNFPA, New York, NY 10158, USA. [9]Australian Demographic and Social Research Institute, Australian National University, Canberra, Australia. [10]Population and Development Branch, UNFPA, New York, NY 10158, USA. [11]Intergrated Assessment Modeling Group, National Center for Atmospheric Research, Boulder, CO 80307, USA. [12]Smith School of Enterprise and the Environment, University of Oxford, Oxford, OX1 2BQ, UK. [13]Division of Globalization and Development Strategies, UNCTAD, 1211 Geneva 10, Switzerland. [14]Club of Rome, CH-8400, Winterthur, Switzerland. [15]Nigerian Institute of Social and Economic Research, Ibadan, Nigeria. [16]Human Settlements Group, International Institute for Environment and Development, London, WC1X 8NH, UK. [17]Policy Section, United Nations Population Division, New York, NY 10017, USA. [18]Department of Economics, State University of New York, Stony Brook, NY 11794, USA. [19]Energy Program, International Institute for Applied Systems Analysis, Laxenburg, 2361, Austria. [20]School of Social Development and Public Policy, Fudan University, Shanghai, 200433, China. [21]Department of Geography, National University of Singapore, Kent Ridge, 117570, Singapore.

*To whom correspondence should be addressed. E-mail: lutz@iiasa.ac.at

Reference

1. IIASA, World Population Program, Demographic Challenges for Sustainable Development (www.iiasa.ac.at/Research/POP/Laxenburg%20Declaration%20on%20Population%20and%20Development.html).

Letters to the Editor

Letters (~300 words) discuss material published in *Science* in the past 3 months or matters of general interest. Letters are not acknowledged upon receipt. Whether published in full or in part, Letters are subject to editing for clarity and space. Letters submitted, published, or posted elsewhere, in print or online, will be disqualified. To submit a Letter, go to www.submit2science.org.

CORRECTIONS AND CLARIFICATIONS

News & Analysis: "New cystic fibrosis drug offers hope, at a price" by J. Kaiser (10 February, p. 645). Paul Negulescu is vice president of research at Vertex Pharmaceuticals, not vice president for discovery biology.

News of the Week: "Crafoord Prizes announced" (27 January, p. 385). In the description of the Green-Tao theorem, the phrase "by adding any integer progressively to a starting number" should have read "by adding some integer progressively to some starting number." The item also incorrectly characterized the Schrödinger equation studied by prizewinner Jean Bourgain. That differential equation, which is the basis for nonrelativistic quantum mechanics, is linear. Bourgain studied the more complicated nonlinear Schrödinger equation, which has applications in nonlinear optics, the study of water waves, and the physics of Bose-Einstein condensates.

News Focus: "Ferreting out the hidden cracks in the heart of a continent" by N. Lubick (27 January, p. 397). In the figure, the label "Cairo, Missouri" should read "Cairo, Illinois."

Research Articles: "EPOXI at comet Hartley 2" by M. F. A'Hearn *et al.* (17 June 2011, p. 1396). The Research Article mentioned a dramatic increase in the flux with the Medium Resolution Instrument (MRI) roughly 6 weeks before the encounter. This effect was most pronounced with the CN narrowband filter in place—as large as a factor of 8—while fluxes measured with the broad band CLEAR1 filter increased by about 50%. Because the sudden onset and long duration of the event was unlike any cometary outburst, it was dubbed a "CN anomaly." The authors have since found that the anomaly was caused by a small light leak that allowed some indirect sunlight to enter the instrument for solar elongations between 118° and 128°. Because of the design of the spacecraft and its instruments, observations at such large solar elongations are rarely made and were assumed out of range in designing the instrument, so the light leak had not previously been seen. No other data are affected by this instrumental artifact.

TECHNICAL COMMENT ABSTRACTS

Comment on "Lévy Walks Evolve Through Interaction Between Movement and Environmental Complexity"

Vincent A. A. Jansen, Alla Mashanova, Sergei Petrovskii

de Jager *et al.* (Reports, 24 June 2011, p. 1551) concluded that mussels Lévy walk. We confronted a larger model set with these data and found that mussels do not Lévy walk: Their movement is best described by a composite Brownian walk. This shows how model selection based on an impoverished set of candidate models can lead to incorrect inferences.

Full text at www.sciencemag.org/cgi/content/full/335/6071/918-c

Response to Comment on "Lévy Walks Evolve Through Interaction Between Movement and Environmental Complexity"

Monique de Jager, Franz J. Weissing, Peter M. J. Herman, Bart A. Nolet, Johan van de Koppel

We agree with Jansen *et al*. that a composite movement model provides a better statistical description of mussel movement than any simple movement strategy. This does not undermine the take-home message of our paper, which addresses the feedback between individual movement patterns and spatial complexity. Simple movement strategies provide more insight in the eco-evolutionary analysis and are therefore our model of choice.

Full text at www.sciencemag.org/cgi/content/full/335/6071/918-d

COMMENTARY

IBI Prize essay

932

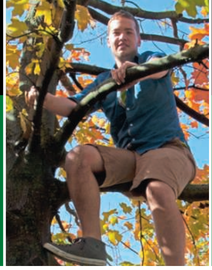

LETTERS

edited by Jennifer Sills

Uniting Church and Science for Conservation

HUMANS HAVE BEEN CUTTING ETHIOPIAN FORESTS FOR FUEL AND AGRICULTURE FOR CENTURIES (*1*). Only about 35,000 fragments remain in the northern highlands, ranging in size from 3 to 300 hectares. These fragments escaped deforestation because of their religious and spiritual importance; they are protected by, and are an integral part of, the Ethiopian Orthodox Tewahido Church (*2*). Within each forest, an Orthodox priest and his disciples live, conduct services, and oversee its use. These forests are both a religious and a biodiversity sanctuary (*3*–*6*), and they provide local people with essential ecosystem services such as fresh water, shade, honey, pollinators, and spiritual value.

The church leadership views biodiversity conservation as one of its primary stewardships, but the lack of perimeter delineation of these forest fragments threatens their future. Presently, less than 4% of the original forest cover remains in the region (*7*, *8*), and the remaining forests continue to be encroached upon (*9*), in part because of population increases—Ethiopia had a population of 43 million in 1984 but almost 80 million by 2000 (*10*). These church forests are also threatened by foraging livestock that increase soil compaction, hindering seed germination and forest regeneration. Sadly, when a forest disappears, the priest, his disciples and others living in the area also leave.

Valued. A church forest stands out against barren surroundings.

With such precious few fragments remaining, Ethiopia faces a conservation crisis. Understanding the role that church forests play in the provision of ecosystem services is critical, particularly for soil conservation, fresh water protection, and carbon sequestration. To preserve these forests, and perhaps even expand them, we must take an immediate, aggressive, and multidisciplinary approach that includes all stakeholders. For example, biologists, social scientists, ethnographers, religious leaders, and local people must collaborate. We must work to understand the relationship between local peoples and the forest and empower them to protect it. More immediately, we must establish perimeters to prevent grazing and encourage the planting of local trees in the forest areas (*8*). By taking these steps, we can protect Ethiopia's forests from further decline.

CATHERINE L. CARDELÚS,[1]* MARGARET D. LOWMAN,[2] ALEMAHEYU WASSIE ESHETE[3]

[1]Department of Biology, Colgate University, Hamilton, NY 13346, USA. [2]Nature Research Center, North Carolina Museum of Natural Sciences, Raleigh, NC 27601, USA. [3]College of Agriculture, Bahir Dar University, Bahir Dar, Ethiopia.

*To whom correspondence should be addressed. E-mail: ccardelus@colgate.edu

References

1. J. C. McCann, *Env. History* **2**, 138 (1997).
2. A. Wassie, "Opportunities, constraints and prospects of the Ethiopian Orthodox Tewahido Churches in conserving forest resources: The case of church forests in South Gonder, Northern Ethiopia," thesis (Swedish University of Agricultural Sciences, Uppsala, Sweden, 2002).
3. F. Bongers, A. Wassie, F. J. Sterck, T. Bekele, D. Teketay, *J. Drylands* **1**, 35 (2006).
4. M. D. Lowman, *Explorers J.* **88**, 26 (2010).
5. M. Tolera, Z. Asfaw, M. Lemenih, E. Karltun, *Agric. Ecosys. Env.* **128**, 52 (2008).
6. A. Wassie, D. Teketay, *Flora-Morphol. Distribut. Funct. Ecol. Plants* **201**, 32 (2006).

CREDIT: GOOGLE EARTH/2112GEOEYE

Comment on "Lévy Walks Evolve Through Interaction Between Movement and Environmental Complexity"

Vincent A. A. Jansen,[1]* Alla Mashanova,[1] Sergei Petrovskii[2]

de Jager *et al*. (Reports, 24 June 2011, p. 1551) concluded that mussels Lévy walk. We confronted a larger model set with these data and found that mussels do not Lévy walk: Their movement is best described by a composite Brownian walk. This shows how model selection based on an impoverished set of candidate models can lead to incorrect inferences.

A Lévy walk is a form of movement in which small steps are interspersed with very long ones, in such a manner that the step length distribution follows a power law. Movement characterized by a Lévy walk has no characteristic scale, and dispersal is superdiffusive so that individuals can cover distance much quicker than in standard diffusion models. de Jager *et al*. (*1*) studied the movements of individual mussels and concluded that mussels move according to a Lévy walk.

The argument of (*1*) is based on model selection, a statistical methodology that compares a number of models—in this case, different step length distributions—and selects the model that describes the data best as the most likely model to explain the data (*2*). This methodology is used to infer types of movements of animals (*3*) and has led to a number of studies that claim Lévy walks are often encountered in the movement of animals. The methodology in (*1*) contrasts a power-law distribution, which is indicative of a Lévy walk, with an exponential distribution, which indicates a simple random walk. If one has to choose between these alternatives, the power-law distribution gives the best description. However, if a wider set of alternatives is considered, this conclusion does not follow.

Heterogeneity in individual movement behavior can create the impression of a power law (*4*–*6*). Mussels' movement is heterogeneous as they switch between moving very little or not at all, and moving much farther (*1*, *7*). If mussels switch between different modes, and in each mode display Brownian motion, this suggests the use of a composite Brownian walk, which describes the movement as a sum of weighted exponential distributions. We confronted this plausible model with the mussel movement data (*8*).

Visual inspection of the data shows that the cumulative distribution of step lengths has a humped pattern that is indicative of a sum of exponentials (Fig. 1A). We applied a model selection procedure based on the Akaike information criterion (AIC) (*2*, *3*). We compared six different step length distributions: an exponential distribution, a power law, a truncated power law, and three hyperexponential distributions (a sum of two, three, or four exponentials to describe composite Brownian walks). We did this for the data truncated as in (*1*) (Fig. 1A) as well as all the full, untruncated data set (Fig. 1B). In both cases, we found that the composite Brownian walk consisting of the sum of three exponentials was the best model (Fig. 1 and Table 1). This convincingly shows that the mussels described in (*1*) do not do a Lévy walk. Only when we did not take the composite Brownian walk models into account did the truncated power law model perform best and could we reproduce the result in (*1*).

Mussel movement is best described by a composite Brownian walk with three modes of movement with different characteristic scales between which the mussels switch. The mean movement in these modes is robust to truncation of the data set, in contrast to the parameters of the power law, which were sensitive to truncation [Table 1;

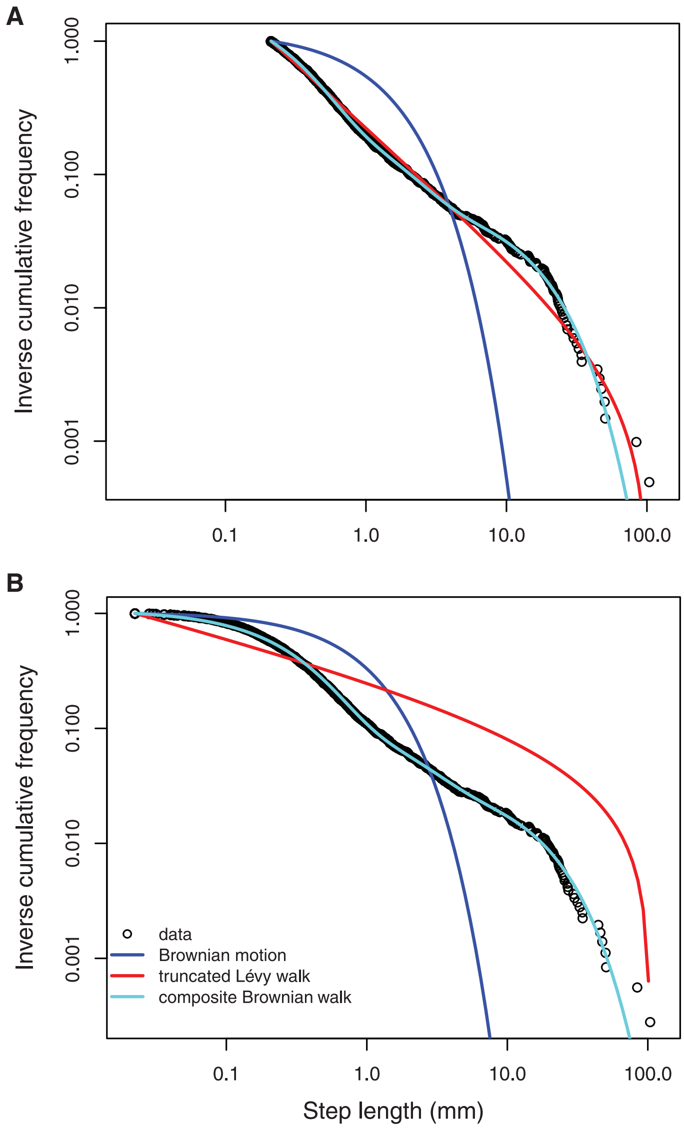

Fig. 1. The step length distribution for mussel movement [as in (*10*)] and curves depicting some of the models. The circles represent the inverse cumulative frequency of step lengths, The curves represent Brownian motion (blue), a truncated power law (red), and a composite Brownian walk consisting of a mixture of three exponentials (blue-green). (**A**) Data as truncated in Fig. 1 in (*1*, *10*) (2029 steps). (**B**) The full untruncated data set (3584 steps).

[1]School of Biological Sciences, Royal Holloway, University of London, Surrey TW20 0EX, UK. [2]Department of Mathematics, University of Leicester, Leicester LE1 7RH, UK.

*To whom correspondence should be addressed. E-mail: vincent.jansen@rhul.ac.uk

Table 1. Model parameters and Akaike weights. The maximum likelihood parameter estimates, log maximum likelihoods (ML), AIC values, and Akaike weights are calculated (for details, see SOM) for the data shown in Fig. 1, A and B. The Akaike weights without the composite Brownian walks are given in brackets. We analyzed the full data set (*) with $x_{\min} = 0.02236$ mm, and the data set truncated as in (*1*) (†) with $x_{\min} = 0.21095$ mm. For $x_{\max}$, the longest observed step length (103.9mm) was used. The mix of four exponentials is not the best model according to the AIC weights. It gives a marginally, but not significantly, better fit and is overfitted.

Models	Formula	Parameters*	Parameters†	ML	AIC	Weight
Exponential (Brownian motion)	$P(X=x)=\lambda e^{-\lambda(x-x_{\min})}$	$\lambda = 1.133$	$\lambda = 0.770$	–3136.89* –2558.67†	6275.78* 5119.37†	0 (0)* 0 (0)†
Power law (Lévy walk)	$P(X=x)=\frac{\mu-1}{x_{\min}^{1-\mu}}x^{-\mu}$	$\mu = 1.397$	$\mu = 1.975$	–2290.10* –1002.32†	4582.20* 2006.64†	0 (0) * 0 (0.006)†
Truncated power law (Lévy walk)	$P(X=x)=\frac{\mu-1}{x_{\min}^{1-\mu}-x_{\max}^{1-\mu}}x^{-\mu}$	$\mu = 1.320$	$\mu = 1.960$	–2119.55* –997.29†	4241.10* 1996.58†	0 (1) * 0 (0.994)†
Mix of two exponentials (Composite Brownian walk)	$P(X=x)=\sum_{i=1}^{2}p_i\lambda_i e^{-\lambda i(x-x_{\min})}$ with $\sum_{i=1}^{2}p_i=1$	p = 0.073, λ_1 = 0.122, λ_2 = 3.238	p = 0.127, λ_1 = 0.123, λ_2 = 3.275	–906.15* –1022.44†	1818.31* 2050.87†	0* 0†
Mix of three exponentials (Composite Brownian walk)	$P(X=x)=\sum_{i=1}^{3}p_i\lambda_i e^{-\lambda i(x-x_{\min})}$ with $\sum_{i=1}^{3}p_i=1$	p_1 = 0.034, p_2 = 0.099, λ_1 = 0.069, λ_2 = 0.652, λ_3 = 3.613	p_1 = 0.063, p_2 = 0.210, λ_1 = 0.072, λ_2 = 0.832, λ_3 = 4.309	–861.55* –966.70†	1733.11* 1943.40 †	0.881* 0.873†
Mix of four exponentials (Composite Brownian walk)	$P(X=x)=\sum_{i=1}^{4}p_i\lambda_i e^{-\lambda i(x-x_{\min})}$ with $\sum_{i=1}^{4}p_i=1$	p_1 = 0.014, p_2 =0.034, p_3 = 0.085, λ_1 = 0.656, λ_2 = 0.069, λ_3 = 0.652 λ_4 = 3.613	p_1 = 0.017, p_2 = 0.060, p_3 = 0.202, λ_1 = 0.377, λ_2 = 0.070, λ_3 = 0.902, λ_4 = 4.345	–861.55* –966.63†	1737.11* 1947.26†	0.119* 0.127†

also see supporting online material (SOM)]. This analysis does not tell us what these modes are, but we speculate that it relates to the stop-move behavior that mussels show, even in homogeneous environments (*1*). We speculate that the mode with the smallest average movement (~0.4 mm) is related to nonmovement, combined with observational error. The next mode (average movement ~1.5 mm) is related to mussels moving their shells but not displacing, and the mode with the largest movements (on average 14 mm, about the size of a small mussel) is related to actual displacement. This suggests that in a homogeneous environment, mussels are mostly stationary, and if they move, they either wobble or move about randomly. Indeed, if we remove movements smaller than half the size of a small mussel (7.5 mm), the remaining data points are best described by Brownian motion. This shows that mussel movement is not scale invariant and not superdiffusive.

de Jager *et al.*'s analysis (*1*) does show that mussels do not perform a simple random walk and that they intersperse relatively long displacements with virtually no displacement. However, one should not infer from that analysis that the movement distribution therefore follows a power law or that mussels move according to a Lévy walk, and there is no need to suggest that mussels must possess some form of memory to produce a power law–like distribution (*9*). Having included the option of a composite Brownian walk, which was discussed in (*1*) but not included in the set of models tested, one finds that this describes mussels' movement extremely well.

Our analysis illustrates why one has to be cautious with inferring that animals move according to a Lévy walk based on too narrow a set of candidate models: If one has to choose between a power law and Brownian motion, often the power law is best, but this could simply reflect the absence of a better model. To make defensible inferences about animal movement, model selection should start with a set of carefully chosen models based on biologically relevant alternatives (*2*). Heterogeneous random movement often provides such an alternative and has the additional advantage that it can suggest a simple mechanism for the observed behavior.

References and Notes

1. M. de Jager, F. J. Weissing, P. M. J. Herman, B. A. Nolet, J. van de Koppel, *Science* **332**, 1551 (2011).
2. K. P. Burnham, D. R. Anderson, *Model Selection and Multimodel Inference: A Practical Information-Theoretic Approach* (Springer-Verlag, New York, ed. 2, 2002).
3. A. M. Edwards *et al.*, *Nature* **449**, 1044 (2007).
4. S. Benhamou, *Ecology* **88**, 1962 (2007).
5. S. V. Petrovskii, A. Y. Morozov, *Am. Nat.* **173**, 278 (2009).
6. S. Petrovskii, A. Mashanova, V. A. A. Jansen, *Proc. Natl. Acad. Sci. U.S.A.* **108**, 8704 (2011).
7. J. van de Koppel *et al.*, *Science* **322**, 739 (2008).
8. We found that the results published in (*1*) were based on a corrupted data set and that there were errors in the statistical analysis. [For details, see our SOM and the correction to the de Jager paper (*10*).] Here, we analyzed a corrected and untruncated data set provided to us by M. de Jager on 20 October 2011. This data set has 3584 data points, of which 2029 remain after truncation. Since doing our analysis, an amended figure has been published (*10*), which appears to be based on ~7000 data points after truncation.
9. D. Grünbaum, *Science* **332**, 1514 (2011).
10. M. de Jager, F. J. Weissing, P. M. J. Herman, B. A. Nolet, J. van de Koppel *Science* **334**, 1641 (2011).

Acknowledgments: We thank M. de Jager for supplying the data to do this analysis and the authors of (*1*) for their constructive comments. This work was funded by Biotechnology and Biological Sciences Research Council Grant BB/G007934/1 (to V.A.A.J.) and Leverhulme Trust Grant F/00 568/X (to S.P.).

Supporting Online Material

www.sciencemag.org/cgi/content/full/335/6071/918-c/DC1
Materials and Methods
SOM Text
References

25 October 2011; accepted 13 January 2012
10.1126/science.1215747

Response to Comment on "Lévy Walks Evolve Through Interaction Between Movement and Environmental Complexity"

Monique de Jager,[1]* Franz J. Weissing,[2] Peter M. J. Herman,[1] Bart A. Nolet,[3,4] Johan van de Koppel[1,2,4]

We agree with Jansen *et al*. that a composite movement model provides a better statistical description of mussel movement than any simple movement strategy. This does not undermine the take-home message of our paper, which addresses the feedback between individual movement patterns and spatial complexity. Simple movement strategies provide more insight in the eco-evolutionary analysis and are therefore our model of choice.

The purpose of our paper (*1*, *2*) was to demonstrate that movement strategies are shaped by the interaction between individual selection and the formation of spatial complexity on the population level. We showed that in a family of movement models ranging from ballistic motion, to Lévy walk, to Brownian motion, a Lévy walk with exponent $\mu \approx 2$ is the optimal strategy for mussels involved in pattern formation. Within this family of models, a single parameter (the scaling exponent μ) distinguishes between the different movement strategies. We intentionally chose a one-dimensional strategy space that can easily be used in pairwise invasibility analyses and the subsequent pairwise invasibility plots. It also keeps focus on the main differences in movement strategy, contrasting ballistic movement, Brownian diffusion, and long-tailed step length distributions, as in Lévy walks. As is often the case, the better fit of the complex model (i.e., composite Brownian walk) trades off with the elegance and clarity of the simpler model.

Nevertheless, it might be interesting to examine the mechanisms behind the composite Brownian walk that was observed in our mussel movement data by Jansen *et al*. (*3*). Below, we investigate three possible causes of the observed movement pattern: (i) mussels switch between multiple movement modes because of changes in environmental conditions; (ii) the (collective) composite Brownian walk might be an ensemble of different individual Brownian walks; or (iii) internal switches between movement modes exist, with which mussels try to approximate a Lévy walk.

The first possible mechanism behind a composite Brownian walk is that mussels switch between movement modes in response to changes in environmental conditions. For example, a composite Brownian walk will result if animals switch between local Brownian search within a resource patch and straight-lined ballistic search between patches (*4*–*6*). Because the solitary mussels in our experiment were situated in a bare, homogeneous environment, repeated switches between movement strategies induced by changing environmental conditions do not provide a plausible explanation for the observed composite walk.

A second possible explanation for the observed composite Brownian walk could be that variation in individual movement behavior can explain the improved fit by the composite Brownian model (*7*)—for example, multiple different Brownian walks together make up the observed composite walk. To investigate this, we examined the individual movement tracks of the 12 mussels in our experiment. We indeed found a large variety of movement trajectories (Fig. 1); some mussels moved a large distance, whereas others stayed approximately at the original location. We fitted a Brownian walk, a Lévy walk, a truncated Lévy walk, and two composite Brownian walks to these individual movement trajectories, using the corrected data set and the analysis suggested by Jansen *et al*. (*2*, *3*). The analysis (Table 1 and Fig. 2) reveals that, in most cases, a Brownian walk fitted very poorly to the data. A truncated Lévy walk provided large improvement over a Brownian walk, whereas a composite Brownian walk provided only small further improvement in fit, indicating that even at the individual level, composite behavior might underlie a long-tailed movement pattern.

A third possibility to mechanistically underpin the improved fit by a composite Brownian walk is that mussels use an internal switching rule to alternate between movement modes, independent from external triggers. Our study (*1*, *2*) shows that a long-tailed step length distribution is a rewarding strategy for mussels living in, and contributing to, a spatially complex system. It is not obvious, however, how an animal should achieve such a step length distribution in prac-

[1]Spatial Ecology Department, Royal Netherlands Institute for Sea Research (NIOZ), Post Office Box 140, 4400 AC Yerseke, Netherlands. [2]Theoretical Biology Group, Centre for Ecological and Evolutionary Studies, University of Groningen, Nijenborgh 7, 9747 AG Groningen, Netherlands. [3]Department of Animal Ecology, Netherlands Institute of Ecology (NIOO-KNAW), Post Office Box 50, 6700 AB Wageningen, Netherlands. [4]Project Group Movement Ecology, Netherlands Institute of Ecology (NIOO-KNAW), Post Office Box 50, 6700 AB Wageningen, Netherlands.

*To whom correspondence should be addressed. E-mail: m.dejager@nioo.knaw.nl

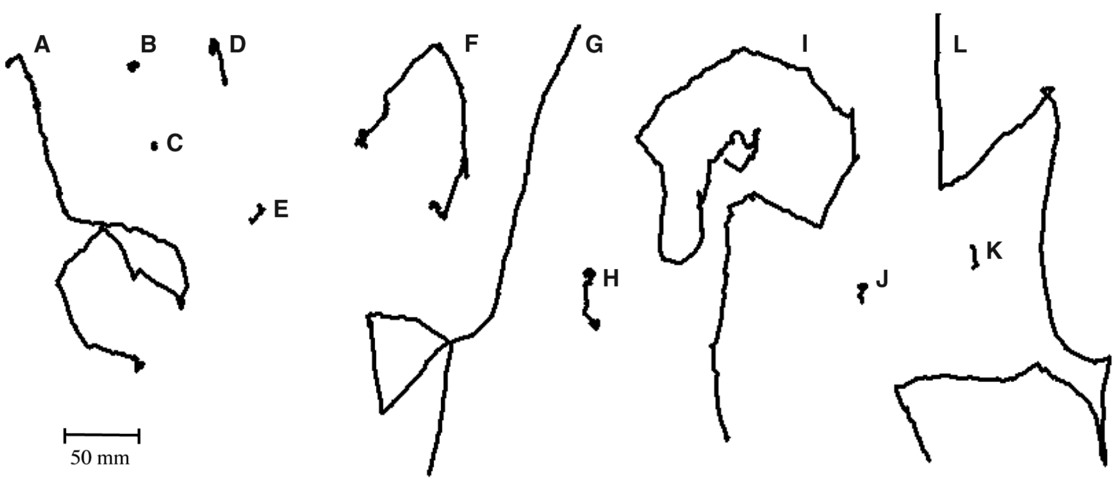

Fig. 1. Movement trajectories of the 12 mussels on which we based the model fitting in (*1*, *4*).

Table 1. Comparison of five movement models (Brownian walk, BW; Lévy walk, LW; truncated Lévy walk, TLW; composite Brownian walk with two movement modes, CBW2; composite Brownian walk with three movement modes, CBW3) for the eight mussels for which sufficient data ($n > 50$) were available. For each mussel, the table presents the Akaike information criterion (AIC) and the Akaike weights (wAIC) for the five movement models. The minimal AIC value (corresponding to the best model) is shown in bold. The Akaike weights correspond to the relative likelihood of each model (*8*). For all model fits, we used a lower boundary (l_{min}) of 0.2 mm.

Mussel	BW		LW		TLW		CBW2		CBW3	
	AIC	wAIC	AIC	wAIC	AIC	wAIC	AIC	wAIC	AIC	wAIC
A	1917.4	0.000	1262.7	0.000	1236.6	0.000	1192.4	0.006	**1182.12**	**0.994**
B	**1293.2**	**0.867**	2030.8	0.000	1618.1	0.000	1297.2	0.117	1301.2	0.016
D	330.4	0.000	282.5	0.000	256.1	0.000	**209.1**	**0.502**	209.2	0.498
F	1101.7	0.000	642.3	0.000	628.9	0.054	638.8	0.000	**623.2**	**0.945**
G	1410.7	0.000	792.4	0.000	770.8	0.000	761.6	0.001	**748.5**	**0.998**
H	625.5	0.000	775.6	0.000	750.3	0.000	**519.9**	**0.881**	523.9	0.119
I	2177.2	0.000	1650.0	0.000	1592.5	0.003	**1582.1**	**0.620**	1583.1	0.376
L	1455.8	0.000	1179.0	0.000	1129.0	0.002	1123.2	0.033	**1116.4**	**0.966**

Fig. 2. Inverse cumulative frequency distribution (e.g., the fraction of step lengths that is larger than or equal to a given step length) of the movement patterns of 12 individual mussels (thin dashed and dotted lines) and the combined data set (thick line and large dots).

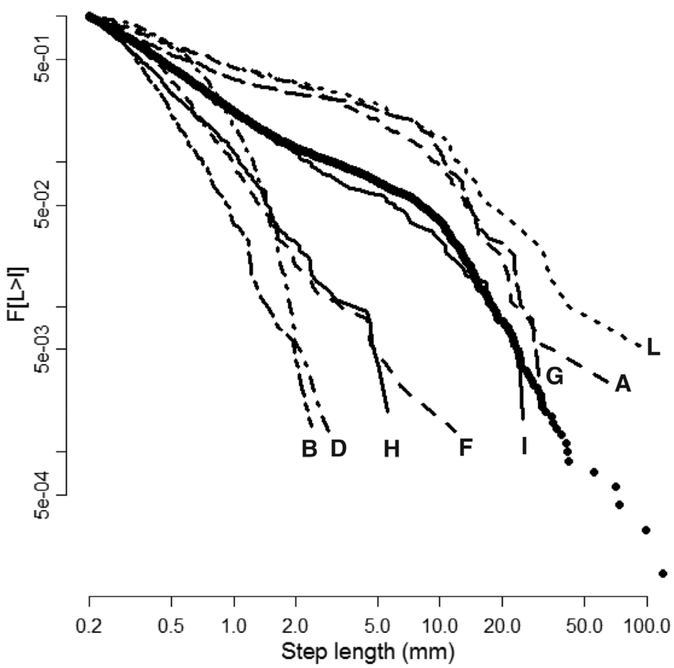

tice. It is possible that animals approximate a Lévy walk by adopting an intrinsic composite movement strategy with different modes (which do not necessarily need to be Brownian). The observation by Jansen *et al*. (*3*) that a composite walk yields a better fit to the observations thus suggests an interesting solution for this problem, which is worth further investigation. However, we think it most advisable to examine this switching behavior by means of temporal and spatial correlations of movement steps within animal tracks rather than fitting multimodal models to step size distributions. In our opinion, the observation by Jansen *et al*. (*3*) does not change the overall conclusion of our paper (*1*), but it may contribute to a better understanding of the behavioral mechanisms by which animals achieve their optimal movement strategy.

References and Notes

1. M. de Jager, F. J. Weissing, P. M. J. Herman, B. A. Nolet, J. van de Koppel, *Science* **332**, 1551 (2011).
2. M. de Jager, F. J. Weissing, P. M. J. Herman, B. A. Nolet, J. van de Koppel, *Science* **334**, 1641 (2012).
3. V. A. A. Jansen, A. Mashanova, S. Petrovskii, *Science* **335**, 918 (2012); www.sciencemag.org/cgi/content/full/335/6071/918-c.
4. M. J. Plank, A. James, *J. R. Soc. Interface* **5**, 1077 (2008).
5. S. Benhamou, *Ecology* **88**, 1962 (2007).
6. A. M. Reynolds, *Physica A* **388**, 561 (2009).
7. S. Petrovskii, A. Mashanova, V. A. A. Jansen, *Proc. Natl. Acad. Sci. U.S.A.* **108**, 8704 (2011).
8. K. P. Burnham, D. R. Anderson, *Model Selection and Multimodal Inference: A Practical Information-Theoretic Approach* (Springer-Verlag, New York, ed. 2, 2002).

Acknowledgments: We thank A. Edwards, F. van Langevelde, and V. Jansen *et al*. for their comments and suggestions. The authors declare no competing financial interests. The research of M.d.J. is supported by a grant from the Netherlands Organization of Scientific Research/Earth and Life Sciences (NWO-ALW). This is publication 5183 of the Netherlands Institute of Ecology (NIOO-KNAW).

18 November 2011; accepted 13 January 2012
10.1126/science.1215903

ENVIRONMENT

The Many Lives of Whales

Gregg Mitman

At one time, the blood-red waters in the protected coves of South Georgia island—waters stained by the butchering of thousands of whales on the shore flensing platforms—were a sign of wealth and progress. In the 1910s, F. Cook, managing director of the Southern Cross Whaling Company, reveled at the whale on land as a source of jobs, money, and commodities. But "in the water," he suggested, whales are "of value to no one, and you cannot make pets of them."

One hundred years later, the sight of a churning sea sullied with cetacean blood inspired quite different sentiments. National Geographic photographer Louie Psihoyos, repentant former dolphin trainer Ric O'Barry, and a team of covert operatives joined forces to document and expose the capture of dolphins by fishermen for the oceanarium trade and the slaughter of the remaining corralled dolphins for the meat markets of Japan. Their film, *The Cove*, took the media and audiences, particularly in the United States, by storm. Winner of the 2010 Oscar for Best Documentary and a darling of the 2009 Sundance Film Festival, *The Cove* vilified Japan's role on the International Whaling Commission (IWC) and upheld the image of dolphins and their larger cetacean cousins as playful, gentle, and intelligent emissaries of the ocean.

How, in the span of just a few generations, could the value of whales and their meaning for humanity change so drastically? In *The Sounding of the Whale*, Graham Burnett answers that question with a history of breathtaking depth. Burnett (a historian of science at Princeton University) plunges into the belly of the beast where hip-booted whale science emerged alongside industrial whaling. He dives into the diplomatic maneuverings and behind-the-scenes work of scientists like Remington Kellogg on the IWC and ultimately surfaces into the "hothouse atmosphere of the *Manchurian Candidate*–era sciences of mind and behavior," where John Lilly emerged as guru and hipster of cetacean science in the counterculture age.

In Burnett's skilled narrative, the whale as scientific object has many lives. Knowledge of whales proves to be dependent on the forms of labor through which scientists come to know their cetacean subjects. In Britain and among the Scandinavian whaling nations, markets for whale products brought biologists into both a "sloppy anatomical intimacy" and a distanced relationship, born of numbers and statistics, made possible by whaling on an industrial scale. In the pressing need to stabilize and regulate the boom-and-bust economy of whale oil, zoologist and director of the British Museum (Natural History) Sidney Harmer oversaw the Discovery Investigations, which surpassed in size and scope the famed 19th-century *Challenger* expedition. Intent on ascertaining precise information on the abundance and geographic reach of the Antarctic whale stocks, this multivessel effort traded on the aspiration that intimate knowledge of whale distribution and abundance would put "conservation on a business basis" and provide the industry with the "promise of a reasonable, *perpetual* yield." Placing Burnett's analysis against the backdrop of ecological science emerging under the British crown reveals how little we understand the extent to which widespread concern for regulating markets tied to forestry, furs, agriculture, and fisheries in the early 20th century went hand in hand with efforts to better understand the cycles of scarcity and abundance of biological organisms vital to the economies of nature and nations.

The Sounding of the Whale
Science and Cetaceans in the Twentieth Century
by D. Graham Burnett
University of Chicago Press, Chicago, 2012. 823 pp. $45, £29. ISBN 9780226081304.

In the United States, by the dawn of the 20th century, the heyday of whaling had long since passed. To the cadre of mammalogists, zoologists, and sportsmen-naturalists who in 1928 founded the Council for the Conservation of Whales (CCW), hunting and game management, not industrial slaughter and regulation, spawned their relationship to and knowledge of whales. Gifford Pinchot, a pillar of the American conservation movement, was delighted to put his "148-foot, three-masted topsail schooner" into the service of science. A porpoise bagged in the Gulf Stream was the first of many big sea trophies and scientific specimens he collected on a 1929 sailing jaunt with his family through the South Seas.

At the center of the CCW was Kellogg, curator of mammals in the Smithsonian's U.S. National Museum. His relationship to whales began with the fossilized bones of their ancestors. Developing interests in living cetaceans led him into the role of scientific diplomat and statesman as a founder of, and U.S. delegate to (1946–1964), the IWC. Nowhere has science and policy by committee come more alive and been clearly shown to be important than in Burnett's treatment and analysis of the IWC. Suffice it to say that Kellogg's hope and vision for a collaborative model of rational regulation based on science, diplomacy, and economic need would be thwarted time and again by bureaucratic processes and structures. By the end of his life, technocratic optimism gave way to moral desperation in his desire to save some of the last great mammals from extinction.

The rationality that brought the end game to commercial whaling, argues Burnett, was not the statistics of blue whale units and the life cycle and age structure of populations but the rationality "*of the whales themselves*." Near the end of the book, he navigates away from land-based whaling stations, pelagic factory ships, diplomatic boardrooms, and baleen whales to the trippy surf of places like Point Mugu Naval Missile Center and the Communication Research Institute (Saint Thomas) and the research-

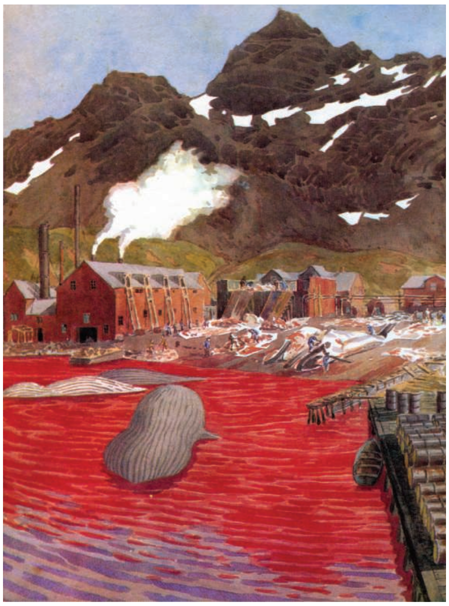

Bloody waters. Alister Clavering Hardy's 1926 painting of the whaling station at Grytviken, South Georgia.

CREDIT: FROM A. C. HARDY'S GREAT WATERS (3)

The reviewer is at the Nelson Institute for Environmental Studies, University of Wisconsin–Madison, 122 Science Hall, 550 North Park Street, Madison, WI 53706–1491, USA. E-mail: gmitman@med.wisc.edu

ers who communed with the small cetaceans they domiciled. By the 1950s, dolphins had already begun their meteoric rise to stardom, thanks to the marketing savvy, scientific research, and technological know-how of the staff behind Marineland, the first oceanarium to successfully house dolphins in captivity. Neurophysiologist Lilly would prove to be their best agent. His 1961 book (*1*) catapulted the respected former National Institute of Mental Health researcher and his scientific subject to fame when he posited that the sophisticated brain structure of dolphins made them the most promising prospect for communication with "alien intelligent life forms." Lilly's work on dolphin communication, intelligence, and behavior reverberated across the domains of science and activism: in papers on the songs of the humpback whale [e.g., (*2*)] and below the decks of the *Rainbow Warrior* with its band of ecopirateers. A rising tide of science, enmeshed in the very different lives of whales, and of sentiment, channeled across different walks of life, would effectively end commercial whaling by 1982, when the IWC passed a moratorium against it, even as certain cultures and traditions reserve their right to the taking.

Numbers rarely move people; emotions do. Lilly harnessed the sciences of affect to bring into being another life of whales, not one of populations, but of individuality and emotion. But Lilly was not alone, and it is this broader context that Burnett does not address. By the 1970s, the study of animal behavior and cognition had transformed not just whales but also other animals—among them elephants, gorillas, and wolves—into charismatic megafauna endowed with similarly rich inner lives. Furthermore, it took the emotional force of a social movement to make whales and other glamour species into paradigmatic symbols endowed with the power to foster a new environmental consciousness.

The Sounding of the Whale offers a telling reminder of just how much ideas matter, literally, in the material relationships that bind the lives of humans to other animals with whom we share Earth.

References

1. J. C. Lilly, *Man and Dolphin* (Doubleday, Garden City, NY, 1961).
2. R. S. Payne, S. McVay, *Science* **173**, 585 (1971).
3. A. C. Hardy, *Great Waters: A Voyage of Natural History to Study Whales, Plankton, and the Waters of the Southern Ocean …* (Collins, London, 1967).

10.1126/science.1216736

SCIENTIFIC ILLUSTRATION

Grand Master of Reconstruction

Mary A. Parrish

Richard Milner's *Charles R. Knight* surveys the life and work of the first and best-known American mural painter of prehistoric life. The beautifully illustrated volume documents why he is also often the most admired.

Knight (born in 1874) grew up in Brooklyn, New York, during the heyday of 19th-century American vertebrate paleontology. In their "bone wars," Othniel Charles Marsh and Edward Drinker Cope amassed hundreds of fossils new to science (e.g., *Stegosaurus*, *Triceratops*, and *Camarasaurus*) from the western United States. Young natural history museums around the country vied for material to display and explain to the public. Knight, a freelance artist, created reconstructions for many of these museums (including the Smithsonian's U.S. National Museum, Chicago's Field Museum, and the Natural History Museum of Los Angeles County), but his primary association was with the American Museum of Natural History (AMNH).

Charles R. Knight
The Artist Who Saw Through Time
by Richard Milner
Abrams, New York, 2012. 180 pp., illus. $40, C$45, £24.99. ISBN 9780810984790.

While Knight's skills as an animal artist were maturing, vertebrate paleontology at AMNH was gaining strength. In 1891, the museum hired Henry Fairfield Osborn to build its new department of vertebrate paleontology. Beginning in 1896, Osborn repeatedly turned to Knight for "beautiful, scientifically accurate paintings and sculptures of extinct animals." Osborn (AMNH president from 1908 to 1933) not only promoted Knight as his protégé, he was the artist's patron and friend for life. Through his efforts, AMNH introduced spectacular dioramas and murals (many by Knight) into its exhibit halls.

Interestingly, when Knight was meticulously studying live animals, dissections, and fossil material and collaborating with some of the best paleontologists of the day in order to achieve scientific accuracy in his work, the art world was rapidly developing in different directions, often leaving traditional realism and aesthetics behind altogether. Knight became an outspoken critic of modern art, describing it as "monstrous and inexplicable creations masquerading in the name of art."

Milner's lively text incorporates excerpts from and letters by Knight, wife Annie, daughter Lucy, Osborn, and others. The book offers insight into Knight's artistic processes, reprinting extracts from his own accounts, and reproduces many rough sketches as well as finished paintings and sculptures. Stretching far and wide, this work includes decorative sculptures of elephant, zebra, and rhinoceros heads at the Bronx Zoo; a bas-relief of ancient and modern pachyderms at the Smithsonian's National Zoological Park; and a drawing of a buffalo that graced both a 10-dollar bill (1901) and a 30-cent postage stamp (1923).

Although legally blind for much of his life, Knight's restorations of fabulous extinct vertebrates in their environments ignited the imagination of all who saw them. They are forever cemented into our collective vision of these ancient worlds. Milner's book shows why Knight retains a prominent place in the worlds of modern wildlife art and, even more so, paleoart.

10.1126/science.1220073

The reviewer is at the Department of Paleobiology, National Museum of Natural History, Smithsonian Institution, Washington, DC 20013–7012, USA. E-mail: parrishm@si.edu

CLIMATE CHANGE

Preserving Montreal Protocol Climate Benefits by Limiting HFCs

With no impending global controls on HFCs, the Montreal Protocol offers a near-term path to preserve its climate benefits.

Guus J. M. Velders,[1]* A. R. Ravishankara,[2] Melanie K. Miller,[3] Mario J. Molina,[4] Joseph Alcamo,[5] John S. Daniel,[2] David W. Fahey,[2] Stephen A. Montzka,[2] Stefan Reimann[6]

The Montreal Protocol is perhaps the most successful international environmental treaty, responsible for global phaseout of the consumption and production of ozone-depleting substances (ODSs), e.g., chlorofluorocarbons (CFCs) and hydrochlorofluorocarbons (HCFCs). Hydrofluorocarbons (HFCs), which do not destroy stratospheric ozone, were considered long-term substitutes for ODSs and are not controlled by the Montreal Protocol. Because most HFCs are potent greenhouse gases (GHGs), they are included in the Kyoto Protocol. But climate benefits provided by this protocol are limited as they apply only to developed countries and over a short time (2008–2012). As we describe below, with no impending global controls on HFCs, inclusion of HFCs under the Montreal Protocol offers a path, starting in the short term, to preserve the climate benefits already achieved by this protocol.

Climate considerations are not new to the Montreal Protocol. Signatory nations acknowledged in the preamble that they are "Conscious of the potential climatic effects of emissions of these substances [ODSs]." The climate contribution of future HCFC emissions was an important consideration for the accelerated phaseout agreed to by the parties in 2007.

Since 2010, 108 nations have signed a declaration stating their "intent to pursue further action under the Montreal Protocol aimed at transitioning the world to environmentally sound alternatives to HCFCs and CFCs" (*1*). Canada, Mexico, and the United States, as well as the Federated States of Micronesia, submitted proposals in 2010 and 2011 to control HFC use by amending the Montreal Protocol. The proposals and declaration were motivated by the interest in limiting climate change from future emissions of HFCs with high global warming potentials (GWPs) (*2*). These proposals were discussed but not adopted at the last two meetings of the Parties to the Montreal Protocol. Negotiations are expected to continue in future meetings as details of the proposals are refined.

At the 2011 Durban climate negotiations, it was decided that new climate commitments will come into effect only from 2020 onward, leaving the coming 8 years or more without any legally binding global measures under a climate agreement to reduce potential climate effects of HFCs and other GHGs. This delay heightens policy and scientific interest in examining the possibilities and consequences of regulating HFCs under the Montreal Protocol.

[1]National Institute for Public Health and the Environment (RIVM), 3720 BA Bilthoven, Netherlands. [2]Earth System Research Laboratory, National Oceanic and Atmospheric Administration (NOAA), Boulder, CO 80305, USA. [3]Touchdown Consulting, 1310 La Hulpe, Belgium. [4]University of California, San Diego, La Jolla, CA 92093, USA. [5]United Nations Environment Programme (UNEP), Nairobi, Kenya. [6]Swiss Federal Laboratories for Materials Science and Technology (Empa), CH-8600 Duebendorf, Switzerland.

*To whom correspondence should be addressed. E-mail: guus.velders@rivm.nl

Climate Benefits of Montreal Protocol

Most ODSs are also potent GHGs (*3*). Thus, reductions in atmospheric ODS concentrations to protect the ozone layer have had the added benefit of providing some climate protection. The radiative forcing (*4*) from ODSs reached 0.32 W/m^2 around 2000 (compared with about 1.5 W/m^2 for CO_2) and has remained nearly constant since. Without the Montreal Protocol, radiative forcing from ODSs could have reached 0.60 to 0.65 W/m^2, or about 35% of that of CO_2, in 2010 (see the graph) (*5*). This direct climate benefit is offset in part (about 30%) by other factors, including indirect radiative forcing from reductions in stratospheric ozone and climate forcing by increased use of ODS substitutes (*5*). Total avoided net annual ODS emissions are estimated to be equivalent to about 10 Gt CO_2/year in 2010, which is about five times the annual reduction target of the Kyoto Protocol for 2008–2012 (*5*). This climate benefit of the Montreal Protocol may be reduced or lost completely in the future if emissions of ODS substitutes with high GWPs, such as long-lived HFCs, continue to increase.

Growth in HFCs as ODS Substitutes

With CFC phaseout completed in 2010 and the scheduled phaseout of most HCFCs by 2030, HFCs are being used more in applications that traditionally used ODSs, e.g., refrigeration and air-conditioning equipment, blowing agents for foams, aerosol sprays, fire protection systems, and solvents (*6*, *7*). The atmospheric abundances of major HFCs used as ODS substitutes (*8*) are increasing 10 to 15% per year in recent years (*9*). Rising use of HFCs is directly attributable to intent and actions of the Montreal Protocol (*7*), hence, the HFC contribution to climate change can be viewed as an unintended negative side effect of these actions.

The current contribution to climate forcing of HFCs used as ODS substitutes is about 0.012 W/m^2 [excluding HFC-23 (*8*)], less than 1% of the total forcing from long-lived GHGs, but it is increasing rapidly (*9*, *10*). Growth rates and projections indicate potential for substantial future increases in emissions and atmospheric abundances of HFCs in the absence of new controls (*9*). These business-as-usual projections are based on increasing demand for ODS substitutes, particularly in developing countries (*11*).

In an upper-range scenario, global radiative forcing from HFCs increases from about 0.012 W/m^2 in 2010 to 0.25 to 0.40 W/m^2 in 2050 (*11*) (see the graph). This corresponds to 14 to 27% of the increase in CO_2 forcing under the range of Intergovernmental Panel on Climate Change (IPCC) business-as-usual scenarios from 2010 to 2050 (*12*). In these scenarios, developing countries replace HCFCs with HFCs by using the same substances and use patterns as adopted by developed countries (*11*).

Wide Range of HFC Lifetimes and GWPs

In recent proposals to amend the Montreal Protocol, production and consumption of HFCs would be reduced in phases from baseline levels. This would encourage the use of alternative substances with low GWPs. The extent to which HFCs or other ODS substitutes will influence climate depends on past and future emissions, atmospheric lifetimes, and the efficiency of these molecules in absorbing infrared radiation. Most fluorocarbons (e.g., CFCs, HCFCs, and HFCs) have a similar ability (within about a factor of three) to trap infrared radiation, on a per-molecule

basis, in Earth's atmosphere. Therefore, differences in their relative impact on climate arise primarily from differences in atmospheric lifetimes. The longer the lifetime of a molecule, the larger its potential contribution to climate forcing.

Fully saturated HFCs (molecules with only single bonds), used in significant quantities commercially (e.g., HFC-32, -125, -134a, -143a, and -152a), have atmospheric lifetimes that range from 1 to 50 years (*9*). Their 100-yr GWPs range from 100 to about 4000. Unsaturated HFCs (also referred to as hydrofluoro-olefins, HFOs) have much shorter atmospheric lifetimes, on the order of days to weeks, with correspondingly smaller GWPs (~20 or less). If the current mix of HFCs with an average lifetime of 15 years (average GWP of 1600) were replaced by HFCs with lifetimes less than 1 month (GWP less than ~20), the total HFC radiative-forcing contribution in 2050, even under the high-emission scenario, would be less than the current forcing from HFCs (see the graph). Such choices are currently available.

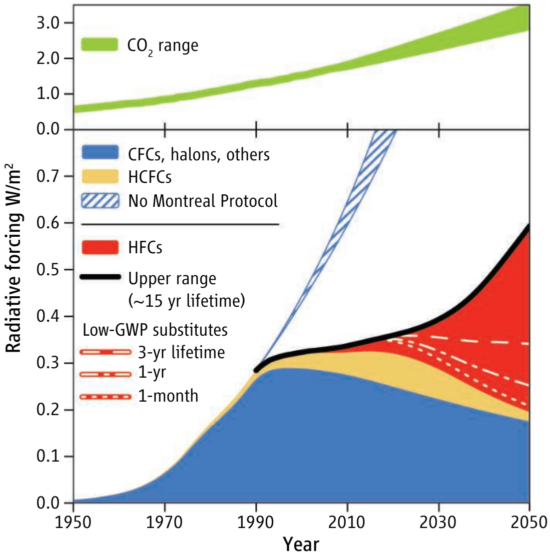

Projected radiative forcing by ODSs, HFCs, low-GWP substitutes, and CO_2 (*12*). The blue hatched region indicates what would have occurred in the absence of the Montreal Protocol, with 2 to 3% annual production increases in ODSs [data taken from (*5*)]. Added to the radiative forcing from ODSs [data from (*9*)] are the contributions from HFCs from the upper-range scenario [data from (*11*)]. Also shown are the radiative forcing from alternative scenarios in which substitution is made with chemicals having shorter lifetimes (lower GWPs); their contribution is calculated using methods described in (*11*) with the parameters from (*16*). Under the Montreal Protocol, use reductions started in 1989 for CFCs and in 1996 for HCFCs.

Choosing Appropriate Alternatives

Approaches to reduce climate forcing from future HFC use and to preserve climate benefits provided by the Montreal Protocol include (*6*, *13*, *14*) these: (i) replacing high-GWP HFCs with substances that have low impact on climate (e.g., hydrocarbons, CO_2 or certain HFCs) and alternative technologies (e.g., fiber insulation materials) and (ii) reducing HFC emissions (e.g., by changing the design of equipment and capturing and destroying HFCs when equipment reaches the end of its useful life). Given the orders-of-magnitude differences in GWPs, it is expected that transitioning to low-climate-impact substitutes with similar life-cycle energy efficiencies as high-GWP HFCs has the potential to provide larger climate benefits than attempts to reduce emissions of HFCs in applications. Low-climate-impact substitutes are already in commercial use in several sectors. These include fiber insulation materials; dry powder asthma inhalers; and non-HFC substances with low or zero GWPs, such as hydrocarbons, ammonia, and CO_2 in some refrigeration systems. Several HFCs with very short atmospheric lifetimes (hence, low GWPs) are now being introduced for foams and aerosols (HFC-1234ze) and mobile air conditioners (HFC-1234yf) (*15*). Also, the Multilateral Fund (MLF) of the Montreal Protocol is funding many projects in developing countries for the transition from ODSs to alternative substances or methods with lower impact on climate. The primary decisions about whether to use high-GWP HFCs or alternatives are currently made by companies and are subject to normal commercial considerations, such as performance; viability; affordability; availability; and health, safety, and environmental factors (*13*). A global framework for regulating future HFC use would provide a clear signal for the commercial sector, guiding the selection of substances for long-term use, as done under the Montreal Protocol for ODSs.

In addition to the direct contribution to climate forcing, indirect climate effects arise from the energy used or saved during the application or product's full life cycle. Ideally, alternative systems would have overall energy efficiencies at least as high as the systems they replace. This is already feasible in a number of sectors, such as domestic, commercial, and industrial refrigeration and some types of air-conditioning systems (*6*, *13*, *15*).

Future Challenge for Policy-Makers

A large number of countries have formally stated their intention to preserve climate benefits of the Montreal Protocol (*1*). A challenge for policy-makers is to identify how this might be accomplished. Given that climate impacts of HFC use can be viewed as unintended side effects of the Montreal Protocol, an option is to expand provisions of this protocol while drawing from parties' experience in formulating successful ODS controls that took scientific, economic, and technical aspects into account. The Montreal Protocol has relevant infrastructure for accomplishing this, including the MLF, expert panels, regional networks, and administrative procedures. This infrastructure and experience suggest that such an approach could effectively and quickly limit continued growth of high-GWP HFCs and preserve the substantial climate benefits that were gained by the Montreal Protocol in phasing out ODSs.

References and Notes

1. UNEP, *Report of the 22nd Meeting of the Parties to the Montreal Protocol, Annex III, Declaration on the Global Transition Away from HCFCs and CFCs* (UNEP, Nairobi, Kenya, 2010).
2. The GWP is an index that enables comparison of climate forcing integrated over a specified time horizon (usually 100 years) of the emissions of GHGs relative to CO_2.
3. V. Ramanathan, *Science* **190**, 50 (1975).
4. Radiative forcing is a measure of how a climate-forcing agent influences the energy balance of Earth.
5. G. J. M. Velders *et al.*, *Proc. Natl. Acad. Sci. U.S.A.* **104**, 4814 (2007).
6. IPCC and Technology and Economic Assessment Panel (TEAP), *Special Report: Safeguarding the Ozone Layer and the Global Climate System: Issues Related to Hydrofluorocarbons and Perfluorocarbons*, B. Metz *et al.*, Eds. (Cambridge Univ Press, New York, 2005).
7. TEAP, *2010 Assessment Report of the Technology and Economic Assessment Panel* (UNEP, Nairobi, Kenya, 2011).
8. The presence of HFCs in the atmosphere arises almost completely from their use as substitutes for ODSs. HFC-23 is an exception. It results primarily from unintentional production and release during the production of HCFC-22.
9. World Meteorological Organization (WMO), *Scientific Assessment of Ozone Depletion: 2010* (Global Ozone Research and Monitoring Project Report no. 52, WMO, Geneva, 2011).
10. S. A. Montzka *et al.*, *Nature* **476**, 43 (2011).
11. G. J. M. Velders *et al.*, *Proc. Natl. Acad. Sci. U.S.A.* **106**, 10949 (2009).
12. IPCC, *Climate Change 2001: The Scientific Basis*, J. T. Houghton *et al.*, eds. (Cambridge Univ. Press, New York, 2001).
13. TEAP, Progress Report of the Technology and Economic Assessment Panel (UNEP, Nairobi, Kenya, 2010), vol. 1.
14. W. Schwarz *et al.*, Preparatory study for a review of Regulation (EC) No 842/2006 on certain fluorinated greenhouse gases (Öko-Institute, Freiburg, Germany, 2011).
15. UNEP, *HFCs: A Critical Link In Protecting Climate and the Ozone Layer* (UNEP, Nairobi, Kenya, 2011).
16. For the substitutes, a molecular mass of 100 g/mol is used and a radiative efficiency of 0.2 W/m² per ppb; typical values for commercially used HCFCs and HFCs. An annual release from the bank of 13% is assumed, typical for refrigeration and air conditioning (*9*). The low-GWP scenarios are based on the assumption that from 2015 onward all demand for HFCs [taken from (*11*)] is met by substitutes with shorter lifetimes.
17. The opinions expressed here are those of the authors and not of their institutions.

10.1126/science.1216414

EVOLUTION

Some Like It Hot

A study of horse evolution illustrates the connection between environmental temperature and mammal body size.

Felisa A. Smith

Body size matters. It sets the energetic demands of organisms, regulates the rates of physiological processes, and influences population densities and other key characteristics of animal communities and populations (*1*). Thus, it is no surprise that most animals have a characteristic (*2*) and highly heritable size (*3*). Yet the body sizes of mammal lineages have varied greatly over evolutionary history. The demise of dinosaurs ~65.5 million years ago marked the onset of rapid morphological and ecological diversification in terrestrial mammals that ultimately led to size increases of more than four orders of magnitude. On page 959 of this issue, Secord *et al*. (*4*) illustrate the critical role of temperature in driving body size evolution between ~55.5 and 54.5 million years ago.

Early horses. This painting by the German artist Heinrich Harder (1858–1935) was part of a series of collector cards illustrating prehistoric animals commissioned by the Reichardt Cocoa Company. It depicts an early species of *Sifrhippus* (*Hyracotherium*) that first appeared about 55 million years ago. Secord *et al*. show that the body size of *Sifrhippus* changed in response to temperature fluctuations between ~55.5 and 54.5 million years ago.

According to Bergmann's rule, within a broadly distributed genus, species of larger size are found in colder environments, and species of smaller size are found in warmer areas (*5*). Some researchers argue that the rule arises as a result of the need for heat conservation or loss; others attribute it to ecosystem properties such as productivity (*6*). Regardless, Bergmann's rule holds for more than 70% of modern endotherms (animals that maintain a constant internal body temperature) (*6*). Moreover, it has been documented over historical and microevolutionary time (*6*, *7*); recent work even suggests that temperature constrained the maximum size that mammals could attain in the course of evolution (*8*). Thus, temperature may be expected to influence body size evolution within lineages.

The early Cenozoic is an interesting chapter in Earth history. Not only does its onset ~65.5 million years ago mark the end of dinosaurs and the beginning of the radiation of mammals, but it was also a time of rapid fluctuation of climate. The most severe hot episode was the Paleocene-Eocene Thermal Maximum (PETM), which occurred ~55 million years ago (*9*). During the PETM, sea surfaces warmed by more than 5°C (*9*, *10*), causing changes in aquatic and terrestrial ecosystems, including substantial changes in mammalian diversity (*11*). In particular, the immigration of modern ungulate taxa (Perissodactyla and Artiodactyla) into North America profoundly and permanently altered ecosystems on the continent (*11*, *12*). Dwarfing of numerous archaic and modern lineages during the PETM has been reported (*13*), but a quantitative assessment of how the PETM influenced mammalian body size evolution has been lacking.

Secord *et al*. examine the consequences of climatic shifts on the body size of the small early horse *Sifrhippus* (also known as *Hyracotherium*), which first appeared in North America during the PETM. They test the two main causal mechanisms underlying Bergmann's rule: temperature and productivity.

The authors build on previous work in the Clarks Fork Basin of northwestern Wyoming, a site rich in mammal fossils with a continuous stratigraphic section between ~60 and 53 million years in age (*13*). They estimate body mass for ~44 adult horses by measuring the area of the first molar. Using $\delta^{13}C$ and $\delta^{18}O$ signatures recorded in the tooth enamel of more than 150 mammalian fossils collected at Cabin Fork, Wyoming, they develop a highly resolved local paleoclimatic record spanning the PETM. The carbon signature mirrors the abrupt negative carbon excursion associated with the PETM in other locations (*9*), whereas the oxygen isotopes yield estimates of changes in air temperature. As expected on the basis of Bergmann's rule, the authors find that changes in $\delta^{18}O$ were significantly related to body size changes in *Sifrhippus*. The size shifts were substantial: Body size decreased by ~30% at the start of the PETM, and increased abruptly by more than 75% at its end.

But was temperature the ultimate driver behind the body size shifts? Or were they caused by changes in productivity? Barring unusual instances of exceptional preservation, direct estimation of vegetation structure or local productivity in the fossil record has been problematic. Secord *et al*. take a clever approach by comparing oxygen isotopes in fossil teeth of mammal taxa that varied in their affinity for aquatic environments. Oxygen isotopes in herbivores largely reflect the composition of local surface and plant water. Isotopic enrichment occurs in species that occupy drier habitats with little surface water. For such evaporation-sensitive species, enrichment tends to be positively related to habitat aridity (*14*). By comparing the evaporation-sensitive *Sifrhippus* with *Coryphodon*, an archaic herbivorous ungulate generally considered to be associated with aquatic habitats, Secord *et al*. develop a proxy for "aridity." This, they argue, is inversely related to productivity.

The correspondence between this metric and mean annual precipitation estimated from analysis of nearby soil sediments of the same age is quite high, suggesting that Secord *et al*. have captured something akin to productivity. However, they find no correlation between productivity and body size. In fact, the opposite trend is evident: a decrease in body size during wetter conditions. Thus, body size evolution over the PETM appears to have been driven by temperature fluctuations, consistent with the original characterization of Bergmann's rule (*5*).

Department of Biology, University of New Mexico, Albuquerque, NM 87131, USA. E-mail: fasmith@unm.edu

At the start of the Cenozoic, mammals rapidly increased in size across the globe, probably as a result of ecological release and the occupation of newly vacated niches (*8*). Ten million years later, the upper boundary of mammalian size was still increasing, but Secord *et al.* also demonstrate the operation of opposing selective forces at this time. Their highly resolved and local paleotemperature and productivity proxy, tested against a single, well-resolved sequence of mammalian fossils, allows a mechanistic and quantitative examination of the processes influencing body size over time.

The findings of Secord *et al.* underscore the importance of the fossil record for examining how future environmental changes may influence life on Earth. Recent climate warming has already led to changes in the phenology, distribution, and morphology of species (*15*). However, it remains unclear how rapidly animals may adapt. Patterns such as Bergmann's rule demonstrate the ability of species to adapt to fluctuating abiotic conditions, and highlight the strong selection imposed on organisms by their environment.

However, some caution is warranted when extrapolating from the past to the future. The extreme change in Earth's surface conditions during the PETM is not unlike that expected to occur in the future, but the time frame was considerably longer. There may be more appropriate analogies for anthropogenic warming in the fossil record, such as the Younger Dryas, when large abrupt temperature shifts took only decades. As we increasingly turn from explaining the present to anticipating the future (*16*), an understanding of evolutionary history becomes imperative for untangling biological complexity. Nowhere is such a deep-time perspective more important than in studies of anthropogenic warming.

References

1. R. H. Peters, *The Ecological Implications of Body Size* (Cambridge Univ. Press, Cambridge, 1983).
2. J. B. S. Haldane, *Possible Worlds and Other Essays* (Harper, New York, 1926).
3. F. A. Smith *et al.*, *Am. Nat.* **163**, 672 (2004).
4. R. Secord *et al.*, *Science* **335**, 959 (2012).
5. E. Mayr, *Evolution* **10**, 105 (1956).
6. V. Millien *et al.*, *Ecol. Lett.* **9**, 853 (2006).
7. F. A. Smith, J. L. Betancourt, J. H. Brown, *Science* **270**, 2012 (1995).
8. F. A. Smith *et al.*, *Science* **330**, 1216 (2010).
9. J. Zachos, M. Pagani, L. Sloan, E. Thomas, K. Billups, *Science* **292**, 686 (2001).
10. M. Pagani, K. Caldeira, D. Archer, J. C. Zachos, *Science* **314**, 1556 (2006).
11. B. Figueirido, C. M. Janis, J. A. Pérez-Claros, M. De Renzi, P. Palmqvist, *Proc. Natl. Acad. Sci. U.S.A.* **109**, 722 (2012).
12. M. O. Woodburne, G. F. Gunnell, R. K. Stucky, *Proc. Natl. Acad. Sci. U.S.A.* **106**, 13399 (2009).
13. P. D. Gingerich, *Univ. Mich. Papers Mus. Paleo.* **28**, 1 (1989).
14. N. E. Levin *et al.*, *Proc. Natl. Acad. Sci. U.S.A.* **103**, 11201 (2006).
15. C. Parmesan, G. Yohe, *Nature* **421**, 37 (2003).
16. S. T. Jackson, *Front. Ecol. Environ.* **5**, 455 (2007).

10.1126/science.1219233

ATMOSPHERIC SCIENCE

Frictional Dissipation—Blame It on the Rain

Satellite observations reveal the extent to which rainfall removes kinetic energy from the atmosphere, and thus its impact on circulation.

Dargan M. W. Frierson

Frictional dissipation in a turbulent flow occurs when kinetic energy is transferred to smaller and smaller scales until it is eventually removed by molecular diffusion. In addition to this turbulent dissipation, kinetic energy in Earth's atmosphere is also removed in the shear zones surrounding falling raindrops and ice particles. On page 953 of this issue, Pauluis and Dias (*1*) provide the first observational estimate of the precipitation-induced dissipation and show that its magnitude is comparable to that of turbulent dissipation in air.

As raindrops or other hydrometeors fall downward, shear zones around the particles develop, providing frictional deceleration and causing the hydrometeor to fall at a terminal velocity (see the figure). Although it is clear that dissipation occurs around any given hydrometeor, the substantial contribution of hydrometeors to the global mean dissipation is disproportionate to the small total mass of these particles. After all, water vapor makes up only around 1% of the mass of the atmosphere, and liquid and ice water are orders of magnitude smaller in atmospheric concentration.

Pauluis and Dias used a precipitation radar for their calculation of the dissipation induced by falling hydrometeors. Instead of the traditional ground-based radars used by TV meteorologists to warn viewers of the location of severe weather bands, the first spaceborne precipitation radar (PR) is used, from the Tropical Rainfall Measuring Mission (TRMM), which launched in 1997. The TRMM PR uses 13.8 GHz radio wave pulses to detect falling hydrometeors throughout the tropics.

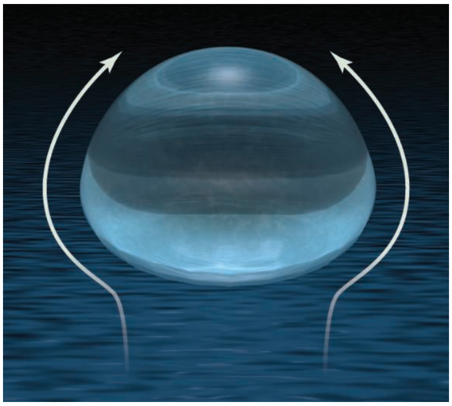

Frictional dissipation around a falling raindrop. Drag forces around falling raindrops deform and decelerate the droplets, causing them to fall at a terminal velocity. There is also kinetic energy dissipation associated with the drag, and this precipitation-induced dissipation makes up an appreciable fraction of the total frictional dissipation on Earth.

CREDIT: P. HUEY/SCIENCE

The TRMM PR measures radar reflectivity and translates this into fall speeds relative to the surrounding air. Because the frictional dissipation surrounding hydrometeors is proportional to the terminal velocity relative to air, the precipitation rate can be translated into a dissipation rate. Thus, Pauluis and Dias calculate a tropically averaged dissipation rate of 1.8 W m^{-2}, a value that is consistent with previous theoretical estimates (*2*).

Pauluis and Dias also show the structure of precipitation-induced dissipation as a function of latitude and longitude. The dissipation field is similar to that of precipitation itself, but can be appreciably larger over continental areas where rain falls into drier air below. If reevaporation of rain occurs in a column,

Department of Atmospheric Sciences, University of Washington, Seattle, WA 98195, USA. E-mail: dargan@atmos.washington.edu

there can be large amounts of dissipation with little rainfall at the ground.

This study is an additional confirmation of the important role of the hydrologic cycle on the dynamics of Earth's atmosphere. Evaporative cooling and latent heat release by precipitation are also key mechanisms by which energy is transferred from the ocean to the atmosphere (*3*), the troposphere becomes stratified (*4*), and energy is transported poleward in the mid-latitudes (*5*). These dynamical impacts of the hydrologic cycle are in addition to the well-known radiative impacts of water vapor and clouds (*6*). The hydrologic cycle is also one of the aspects of the climate system that is changing most rapidly with global warming, because of the rapid increase of humidity with temperature.

The Pauluis and Dias study has implications for theories of the atmospheric general circulation. As the atmosphere transports heat from the warm ocean surface to the colder troposphere, it acts as a heat engine that generates kinetic energy, with efficiency less than or equal to the Carnot efficiency. Previous studies (*7*, *8*) suggested that the work done by the atmosphere is appreciably less than a Carnot cycle because of inefficiencies tied to the hydrologic cycle. In this regard, the fact that precipitation dissipates a substantial amount of kinetic energy implies that a large fraction of the work done by the atmospheric circulation is used to lift water and not to sustain winds. This presumably means that a precipitating atmosphere generates less kinetic energy for maintaining atmospheric circulations on a large scale.

Precipitation-induced dissipation presents a particular challenge for theories of atmospheric circulation based on the maximum entropy production principle, a topic that generates spirited debate (*9*, *10*). Because these theories typically attempt to predict the turbulent dissipation from thermodynamic properties alone, it remains to be seen whether such theories can be modified to include a dissipation component that is a function of precipitation, or whether alternative thermodynamic configurations can be used [for example, the steam cycle proposed in (*11*)].

The importance of precipitation-induced dissipation will increase with global warming. Global average precipitation is projected to increase at a rate of approximately 1 to 2% per degree of warming (*12*), and the depth of convection should increase in a warmer climate; both of these allow for more frictional dissipation. Changes in the latitudinal structure of precipitation, or in the fraction of precipitation that is reevaporated, could change the importance of this term as well. A naïve expectation based on kinetic energy production is that circulations would decrease in strength in response to this, and such weakening of large-scale circulations in the tropics is found in simulations of global warming (*13*). It remains to be seen whether arguments based on kinetic energy dissipation can be useful to explain these simulation results, or whether more traditional arguments based on the effect of increased stratification on the energy budget (*14*) are more generally applicable. Observational constraints will of course be central to this and other future research directions. The work of Pauluis and Dias is unique because it provides an observational estimate within a budget where the terms are usually too small to measure with accuracy.

References

1. O. Pauluis, J. Dias, *Science* **335**, 953 (2012).
2. O. M. Pauluis, V. Balaji, I. M. Held, *J. Atmos. Sci.* **57**, 989 (2000).
3. K. E. Trenberth, J. T. Fasullo, J. Kiehl, *Bull. Am. Meteorol. Soc.* **90**, 311 (2009).
4. D. M. W. Frierson, I. M. Held, P. Zurita-Gotor, *J. Atmos. Sci.* **63**, 2548 (2006).
5. R. T. Pierrehumbert, *Nature* **419**, 191 (2002).
6. D. L. Hartmann, *Global Physical Climatology* (Academic Press, San Diego, CA, 1994).
7. O. M. Pauluis, I. M. Held, *J. Atmos. Sci.* **59**, 125 (2002).
8. R. Goody, *J. Atmos. Sci.* **60**, 2827 (2003).
9. R. Goody, *J. Atmos. Sci.* **64**, 2735 (2007).
10. K. Caldeira, *Clim. Change* **85**, 267 (2007).
11. O. M. Pauluis, *J. Atmos. Sci.* **68**, 91 (2011).
12. I. M. Held, B. J. Soden, *J. Clim.* **19**, 5686 (2006).
13. G. A. Vecchi, B. J. Soden, *J. Clim.* **20**, 4316 (2007).
14. T. R. Knutson, S. Manabe, *J. Clim.* **8**, 2181 (1995).

10.1126/science.1219015

DEVELOPMENT

Cell Death by Glutamine Repeats?

A glutamine-rich protein plays a role in developmentally regulated cell death in *C. elegans*.

Christopher D. Link and Tassa K. Saldi

A number of eukaryotic proteins contain stretches of repeating glutamine residues (*1*). For example, huntingtin pro- tein contains a glutamine-repeat sequence of 6 to 35 residues, and prion protein has a domain rich in glutamine and asparagine residues (Q/N-rich domain). Expansion of the glutamine repeat in huntingtin and at least seven other proteins results in neurodegenerative disease (*2*), whereas conformational changes in prion protein cause a range of spongiform encephalopathies (*3*). Glutamine repeats and Q/N-rich domains can form α-helical and coiled-coil secondary structures, driving protein aggregation. Aggregation of numerous disease-associated proteins that do not contain polyglutamine domains has been associated with neurodegeneration (such as the β-amyloid peptide and the tau protein in Alzheimer's disease). Thus, the presence of glutamine-rich domains in proteins associated with neurodegeneration could be due to their ability to induce protein aggregation per se. Alternatively, glutamine-rich proteins could have a "natural role" in inducing cell death that becomes dysregulated in neurodegenerative disease. On page 970 of this issue, Blum *et al*. (*4*) identify a Q/N-rich protein that aids in the programmed cell death of a specific cell in the model nematode *Caenorhabditis elegans*. This result provides support for the "natural role" explanation for the association of glutamine-rich proteins and neurodegeneration.

During postembryonic development of *C. elegans* male worms, the extension of the growing somatic gonad is led by the male-specific linker cell (see the figure). In the fourth larval stage, the somatic gonad must connect to the cloaca to allow adult males to inseminate hermaphrodites. This connection requires an additional "sacrificial" function of the linker cell, which undergoes programmed cell death and is subsequently engulfed by the cloacal cells, leading to a clear conduit from the gonad to the exterior of the worm. Unlike other known programmed cell deaths in *C. elegans*, that of the linker cell does not require any of the genes involved in typical apoptotic cell death, and results in a dying cell morphology more akin to necrotic cell death (*5*). To identify genes involved in the nonapoptotic killing of the linker cell, Blum *et al*. performed a whole-genome RNA interference screen. Among the five genes they found was *pqn-41*, which encodes a protein

Institute for Behavioral Genetics, University of Colorado, Boulder, CO 80309, USA. E-mail: linkc@colorado.edu

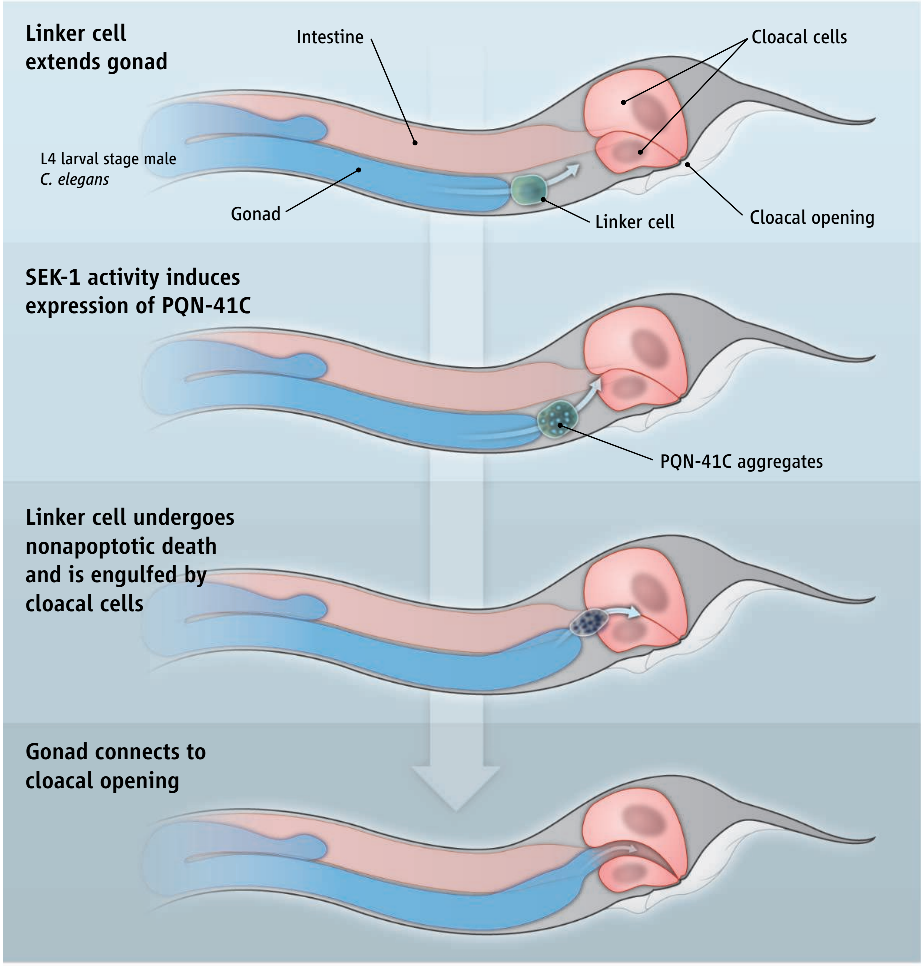

Sacrificial cell. During *C. elegans* development, expression of the polyglutamine protein PQN-41C in the linker cell triggers a type of programmed cell death (nonapoptotic) that is required for the male gonad to connect to the exterior of the animal to facilitate dissemination. This death process may be relevant to neurodegenerative conditions that are associated with polyglutamine-repeat proteins.

that contains a glutamine-rich domain. Only *pqn-41* isoform "C" is required for linker cell death. Blum *et al.* show that the glutamine-rich domain in PQN-41C and its ability to form a coiled-coil structure are essential for this protein to aid in the killing of the linker cell. They further observed that the glutamine-rich domain drives the formation of cytoplasmic inclusions in vivo.

pqn-41 is expressed in many cell types throughout development, but it is expressed in the linker cell only shortly before cell death. This induction of *pqn-41C* expression involves the activity of the stress-activated protein kinase kinase SEK-1 and the Toll–interleukin-1 receptor scaffolding protein, but not other components of the SEK-1 signaling pathway that function in innate immunity. The *pqn-41* gene is not essential for linker cell killing (loss of *pqn-41* function still results in ~80% of the linker cells dying), and it likely functions in parallel to another nonapoptotic cell death pathway controlled by the transcription factor LIN-29. Given that PQN-41 is expressed in many cells that do not undergo programmed cell death, it is unlikely that PQN-41C is by itself a "killer" protein. Presumably, the coordinated expression of PQN-41C and other proteins aid in the killing of the linker cell. Alternatively, coexpression in other cells of the other *pqn-41* isoforms (A and B), which appear to reduce linker cell death, could block PQN-41C–promoted cell killing. Further studies will be needed to determine if PQN-41A and B are negative regulators of PQN-41C, and if they inhibit PQN-41C aggregation.

What is the molecular function of PQN-41C, and could this be relevant to human glutamine-rich proteins associated with neurodegenerative diseases? The carboxyl-terminal Q/N-rich domain of a conserved RNA binding protein (called T cell–restricted intracellular antigen-1) is essential for the formation of cytoplasmic stress granules (which sequester mRNAs and translation machinery to limit protein expression) under adverse cellular conditions (*6*). Indeed, many proteins that localize to stress granules and their close cousin, processing bodies (which sequester and degrade mRNA to control protein production), contain proteins with Q/N-rich domains (*7*). Conceivably, PQN-41C could nucleate a multicomponent complex that either actively promotes linker cell killing, or sequesters factors that oppose cell killing. In this regard, wild-type huntingtin protein sequesters the repressor element–1 transcription factor/neuron restrictive silencer factor, leading to enhanced expression of brain-derived neurotrophic factor (which prevents neuron degeneration) (*8*).

The PQN isoform that restores cell killing (PQN-41C) has no conserved domains and has homologs only among *Caenorhabditis* species. Perhaps the most intriguing connection between *pqn-41*–promoted linker cell death and mammalian neurodegeneration associated with polyglutamine-repeat proteins is the distinct ultrastructural pathology observed in dying linker cells, particularly the crenellation (infolding) of the nuclear envelope. Blum *et al.* point out that distortion of the nuclear membrane has been observed in multiple models of polyglutamine protein toxicity. It is unclear if this ultrastructural similarity is indicative of a conserved, nonapoptotic cell death pathway acting both in *C. elegans* linker cell killing and polyglutamine protein–induced neurodegeneration in mammals. Further research will be needed to determine if PQN-41 and mammalian polyglutamine-repeat proteins have any interacting protein partners in common. Understanding how PQN-41C expression results (or fails to result) in cell death may yield insights into how polyglutamine-repeat disease proteins induce neuronal dysfunction, and how this can be prevented.

References

1. M. D. Michelitsch, J. S. Weissman, *Proc. Natl. Acad. Sci. U.S.A.* **97**, 11910 (2000).
2. C. J. Cummings, H. Y. Zoghbi, *Hum. Mol. Genet.* **9**, 909 (2000).
3. D. W. Colby, S. B. Prusiner, *Cold Spring Harb. Perspect. Biol.* **3**, a006833 (2011).
4. E. S. Blum, M. C. Abraham, S. Yoshimura, Y. Lu, S. Shaham, *Science* **335**, 970 (2012).
5. M. C. Abraham, Y. Lu, S. Shaham, *Dev. Cell* **12**, 73 (2007).
6. N. Gilks *et al.*, *Mol. Biol. Cell* **15**, 5383 (2004).
7. M. G. Thomas, M. Loschi, M. A. Desbats, G. L. Boccaccio, *Cell. Signal.* **23**, 324 (2011).
8. C. Zuccato, *Nat. Genet.* **35**, 76 (2003).

10.1126/science.1219834

STRUCTURAL BIOLOGY

How a Neurotoxin Survives

Botulinum neurotoxin must form a complex with a structurally similar protein to survive in the gastrointestinal tract.

Michael Adler

Botulinum neurotoxins are secreted by the spore forming Gram-positive bacteria *Clostridium botulinum* and some other *Clostridium* strains under suitable anaerobic conditions (*1*). Ingestion or inhalation of botulinum neurotoxin leads to a severe neuroparalytic disease, termed botulism, which is characterized by muscle paralysis and autonomic dysfunction. Both conditions stem from inhibition of acetylcholine release, which results from botulinum neurotoxin-mediated proteolysis of one of three SNARE (soluble *N*-ethylmaleimide–sensitive factor attachment protein receptor) proteins involved in the release of this neurotransmitter from nerve terminals (*2*). On page 977 of this issue, Gu *et al*. (*3*) provide a key insight into how botulinum neurotoxin can survive passage through the gastrointestinal tract, allowing the intact toxin to reach the bloodstream.

Botulinum neurotoxin is synthesized as a single 150 kD protein, which is modified posttranslationally to the active two-chain form (*2*). The smaller light chain (LC) catalyses SNARE protein cleavage by a Zn^{2+}-dependent mechanism. The larger heavy chain contains a binding domain (H_C) for selective attachment to cholinergic nerve terminals and a translocation domain (H_N) for intracellular delivery of the LC to the nerve-terminal cytosol, where it can cleave the appropriate SNARE protein. Owing to its extreme potency and history of weaponization, botulinum neurotoxin has been designated by the U.S. Centers for Disease Control and Prevention as a category A bioterrorism agent (*4*). Yet, its exquisite selectivity and long duration of action has also enabled dilute formulations to be used for clinical indications such as focal dystonias, spasticity, wound healing, and aesthetics (*5*).

Unlike botulinum neurotoxin/A, which is the most lethal substance known, neurotoxin-associated proteins are completely devoid of toxicity (*2*). Three of these (HA17, HA33, and HA70) have hemagglutinin activity; the fourth and largest lacks this activity and is called nontoxic nonhemagglutinin (NTNHA). When associated with these proteins, botulinum neurotoxin is referred to as the toxin complex or progenitor toxin, with molecular weights of 300 to 900 kD depending on the degree of aggregation (*6*).

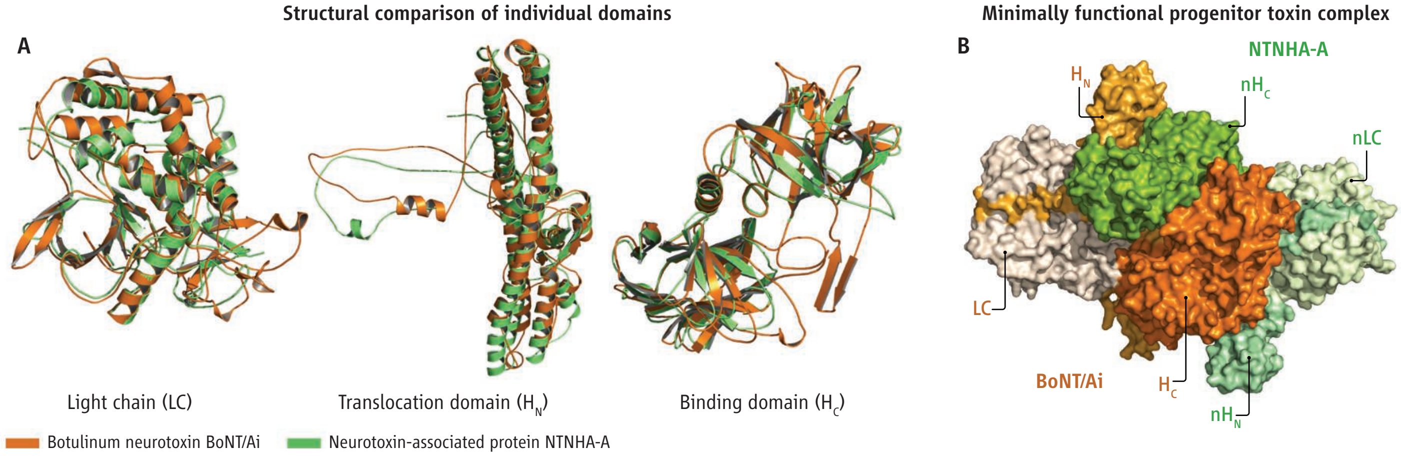

Interlocked complex. Gu *et al*. report the crystal structure of a complex between the botulinum neurotoxin BoNT/Ai and the neurotoxin-associated protein NTNHA-A. The two proteins have surprisingly similar domain structures (**A**). The complex formed by the two proteins (**B**) can survive the conditions of the gastrointestinal tract, whereas neither protein can survive these conditions in isolation. nLC, nH_N, and nH_C denote the regions in NTNHA-A that correspond to the LC, H_N, and H_C of the neurotoxin, respectively. Data from Gu *et al*.'s (*3*) supporting online material: (A) modified from figure S6; (B) modified from figure S3.

Botulinum neurotoxin can intoxicate the host by inhalation or ingestion. Both routes involve transcytosis of the neurotoxin across epithelial barriers to reach the circulation, and from there, the nerve terminal targets (*6*). During passage through the gastrointestinal tract the toxin must endure extremes in pH and potential destruction by proteolysis to emerge as active toxin in the bloodstream. Gu *et al*. demonstrate how botulinum neurotoxin achieves this feat, the subject of conjecture for more than half a century. The key to this mystery lies in the accessory proteins that are cosecreted by botulinum neurotoxin-producing bacteria. Thus, botulinum neurotoxin exists in nature not as the pure toxin but rather as a complex bound noncovalently with neurotoxin-associated proteins.

Gu *et al*. focus on the role of NTNHA, which together with botulinum neurotoxin constitutes the minimally functional progenitor toxin complex (M-PTC) (*3*). The authors coexpressed a catalytically inactive mutant of botulinum neurotoxin/A (BoNT/Ai) with an NTNHA identical to that associated with wild-type botulinum neurotoxin/A (NTNHA-A) in *Escherichia coli*. The proteins form a tight 1:1 complex at acidic pH similar to that found in native M-PTC. The crystal structure of this complex at high resolution (2.7 Å) shows the detailed interactions between the toxin and the associated protein. Unexpectedly, NTNHA-A exhibits a very similar domain architecture to BoNT/Ai (see the figure, panel A), although the two proteins share only 20% sequence identity. Despite this structural similarity, NTNHA-A lacks

Neurobehavioral Toxicology Branch, Analytical Toxicology Division, U.S. Army Medical Research Institute of Chemical Defense, 3100 Ricketts Point Road, Aberdeen Proving Ground, MD 21010–5400, USA. E-mail: michael.adler2@us.army.mil

the specialized motifs required for binding to nerve terminals or cleaving SNARE proteins.

Gu *et al*. subjected NTNHA-A, BoNT/Ai and M-PTC to conditions resembling those relevant to the absorption of botulinum neurotoxin in the gastrointestinal tract (*7*). Only M-PTC was stable in pepsin at pH 2.6 and in trypsin at pH 6. Neutral or alkaline pH promoted dissociation of the complex, resulting in loss of protection against trypsin inactivation. The essential residues involved in the interaction between BoNT/Ai and NTNHA-A were identified by site-directed mutagenesis. The results suggest that small molecule inhibitors could be developed to weaken this interaction and inactivate the neurotoxin early in intoxication, when intervention would be most effective. However, because there are no signs of botulism until SNARE protein cleavage is in progress (*2*), the inhibitors would need to be taken before exposure, requiring prior knowledge of an attack.

Examination of the crystal structure of the M-PTC complex helps to understand how NTNHA-A protects BoNT/Ai. The domain of botulinum neurotoxin most susceptible to proteolysis is the H_C (*8*), and all three domains of NHTHA-A interact extensively with this domain, thereby protecting it against proteolysis (see the figure, panel B). In contrast, the catalytically active LC domain of botulinum neurotoxin does not appear to interact with NTNHA-A, suggesting that it is inherently resistant to proteolytic degradation in the M-PTC complex. These results suggest that it may be possible to orally deliver protein-based therapeutics—both for botulism and for other conditions where a protein- or peptide-based drug is indicated—by coupling them to modified M-PTCs to protect the cargo from degradation.

The seminal findings of Gu *et al*. raise important questions for future studies. Is the domain homology of NTNHA unique to serotype A, or is it the general pattern for all serotypes? What are the roles of the other neurotoxin-associated proteins, especially HA33, which resists proteolysis and enhances transcytosis of neurotoxin (*9*)? Finally, given that the 900 kD complex provides the best protection against degradation of botulinum neurotoxin (*5*), how is this complex assembled, and how does each component contribute to keeping the toxin structurally intact and able to invade and inactivate cholinergic nerve cells in the host organism?

References

1. J. Sobel, *Clin. Infect. Dis.* **41**, 1167 (2005).
2. L. L. Simpson, *Annu. Rev. Pharmacol. Toxicol.* **44**, 167 (2004).
3. S. Gu *et al.*, *Science* **335**, 977 (2012).
4. www.bt.cdc.gov/agent/agentlist-category.asp
5. K.-H. Eisele *et al.*, *Toxicon* **57**, 555 (2011).
6. L. W. Cheng *et al.*, *Toxicology* **249**, 123 (2008).
7. A. B. Maksymowych *et al.*, *Infect. Immun.* **67**, 4708 (1999).
8. F. Chen *et al.*, *Infect. Immun.* **65**, 1626 (1997).
9. S. K. Sharma, B. R. Singh, *J. Nat. Toxins* **7**, 239 (1998).

10.1126/science.1219602

MATERIALS SCIENCE

Solving Amorphous Structures—Two Pairs Beat One

Consideration of atomic ordering beyond just pairs of atoms shows that amorphous silicon is better modeled as paracrystalline material than as a disordered network.

J. Murray Gibson

Diffraction data can be used to determine atomic structures by creating and refining a structural model. If the calculated diffraction pattern is in sufficiently good statistical agreement with the data, we trust that a unique structure has been found. For single crystals, the data are well-defined diffraction spots that represent reflections off the repeating lattice of atoms. For amorphous materials, the data are transformed into a radial distribution function (RDF) that provides the distribution of interatomic distances, typically over the range from 1 to 10 Å. In such cases, structural models can be tested against the RDF by analyzing the distribution of distances between random pairs of atoms. It is tempting to treat a model that has good agreement with the RDF as a unique structure, but on page 950 of this issue, Treacy and Borisenko (*1*) show that we cannot always rely on the RDF to fingerprint the correct medium-range structure (5 to 30 Å) of a material that is disordered on the nanoscale. They show that more than one structure, including some that resemble crystals in their topology, can equally well fit the RDF of amorphous silicon (a-Si).

The limitation of the RDF arises because it depends only on two-atom ("pair") correlations. New experimental data that revealed higher-order atom pair-pair correlations, used by Treacy and Borisenko to constrain modeling, points against the random network (see the figure) as a good model for most a-Si samples. Although the lack of uniqueness of the RDF beyond very short-range structure (beyond 5 Å) has been recognized [for example, see (*2*)], the RDF has still been repeatedly used to make structural inferences because it had been generally assumed that no competing nonrandom network model could fit the data equally well.

Because it has a pure, tetrahedrally bonded network of just one type of atom, a-Si is an excellent model of a disordered material. Interest accelerated when it was demonstrated in the 1960s that a-Si and amorphous germanium could be made semiconducting by preparation in the presence of hydrogen, followed by demonstration of doping by Spear and LeComber (*3*) and Anderson's work on localization (*4*). Applications of a-Si now include photovoltaics and thin-film-transistor displays.

The structure of a-Si was assumed to be

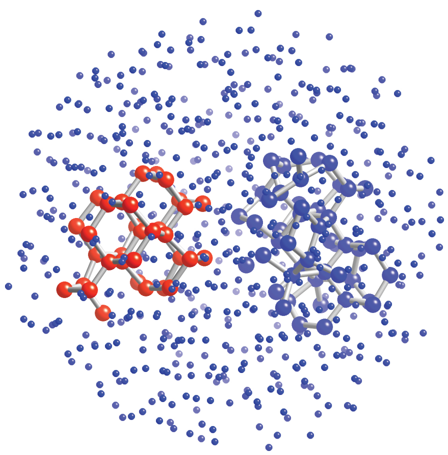

Testing amorphous structure models. One of the atomic models used by Treacy and Borisenko to fit the radial distribution function and fluctuation microscopy data. Highlighted are regions illustrative of the continuous random network (in blue) and the paracrystalline cubic structure (red).

Physics Department, Northeastern University, Boston, MA 02115, USA. E-mail: m.gibson@neu.edu

a random network. The continuous random network (CRN) model, originally introduced by Zachariasen (*5*) for silica glasses, was extended to amorphous silicon by Polk (*6*) and since has repeatedly been shown to fit the RDF well. Microcrystalline models, based on interconnecting regions of very small crystal grains, had earlier been dismissed as unable to fit the RDF, but it now appears that these models were too simple and did not properly include strains introduced between crystalline regions. The figure highlights examples of a random network, and a topologically cubic ("paracrystalline") region, in one of Treacy and Borisenko's models used to fit the experimental data for a-Si.

Problems with the CRN model were identified many years ago. Early qualitative transmission EM (TEM) seemed to show that a more ordered microcrystalline structure may better explain the first high-resolution TEM images (*7*), yet it was soon realized that even a random model could have fluctuations that mimic ordering so that qualitative inspection of images could not distinguish these models (*8*). This limitation was taken as further evidence for the random network model.

In the 1990s, Treacy and Gibson (*9*) developed a quantitative approach for examining scattering fluctuations on the atomic scale from TEM, which they named fluctuation EM (FEM). Their initial results showed high sensitivity of FEM to topological ordering and suggested experimentally that it would be hard to obtain a continuous random network in a-Si unless it has been well annealed.

Controversy has remained. Although most workers who have attempted FEM on a-Si have found similar results to Treacy and coworkers, some have assumed that the volume fraction of ordered regions is small (*10*). Gibson *et al*. (*11*) demonstrated experimentally that the volume fraction of paracrystalline material is substantial (~50%).

The importance of including other constraints together with the RDF in structural refinement has been recognized, for example, by Billinge (*12*). The blind spot in the RDF is particularly pronounced at the medium range; it is very insensitive to topology because it only examines the distribution of randomly selected pairs. The FEM data, which come from statistical studies of coherent nanodiffraction, depend on higher-order correlations, such as the four-body pair-pair or "bond correlation" functions. Because this function starts with the local orientation of a bond and can reveal whether there are other bonds in the vicinity that are correlated in direction, it is much more sensitive to topology.

Treacy and Borisenko have reported here a major step forward by carrying out an experimentally constrained relaxation of structural models with both RDF and FEM data, combined with exploration of the topological characteristics for the structures that emerged. They show that previous studies that assumed only the CRN can fit the RDF data were misguided. Just as good a fit can be obtained from either a random or paracrystalline model. However, the FEM data can only be fitted by a structure with a substantial fraction of paracrystallinity. Their result shows that the identification of an RDF with good fit to a CRN is not sufficient to conclude that the CRN is a good model of the structure. Other data that are more sensitive to topological or medium-range order are necessary to constrain structures.

That a-Si does not readily form a random network is consistent with our knowledge that no glass transition from the liquid state to the solid state can occur for symmetry reasons, in contrast to silica or metallic glasses. It appears that the topologically paracrystalline state is not thermally stable and that well-annealed a-Si approaches the random network structure. Because the nature of defects in amorphous networks would be controlled by local topology, experimentally constrained molecular modeling should be an important line of study in understanding electrical, mechanical, and other properties of amorphous materials.

References

1. M. M. J. Treacy, K. B. Borisenko, *Science* **335**, 950 (2012).
2. R. A. Street, *Hydrogenated Amorphous Silicon* (Cambridge Univ. Press, Cambridge, UK, 1991), p. 36.
3. W. E. Spear, P. G. LeComber, *Solid State Commun.* **17**, 1193 (1975).
4. P. Anderson, *Phys. Rev. Lett.* **34**, 953 (1975).
5. W. H. Zachariasen, *J. Am. Chem. Soc.* **54**, 3841 (1932).
6. D. E. Polk, *J. Non-Cryst. Solids* **5**, 365 (1971).
7. M. L. Rudee, A. Howie, *Philos. Mag.* **25**, 1001 (1972).
8. J. F. Graczyk, P. Chaudhari, J. Non-Cryst. Solids 17, 299 (1975)
9. M. M. J. Treacy, J. M. Gibson, *Acta Crystallogr.* **52**, 212 (1996).
10. S. N. Bogle *et al*., *J. Phys. Condens. Matter* **19**, 455204 (2007).
11. J. M. Gibson *et al*., *Phys. Rev. Lett.* **105**, 125504 (2010).
12. S. J. L. Billinge, *Physics* **3**, 25 (2010).

10.1126/science.1218723

GENETICS

Mendelian Puzzles

Aravinda Chakravarti and Ashish Kapoor

Variations that lie outside of the coding region of a mutated gene can give rise to a range of clinical phenotypes for a Mendelian genetic disorder.

Mendelian genetic disorders, rare clinical phenotypes arising from a single-gene mutation, are extremely diverse traits that affect every organ system, age group, and human population (*1*). Their cumulative incidence is rare (under 5%) because the clinical phenotypes are deleterious and affected individuals rarely reproduce. They persist in the population by de novo mutation in the past few generations, but some recessive mutations are an exception because their effects can be sheltered in carriers for hundreds of generations. Identifying the genes and mutations for over 2500 Mendelian disorders—one of the early fruits of the Human Genome Project (*2*)—has been recently spectacularly advanced by sequencing entire exomes (the protein-coding content of the genome) (*3*). Nevertheless, we will need to closely examine gene-regulatory sequences to understand the full spectrum of Mendelian phenotypic variation. Indeed, on page 966 of this issue, Lee *et al*. (*4*) demonstrate that a disorder called Joubert syndrome is caused by mutations in either of two different, adjacent genes that share a common regulatory region (constituting a so-called cis-regulatory module). This is one example of how human genetics is maturing from a focus on single genes into a more genomic view.

Mutation analyses of single-gene defects have identified two puzzles: One is that not all individuals with a specific disorder have identifiable coding mutations; the other is that not all individuals with identical mutations, even in the same family, are equally affected, and some may be symptom-free. The first mystery has many suspected causes: The disorder may be due to another gene—even the adjacent one, as Lee *et al*. demonstrate—or arise from mutations in a gene's regulatory sequences, or be a phenocopy (a trait that is not of genetic origin but is environmentally induced and mimics the phenotype produced by a gene) (*5*). This is a persis-

Center for Complex Disease Genomics, McKusick-Nathans Institute of Genetic Medicine, Johns Hopkins University School of Medicine, Baltimore, MD 21205, USA. E-mail: aravinda@jhmi.edu

tent challenge in studying an outbred organism like humans; just because a disorder is monogenic does not imply that it is monocausal. The second problem is more mysterious and far less understood. Phenotypic discordance, or variation in disease penetrance, between identical mutation bearers could result from differential environmental exposures (such as normal intelligence versus mental retardation in diet-treated versus untreated phenylketonuria). But most discordant cases probably arise from interactions of the primary gene with modifier genes (*6*). Another explanation is that genetic variation in the primary gene's regulatory sequences is sufficient to explain both Mendelian puzzles.

The human genome sequence has revealed a relatively small gene repertoire and widespread conservation of noncoding DNA (*7*). The noncoding DNA harbors a variety of regulatory elements (sequences) that enhance (enhancers), suppress (silencers), and locally limit (insulators) the transcription of genes, as well as produce the varying transcripts needed (splice site controllers) at any given time (*8*). The details of such control across the human genome, and across various tissues and developmental stages, are far from clear, but its general importance is certain. The development of sequence variation maps has also demonstrated that such regulatory sequences can harbor genetic variants that have deleterious effects in human disease (*9*, *10*). Although we are only in the early stages of identifying noncoding sequences that are important to Mendelian disease, their impact is expected to be important.

Individuals with a Mendelian disorder harbor one or two copies (depending on the mode of inheritance) of a loss-of-function, gain-of-function, or dominant negative mutation at a specific gene. The repertoire of such a gene's regulatory elements, usually spread out within and outside a gene and at times at considerable distance from that gene, can also harbor mutations that enhance or suppress the genetic effect of either the normal or the mutant allele(s). For example, for an autosomal dominant disorder in which individuals harbor one normal (wild-type) and one mutant gene copy (allele), additional variants at a physically close silencer or enhancer can modulate the wild-type versus mutant transcripts so as to yield more or less mutant transcript (*11*) and protein, thus leading to more severe or less severe disease (see the figure).

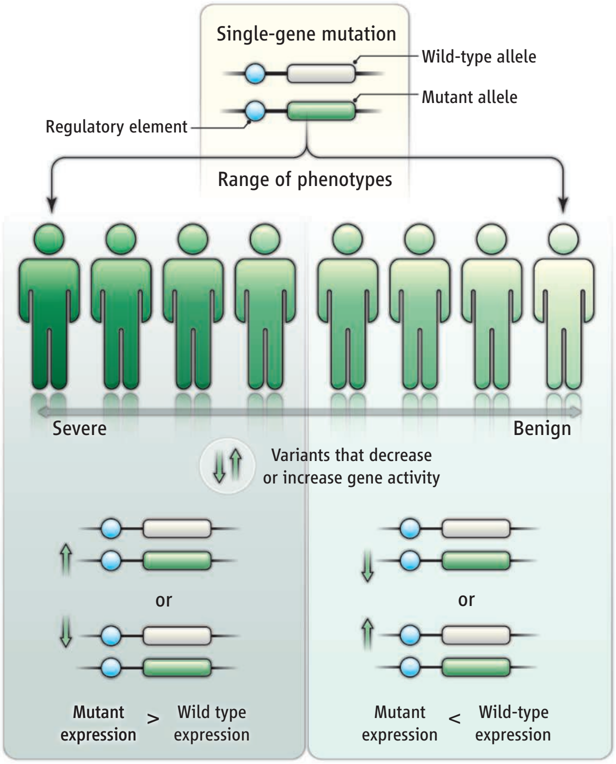

Phenotypic variation. Not all individuals with an identical mutation are equally affected. Genetic alterations in a regulatory element can alter dosage of a mutant or a wild-type allele, giving rise to variations in phenotype.

The specific outcomes depend on the function of the regulatory sequence and whether the regulatory variant is physically linked to the wild-type or the mutant allele. More complex situations may arise when either the regulatory variant or the mutant allele, or both, exist on both homologous chromosomes, and when regulatory variants exist at physically unlinked sites on nonhomologous chromosomes. In all such cases, the relative abundance of mutant to wild-type transcript (and protein) can determine consequent variation in disease penetrance. In one such family with congenital Hirschsprung disease, where the gastrointestinal tract fails to develop a nervous system, disease manifestation depends not solely on a null mutation in the gene encoding the tyrosine kinase RET, but also on a common population variant in an intronic enhancer of the gene that is inherited from the parent that does not contribute the actual *RET* mutation (*10*). As reported by Lee *et al.* for Joubert syndrome, the control of neighboring Mendelian disease genes based on a common set of regulators can add even greater complexity to possible outcomes.

The key to understanding such effects is the role of natural selection. Purifying negative selection against deleterious coding mutations is the basis for their rarity and continued occurrence by de novo mutation. However, natural selection against variants in regulatory elements is much weaker, allowing them to be common in human populations (*9*). By themselves, these variants may have only small effects and add to transcriptional "noise," but these effects can be amplified in conjunction with a disease mutation (*10*). Indeed, these types of local allelic interactions may be exceedingly common, given that polymorphisms in such elements are widespread. The combination of rare coding mutations with common regulatory variants can lead to complex patterns of inheritance and thus provide a singular mechanistic explanation of Mendelian families that do not carry a mutation in the coding gene associated with the disease, as well as variable disease penetrance in individuals that carry the Mendelian gene mutation.

In common chronic diseases, the focus on common polymorphisms is extending to the search for rare variants (*12*). Studies of Mendelian disease should also move from its preoccupation with rare variants to a focus on common polymorphisms, particularly at regulatory sequences affecting either rare disorders like Hirschsprung disease (*10*) or common disorders like myocardial infarction (*13*). An early argument for sequencing only the protein-encoding component of the human genome was fortunately settled with the decision to sequence the entire genome, including the poorly understood noncoding segments. In retrospect, this was a wise choice. It is now clear that to understand protein-encoding genes, we need to fathom their regulation and how this is compromised in Mendelian disease.

References

1. V. A. McKusick, *Mendelian Inheritance in Man. A Catalog of Human Genes and Genetic Disorders* (Johns Hopkins Univ. Press, Baltimore, ed. 12, 1998).
2. J. Amberger *et al.*, *Hum. Mutat.* **32**, 564 (2011).
3. S. B. Ng *et al.*, *Nat. Genet.* **42**, 30 (2010).
4. J. H. Lee *et al.*, *Science* **335**, 966 (2012); 10.1126/science.1213506.
5. T. Strachan, A. P. Read, *Human Molecular Genetics* (Garland Science, New York, ed. 4, 2011).
6. J. B. S. Haldane, *J. Genet.* **41**, 149 (1941).
7. E. S. Lander, *Nature* **470**, 187 (2011).
8. G. A. Maston *et al.*, *Annu. Rev. Genomics Hum. Genet.* **7**, 29 (2006).
9. E. S. Emison *et al.*, *Nature* **434**, 857 (2005).
10. E. S. Emison *et al.*, *Am. J. Hum. Genet.* **87**, 60 (2010).
11. H. Yan *et al.*, *Science* **297**, 1143 (2002).
12. M. A. Rivas *et al.*, *Nat. Genet.* **43**, 1066 (2011).
13. K. Musunuru *et al.*, *Nature* **466**, 714 (2010).

10.1126/science.1219301

IBI* SERIES WINNER

A Season for Inquiry: Investigating Phenology in Local Campus Trees

Campus Trees, the IBI Prize–winning module, uses local phenology to create authentic inquiry experiences in undergraduate biology.

Tammy Long[1,†] and Sara Wyse[2]

Michigan State University rightfully claims one of the most beautiful campuses in the Midwest. Each spring, we anticipate a commencement gilded with tulips and crabapple blossoms. In autumn, the campus beams with golden oaks and fiery maples. As a potential subject for inquiry learning, phenology, the study of recurrent natural events, is appealing for many reasons.

Phenologic studies have relatively few logistical constraints compared with many topics in biology. Virtually every habitat imaginable undergoes cyclical or seasonal changes that can be observed through local plants, animals, or other organisms. Documenting phenological patterns can be a straightforward and cost-effective strategy for engaging students in the science of observation with little need for additional equipment or supplies.

The subject of phenology is both timely and scientifically relevant. Interannual variability in factors such as temperature and precipitation can shift the timing of phenologic events by days to months, with real-world impacts ranging from ecosystem function (e.g., plant-pollinator interactions) to regional economies (e.g., agriculture and tourism). Larger-scale trends over long periods of time serve as important indicators of environmental changes, including climate change (*1*).

Finally, phenology is complex. Seemingly simple processes, such as the changing color of leaves, actually result from myriad interactions occurring across molecular- to ecosystem-level scales. As a complex system, phenology encompasses multiple biological processes that can be explored from diverse disciplinary perspectives across scales of space and time (*2*, *3*) (see the first photo).

Our introductory labs are taught by graduate teaching assistants (TAs) ranging in both teaching experience and disciplinary expertise. As the real face of the lab, TAs bear immediate responsibility for motivating student learning and bringing new instructional strategies into the classroom. They recognized that the labs we had been teaching, in which students followed protocols to confirm known outcomes, did not reflect the biology that motivated each of us to become biologists. We believed that in order to change both the content and culture of our labs, we would need to fully engage TAs as collaborators in the reform process.

Inquiry investigation. Students worked with collaborative teams to develop innovative methods for quantifying leaf color change and abscission in campus trees. Most groups combined both new technology and lower-tech approaches in their data collection strategy.

In summer 2008, we invited TAs to a 2-day "boot camp" to learn about evidence-based teaching practices (*2*, *3*) and to provide input about goals for reforming labs. TAs said that labs should provide students opportunities to experience how science is done—not as a series of methodological steps, but as a way to ask questions, test ideas, and evaluate evidence. In addition, TAs wanted labs to be more authentic and to reflect the uncertainty of science as it is practiced. Students would pursue questions in which a "right" answer might not be known.

To incorporate these goals, TAs worked in small groups to rewrite existing labs, framing them as inquiry investigations with explicit and measurable learning objectives. Five TAs collaborated with us to take on the larger task of developing a new, semester-long phenology study, Campus Trees (see the second photo). Inspired by the citizen-scientist model of the National Phenology Network (*4*), we envisioned the outgrowth of a long-term, student-generated database documenting phenology in our local cam-

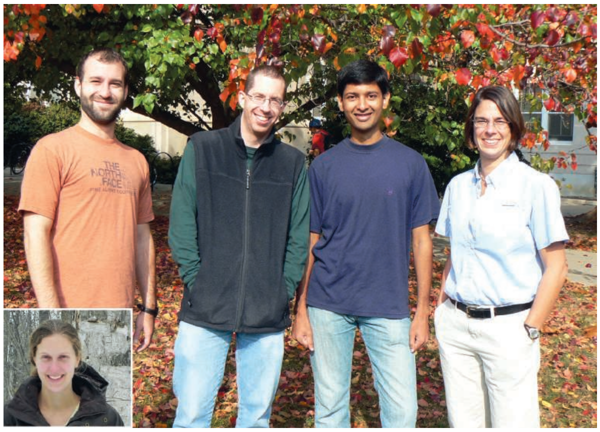

Curriculum developers. Graduate TAs, Jeffrey Pierce, Todd Robinson, Mridul Thomas, Sherry Martin (left to right), and Kristen Schmitt (inset) collaborated in the original design and implementation of the phenology project in Fall 2008 and contributed as authors on supporting lab materials.

PHOTO CREDITS: THOMAS HARPSTEAD

[1]Department of Plant Biology, Michigan State University, East Lansing, MI 48824, USA. [2]Bethel University, St. Paul, MN 55112, USA.

*IBI, Science Prize for Inquiry-Based Instruction; www.sciencemag.org/site/feature/data/prizes/inquiry/.

†Author for correspondence. E-mail: longta@msu.edu

pus trees. Our primary challenge was how to engage students in original inquiry, while at the same time, ensuring consistency and reliability in the student-generated data. Ultimately, we decided that students would mirror authentic ecological research by working collaboratively to design, field-test, and evaluate original methods for quantifying phenologic change.

In order to embed replication within the project design, we restricted the study to 200 trees representing four genera: *Acer*, *Quercus*, *Malus*, and *Ginkgo*. The Office of Campus Parks and Planning provided maps with locations and identification codes for all trees in the study (*5*). Students working in groups of four were assigned three trees to study for the semester; each tree was independently sampled by at least three different student groups across different lab sections. Students would not know that others were studying "their" trees until later in the semester.

Students began by locating their trees in the field, making detailed sketches about location and identifying characteristics, and recording tree height and diameter. Students had 2 weeks to brainstorm alternative approaches for quantifying color change and leaf fall and then present their proposals in class. Feedback from classmates and TAs helped students clarify study objectives and solidify their data collection plans.

For the next several weeks, students applied their methods in the field and managed all logistical and troubleshooting issues that arose. After leaves had fallen, students uploaded their final data and methods to our course-management system, LON-CAPA (*6*). Students used their tree codes to search for and retrieve the data and methods of other groups that had studied the same trees. In a final presentation, students evaluated alternative methods and compared the quality of data produced. Groups wrote short papers based on their analyses and proposed an "ideal" method that would best meet the criteria for (i) producing reliable and accurate phenologic data, (ii) generating high-quality data that can be used in future research, and (iii) feasible implementation in a course enrolling large numbers of students (up to 1000 per semester).

What did we learn from this experience? First, students are capable of achieving far more than we expect. Our concern that students might converge on a common approach was not realized. In fact, students used diverse and innovative methods for data collection [e.g., determining which branches to sample using a Twister spinner, quantifying leaf color with electronic color-pickers and RGB (red-green-blue) codes] and for troubleshooting (e.g., What should you do if the landscaping staff prunes the branches you were sampling? Should a leaf be counted in your sample if it's half eaten?). Another concern—that students would regard their own method as "best" and not critically evaluate alternatives—was also not realized. In their final analyses, few groups suggested that they had developed an ideal method and, instead, weighed strengths and weaknesses of multiple methods. TAs noted that by the end of the semester, students better understood how nuances in experimental approach could have an impact on both the nature and interpretation of data—an important benchmark in the development of science literacy (*7*).

Second, TAs have much to offer in terms of innovating curricula and providing insights that can improve students' learning experiences. Our TAs cared deeply about the quality of their students' learning and took pride in their successes. However, in order to realize the potential of TAs to rejuvenate labs, programs must be willing to liberate some creative control and to provide substantial mentoring along the way. Inquiry teaching is not easy and represents a significant departure from traditional, lecture-based instruction. TAs' transition to inquiry teaching involved discussing real examples in practice. Iterative feedback and a supportive network of peers also helped TAs develop confidence in their classrooms. Our program included TAs in decision-making about curricula and acknowledged authorship on TA-developed materials. This can do much to illustrate the value of TA input, not to mention bolstering TAs' curriculum vitae and teaching portfolios.

Finally, we advocate for including creativity in the reward structure of college-level biology. Confirmatory labs do not provide sufficient opportunities for students to experience the cycles of failure and recovery that practicing scientists experience as an ordinary part of scientific inquiry. Indeed, learning how to deploy creative strategies for managing the unexpected is a critical part of becoming a scientist yet is rarely reflected in most lab curricula. If we truly want to cultivate a nation of problem-solvers, we must allow students opportunities to wrestle with real problems and be rewarded for conceiving creative strategies for solving them. Our students have shown us they are ready for the challenge.

About the authors

Tammy Long is an assistant professor in the Department of Plant Biology at Michigan State University. She earned her Ph.D. at the University of Michigan for her work on the impact of CO_2 enrichment on resource allocation in plants. Her current research evaluates the long-term impacts of reforming introductory biology and explores how students use models and visual representations to reason about complex biological systems. **Sara Wyse** is an assistant professor of Biological Sciences at Bethel University and a collaborator with Long on this project and others. Sara earned her Ph.D. at Michigan State University, where she explored the impacts of alternative professional development models on graduate TAs' classroom performance. In addition, she researches student understanding of biological systems and the impact of collaborative learning on student understanding.

References and Notes

1. C. Parmesan, G. Yohe, A globally coherent fingerprint of climate change impacts across natural systems. *Nature* **421**, 37 (2003).
2. National Research Council, *BIO 2010: Transforming Undergraduate Education for Future Research Biologists* (National Academies Press, Washington, DC, 2003).
3. C. A. Brewer, D. Smith, Eds., *Vision and Change in Undergraduate Biology Education: A Call to Action* (American Association for the Advancement of Science, Washington, DC, 2011).
4. USA National Phenology Network, (www.usanpn.org).
5. Detailed tree records are not a constraint for this project. At Bethel University, students identified trees on campus, mapped their trees in Google Maps, and provided verbal descriptions of how to locate their tree from a campus landmark.
6. The Learning Online Network with Content Management and Assessment System, www.lon-capa.org.
7. Project 2061, *Benchmarks for Science Literacy* (American Association for the Advancement of Science, Washington, DC, 1993).

8. We acknowledge the support of MSU's Biological Sciences Program, including S. Lawrence, C. Elzinga, and J. Merrill. We thank D. Ebert-May for workshop assistance and advice throughout regarding TA professional development and J. Momsen for her invaluable editorial comments. We are especially grateful to the cohort of TAs and undergraduate learning assistants for providing vision and feedback during the reform process. This material is based on work supported by the NSF under grant no. DUE-0736928; Principal Investigator, T.L.

Supporting Online Material
www.sciencemag.org/cgi/content/full/335/6071/932/DC1

10.1126/science.1213528

INTERNATIONAL

Experts See Progress, Challenges in Advancing Science Diplomacy


Norman P. Neureiter

In the late 1990s, science and engineering leaders were deeply concerned that the U.S. State Department lacked the scientific expertise that would be needed for the 21st century. Now, after a sustained effort, State has built significant scientific and technical strength and a promising capacity for science diplomacy, high-level experts concluded during a day-long discussion at AAAS.

Starting in 2000 with the appointment of veteran scientist-diplomat Norman P. Neureiter, four senior scientists have been appointed to 3-year terms as science adviser to the Secretary of State. Fellowship programs now bring dozens of scientists every year to the State Department and the U.S. Agency for International Development (USAID); some have stayed on after their fellowships ended. And President Barack Obama has embraced a program proposed by U.S. Senator Richard Lugar (R–Indiana), appointing six widely respected researchers as science envoys.

Still, participants said, the gains remain fragile. U.S. leadership of global science diplomacy initiatives could be put at risk by severe budget pressures and increasing wariness of science in some quarters of Congress.

"Science diplomacy is becoming a more integral part of foreign policy," said Vaughan Turekian, the AAAS chief international officer and director of its Center for Science Diplomacy. "It has the potential to open new dimensions both in international relations and in research. And so it's critical to identify mechanisms and approaches for increasing the capacity of foreign ministries to utilize science and scientists."

The 25 January roundtable was convened as a substantive way to celebrate Neureiter's birthday and his contributions to the field. Trained as a chemist, in 1967 he became the first U.S. science attaché in Eastern Europe, based at the U.S. Embassy in Warsaw. In the early 1970s, while working in President Richard Nixon's Office of Science and Technology, he helped craft science initiatives with China and the Soviet Union that brought a thaw to the Cold War. He joined AAAS in 2004 and serves as senior adviser to the AAAS Center for Science Diplomacy and acting director of the AAAS Center for Science, Technology and Security Policy.

In that time, AAAS has emerged as a global hub for science diplomacy. In December, Turekian and Nobel laureate Peter Agre, a former AAAS president, joined other scientists on a visit to Havana, where they met Cuban colleagues to discuss possible joint research on coral reefs, hurricane dynamics, and other areas. This month, Turekian and Neureiter led a delegation to Myanmar, where they met with representatives of seven government ministries to discuss issues such as health science, forestry, education, and linking science to public policy.

And AAAS will soon launch a quarterly online publication, *Science and Diplomacy,* to support global dialogue among scientists and foreign policy stakeholders (www.sciencediplomacy.org).

The roundtable featured 32 participants from six countries, including high-ranking officials in the U.S. State Department and their counterparts from other nations. Among them were three of the first four science advisers to the Secretary of State: Neureiter; George H. Atkinson, an internationally known professor of chemistry and optical sciences at the University of Arizona; and current adviser William Colglazier, who served 17 years as executive officer of the National Academy of Sciences. (The third science adviser, AAAS President Nina V. Fedoroff, was in Saudi Arabia and unable to attend the event.)

In 1999, a report by the National Research Council detailed the role of science in a range of foreign policy issues, including innovation, energy, health, agriculture, and nuclear proliferation, among others. Based on its recommendations, Congress and President Bill Clinton created the position of science and technology adviser to the Secretary of State.

In remarks at the roundtable, Neureiter described his early challenges in establishing a strong role for science, and the science adviser, in the culture of diplomats. Where there were only a handful of AAAS Science and Technology Policy Fellows at the department in 2000, this year there are about 40, and a similar number at USAID. The Jefferson Science Fellows, initiated by Atkinson, now has 13 tenured faculty from U.S. colleges and universities assigned to State and USAID.

But experts stressed that challenges lie ahead. To take science diplomacy to the next level, and to make it sustainable, world leaders must find new ways to develop mutually beneficial partnerships. And they must engage young researchers, engineers, and diplomats who will shape the next generation of international science and the related diplomacy.

SCIENCE POLICY

Campaign 2012 Site to Track Candidates, S&T Issues

With the U.S. presidential election shifting to high gear, AAAS has debuted a Web site that offers a detailed look at the candidates and their positions on science-related issues.

The site (http://elections.aaas.org/2012/) will focus on five areas: competitiveness and innovation; science, technology, engineering, and mathematics education and the workforce; climate and energy; health and medical research; and national security. It also will offer a range of other information, from reports, polls, and news articles to election calendars and event listings.

"We think it's important that the many communities interested in U.S. science, technology, and innovation have high-quality materials to help them assess all the candidates during the campaign season," said Joanne Carney, director of the nonpartisan AAAS Office of Government Relations.

Disease Tolerance as a Defense Strategy

Ruslan Medzhitov,[1]* David S. Schneider,[2]* Miguel P. Soares[3]*

The immune system protects from infections primarily by detecting and eliminating the invading pathogens; however, the host organism can also protect itself from infectious diseases by reducing the negative impact of infections on host fitness. This ability to tolerate a pathogen's presence is a distinct host defense strategy, which has been largely overlooked in animal and human studies. Introduction of the notion of "disease tolerance" into the conceptual tool kit of immunology will expand our understanding of infectious diseases and host pathogen interactions. Analysis of disease tolerance mechanisms should provide new approaches for the treatment of infections and other diseases.

Animal host defense mechanisms have traditionally been thought to be a function of the immune system that aims to detect and eliminate invading pathogens. However, ecological analyses have long described a genetic variation in disease susceptibility in plants that could be dissociated from their ability to control pathogen burden (*1*, *2*). This variation is due to differential ability to tolerate the presence of pathogens, and tolerance to infection was thus realized to constitute a distinct strategy of host defense. The concept of tolerance was only recently introduced into the field of animal immunity (*3*–*6*), and concerted efforts will be required to fully explain the role of tolerance in host protection from infectious diseases.

In principle, the host can protect itself from infectious disease using three distinct strategies: avoidance, resistance, and tolerance. Avoidance reduces the risk of exposure to infectious agents. Resistance reduces pathogen burden once the infection is established. Tolerance reduces the negative impact of an infection on host fitness without directly affecting the pathogen burden (*3*, *5*, *6*). The term tolerance used in this context is not to be confused with immunological tolerance, which is defined as unresponsiveness to self antigens. In some contexts, however, the two terms can be used interchangeably because immunological tolerance is a special case of a multitude of mechanisms that protect the host from immune- or pathogen-inflicted damage.

Avoidance

The avoidance strategy works through alteration of host behavior and requires that the host detect the risk of pathogen exposure before being infected. Sensing pathogens before infection is mediated primarily through the olfactory and gustatory systems, although visual cues can also be used in some species. Pathogen presence in the environment is detected through various molecular proxies of high pathogen density, such as volatile metabolites specifically produced by microorganisms, including pathogens. For example, cadaverine, putrescine, and skatole (3-methylindole) are chemicals produced by bacterial metabolism of amino acids that occurs during putrefaction of animal tissues. Methane thiol is produced by bacterial breakdown of L-methionine and contributes to the characteristic body odor associated with high bacterial densities on the skin. At high doses, these chemicals have foul odor (as perceived by humans) and thus report on high bacterial densities and therefore high risk of infection. Their detection by the olfactory system triggers aversive behavior (at least in some species) that helps to reduce the risk of infection (*7*). For example, a subset of formyl-peptide receptors is expressed in the mammalian vomeronasal organ, where they function as olfactory receptors and presumably detect pathogens or infected conspecifics (*8*, *9*). The gustatory sensory system is also involved in triggering aversive behaviors and reflexes. Interestingly, the chemosensory system used to sense bitter taste also appears to be used to detect acyl-homoserine lactone, a bacterial quorum-sensing molecule that signals high bacterial density (*10*). It is unclear to what extent different aversive behaviors are innate or learned; this likely depends on the stimulus and the host species. The mechanism of aversive behavior is best understood in *Caenorhabditis elegans*, where avoidance of pathogens is a learned behavior, mediated by the olfactory neurons (*11*, *12*). Social insects also have well-documented avoidance behaviors that help minimize colony exposure to pathogens (*13*). Bullfrog tadpoles use chemical cues to detect and avoid infected conspecifics (*14*). In rodents, detection of infected conspecifics through the olfactory

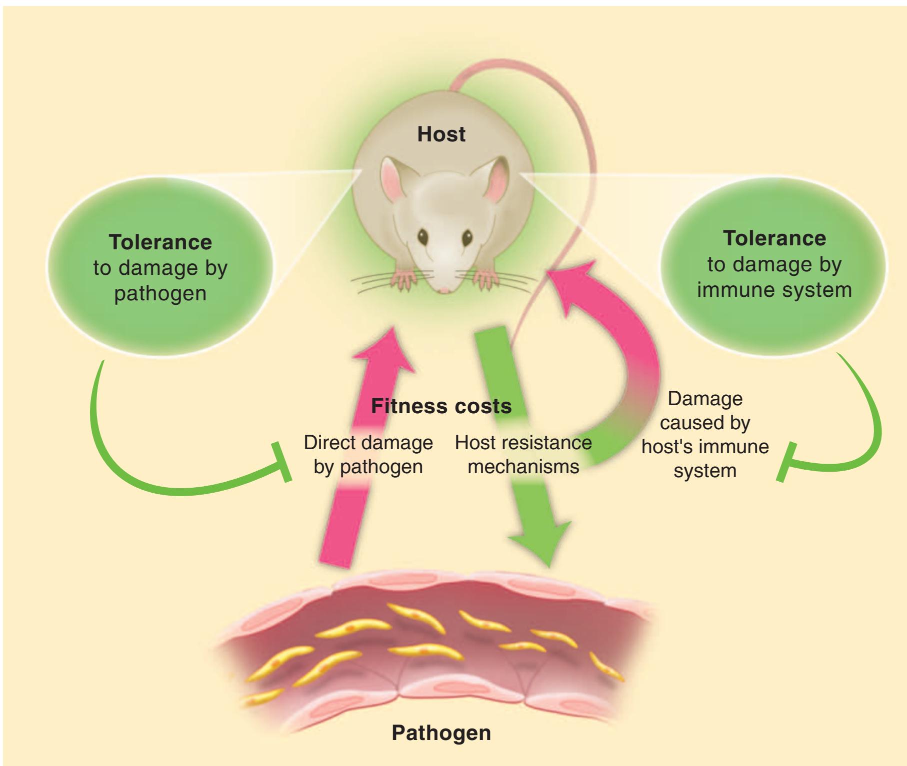

Fig. 1. Two types of fitness costs associated with infections. Pathogens can directly damage the host tissues. The immune system of the host reduces the pathogen burden through the resistance mechanism. The immune response can also damage the host tissues. The host can reduce fitness costs through tolerance mechanisms that reduce both the direct tissue damage by pathogens, and immunopathology.

[1]Howard Hughes Medical Institute, Department of Immunobiology, Yale University School of Medicine, New Haven, CT 06510, USA. [2]Department of Microbiology and Immunology, Stanford University, Palo Alto, CA 94305, USA. [3]Instituto Gulbenkian de Ciência, Oeiras 2780-156, Portugal.

*To whom correspondence should be addressed. E-mail: ruslan.medzhitov@yale.edu (R.M.); dschneider@stanford.edu (D.S.S); mpsoares@igc.gulbenkian.pt (M.S.)

system controls mate selection and avoidance of social contact (*7*). Aversive behavior and feelings of disgust also play an important role in humans, helping to reduce pathogen exposure (*15*). Although pathogen avoidance can have a clear adaptive value, extreme forms of aversive behavior can be a considerable handicap, as exemplified by germophobia, a common type of obsessive-compulsive disorder.

Resistance

Resistance mechanisms protect the infected host by reducing its pathogen burden. Resistance is a function of the immune system, which works by detection, neutralization, destruction, or expulsion of the pathogens. Both innate and adaptive immune systems contribute to host resistance to infections. Although the resistance strategy is clearly crucial for host protection from infections, it carries a substantial cost to host fitness (*16*). Destruction and elimination of pathogens is often accompanied by collateral tissue damage. Even in the absence of overt tissue damage, resistance mechanisms commonly occur at a cost to normal tissue function. For example, infection-induced inflammation alters normal vascular function, and increased permeability of airway epithelium can compromise normal respiratory function (*17*). Collectively, the negative impact of immune defenses on host fitness is referred to as immunopathology (*18*). Immunopathology is an unavoidable consequence of immune defenses. In general, the degree of immunopathology is positively correlated with the magnitude and duration of the immune response. Consequently, the trade-off between immunity and immunopathology constrains both the evolution and the deployment of resistance mechanisms. Thus, the optimal immune response is determined by the balance between efficient pathogen clearance and an acceptable level of immunopathology (*19*). Because insufficient immunity results in a high rate of mortality from infections, the acceptable level of immunopathology can be high, making it a common cause of infectious disease symptoms. The trade-off between protective immunity and immunopathology can be deconstrained, to an extent, by the tolerance mechanisms, which limit tissue damage, thus allowing for a higher magnitude and duration of the immune response than would have been otherwise possible.

Tolerance

Tolerance is a host defense strategy that reduces the negative impact of infection on host fitness. Unlike resistance mechanisms, tolerance does not directly affect pathogen burden. Rather, tolerance decreases the host susceptibility to tissue damage, or other fitness costs, caused by the pathogens or by the immune response against them (Fig. 1).

The concept of tolerance as a defense strategy has been developed and used in studies of plant immunity for decades (*1*, *2*). However, it was only recently introduced into the field of animal immunity (*3*, *5*, *6*). The original observation by Råberg *et al*. (*4*) demonstrated that disease severity in *Plasmodium*-infected mice can be dissociated from pathogen burden, thus providing the first clear example in which this ecological definition of host tolerance was applied to infections in animals. This study also demonstrated differences in tolerance between inbred mouse strains, demonstrating that tolerance is genetically determined. Tolerance as a common host defense strategy in animals was demonstrated by a genetic screen of flies. When survival of a lethal bacterial infection was used as a readout, tolerance mutants were isolated as frequently as resistance mutants (*20*). The subsequent study demonstrated that the balance of tolerance and resistance was pathogen specific and that a set of conditions that might favor tolerance for one pathogen could promote resistance against another (*21*). Another study in *Drosophila* identified a phagocytosis-dependent tolerance mechanism (*22*), illustrating involvement of the same process in both resistance and tolerance. Studies in *C. elegans* demonstrated that the unfolded protein response (UPR) plays a role in promoting tolerance to *Pseudomonas aeruginosa* infection, providing an example of how a stress response can help a host endure an infection (*23*). Interestingly, this UPR in worms can be triggered systemically through a neuronal mechanism, illustrating that the nervous system can play a role in tolerance to infection (*24*).

In mice, tolerance mechanisms have been best characterized in experimental models of *Plasmodium* infection, the causative agent of malaria. The blood stage of *Plasmodium* infection is associated with hemolysis and the release of hemoglobin. Cell-free hemoglobin promotes tissue damage and organ failure, and its toxic effect does not scale with the *Plasmodium* burden (*25*, *26*). This suggests that, within a certain range, protecting the tissues from the toxic effect of hemoglobin can promote host fitness and survival independently of pathogen load. Indeed, this was shown to be the case (*27*, *28*). Tolerance to *Plasmodium* infection is conferred by a mechanism involving heme oxygenase-1 (HO-1), encoded by a stress-inducible gene, *Hmox1*, which is induced in response to oxidative stress (*28*, *29*). Interestingly, sickle cell mutations, selected in areas where malaria is endemic, confer tolerance to *Plasmodium* infection via a genetic program involving inducible HO-1 expression (*27*). The same pathway is also essential to promote tolerance to severe sepsis, illustrating the broad role of stress-responsive genes in host tolerance (*30*).

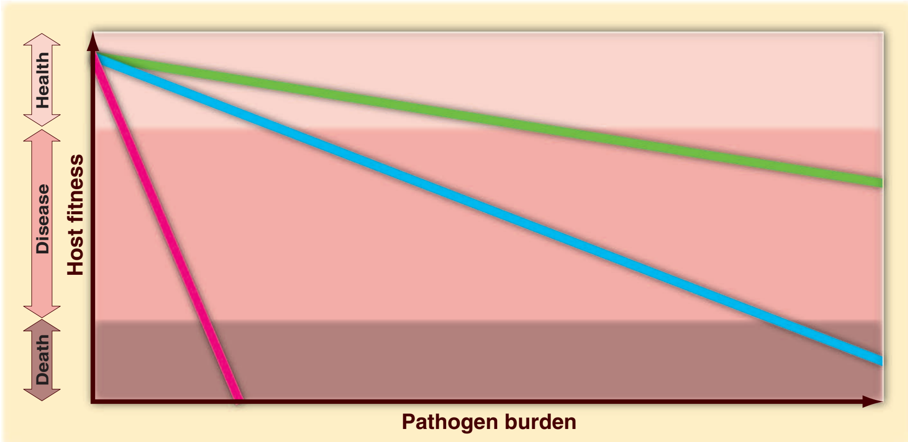

Fig. 2. Different tissues and physiological processes vary in tolerance capacity. Tissues depicted in red have the lowest tolerance to damage, the blue has an intermediate tolerance, and the green has the highest tolerance capacity.

Currently, very little is known about the full spectrum of tolerance mechanisms, and the few available studies in animals cited above already hint at their diversity in different species and in different types of infection. Because pathogens and immunopathology can potentially affect almost any physiological process, tolerance is not restricted to a single protective pathway but rather encompasses multiple mechanisms that help reduce the host vulnerability to damage.

Infection-Associated Fitness Costs

During an infection, the host can sustain two types of tissue damage: direct damage by the pathogen and immunopathology. Accordingly, the host can employ two types of tolerance mechanisms, one minimizing direct pathogen-induced damage, the other minimizing immunopathology. Both pathogens and the immune response can cause tissue damage by a variety of mechanisms: They can directly kill infected cells or disrupt normal tissue architecture, homeostasis, and function. Therefore, protection from infection-induced tissue damage in principle can be achieved by multiple mechanisms. For example, metaplasia of columnar epithelium into stratified squamous epithelium or hyperplasia and increased mucus production by goblet cells will both decrease susceptibility to epithelial damage by path-

ogens or other environmental insults (*17*). Other types of increased tissue protection will have a similar effect. Efficient repair of damaged tissues and adaptation to the consequences of tissue damage, such as hypoxia, can also increase the level of tolerance. Thus, efficient replacement of damaged red blood cells through induced erythropoiesis may help tolerate infections with hemolytic pathogens. Clearly, the same mechanism would not be effective in the case of infections that do not cause anemia. In general, different infections cause different spectra of tissue damage, and these can, in turn, be ameliorated by different tolerance mechanisms. Increased tolerance to tissue damage can be achieved, in general, through tissue protection and repair.

Although tissue damage caused by pathogens or by the immune response is the most obvious negative outcome of an infectious disease, overt tissue damage is only one of many possible fitness costs associated with infections. In principle, almost any physiological process can be negatively affected by pathogens or by the immune and inflammatory responses they elicit. Although specific tolerance mechanisms employed in these cases are largely unknown, they would be expected to prevent, reduce, or counter the pathological alterations caused by infections. Therefore, the mechanisms that normally maintain homeostasis of various physiological systems are likely to contribute to host tolerance to infections. Alterations in host metabolism and electrolyte balance, changes in blood pressure, impaired absorptive functions of intestinal and respiratory epithelia, local tissue hypoxia, and excessive extracellular matrix remodeling are all examples of disturbances in host physiology that can be caused by pathogens or the immune responses they elicit (*17*, *31*). In each case, there are dedicated mechanisms that restore homeostasis and normal tissue function (regardless of what caused their dysregulation), and engagement of these mechanisms helps to reduce the fitness costs associated with infections. When these mechanisms are sufficient to prevent major disruptions of physiological functions, infections remain asymptomatic. The pathological outcomes of infections arise when the degree of tissue damage or alteration of host physiology exceeds the capacity of tolerance mechanisms (Fig. 2). Conversely, enhancement of tolerance mechanisms should help reduce morbidity and mortality associated with infectious diseases.

Tolerance Capacity

The tolerance capacity varies between different tissues and physiological processes. Four factors define the tolerance level (Fig. 3). First, tissues and organs vary in terms of intrinsic damage susceptibility. For example, neurons and cardiomyocytes rely primarily on oxidative metabolism and therefore have low tolerance to hypoxia, compared with most other cell types that can switch to glycolysis under hypoxic conditions (*17*). Highly proliferative tissues, on the other hand, are more sensitive to apoptosis induced by DNA-damaging agents.

Second, different tissues have different repair capacity. This capacity generally correlates with tissue renewal rates, which can range from several days (intestinal epithelium and granulocytes) to decades or even the entire life span of the organism (many neuronal cell types). Tissues with high turnover rates—including most epithelia and hematopoietic cell types—are repaired very efficiently and therefore have higher intrinsic tolerance to damage compared with tissues with low or no renewal capacity, such as neurons and cardiomyocytes, where damage can be irreversible and often lethal.

Third, tolerance capacity depends on functional autonomy of cells that make up a given tissue. This is because functional autonomy affords compensation. Hepatocytes and red blood cells have a high degree of functional autonomy, and therefore loss of individual cells can be compensated by the remaining cells performing the same function. The function of most neurons, on the other hand, is integrated within neuronal circuits and their target tissues. Their loss, therefore, cannot be compensated and can have devastating consequences.

Fourth, depending on a tissue, the consequences of a given degree of damage or malfunction can vary dramatically. Thus, infections with hemorrhagic viruses, such as Ebola virus or Marburg virus, tend to be fatal because they infect and damage vascular endothelium. Extensive endothelial damage can have severe consequences because it can lead to disruption of vascular integrity, disseminated microvascular clotting, and ischemia with subsequent tissue necrosis (*32*). Likewise, infections that cause pneumonia have high mortality rates because defects in respiratory function are poorly tolerated. In contrast, many skin infections are well tolerated and not life threatening.

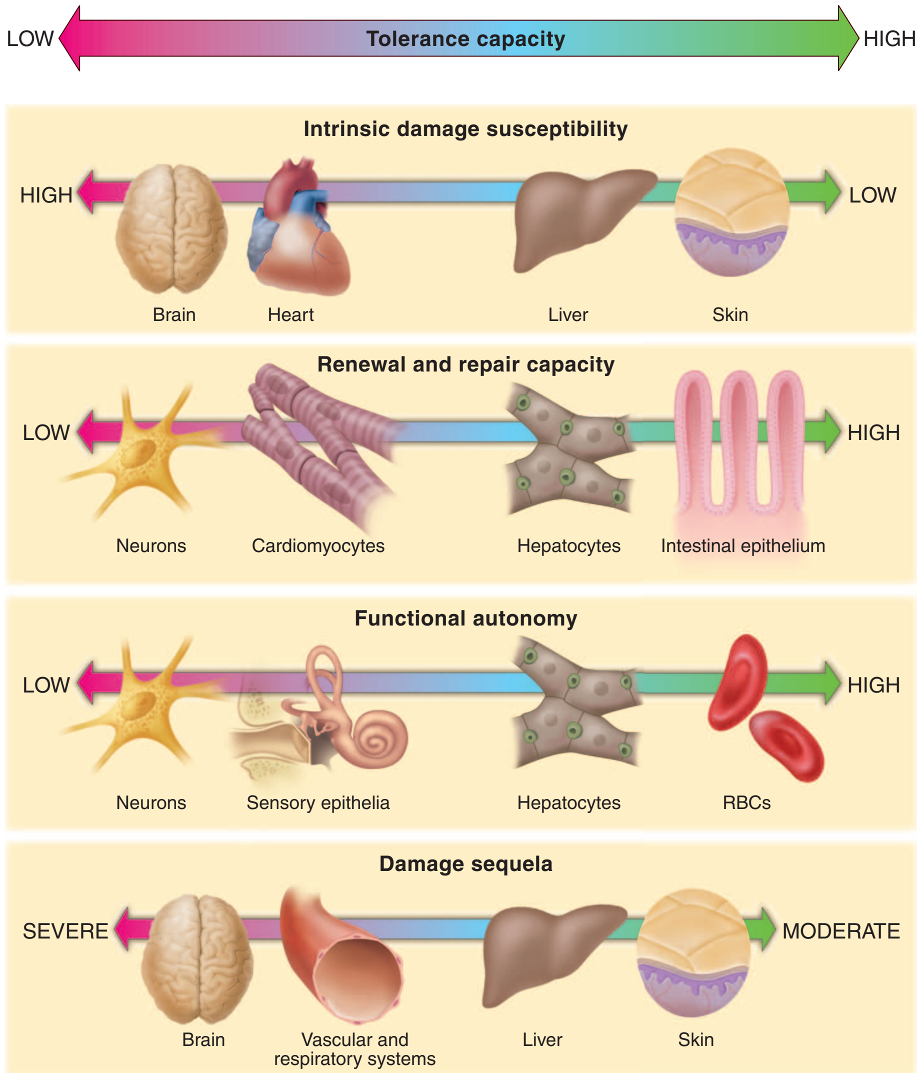

Fig. 3. Tolerance capacity is a function of intrinsic damage susceptibility, repair capacity, functional autonomy, and damage sequelae of different tissues and organs. Although tissues generally tend to fall at the same ends of the four spectra, the four characteristics do not necessarily correlate with each other.

The tissues that have particularly low tolerance capacity tend to be well insulated from the internal and external threats. Blood-brain barrier, skull, and ribs are examples of the protective infrastructure that helps prevent damage to brain, lungs, and the heart—the vital organs with low tolerance to damage. One special example of the same protective strategy is the immune-privileged sites, which are the tissues and organs with low tolerance to immunopathology. These tissues and organs, including brain, eye chamber, placenta, and gonads, are not permissive to tissue-destructive immune responses and are thus better protected from immunopathology than other tissues. They are not completely devoid of immune defensive mechanisms, however. Rather, immune-privileged sites employ immune defenses that have low immunopathological potential (for example, secretory immunoglobulin A and antimicrobial peptides) (*33*).

General Strategies of Stress Tolerance

Cellular stress responses are inducible adaptations to adverse conditions, such as elevated temperature, reactive oxygen species (ROS), osmotic pressure, endoplasmic reticulum (ER) overload, hypoxia, or exposure to noxious xenobiotics. Each of the common adverse conditions is sensed by dedicated stress-response pathways that activate a transcriptional master regulator, leading to the induction of a battery of stress-response genes. These genes perform various emergency functions that help the affected cells survive the adverse condition. For example, heat shock activates the transcription factor HSF-1 (heat shock factor 1), leading to the induction of genes that control refolding or degradation of misfolded proteins, thereby preventing proteotoxicity (*34*). Oxidative stress leads to activation of transcription factor Nrf2, which in turn induces dozens of proteins that scavenge free radicals, eliminate damaged proteins, metabolize oxidized membrane lipids, and repair damaged DNA (*35*). ER stress activates three stress-response pathways (ATF6, PERK, and IRE1), which reduce new protein synthesis, eliminate misfolded proteins from the ER, and restore Ca^{2+} and ROS homeostasis (*36*). In each case, a given stress stimulus activates dedicated sensors and transcription factors that induce the expression of genes required to tolerate the stressor. In the absence of the stress-response pathways, cells and tissues become hypersensitive to the adverse conditions. On the other hand, each stress-response pathway operates at the cost of normal cell and tissue function, which is why these genes cannot be constitutively turned on and have to be inducible only when needed.

When cellular stress-response pathways are activated by a mild stressor, they become more tolerant of a more severe insult, a phenomenon known as preconditioning, or hormesis. The basis of preconditioning is the induction of protective mechanisms by a mild insult that, in turn, permits tolerance to a greater and potentially damaging insult. A similar phenomenon exists in the case of inflammatory tissue damage; for example, exposure to low levels of inflammatory stimuli, like bacterial lipopolysaccharide (LPS), can protect from otherwise lethal doses of LPS. This occurs through induction of negative regulators of LPS signaling and selective suppression of LPS-inducible genes that have high tissue-damage potential (*37*). Although it is not yet known to what extent this phenomenon extends to other aspects of inflammatory and immune responses, it is clear that tissue tolerance to inflammatory and other types of damage can be transiently increased upon exposure to the appropriate stressor. Moreover, it can be hypothesized that the same tolerance mechanisms can be induced by endogenous signals that report on the potential or imminent damage, before the damage actually occurred. For example, mitochondrial stress or heat shock in one tissue can induce stress adaptation in remote tissues in *C. elegans* (*38*, *39*). The signals involved in stress communication presumably regulate tissue tolerance to the anticipated damage. In some contexts, this type of signal is already known to exist: The protective effect against malaria afforded by sickle hemoglobin mutations results from the accumulation of free heme in plasma, a mild stressor that induces tolerance mechanisms and provides host protection against a subsequent *Plasmodium*-induced tissue damage (*27*). A similar mechanism operates in severe sepsis (*30*). In addition, activation of the hypothalamic-pituitary-adrenal axis by anticipated threats, or by the inflammatory cytokines and tissue damage, leads to a transient reprogramming of multiple physiological processes by glucocorticoid hormones, thus promoting tolerance to the anticipated or ongoing tissue damage (*40*). One can expect that during different infections and other noxious insults, distinct sets of tolerance-promoting signals are induced to prepare the host tissues for the imminent damage associated with the particular type of infection or noninfectious insult. Identities of these signals remain to be established.

Basal and Inducible Tolerance

Each tissue has an intrinsic ability to tolerate some degree of stress, damage, or malfunction and is thus characterized by a basal level of tolerance. The basal tolerance is afforded by constitutively active cytoprotective mechanisms, and the degree of basal tolerance varies between tissues and organs. For example, cornified epithelium has higher intrinsic tolerance to damage compared with mucosal epithelium (*17*). The tolerance mechanisms that operate at the expense of normal tissue functions are inducible. Although some cytoprotective genes are constitutively expressed at low levels, most are induced only in response to tissue stress and damage. Furthermore, some tissue-protective and repair mechanisms can only operate once the damage has occurred. On the other hand, the constitutive counterpart of tissue repair, tissue renewal, is operative under basal conditions. It should be noted that, just like a dysregulated immune response, dysregulated tolerance can lead to pathology. A notable example is fibrosis that can result from excessive tissue repair.

General and Specific Tolerance

Tissue-protective tolerance mechanisms can be general in the sense that they are protective against most or all types of tissue stress and damage. For example, mechanisms that reduce toxic levels of ROS have cytoprotective functions for most types of stress, because ROS is elevated under most stress conditions and high levels of ROS make cells more sensitive to the damaging effects of most types of stress (*41*). Similarly, in some contexts, antiapoptotic and antinecrotic genes likely have a general tolerance-enhancing effect regardless of the cause of cell death. Finally, tissue-repair mechanisms can be expected to confer tolerance no matter the cause of tissue damage. On the other hand, specific tolerance mechanisms are only protective against some but not other forms of stress and damage. Thus, the mechanisms that maintain electrolyte balance are protective against diarrheal infections, whereas erythropoiesis is protective against hemolytic pathogens.

Activation of the general tolerance mechanisms should result in positive preconditioning, such that the tolerance mechanisms induced upon infection with one pathogen would increase tolerance to an unrelated pathogen. Activation of specialized tolerance mechanisms can also lead to positive preconditioning, as long as the response to pathogen A is also protective against pathogen B. However, the response to pathogen A can also be incompatible with the tolerance to pathogen B, resulting in a negative preconditioning. Some coinfections—for example, influenza virus followed by respiratory bacterial infections—result in severe morbidity and mortality. This is generally thought to be a result of compromised immunity; however, it may also be a result of compromised tolerance. Indeed, it is conceivable that inducible tolerance to flu infection is incompatible with tolerance to respiratory bacterial infections. Analysis of mechanisms of preconditioning is important because it can provide the means to reduce morbidity and mortality by targeting the compromised tissue-protective pathway(s).

Sickness Behavior: Resistance or Tolerance?

Infections in animals and humans lead to dramatic changes in behavior, resulting in fatigue, anorexia, social withdrawal, fever, and sleep alterations. Collectively, these are known as sickness behaviors (*42*). Although sickness behavior is assumed to be adaptive, it is not clear whether and how it helps the infected host. For example, fatigue is thought to preserve energy so as to fight infection better; however, fatigue is commonly accompanied by anorexia and therefore

reduced energy consumption. Fever is thought to enhance immune function, but there is little evidence of the positive effect of increased temperature on immune defenses. Fever is also thought to make the host a less suitable niche for the pathogens. Different pathogens can have very different temperature preferences, however, yet fever is induced whenever an infection results in systemic inflammation. Although sickness behavior may have some undefined positive effects on the host resistance, we suggest that its benefits may have to do largely with promoting host tolerance to infection. Thus, fever may induce tissue protection by inducing HSF-1–mediated cellular heat-shock response. Consistent with this view, heat shock can render cells transiently resistant to tumor necrosis factor–mediated killing (*43*). Anorexia and fatigue may similarly help preserve vital processes and promote stress tolerance in multiple tissues. Indeed, anorexia has been shown to enhance tolerance to *Salmonella* infection in flies, while at the same time it reduces resistance to *Listeria* infection (*44*). Therefore, the presence or absence of protective effects of sickness behavior and their mechanisms are pathogen specific.

Failed Host Defenses: Immunodeficiencies versus Deficiencies in Tolerance

Despite highly elaborate immune defense mechanisms, the host can and often does succumb to infectious diseases. Host defenses can fail because the resistance mechanisms are insufficient, overpowered, or evaded by the pathogen. Alternatively, morbidity and mortality can result from the failure of tolerance mechanisms, even in the context of effective resistance. Most commonly, this would be reflected in a comparable pathogen burden in hosts with different morbidity or mortality profiles. The distinction between failed resistance and failed tolerance is important because it can dictate the choice of therapeutic approaches. When the primary problem is the failed tolerance, boosting immunity and reducing pathogen burden (for example, using antibiotics or antimalarial drugs) may be ineffective, whereas enhancing tolerance may have salutary effects. Therapeutic or prophylactic targeting of tolerance pathways may also be the best strategy when immune defenses are either inefficient, compromised, or cause excessive immunopathology. For example, severe malaria can be effectively ameliorated, at least in experimental animals, by preventing tissue damage to liver or brain, and this protection can be uncoupled from the pathogen burden (*28*, *29*). The same is true for severe sepsis, where limiting tissue damage prevents multiorgan failure, a hallmark of this disease (*30*). In the case of diarrheal diseases, an effective treatment is continuous rehydration. It does not directly affect pathogen burden but does promote host survival. Finally, flu symptoms caused by excessive inflammatory response are commonly treated by COX2 (cyclooxygenase 2) inhibitors that reduce immunopathology driven by excessive prostaglandin production, without directly affecting the pathogen burden.

Boosting tissue tolerance is also likely to be a useful strategy in the case of infectious diseases that remain a major cause of morbidity and mortality worldwide. Besides malaria, these include tuberculosis and HIV, the infectious diseases for which pathogen control through vaccination or antimicrobial drugs is currently unattainable. This strategy will require identification of the tolerance mechanisms relevant to a particular infectious disease, as has been recently done for *Plasmodium* infections (*27*–*29*). A related strategy is the idea of an "antipathology" vaccine, as an alternative to the traditional vaccine approach that aims to reduce pathogen burden (*45*, *46*). Thus, vaccination that targets and neutralizes a toxin rather than the pathogen that produces it may have a powerful therapeutic effect even without directly affecting the pathogen load. In this case, the immune system can contribute to tolerance rather than resistance (*3*).

Primary immunodeficiencies are commonly thought to result from mutations that affect immune functions. They may also result from defects in tolerance mechanisms, however, a possibility that is largely overlooked in both human and animal studies. To distinguish between failed resistance and failed tolerance, it is important to measure pathogen burden and a relevant indicator of host fitness status. The former is not always possible in humans, however, and the latter is complicated by the fact that we almost never know what the relevant fitness characteristics are. Instead, various easily measurable indicators of health (such as body weight and temperature) are commonly used as proxies of host fitness. Systematic characterization of biomarkers of the relevant pathological processes for common infectious diseases would be useful for the development of therapies that promote host tolerance to infections.

Pathogen Virulence and Host Tolerance

Every pathogen is characterized by a certain degree of virulence, the ability to cause disease in a given host. Virulence can reflect either the pathogen's ability to cause direct tissue damage or the immunopathology it elicits. Highly virulent influenza viruses, for example, cause disease primarily by eliciting a "cytokine storm"—an excessive and sometimes life-threatening inflammatory response (*47*). It is important to emphasize that virulence is a complex function that has at least two components. The pathogen-intrinsic component is defined, among other things, by the expression of toxins and other virulence factors, as well as by tissue tropism and replication rates of the pathogen. The host-intrinsic component is defined by its susceptibility (or tolerance) to the damage that can be caused by the pathogen or by the immune response it elicits. Both pathogen-intrinsic and host-intrinsic characteristics can affect host fitness (*48*). For example, differences in avian influenza virus tissue tropism in humans and birds are a critical determinant of virulence, which reflects the ability of influenza virus to cause immunopathology in humans and not in birds (*49*). Because virulence is a function of both the pathogen- and the host-intrinsic characteristics, it follows that the evolution of virulence can reflect changes that are either pathogen- or host-specific. Thus, a pathogen can become more virulent in a new host species, and this most likely reflects the difference in the host's tolerance because pathogen-intrinsic characteristics remain unchanged. For example, the Ebola virus is highly virulent in humans because it infects and kills vascular endothelium causing lethal hemorrhages. In the natural host (which is believed to be a fruit bat), the same virus is not virulent and presumably does not cause hemorrhage (*32*).

In the opposite scenario, a pathogen can become less virulent in a given host because of an increase in host tolerance to damage that can be caused by the pathogen. At the extreme, a pathogen may even become a part of a normal "commensal" microbiota and colonize the host

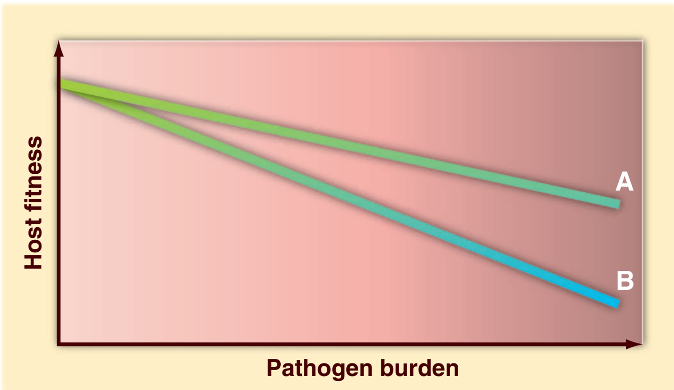

Fig. 4. When host fitness is plotted against pathogen burden, the slope of the lines reflects host tolerance to a given infection. In this example, A is more tolerant to a given level of pathogen burden than B. An equivalent increase in pathogen burden will have greater negative impact on B than on A. A and B are typically different genotypes studied in the same environment. Alternatively, A and B can be two different environments where an organism with the same phenotype has different tolerance to infection. Modified from (*3*).

constitutively without causing a disease (*50*, *51*). Thus, host-microbial symbiosis could be due to decreased pathogen-intrinsic virulence or due to increased host tolerance.

Tolerance as a Function of Age

The severity of infectious diseases can vary dramatically across different ages. Interestingly, both the very young and the very old are often particularly susceptible to infections. This is typically thought to reflect insufficient (immature or deteriorated) immunity in young and old, respectively. Although the immune system does deteriorate with advanced age (*52*), the effect of aging is more complex than a simple decline in immune resistance. For example, it is now well documented that inflammatory responses, and at least some immune responses, in very old people can be either comparable to the young or, in some cases, even enhanced (*53*). An alternative explanation to the higher morbidity and mortality rates in the very young and the very old is the compromised tolerance to infection. In babies, optimal tolerance may be constrained by growth and developmental pathways. In the aged, tolerance may be impaired because of the overall decline in tissue maintenance and repair capacities that occurs with advanced age. Frailty may be an extreme case of decline in tolerance, although its causes are not well understood.

Conclusions and Perspectives

Resistance and tolerance are two alternative but complementary host defense strategies. Understanding the mechanisms that are critical for host survival is important for the choice of therapeutic approaches. Generally, the contribution of resistance and tolerance can be distinguished by plotting pathogen burden against a health status (Fig. 4) (*3*). It is impossible to tell the reason for morbidity and mortality when pathogen load or health status are measured alone. Because resistance, by and large, is the only mechanism considered in animal and human studies, when the host succumbs to infection it is usually, and often incorrectly, ascribed to the failure of the immune system.

The concept of tolerance may also be applicable to the "Typhoid Mary" phenomenon. Healthy carriers that remain asymptomatic despite being infected are likely to have a high level of tolerance to the pathogen with which they are infected. A high level of tolerance is also likely to be a characteristic of pathogen vectors. From the pathogen's perspective, the vector needs to remain healthy to transmit the pathogen. Therefore, the pathogen may actually promote the vector's tolerance to infection.

The concept of tolerance is not restricted to infection but can be applied to most diseases. The severity of autoimmune disease, for example, depends not only on the magnitude of self-destructive immune response but also on the susceptibility of target tissues to the damage caused by a given level of response. It would be important to characterize the tissue-protective tolerance mechanisms that help minimize negative consequences of autoimmune responses. Similarly, the concepts discussed here are applicable to any diseases associated with tissue damage, stress, malfunction, or loss of homeostasis.

The level of tolerance to stress and tissue damage can be adjusted to the environment, at least in some animals. For example, unfavorable environments (scarce food and water sources, nonoptimal temperature and humidity, and the like) promote the states of suspended animation, such as spores (in protozoa), dauer (in the larval stage of *C. elegans*), hibernation, and estivation (a state of dormancy in animals entered into as a response to high temperatures and arid conditions). In these states, the animals are highly tolerant of tissue damage and appear to be less susceptible to infections. Hibernating ground squirrels, for example, can sustain –2.9°C core body temperature and are protected from ischemia-reperfusion injury (*54*). This suggests that suspended animation is associated with extreme tolerance to stress and damage and that tolerance can be regulated by environmental cues. Notably, at least in worms and flies, these environmental signals are linked to the insulin growth factor-1–FoxO pathway that controls longevity (*55*). Defining molecular details of such pathways may pave the way to new treatment strategies for many human maladies, including infectious, inflammatory, and autoimmune diseases.

References and Notes

1. R. M. Caldwell, J. F. Schafer, L. E. Compton, F. L. Patterson, *Science* **128**, 714 (1958).
2. J. Schafer, *Annu. Rev. Phytopathol.* **9**, 235 (1971).
3. L. Råberg, A. L. Graham, A. F. Read, *Philos. Trans. R. Soc. London B Biol. Sci.* **364**, 37 (2009).
4. L. Råberg, D. Sim, A. F. Read, *Science* **318**, 812 (2007).
5. A. F. Read, A. L. Graham, L. Råberg, *PLoS Biol.* **6**, e4 (2008).
6. D. S. Schneider, J. S. Ayres, *Nat. Rev. Immunol.* **8**, 889 (2008).
7. M. Kavaliers, E. Choleris, A. Agmo, D. W. Pfaff, *Horm. Behav.* **46**, 272 (2004).
8. S. D. Liberles *et al.*, *Proc. Natl. Acad. Sci. U.S.A.* **106**, 9842 (2009).
9. S. Rivière, L. Challet, D. Fluegge, M. Spehr, I. Rodriguez, *Nature* **459**, 574 (2009).
10. M. Tizzano *et al.*, *Proc. Natl. Acad. Sci. U.S.A.* **107**, 3210 (2010).
11. E. Pradel *et al.*, *Proc. Natl. Acad. Sci. U.S.A.* **104**, 2295 (2007).
12. Y. Zhang, H. Lu, C. I. Bargmann, *Nature* **438**, 179 (2005).
13. S. Cremer, M. Sixt, *Philos. Trans. R. Soc. London B Biol. Sci.* **364**, 129 (2009).
14. J. M. Kiesecker, D. K. Skelly, K. H. Beard, E. Preisser, *Proc. Natl. Acad. Sci. U.S.A.* **96**, 9165 (1999).
15. V. Curtis, M. de Barra, R. Aunger, *Philos. Trans. R. Soc. London B Biol. Sci.* **366**, 389 (2011).
16. P. Schmid-Hempel, *Evolutionary Parasitology* (Oxford Univ. Press, Oxford, 2011).
17. G. Majno, I. Joris, *Cells, Tissues, and Disease: Principles of General Pathology* (Oxford Univ. Press, New York, ed. 2, 2004).
18. A. Graham, J. Allen, A. Read, *Annu. Rev. Ecol. Evol. Syst.* **36**, 373 (2005).
19. A. Casadevall, L. A. Pirofski, *Infect. Immun.* **67**, 3703 (1999).
20. J. S. Ayres, N. Freitag, D. S. Schneider, *Genetics* **178**, 1807 (2008).
21. J. S. Ayres, D. S. Schneider, *PLoS Biol.* **6**, 2764 (2008).
22. N. Shinzawa *et al.*, *Cell Host Microbe* **6**, 244 (2009).
23. C. E. Richardson, T. Kooistra, D. H. Kim, *Nature* **463**, 1092 (2010).
24. J. Sun, V. Singh, R. Kajino-Sakamoto, A. Aballay, *Science* **332**, 729 (2011).
25. A. Ferreira, J. Balla, V. Jeney, G. Balla, M. P. Soares, *J. Mol. Med.* **86**, 1097 (2008).
26. R. Gozzelino, V. Jeney, M. P. Soares, *Annu. Rev. Pharmacol. Toxicol.* **50**, 323 (2010).
27. A. Ferreira *et al.*, *Cell* **145**, 398 (2011).
28. E. Seixas *et al.*, *Proc. Natl. Acad. Sci. U.S.A.* **106**, 15837 (2009).
29. A. Pamplona *et al.*, *Nat. Med.* **13**, 703 (2007).
30. R. Larsen *et al.*, *Sci. Transl. Med.* **2**, 51ra71 (2010).
31. C. A. Mims, A. Nash, J. Stephen, *Mims' Pathogenesis of Infectious Disease* (Academic Press, San Diego, CA, ed. 5, 2001).
32. D. Bente, J. Gren, J. E. Strong, H. Feldmann, *Dis. Model. Mech.* **2**, 12 (2009).
33. P. Matzinger, T. Kamala, *Nat. Rev. Immunol.* **11**, 221 (2011).
34. W. E. Balch, R. I. Morimoto, A. Dillin, J. W. Kelly, *Science* **319**, 916 (2008).
35. T. W. Kensler, N. Wakabayashi, S. Biswal, *Annu. Rev. Pharmacol. Toxicol.* **47**, 89 (2007).
36. P. Walter, D. Ron, *Science* **334**, 1081 (2011).
37. S. L. Foster, D. C. Hargreaves, R. Medzhitov, *Nature* **447**, 972 (2007).
38. J. Durieux, S. Wolff, A. Dillin, *Cell* **144**, 79 (2011).
39. V. Prahlad, T. Cornelius, R. I. Morimoto, *Science* **320**, 811 (2008).
40. R. M. Sapolsky, L. M. Romero, A. U. Munck, *Endocr. Rev.* **21**, 55 (2000).
41. R. Pamplona, D. Costantini, *Am. J. Physiol. Regul. Integr. Comp. Physiol.* **301**, R843 (2011).
42. B. L. Hart, *Neurosci. Biobehav. Rev.* **12**, 123 (1988).
43. S. H. Gromkowski, J. Yagi, C. A. Janeway Jr., *Eur. J. Immunol.* **19**, 1709 (1989).
44. J. S. Ayres, D. S. Schneider, *PLoS Biol.* **7**, e1000150 (2009).
45. J. H. Playfair, J. Taverne, C. A. Bate, J. B. de Souza, *Immunol. Today* **11**, 25 (1990).
46. L. Schofield, M. C. Hewitt, K. Evans, M. A. Siomos, P. H. Seeberger, *Nature* **418**, 785 (2002).
47. J. S. Peiris, K. P. Hui, H. L. Yen, *Curr. Opin. Immunol.* **22**, 475 (2010).
48. T. J. Little, D. M. Shuker, N. Colegrave, T. Day, A. L. Graham, *PLoS Pathog.* **6**, e1001006 (2010).
49. D. M. Tscherne, A. García-Sastre, *J. Clin. Invest.* **121**, 6 (2011).
50. M. R. Miller, A. White, M. Boots, *Evolution* **60**, 945 (2006).
51. B. A. Roy, J. W. Kirchner, *Evolution* **54**, 51 (2000).
52. R. A. Miller, *Science* **273**, 70 (1996).
53. A. C. Shaw, S. Joshi, H. Greenwood, A. Panda, J. M. Lord, *Curr. Opin. Immunol.* **22**, 507 (2010).
54. C. C. Kurtz, S. L. Lindell, M. J. Mangino, H. V. Carey, *Am. J. Physiol. Gastrointest. Liver Physiol.* **291**, G895 (2006).
55. C. J. Kenyon, *Nature* **464**, 504 (2010).

Acknowledgments: Work in the authors' laboratories was supported by the Howard Hughes Medical Institute (R.M.); NIH grants RO1AI055502, RO1DK071754, and R37AI046688 (R.M.); NIH grants RO1AI060164 and 1DP1OD008167-01 (D.S.S.); New England Regional Center of Excellence (R.M.); Ellison Medical Foundation (D.S.S.); Fundação para a Ciência e Tecnologia grants PTDC/SAU-TOX/116627/2010, PTDC/BIA-BCM/101311/2008, and PTDC/SAU-FCF/100762/2008 (M.S.); European Community, 6th Framework Grant, XENOME, LSH-2005-1.2.5-1. (M.S.); and the Bill & Melinda Gates Foundation (M.S.).

10.1126/science.1214935

Extremely Long-Lived Nuclear Pore Proteins in the Rat Brain

Jeffrey N. Savas,[1]* Brandon H. Toyama,[2]* Tao Xu,[1] John R. Yates III,[1] Martin W. Hetzer[2]†

Functional deterioration and accumulation of damage to the proteome is largely repaired through protein turnover where potentially impaired polypeptides are replaced with new, functional copies. These turnover mechanisms are particularly important in postmitotic cells such as neurons, because they cannot dilute potentially toxic species through cell division. Nearly all proteins within the human proteome are recycled in less than a few days (*1*, *2*). However, a few extremely long-lived proteins (ELLPs) with half-lives on the order of months have been identified (*3*, *4*), including myelin basic protein (MBP). A subset of nuclear pore complex (NPC) proteins, which form transport channels responsible for mediating nuclear trafficking (*5*), are present but no longer expressed in differentiated cells (*6*). Thus, at least a subset of nucleoporins (Nups) are not, or are only very slowly, replaced during adulthood. However, because worms have a life span of a few weeks, it remains unclear whether NPC components remain incorporated in the nuclear membrane over years, particularly in the central nervous system of mammals, which contain nondividing cells that are as old as the organism itself (*7*).

To explore this question, we performed pulse chase labeling of whole rats with the stable isotope ^{15}N followed by mass spectrometry to monitor global protein turnover on a time scale of years (the average life span of a lab rat is 2 years). Two female rats and their progeny were fed a ^{15}N-enriched algal cell diet, and at 6 weeks all progeny rats were switched to a ^{14}N diet. Fully ^{15}N labeled rats were immediately killed and their tissues harvested. Nuclei from liver, an organ that turns over within 4 to 6 months, and brain were purified, digested with trypsin, and analyzed by MudPIT (multidimensional protein identification technology) LCLC-MS/MS (multidimensional liquid chromatography–tandem mass spectrometry). At time = 0, we calculated ^{15}N isotopic protein labeling efficiency of >98% and identified more than 3400 fully ^{15}N proteins (20,754 peptides) and only 9 ^{14}N proteins (14 peptides). Two additional animals were killed at 6 and 12 months, and $^{15}N/^{14}N$ ratios were determined for more than 3500 unique proteins. Only seven heavy (^{15}N) proteins (11 peptides) were found in the liver after 6 months, consistent with the relatively rapid turnover of hepatocytes. In contrast, the brain contained a large number of heavy peptides (92 peptides) even after 12 months (Fig. 1, A and B, and fig. S1E). These peptides corresponded to 25 proteins and included MBP and histones, the latter having reported half-lives of ~220 days in mouse brain (*8*), confirming the validity of our approach. All the other heavy proteins identified were components of the two essential core modules of the NPC, the pentameric Nup205 complex and the nonameric Nup107-160 complex (*6*) (Fig. 1C and table S1). This represents an essential intracellular protein machine with protein components in excess of a year in age.

Detailed analysis of ^{15}N spectral counts and $^{15}N/^{14}N$ MS1 ratios revealed that, in contrast to the stable scaffold, the peripheral Nups and components of the central transport channel were devoid of heavy peptides, suggesting they were completely replaced after 6 months (Fig. 1C). Thus, unlike other large protein complexes in which all components have similar turnover values (*1*, *2*), the individual components of NPCs have very different lifetimes. This supports the idea that NPCs are built to last the entire life span of the cell and are not completely removed and assembled anew in postmitotic cells. Rather, NPC maintenance in nondividing cells relies on the non- or extremely slow exchange of scaffold and rapid replacement of peripheral Nups.

A lack of protein turnover exposes the proteome to an increased risk of aberrant chemical modifications and oxidative damage during aging. Indeed, healthy rats exhibit age-dependent decline of NPC function (*6*). Our results suggest that ELLPs represent a diverse class of proteins that regulate essential cellular functions and could be linked directly to the decline of the aging proteome.

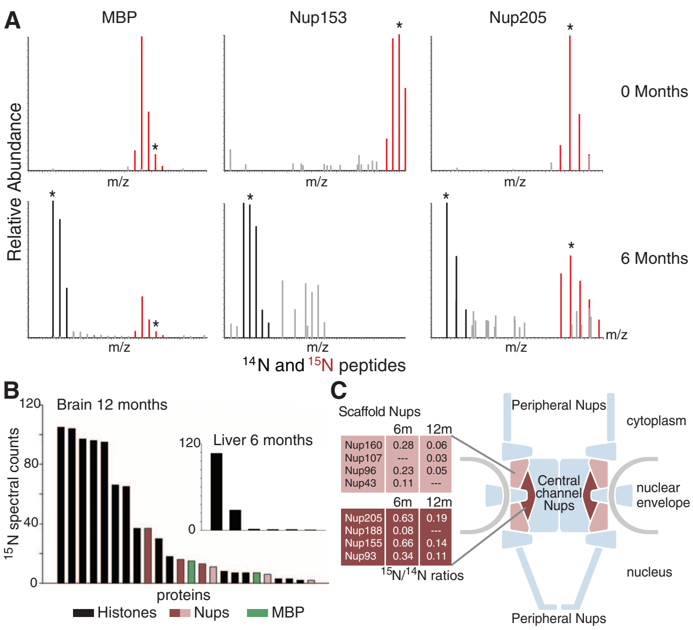

Fig. 1. Identification of NUPs and histones as ELLPs in mammalian brain. (**A**) MS1 scans [indicated mass/charge (*m/z*) ranges] at 0 and 6 months. Distinct peptides for indicated proteins; red indicates ^{15}N peptide peaks; black, ^{14}N; gray, other peptides. Asterisk peaks were successfully identified by MS/MS. (**B**) Distribution of ^{15}N MS/MS spectral counts (485) grouped as proteins (25) from 12-month brain nuclei and 6-month liver nuclei (inset). (**C**) Relative MS1 peak quantitation for each Nup with heavy peptide hits indicated as $^{15}N/^{14}N$ ratios when possible.

References and Notes

1. S. B. Cambridge *et al.*, *J. Proteome Res.* **10**, 5275 (2011).
2. J. C. Price, S. Guan, A. Burlingame, S. B. Prusiner, S. Ghaemmaghami, *Proc. Natl. Acad. Sci. U.S.A.* **107**, 14508 (2010).
3. C. A. Fischer, P. Morell, *Brain Res.* **74**, 51 (1974).
4. R. Shapira, M. R. Wilhelmi, R. F. Kibler, *J. Neurochem.* **36**, 1427 (1981).
5. M. Capelson, C. Doucet, M. W. Hetzer, *Cold Spring Harb. Symp. Quant. Biol.* **75**, 585 (2010).
6. M. A. D'Angelo, M. Raices, S. H. Panowski, M. W. Hetzer, *Cell* **136**, 284 (2009).
7. K. L. Spalding, R. D. Bhardwaj, B. A. Buchholz, H. Druid, J. Frisén, *Cell* **122**, 133 (2005).
8. S. L. Commerford, A. L. Carsten, E. P. Cronkite, *Proc. Natl. Acad. Sci. U.S.A.* **79**, 1163 (1982).

Acknowledgments: We are supported by the Hewitt Foundation (B.H.T.); the Ellison Medical and Glenn foundations (M.W.H.); National Institute of Aging fellowship F32AG039127 (J.N.S.); and NIH grants P41 RR011823, P01 AG031097, HHSN268201000035C, and R01 MH067880 (J.R.Y. and J.N.S.) and P30 CA014195 (M.W.H.). The RAW files and parameter files are publicly available at http://fields.scripps.edu/published/ellnpp2011/.

Supporting Online Material

www.sciencemag.org/cgi/content/full/science.1217421/DC1
Materials and Methods
Fig. S1
Table S1
References (*9*–*19*)

5 December 2011; accepted 19 January 2012
Published online 2 February 2012;
10.1126/science.1217421

[1]Department of Chemical Physiology, The Scripps Research Institute, 10550 North Torrey Pines Road, La Jolla, CA 92037, USA. [2]Molecular and Cell Biology Laboratory, Salk Institute for Biological Studies, 10010 North Torrey Pines Road, La Jolla, CA 92037, USA.

*These authors contributed equally to this work.
†To whom correspondence should be addressed. E-mail: hetzer@salk.edu

Evolution of Shape by Multiple Regulatory Changes to a Growth Gene

David W. Loehlin*† and John H. Werren†

The genetic changes responsible for morphological differences between species are largely unidentified. Such changes can involve modifications of growth that are relevant to understanding evolution, development, and disease. We identified a gene that induces male-specific wing size and shape differences between *Nasonia* wasp species. Fine-scale mapping and in situ hybridization reveal that changes in at least three regions (two strictly in noncoding sequence) around the gene *unpaired-like* (*upd-like*) cause changes in spatial and temporal expression of *upd-like* in the developing wing and corresponding changes in wing width. *Upd-like* shows homology to the *Drosophila unpaired* gene, a well-studied signaling protein that regulates cell proliferation and differentiation. Our results indicate how multiple changes in the regulation of *upd-like* are involved in microevolution of morphological and sex-specific differences between species.

The diversity of animal size and shape has fascinated scientists for centuries (*1*, *2*). Changes in morphology, such as the beaks of birds, toes of lizards, and hands of humans, underpin diversification and adaptation into different ecological niches (*3*–*5*). Yet the genes and genetic changes responsible for animal shape differences between species remain poorly understood (*6*–*8*). Genetic studies have revealed some genes and pathways required for growth and regulation of size and shape during development, many of which are also involved in human disease such as cancer and diabetes (*9*). These include signaling genes that regulate organ-specific patterning and growth [e.g., Wnt, Hippo, and Janus kinase–signal transducers and activators of transcription (JAK/STAT)], nutritional and hormonal regulators of body size (such as insulin signaling) and effector genes of cell growth and proliferation (cell cycle, apoptosis, and protein synthesis) (*9*, *10*). However, it is not yet clear whether evolutionary changes in these genes or others underlie size and shape differences between animal species (*7*).

The parasitoid jewel wasp *Nasonia* is emerging as a model system for investigating the genetics of species differences in development and morphology. The *Nasonia* genus consists of four closely related species, each of which has evolved a distinct male wing size (*8*, *11*–*13*). The greater than twofold difference in male wing size between *N. vitripennis* and *N. giraulti* (Fig. 1A) provides a tool for investigating the evolution of growth regulation. We isolated the two largest effect quantitative trait loci (QTLs) for this male wing size difference (*11*, *14*), *wing-size1* (*ws1*) (*14*) and *widerwing* (*wdw*) (*11*), which increase wing

Department of Biology, University of Rochester, Rochester, NY 14627, USA.

*Present address: Howard Hughes Medical Institute and Laboratory of Molecular Biology, University of Wisconsin, Madison, WI 53706, USA.

†To whom correspondence should be addressed. E-mail: loehlin@wisc.edu (D.W.L.); werr@mail.rochester.edu (J.H.W.)

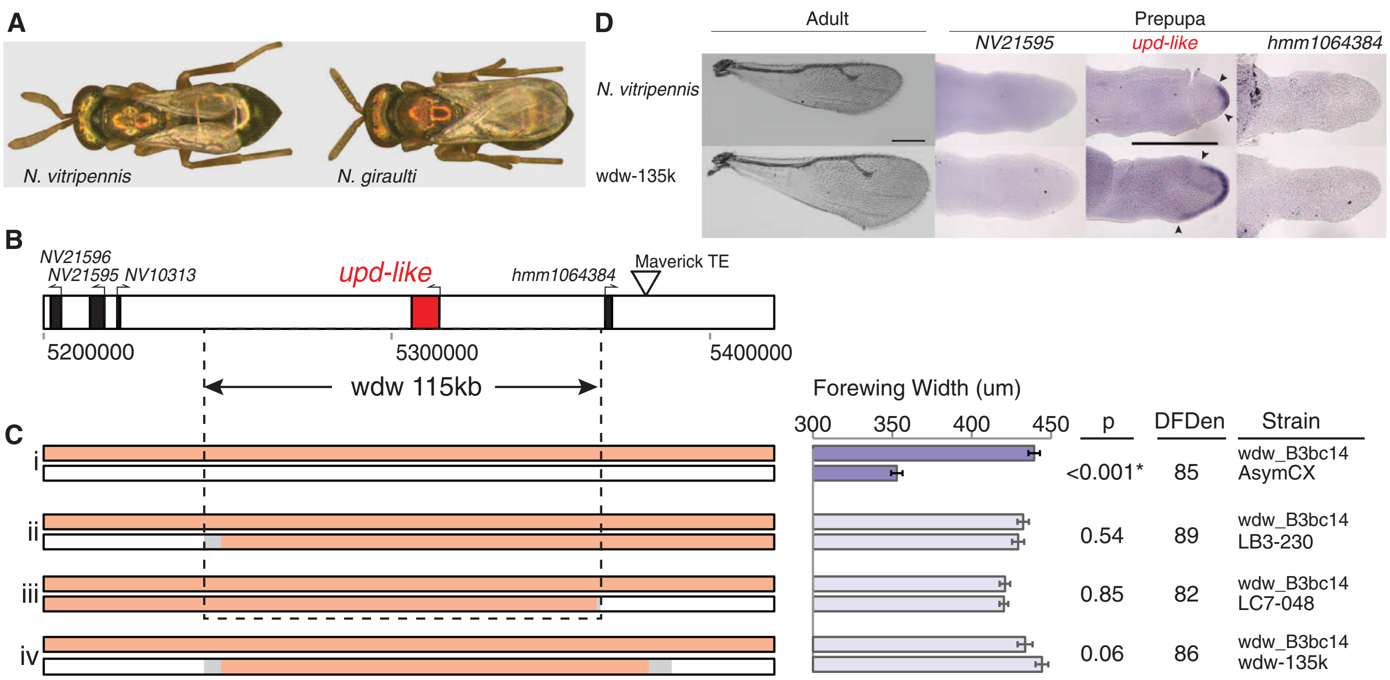

Fig. 1. *Wdw* maps to the *upd-like* locus and affects its expression. (**A**) Male *N. vitripennis* and *N. giraulti* have diverged in wing size. (**B**) Genes in the 200-kb region around *wdw* in *N. vitripennis,* including a Maverick transposable element that is absent in *N. giraulti* and does not appear to affect wing size (*18*). (**C**) Recombinant genotypes (left) and phenotypes (right) map the full *wdw* effect to a 115-kb region. The wing width of haploid males of two genotypes of interest was measured using crosses (fig. S1) (*17*) between the original *wdw* introgression (solid orange bar) and one of the following: (i) *N. vitripennis*, (ii) an introgression recombinant on the left, (iii) an introgression recombinant on the right, and (iv) an introgression recombinant on both sides (wdw-135k). White, *N. vitripennis* genotype; orange, *N. giraulti* genotype; gray, genotype between markers is unknown. Dark blue bars and * show statistically significant difference in wing width between genotypes, corrected for multiple testing (Bonferroni); light blue bars, no significant difference. DFDen, Denominator degrees of freedom from restricted maximum likelihood analysis of variance (ANOVA). Error bars show standard error. (**D**) RNA in situ hybridization reveals that the *wdw* introgression (wdw-135k line) has broader *upd-like* expression than *N. vitripennis*, consistent with the larger wing size. No expression pattern is seen for neighboring genes *NV21595* and *hmm1064384*. *NV10313* is not expressed in wing (*18*). Arrowheads denote boundaries of *upd-like* expression. Quantification of the size of the expression domain is in fig. S3. Scale bars, 200 μm.

size through different mechanisms. The *giraulti* allele of *ws1* increases overall male wing size relative to *N. vitripennis*. The genetic change underlying *ws1* has been mapped to a 13.5-kb noncoding interval containing the 5′-untranslated region of the sex-determining factor *doublesex* (*8*). Changes in *doublesex* expression level in the developing wing are correlated with the wing size difference. *doublesex* is a major sex-determining factor in animals, found from humans to worms, which provides the downstream signal of somatic sex (*15*) and which also can have a role in growth regulation (*8*, *16*).

Positional cloning and identification of *wdw*. *Widerwing* (*wdw*) alters male-specific wing shape, as well as wing size, by changing cell numbers differentially across the width of the male wing, but with no effect on female wing size (*11*). The male wing size phenotype was initially mapped to a

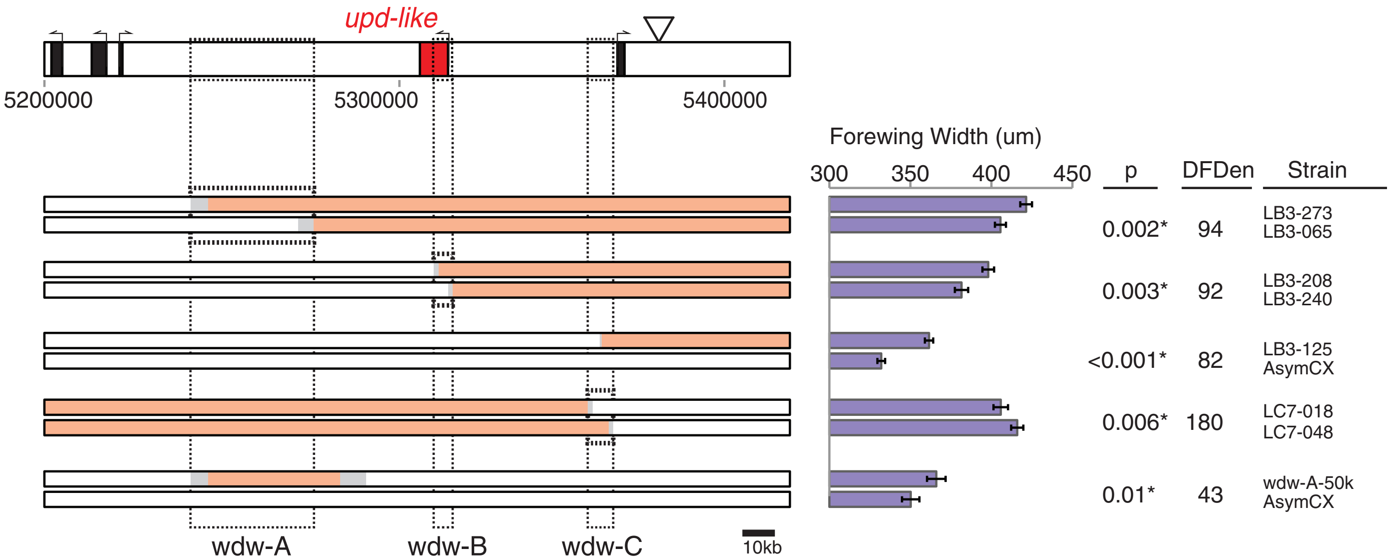

Fig. 2. Multiple intervals within the wdw region affect wing size. The *wdw* phenotype splits into at least three subregions (light dotted lines), each with significant effects on wing size. Heavy dotted lines mark sequence differences between three pairs of adjacent recombinant lines that best define these subregions. Also shown are two recombinants (wdw-A-50k and LB3-125, also used in Figs. 3 and 4) where recombination has isolated the wdw-A and wdw-C subregions.

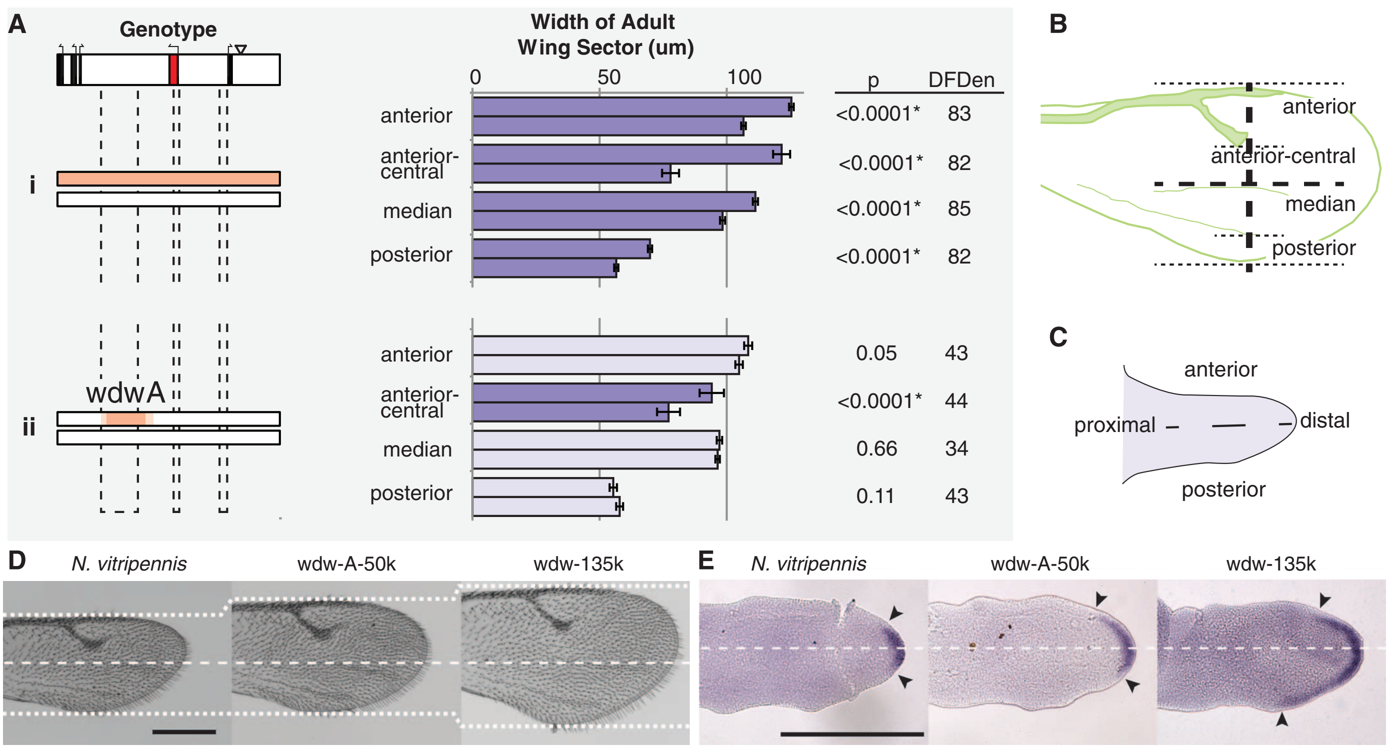

Fig. 3. Anterior-specific effects of the wdw-A subregion. (**A**) The original *wdw* introgression affects the size of sectors across the width of the adult wing, whereas the wdw-A subregion only affects the anterior-central sector. The width of four A-P sectors was measured for the genotype pairs indicated on the left (*17*). (i) Original *wdw* introgression compared with *N. vitripennis*; (ii) wdw-A-50k compared with *N. vitripennis*. Dark blue bars and * show statistically significant difference in sector width between genotypes, corrected for multiple testing (Bonferroni). Error bars show standard error. (**B**) Diagram of the adult wing sectors used in part A and Fig. 4A. (**C**) Illustration of *Nasonia* wing imaginal disc, which develops in a similar orientation to the adult wing. (**D**) Adult wings reveal anterior-specific expansion in wdw-A. Dashed line marks position of median vein (inferred A-P boundary). Dotted lines mark wing edges. (**E**) wdw-A also regulates anterior-specific expression of *upd-like* in prepupae. Dashed line marks wing tip (A-P boundary, fig. S3). Arrowheads denote boundaries of *upd-like* expression. Scale bars, 200 μm.

1-Mb region by introgressing chromosome segments from *N. giraulti* into *N. vitripennis*. Recombination mapping using generated recessive lethal mutations linked to the introgression (fig. S1) (*17*) mapped *wdw* further to 115 kb (Fig. 1). During this process, we broke the region into intervals differentially affecting male wing width, which we made into inbred lines for further analysis (*18*). We also created a 135-kb introgression (wdw-135k line) of *N. giraulti* sequence in *N. vitripennis*, resulting in males with wide wings that are not significantly different in wing width from the original *wdw* introgression line (Fig. 1).

Only one gene, *NV21594*, occurs within the 115-kb *wdw* region (Fig. 1) (*18*), which suggests that it could be the gene behind the wing size difference. However, it is also possible that genes adjacent to the 115-kb region are responsible, as their expression patterns could be encoded in *cis*-regulatory elements within this region. We tested the expression of *NV21594* and adjacent genes *NV10313*, *NV21595*, and *hmm1064384* in wings using reverse transcription polymerase chain reaction. We detected expression of all but *NV10313* in male wings (*18*). We further investigated whether *NV21594* or adjacent genes have spatial expression patterns in developing wings by using RNA in situ hybridization (*17*). Whereas *NV21595* and *hmm1064384* do not show a spatial pattern of expression (Fig. 1) (*18*), *NV21594* shows a clear spatial expression pattern that differs between *N. vitripennis* and the *N. giraulti* introgression. Specifically, it is expressed in the tip of the *N. vitripennis* prepupal male wing but is expressed much more broadly along the wing edge in the *giraulti* allele of *wdw* in a *vitripennis* background (wdw_gV) and also in *N. giraulti* male wings (Fig. 1 and figs. S3 and S4) (*18*). Thus, the correlation between expression pattern and wing size suggests *NV21594* as the likely candidate for *wdw*.

Through searches of other arthropod genomes, we have identified genes with homology to *NV21594* in the holometabolous insect orders Hymenoptera, Coleoptera, and Diptera (fig. S5) (*18*), which include the *Drosophila melanogaster* gene *unpaired* (*upd*). The *upd* candidates from these orders share five conserved peptide motifs, including an unusual short motif (WXNPCG) that is diagnostic for *upd* candidate protein genes in *Nasonia*, *Apis*, *Tribolium*, and *D. melanogaster* (table S1) (*18*). We therefore refer to *NV21594* as *unpaired-like* (*upd-like*). The *upd* candidates occur in clusters with two paralogous genes (*upd-like2* and *upd-like3*) in each of these taxa, as is also found in *D. melanogaster*. These proteins are also highly alpha-helical (fig. S5), which is typical of cytokines (*19*). *Upd* in *Drosophila* regulates cell proliferation as a ligand of the JAK-STAT pathway and is thus a reasonable candidate for a wing-growth gene. *Upd* is thought to play a similar role in *Drosophila* as the mammalian cytokine interleukin-6 (IL-6), which is involved in a number of human diseases (*19*).

The wdw_g introgression both increases wing width (by 25%) and expands the length of the *upd-like* expression domain along the wing edge (by 159%) relative to *N. vitripennis* (fig. S3). It may be that wdw_g introgression could be causing the observed expansion in *upd-like* expression, but it is also possible that this expansion is simply a by-product of the larger wing. We thus examined *upd-like* expression using the large winged $ws1_g$ QTL, which increases wing width by 30% (*8*). Although $ws1_g$ and wdw_g have wings similarly wider than *N. vitripennis*, *upd-like* expression in $ws1_g$ is *vitripennis*-like (fig. S4). Specifically, expression is absent from the posterior wing margin and significantly contracted relative to wdw_g, with a 54% smaller expression edge length (fig. S3). These results suggest that the *wdw* region is a driver of both *upd-like* expression and male wing size. In females, the wdw_g introgression does not affect wing size (*11*), and *upd-like* is expressed in a broad curve in both introgression and *N. vitripennis* female wings (fig. S6). This indicates that *upd-like* is not a male-specific gene, but rather that its expression is regulated in a male-specific fashion. The dependence of both male wing size and expression pattern on the *wdw* allele strongly indicates that *upd-like* is the gene that mediates the wing size difference.

Multiple noncoding intervals around *upd-like* contribute to the wing size difference. Several recombinants within the 115-kb *wdw* region had intermediate wing sizes, which indicated

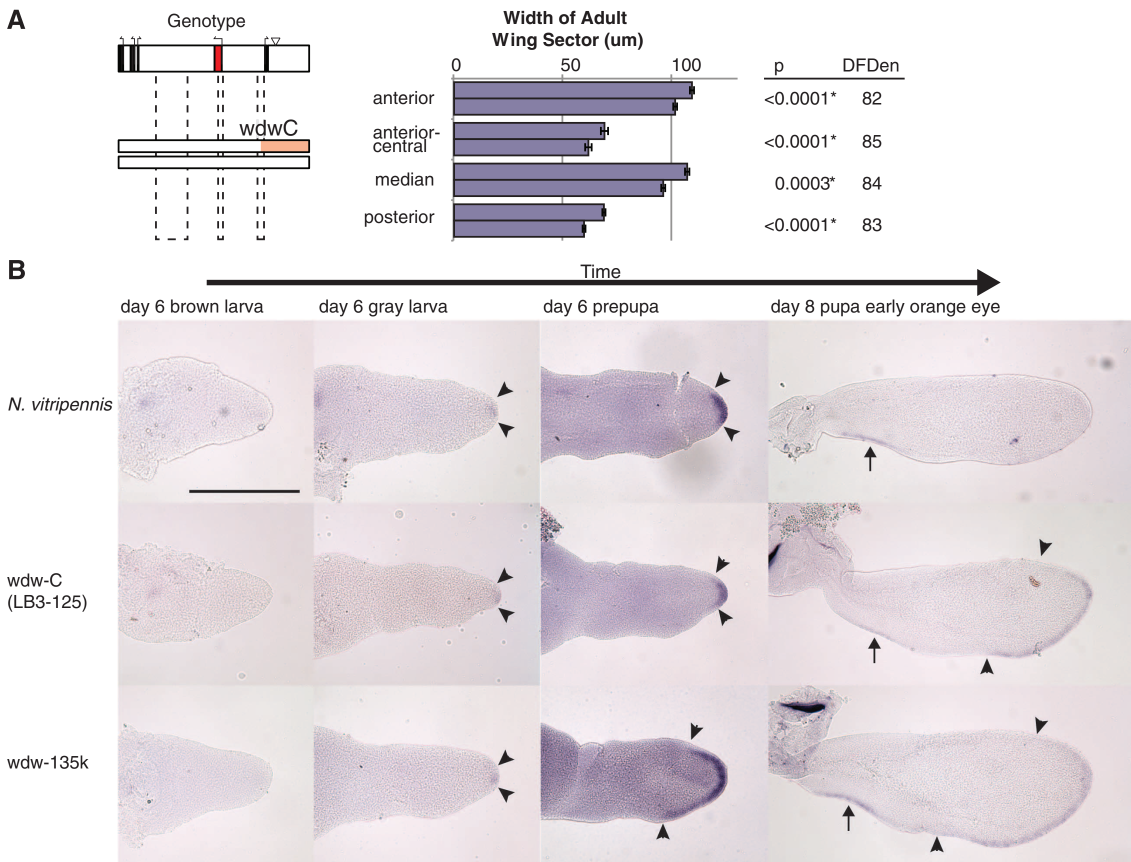

Fig. 4. Temporal regulation of *upd-like* by wdw-C. (**A**) A recombinant line containing the *giraulti* allele of wdw-C (LB3-125) is wider than *N. vitripennis* in each of four sectors across the adult wing. (**B**) Expression of *upd-like* before and after pupation reveals a temporal shift in wdw-C. In *N. vitripennis*, *upd-like* expression in the tip of the wing is visible only in gray larvae and prepupae. In pupal wings, expression is only apparent in the proximal posterior wing (arrow). In wdw-135k, expression is similar to *N. vitripennis* in gray larvae but expands apically in prepupae and is active later into pupation. In wdw-C (LB3-125), expression is *vitripennis*-like in the prepupa and *giraulti*-like in the pupa, which suggests that this subregion controls temporal regulation of *upd-like.* Control gene *wingless* is expressed at all stages (fig. S8).

that it is likely that multiple functional sequence changes contribute to the full *wdw* phenotype. Experimental crosses between recombinant lines that differ in *giraulti* sequence within the 115-kb region around *upd-like* (fig. S1) identified three subregions within the 115-kb *wdw* region that differentially contribute to wing size (Fig. 2). The middle subregion (wdw-B) contains both noncoding differences and a few coding changes in the first exon of *upd-like*. However, two of the three subregions, wdw-A and wdw-C, contain exclusively noncoding DNA. We created a wdw-A recombinant line (wdw-A-50k) that contains only 50 kb of *giraulti* noncoding sequence spanning the wdw-A subregion. These wdw-A-50k males have significantly larger wings than *N. vitripennis* (Fig. 2), which suggests that noncoding changes in the region are sufficient to alter wing size, regardless of whether the *upd-like* protein coding sequence comes from *N. giraulti* or *N. vitripennis*.

The three *wdw* subregions appear to each regulate distinct spatial parts of the wing width difference. We measured changes in width along the wing anterior-posterior (AP) axis in our recombinant lines (Figs. 3 and 4 and fig. S7) and documented that the full wdw_g introgression increases wing width in each sector along the AP axis, with a particularly strong effect in the anterior-central sector (Fig. 3). The three subregions subdivide this pattern. Wdw-A only affects wing size in the anterior half of the wing and appears to contribute primarily to the size of the anterior-central sector (Fig. 3 and fig. S7). In contrast, wdw-B and wdw-C have broader effects on wing width, and their specific effects appear to depend on the genotype at other subregions. Specifically, whereas the spatial effects of wdw-A are similar whether we compare recombinants from the left side or from the right side of the region, the spatial effects of wdw-B and wdw-C show significant differences (fig. S7) across all sectors or modestly spatially restricted effects, depending on the direction of the comparison. This suggests either that the subregions interact epistatically to produce the full wing size difference or that there are additional modifier QTLs, most likely located between wdw-B and C. For subsequent analysis of wdw-C, we focused on a recombinant line (LB3-125) that contains *giraulti* sequence only at wdw-C. This line has a fairly uniform effect, a 7.4 ± 0.2 μm to 11.0 ± 0.9 μm (7 to 15%) increase in each wing sector relative to *N. vitripennis* (Fig. 4).

Wdw-A causes an increase in wing width in the anterior half of the wing. It also causes an anterior-specific change in *upd-like* expression, which is broad and *giraulti*-like in the anterior of wdw-A (wdw-A-50k line) prepupal wings and yet contracted and *vitripennis*-like in the posterior (Fig. 3 and fig. S3). We verified that this was a shift in the anterior expression pattern and not a shift in the A-P compartment boundary by costaining with an antibody against the posterior compartment–specific protein Engrailed (fig. S3).

In contrast to wdw-A's spatial effects, wdw-C (LB3-125 recombinant line) increases wing width across each A-P axis region (Fig. 4). To our surprise, *upd-like* expression in prepupal wings is *vitripennis*-like in this line (Fig. 4), despite the increase in adult wing size. An alternative mechanism that could produce a change in wing size is a temporal expansion of *upd-like* expression. Indeed, a broad *giraulti*-like expression pattern emerges in wdw-C pupal wings at a stage where expression in the wing tip is absent in *N. vitripennis* (Fig. 4) (*18*). Together, these observations suggest that wdw-C is a late-acting regulatory element with a broad effect.

We inferred the effects of wdw-B even though we did not genetically isolate it as cleanly as wdw-A and wdw-C. *Upd-like* has a broad expression pattern in recombinants bearing *giraulti* alleles at wdw-B+C (LB3-208 line), not significantly different from the full introgression (figs. S3 and S9). These data suggest that this subregion controls the early expression pattern, whereas wdw-C controls the late expression pattern. This expression pattern also suggests that both wdw-A and wdw-B activate *upd-like* expression in anterior cells, perhaps in an overlapping pattern.

Interspecific patterns of *unpaired-like* expression and wing size. Male wing size and *upd-like* expression were compared in three *Nasonia* and two large-winged outgroup species, the closely related *Trichomalopsis sarcophagae* and more distant *Muscidifurax raptorellus* (Fig. 5). Small male wings appear to be derived, occurring in both *N. vitripennis* and *N. longicornis*, even though *N. longicornis* is more closely related to *N. giraulti* (*12*, *20*). The reduced male wing width in *N. longicornis* appears to be due, in part, to evolution at the *wdw* locus: introgression of the wdw_l region into *N. vitripennis* (wdw_lV) increases adult wing size by 11%, intermediate between *N. vitripennis* and wdw_gV (*11*). Contraction of the *upd-like* expression pattern has occurred in both *N. vitripennis* and *N. longicornis* males (Fig. 5). Furthermore, the *N. longicornis upd-like* expression pattern change is also caused by evolution at *wdw*, as the wdw_lV introgression has a contracted expression pattern relative to wdw_gV (Fig. 5 and fig. S3).

Although the smaller wing size and *upd-like* expression in *N. vitripennis* and *N. longicornis* could be the result of a hybridization event between the species followed by introgression of the *wdw* region, the data do not support this. Sequence divergence in the three subregions is consistent with the species tree; there is 1.2% divergence between *N. longicornis* and *N. giraulti*, less than the respective 2.4% and 2.8% between these species and *N. vitripennis* (*18*). Furthermore, analysis of phylogenetic tree topology with a sliding window across the *wdw* region, as well as examination of parsimony-informative sites, revealed no evidence

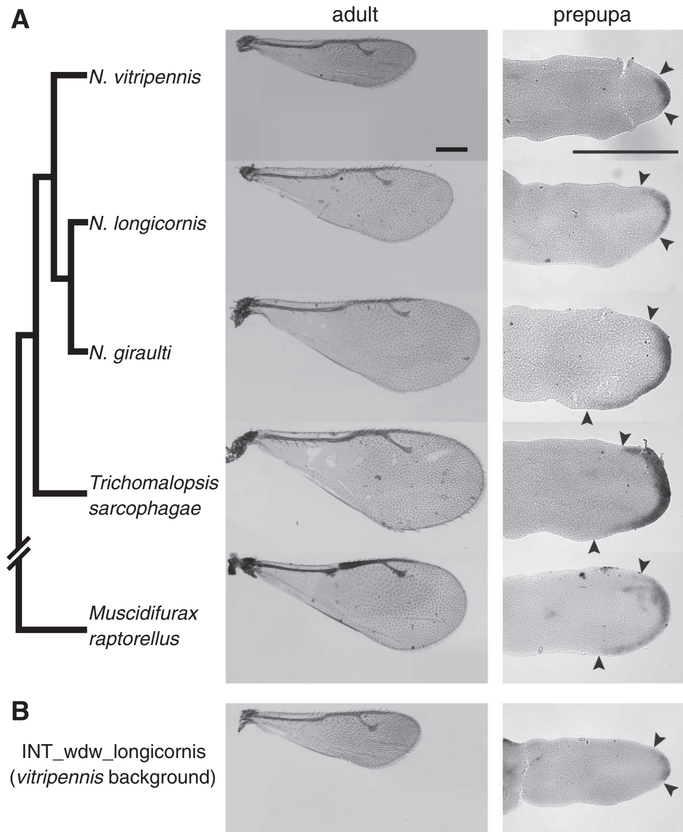

Fig. 5. Evolution of wing size and *unpaired-like* expression. (**A**) Adult wings and *upd-like* expression in prepupal wings from *Nasonia* males and outgroup species. Both *N. vitripennis* and *N. longicornis* males have a contracted expression pattern. The species cladogram is adapted from (*29*). (**B**) A *N. longicornis* introgression of *upd-like* into *N. vitripennis* also shows a contracted expression pattern.

of sequence introgression between *N. vitripennis* and *N. longicornis* (*18*). These results indicate that regulatory evolution of *upd-like* probably occurred in two separate *Nasonia* lineages, either by parallel reductions in *N. vitripennis* and *N. longicornis* or by reduction in an ancestral *Nasonia* lineage followed by expansion in the *N. giraulti* lineage. This observation plus the role of three subregions that we have identified between *N. vitripennis* and *N. giraulti* suggests that *unpaired-like* is a hotspot for wing size evolution in *Nasonia*.

Discussion. This study determined the genetic basis of *wdw*, a major component of the male-specific wing size difference between *N. vitripennis* and *N. giraulti*. Our data indicate that *upd-like* causes the spatial changes in cell proliferation and growth within the wing and that *upd-like* is a hotspot for size and shape evolution in *Nasonia*. *Unpaired* (*upd*) in *D. melanogaster* is a ligand for the JAK/STAT pathway (*21*). This pathway's role in cell proliferation makes it a plausible target of morphological evolution, though it is not yet known whether *upd-like* mediates its effects in *Nasonia* through JAK/STAT or other pathways. *Nasonia upd-like* appears to be particularly susceptible to wing growth–altering changes, which indicates that the gene might have a specialized role in specifying organ size in the growth gene network. Considering that many size and shape differences between animals are due to differences in cell numbers (*9*), *upd-like* genes could be hotspots of size and shape evolution in other species as well.

Using a phenotype-based positional cloning approach, we have identified two different major QTL genes (*wdw* and *ws1*) that are responsible for sex-specific differences in wing development between closely related *Nasonia* species. From what is known about fly wing development (*22–24*), the alternative candidate gene approach would not have predicted the role of either *upd* or *dsx* in *Nasonia* wing size. Nevertheless, both genes appear to be homologs of functionally conserved developmental regulatory genes, which is consistent with the hypothesis that core developmental genes tend to be involved in morphological evolution (*25*, *26*). It has also been argued that noncoding *cis*-regulatory changes could play a central role in developmental differences between species (*27*, *28*). Our findings support this view and further implicate growth-regulating genes in organ-specific size and shape evolution.

References and Notes

1. G. Galilei, *Dialogues Concerning Two New Sciences*, H. Crew, A. De Salvio, Transls. (MacMillan, New York, 1914).
2. C. Darwin, *On the Origin of Species by Means of Natural Selection, or the Preservation of Favored Races in the Struggle for Life* (John Murray, London, 1859).
3. J. B. Losos, T. R. Jackman, A. Larson, K. Queiroz, L. Rodriguez-Schettino, *Science* **279**, 2115 (1998).
4. A. Abzhanov, M. Protas, B. R. Grant, P. R. Grant, C. J. Tabin, *Science* **305**, 1462 (2004).
5. S. W. McKechnie *et al.*, *Mol. Ecol.* **19**, 775 (2010).
6. M. D. Shapiro *et al.*, *Nature* **428**, 717 (2004).
7. D. L. Stern, V. Orgogozo, *Evolution* **62**, 2155 (2008).
8. D. W. Loehlin *et al.*, *PLoS Genet.* **6**, e1000821 (2010).
9. B. A. Edgar, *Nat. Rev. Genet.* **7**, 907 (2006).
10. T. Lecuit, L. Le Goff, *Nature* **450**, 189 (2007).
11. D. W. Loehlin, L. S. Enders, J. H. Werren, *Heredity* **104**, 260 (2010).
12. R. Raychoudhury *et al.*, *Heredity* **104**, 278 (2010).
13. J. H. Werren, D. W. Loehlin, in *Emerging Model Organisms*, vol. 2, D. A. Crotty, A. Gann, Eds. (Cold Spring Harbor Laboratory Press, Cold Spring Harbor, NY, 2009), pp. 267–298.
14. R. F. Weston, I. Qureshi, J. H. Werren, *J. Evol. Biol.* **12**, 586 (1999).
15. C. S. Raymond, M. W. Murphy, M. G. O'Sullivan, V. J. Bardwell, D. Zarkower, *Genes Dev.* **14**, 2587 (2000).
16. L. E. Sanders, M. N. Arbeitman, *Dev. Biol.* **320**, 378 (2008).
17. Materials and methods are available as supporting material on *Science* Online.
18. Supporting text is available as supporting material on *Science* Online.
19. J. S. Rawlings, K. M. Rosler, D. A. Harrison, *J. Cell Sci.* **117**, 1281 (2004).
20. J. H. Werren *et al.*, *Science* **327**, 343 (2010).
21. N. I. Arbouzova, M. P. Zeidler, *Development* **133**, 2605 (2006).
22. J. C. Hombría, S. Brown, S. Häder, M. P. Zeidler, *Dev. Biol.* **288**, 420 (2005).
23. T. Mukherjee, J. C. Hombría, M. P. Zeidler, *Oncogene* **24**, 2503 (2005).
24. C. C. Robinett, A. G. Vaughan, J. M. Knapp, B. S. Baker, *PLoS Biol.* **8**, e1000365 (2010).
25. T. Werner, S. Koshikawa, T. M. Williams, S. B. Carroll, *Nature* **464**, 1143 (2010).
26. B. R. Wasik, D. J. Rose, A. P. Moczek, *Evol. Dev.* **12**, 353 (2010).
27. D. L. Stern, *Evolution* **54**, 1079 (2000).
28. S. B. Carroll, *PLoS Biol.* **3**, e245 (2005).
29. R. Raychoudhury, L. Baldo, D. C. Oliveira, J. H. Werren, *Evolution* **63**, 165 (2009).

Acknowledgments: We thank L. Gu and J. Sysol for volunteer assistance with mapping; M. Rosenberg for sharing the *Nasonia* wingless plasmid; and H. Jasper, J. D. Lambert, M. Welte, D. Stern, D. Presgraves, D. Wheeler, R. Edwards, A. Avery, and M. Clark for advice and technical assistance. This work was supported by NSF Doctoral Dissertation Improvement Grant DEB-0910017 to D.W.L. and NIH grants 5R01 GM070026-04 and 5R24 GM084917-04 to J.H.W. Sequences are deposited at GenBank with accessions JQ082366 to JQ082369.

Supporting Online Material
www.sciencemag.org/cgi/content/full/335/6071/943/DC1
Materials and Methods
SOM Text
Figs. S1 to S9
Tables S1 to S3
References (*30–32*)

12 October 2011; accepted 10 January 2012
10.1126/science.1215193

Field-Effect Tunneling Transistor Based on Vertical Graphene Heterostructures

L. Britnell,[1] R. V. Gorbachev,[2] R. Jalil,[2] B. D. Belle,[2] F. Schedin,[2] A. Mishchenko,[1] T. Georgiou,[1] M. I. Katsnelson,[3] L. Eaves,[4] S. V. Morozov,[5] N. M. R. Peres,[6,7] J. Leist,[8] A. K. Geim,[1,2]* K. S. Novoselov,[1]* L. A. Ponomarenko[1]*

An obstacle to the use of graphene as an alternative to silicon electronics has been the absence of an energy gap between its conduction and valence bands, which makes it difficult to achieve low power dissipation in the OFF state. We report a bipolar field-effect transistor that exploits the low density of states in graphene and its one-atomic-layer thickness. Our prototype devices are graphene heterostructures with atomically thin boron nitride or molybdenum disulfide acting as a vertical transport barrier. They exhibit room-temperature switching ratios of ≈50 and ≈10,000, respectively. Such devices have potential for high-frequency operation and large-scale integration.

The performance of graphene-based field effect transistors (FETs) has been hampered by graphene's metallic conductivity at the neutrality point (NP) and the unimpeded electron transport through potential barriers caused by Klein tunneling, which limit the achievable ON-OFF switching ratios to ~10^3 and those achieved so far at room temperature to <10 (*1–7*). These low ratios are sufficient for individual high-frequency transistors and analog electronics (*4–7*), but they present a fundamental problem for any realistic prospect of graphene-based integrated circuits (*1–7*). A possible solution is to open a band gap in graphene—for example, by using bilayer

[1]School of Physics and Astronomy, University of Manchester, Manchester M13 9PL, UK. [2]Manchester Centre for Mesoscience and Nanotechnology, University of Manchester, Manchester M13 9PL, UK. [3]Institute for Molecules and Materials, Radboud University of Nijmegen, 6525 AJ Nijmegen, Netherlands. [4]School of Physics and Astronomy, University of Nottingham, Nottingham NG7 2RD, UK. [5]Institute for Microelectronics Technology, 142432 Chernogolovka, Russia. [6]Departamento de Física, Universidade do Minho, P-4710-057, Braga, Portugal. [7]Graphene Research Centre and Department of Physics, National University of Singapore, 2 Science Drive 3, 117542 Singapore. [8]Momentive Performance Materials, 22557 West Lunn Road, Strongsville, OH 44070, USA.

*To whom correspondence should be addressed. E-mail: geim@manchester.ac.uk (A.K.G.); kostya@manchester.ac.uk (K.S.N.); leonid.ponomarenko@manchester.ac.uk (L.A.P.)

graphene (8, 9), nanoribbons (10, 11), quantum dots (11), or chemical derivatives (12)—but it has proven difficult to achieve high ON-OFF ratios without degrading graphene's electronic quality.

We report an alternative graphene transistor architecture—namely, a field-effect transistor based on quantum tunneling (13–17) from a graphene electrode through a thin insulating barrier [in our case, hexagonal boron nitride (hBN) or molybdenum disulfide of ~1 nm thickness]. The operation of the device relies on the voltage tunability of the tunneling density of states (DOS) in graphene and of the effective height Δ of the tunnel barrier adjacent to the graphene electrode. To illustrate the proposed concept, we concentrate on graphene-hBN-graphene devices [an alternative barrier material (MoS_2) is discussed in (18)].

The structure and operational principle of our FET are shown in Fig. 1. For convenience of characterization, both source and drain electrodes were made from graphene layers in the multiterminal Hall bar geometry (18). This device configuration allowed us to not only measure the tunnel current-voltage curves (I-V) but also characterize the response of the graphene electrodes, thus providing additional information about the transistor operation. The core graphene-hBN-graphene structure was encapsulated in hBN so as to allow higher quality of the graphene electrodes (19, 20). To fabricate the device shown in Fig. 1A, we first used the standard cleavage technique (21) to prepare relatively thick hBN crystals on top of an oxidized Si wafer (300 nm of SiO_2), which acted as a gate electrode (Fig. 1 and fig. S1). The crystals served as a high-quality atomically flat substrate and a bottom encapsulation layer (19). Monolayer graphene (Gr_B) was then transferred onto a selected hBN crystal (20 to 50 nm thick) using a dry transfer procedure (19, 22). After deposition of metal contacts (5 nm Ti/50 nm Au) and etching to form a multiterminal Hall bar mesa, the structure was annealed at 350°C in forming gas. A few-atom-thick hBN crystal was identified (23) and transferred on top of Gr_B by using the same procedures. This hBN layer served as the tunnel barrier. The whole process of positioning, annealing, and defining a Hall bar was repeated to make the second (top) graphene electrode (Gr_T). Last, a thick hBN crystal encapsulated the entire multilayer structure (Fig. 1A and fig. S1). Further details of our multistep fabrication procedures can be found in (18, 22). We tested devices with tunnel barriers having thickness d from 1 to 30 hBN layers (18). To illustrate the basic principle of the tunneling FETs, we focus on the data obtained from four devices with a tunnel barrier made of 4 to 7 layers and discuss the changes observed for other d.

When a gate voltage V_g was applied between the Si substrate and the bottom graphene layer (Gr_B), the carrier concentrations n_B and n_T in both bottom and top electrodes increased because of the weak screening by monolayer graphene (24), as shown schematically in Fig. 1C. The increase of the Fermi energy E_F in the graphene layers could lead to a reduction in Δ for electrons tunneling predominantly at this energy (18). In addition, the effective height also decreased relative to the NP because the electric field penetrating through Gr_B altered the shape of the barrier (25, 26). Furthermore, the increase in the tunneling DoS as E_F moved away from the NP (24) led to an increase in the tunnel current I. Depending on parameters, any of the above three contributions could dominate changes in I with varying V_g. We emphasize that the use of graphene in this device architecture is critical because this exploits graphene's low DOS, which for a given change in V_g led to a much greater increase in E_F as compared with a conventional two-dimensional gas with parabolic dispersion (13–17). This difference translated into much greater changes of both Δ and tunneling DOS.

The behavior of in-plane resistivity ρ for the Gr_B and Gr_T layers as a function of V_g is shown in Fig. 2A. The curves indicate little residual doping for encapsulated graphene (≈0 and $<10^{11}$ cm^{-2} for Gr_B and Gr_T, respectively). In both layers, ρ strongly depended on V_g, showing that Gr_B did not screen out the electric field induced by the Si-gate electrode. The screening efficiency was quantified by Hall effect measurements (Fig. 2, B to D), which showed that the gate induced approximately the same amount of charge in both layers at low concentrations—that is, there was little screening if n_B was small. As the concentration in Gr_B increased, the $n_B(V_g)$ and $n_T(V_g)$ dependences became super- and sublinear, respectively (Fig. 2, B and C), because of the increase in n_B, which led to an increasingly greater

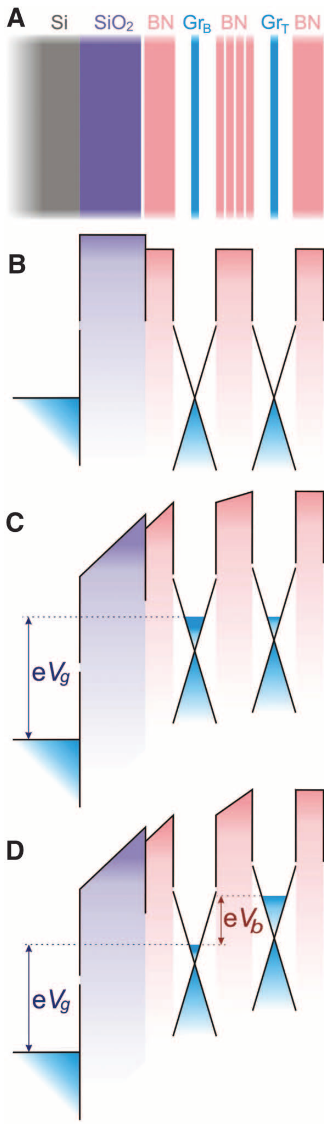

Fig. 1. Graphene field-effect tunneling transistor. (**A**) Schematic structure of our experimental devices. In the most basic version of the FET, only one graphene electrode (Gr_B) is essential, and the outside electrode can be made from a metal. (**B**) The corresponding band structure with no gate voltage applied. (**C**) The same band structure for a finite gate voltage V_g and zero bias V_b. (**D**) Both V_g and V_b are finite. The cones illustrate graphene's Dirac-like spectrum and, for simplicity, we consider the tunnel barrier for electrons.

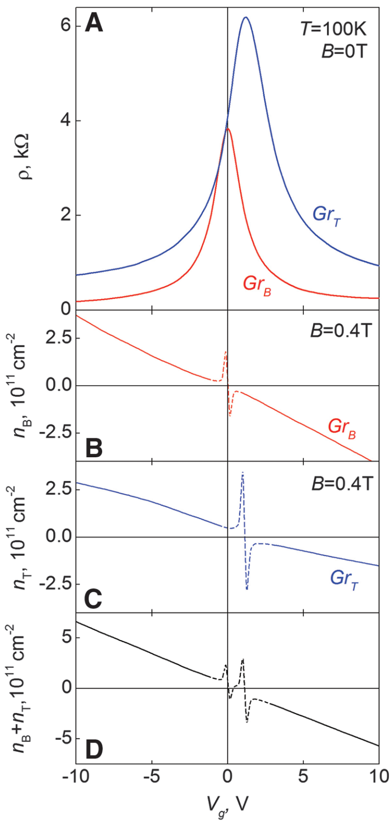

Fig. 2. Graphene as a tunneling electrode. (**A**) Resistivities of the source and drain graphene layers as a function of V_g. (**B** to **D**) Carrier concentrations in the two layers induced by gate voltage, which were calculated from the measured Hall resistivities ρ_{xy} by using the standard expression $n = B/e\rho_{xy}$, where B is the magnetic field and e is the electron charge. Close to the NP, the spikes appear (shown by dotted curves) because the above expression is not valid in the inhomogeneous regime of electron-hole puddles. The shown device has a 4-layer hBN barrier.

fraction of the gate-induced electric field being screened out by Gr_B (18). Hence, more electrons accumulated in the bottom graphene electrode, and fewer reached the top electrode. The total charge accumulated in both layers varied linearly in V_g (Fig. 2D), as expected. We could describe the observed redistribution of the charge between the two graphene layers in terms of the corresponding sequential circuit including the quantum capacitance (13, 27) of the graphene layers (fig. S2). For a parabolic band, the ratio between n_B and n_t would be independent on V_g, and therefore, the electric field penetrating into the tunnel barrier would be substantially reduced even in the limit of zero n_B (13).

A bias voltage V_b applied between Gr_B and Gr_T gave rise to a tunnel current through the thin hBN barrier that scaled with device area. *I-V* characteristics for one of our devices at various V_g are shown in Fig. 3A. First, we consider the case of zero V_g. At low V_b, I was linear in bias, yielding a tunnel resistivity $\rho^T = V_b/I \approx 100$ gigohms μm^2 for this hBN thickness. At higher voltages (V_b above ~0.1 V), I grew more rapidly. The *I-V* curves could be described (Fig. 3A, inset, and fig. S3) by the standard quantum-tunneling formulae (25, 26), assuming energy conservation but no momentum conservation at the mismatched graphene-hBN interface (28).

As shown below, we could distinguish experimentally between electron and hole tunneling and found that the tunneling was due to holes. This result is in agreement with a recent theory for the graphene-hBN interface (29), which reports a separation between the Dirac point in graphene and the top of the hBN valance band of ≈1.5 eV, whereas the conduction band is >4 eV away from the Dirac point. The fit to our data with $\Delta = 1.5$ eV yielded a tunneling mass $m \approx 0.5\ m_0$ (m_0 is the free electron mass), which is in agreement with the effective mass for holes in hBN (30). Furthermore, our analysis indicated that I varied mainly with the change in the tunneling DOS, whereas the change in tunneling probability with applied bias was a secondary (albeit important) effect (18). For our atomically thin hBN barriers with relatively low ρ^T, we were not in a regime of exponential sensitivity to changes in $\Delta[E_F(V_b)]$.

We demonstrate transistor operation in Fig. 3A, which plots the influence of gate voltage on I. V_g substantially enhanced the tunnel current, and the changes were strongest at low bias. The field effect was rather gradual for all gate voltages up to ±50 V, a limit set by the electrical breakdown of our SiO_2 gate dielectric (typically ≈60 V). This response is quantified in Fig. 3B, which plots the low-bias tunneling conductivity $\sigma^T = I/V_b$ as a function of V_g. The influence of V_g was highly asymmetric: σ^T changed by a factor of ≈20 for negative V_g (holes) and by a factor of 6 for positive V_g (electrons). We observed changes up to ≈50 for hole tunneling in other devices and always the same asymmetry (fig. S4) (18). Also, the ON-OFF ratios showed little change between room and liquid-helium temperatures, as expected for $\Delta >>$ thermal energy.

To analyze the observed behavior of $\sigma^T(V_g)$, we modeled the zero-bias conductivity by using the relation $\sigma^T \propto DOS_B(V_g) \times DOS_T(V_g) \times T(V_g)$, where the indices refer to the two graphene layers and $T(V_g)$ is the transmission coefficient through the hBN barrier (25, 26). The resulting curve shown in Fig. 3B accounts qualitatively for the main features in the measured data, using self-consistently the same tunneling parameters m and Δ given above. At V_g near zero, corresponding to tunneling from states near the NP, the tunneling DOS in both graphene layers was small and nonzero and was the result of residual doping, disorder, and temperature effects (18). The application of a gate voltage of either polarity led to a higher DOS and, therefore, higher σ^T. The gradual increase in $\sigma^T(V_g)$ for both polarities in Fig. 3B was therefore caused by the increasing DOS. However, V_g also affected the transmission coefficient. Because of the shift of E_F with changing V_g, the effective barrier height Δ decreased for one sign of charge carriers and increased for the other (Fig. 1B), which explains the asymmetry in both experimental and calculated $\sigma^T(V_g)$ in Fig. 3B in terms of the change in $T(V_g)$. For our devices, the effect of V_g on $T(V_g)$ was relatively weak (nonexponential) and comparable with the effect caused by changes in the tunneling DOS. The sign of the asymmetry infers that the hBN barrier height was lower for holes than for electrons, which is in agreement with the graphene-hBN band structure calculations (29). The weaker dependence of I on V_g at high bias can also be understood in terms of the more gradual increase in the tunneling DOS and in E_F at high doping ($V_b = 0.5$V correspond to $n_B \approx 10^{13}$ cm^{-2}).

Our results and analysis suggest that higher ON-OFF ratios could be achieved by using either higher V_g or making devices with larger d, so that the tunneling depends exponentially on bias and is controlled by the barrier height rather than the DOS. The former route is limited by the electrical breakdown of dielectrics at ~1 V/nm ($V_g \approx 300$V for our SiO_2 thickness). By extrapolating the analysis shown in Fig. 3B to such voltages, we found that ON-OFF ratios $>10^4$ would be possible for our 4-to-7-layer devices if SiO_2 of highest quality were used. However, it would still require unrealistically large V_g to enter the regime where E_F becomes comparable with Δ and changes in $\sigma^T(V_g)$ are exponentially fast. Therefore, we explored the alternative option and investigated devices with both thinner and thicker hBN barriers. For 1- to 3-hBN layers, zero-bias σ^T increased exponentially with decreasing number of layers, which is consistent with quantum tunneling, and we observed a weaker influence of V_g on I, as expected for the more conductive regime. On the other hand, the thicker hBN barriers were prone to electrical breakdown. Nonetheless, for a few devices with $d \approx 6$ to 9 nm, we were able to measure a tunnel current without breakdown. A current >10 pA appeared at biases of several volts and increased exponentially with V_b. The thicker devices' *I-V* characteristics could be fitted by using the same hole-tunneling parameters used above, thus indicating quantum tunneling rather than an onset of electrical breakdown. Unfortunately, no substantial changes (exceeding 50%) in the tunnel current could be induced by V_g. This insensitivity to gate voltage remains to be understood but was

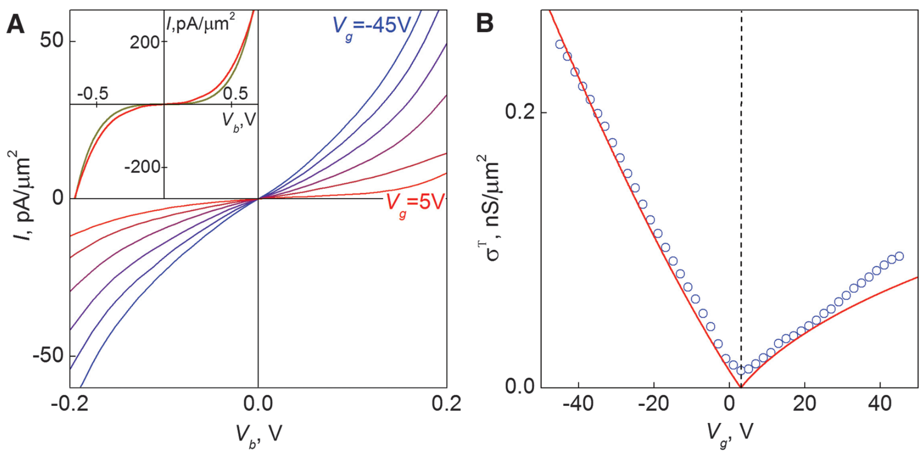

Fig. 3. Tunneling characteristics for a graphene-hBN device with 6 ± 1 layers of hBN as the tunnel barrier. (**A**) *I-Vs* for different V_g (in 10-V steps). Because of finite doping, the minimum tunneling conductivity is achieved at $V_g \approx 3$V. The inset compares the experimental *I-V* at $V_g = 5$ V (red curve) with theory (dark), which takes into account the linear DOS in the two graphene layers and assumes no momentum conservation. Further examples of experimental curves and their fitting can be found in (18). (**B**) Zero-bias conductivity as a function of V_g. The symbols are experimental data, and the solid curve is our modeling. The curve is slightly shifted with respect to zero V_g because of remnant chemical doping. In all the calculations, we assumed the hole tunneling with $m = 0.5\ m_0$ and $\Delta \approx 1.5$ eV (29, 30) and used d as measured by atomic force microscopy. Both I and σ are normalized per tunnel area, which was typically 10 to 100 μm^2 for the studied devices. Temperature, 240 K.

probably caused by charge traps that screened the influence of the gate.

An alternative method to achieve an exponential dependence of the tunneling current on gate voltage would be to use a barrier dielectric with a smaller Δ, which would be comparable with typical E_F realizable in graphene. One of such candidate materials is MoS_2, which has a band gap of about 1.3 eV and can be obtained in a mono- or few-layers state similar to hBN and graphene (*21*). Our first graphene-MoS_2–based devices demonstrate ON-OFF ratio close to 10.000 (fig. S5), which is sufficient for certain types of logic circuits.

We conclude that our tunneling devices offer a viable route for high-speed graphene-based analog electronics. The ON-OFF ratios already exceed those demonstrated for planar graphene FETs at room temperature by a factor of 10 (*3*–*7*). The transit time for the tunneling electrons through the nanometer-thick barriers is expected to be extremely fast (a few femtoseconds) (*13*–*17*) and exceeds the electron transit time in submicrometer planar FETs. It should also be possible to decrease the lateral size of the tunneling FETs down to the 10 nm scale, a requirement for integrated circuits. Furthermore, there appears to be no fundamental limitation to further enhancement of the ON-OFF ratios by optimizing the architecture and by using higher-quality gate dielectrics and, in particular, lower tunnel barriers (Δ < maximum achievable E_F).

References and Notes

1. P. Avouris, Z. H. Chen, V. Perebeinos, *Nat. Nanotechnol.* **2**, 605 (2007).
2. A. K. Geim, *Science* **324**, 1530 (2009).
3. F. Schweirz, *Nat. Nanotechnol.* **5**, 487 (2010).
4. Y. Wu *et al.*, *Nature* **472**, 74 (2011).
5. L. Liao *et al.*, *Nature* **467**, 305 (2010).
6. S. J. Han *et al.*, *Nano Lett.* **11**, 3690 (2011).
7. Y. M. Lin *et al.*, *Science* **332**, 1294 (2011).
8. E. V. Castro *et al.*, *Phys. Rev. Lett.* **99**, 216802 (2007).
9. J. B. Oostinga, H. B. Heersche, X. Liu, A. F. Morpurgo, L. M. K. Vandersypen, *Nat. Mater.* **7**, 151 (2008).
10. M. Y. Han, B. Ozyilmaz, Y. B. Zhang, P. Kim, *Phys. Rev. Lett.* **98**, 206805 (2007).
11. C. Stampfer *et al.*, *Front. Phys.* **6**, 271 (2011).
12. D. C. Elias *et al.*, *Science* **323**, 610 (2009).
13. S. Luryi, *Appl. Phys. Lett.* **52**, 501 (1988).
14. M. Heiblum, M. V. Fischetti, *IBM J. Res. Develop.* **34**, 530 (1990).
15. J. A. Simmons *et al.*, *J. Appl. Phys.* **84**, 5626 (1998).
16. A. Zaslavsky *et al.*, *Appl. Phys. Lett.* **83**, 1653 (2003).
17. A. Sciambi *et al.*, *Phys. Rev. B* **84**, 085301 (2011).
18. Materials and methods are available as supporting material on *Science* Online.
19. C. R. Dean *et al.*, *Nat. Nanotechnol.* **5**, 722 (2010).
20. A. S. Mayorov *et al.*, *Nano Lett.* **11**, 2396 (2011).
21. K. S. Novoselov *et al.*, *Proc. Natl. Acad. Sci. U.S.A.* **102**, 10451 (2005).
22. L. A. Ponomarenko *et al.*, *Nat. Phys.* **7**, 958 (2011).
23. R. V. Gorbachev *et al.*, *Small* **7**, 465 (2011).
24. A. H. Castro Neto, F. Guinea, N. M. R. Peres, K. S. Novoselov, A. K. Geim, *Rev. Mod. Phys.* **81**, 109 (2009).
25. J. G. Simmons, *J. Appl. Phys.* **34**, 1793 (1963).
26. E. L. Wolf, *Principles of Electron Tunneling Spectroscopy* (Oxford Univ. Press, Oxford, 1985).
27. L. A. Ponomarenko *et al.*, *Phys. Rev. Lett.* **105**, 136801 (2010).
28. J. M. Xue *et al.*, *Nat. Mater.* **10**, 282 (2011).
29. N. Kharche, S. K. Nayak, *Nano Lett.* **11**, 5274 (2011).
30. Y. N. Xu, W. Y. Ching, *Phys. Rev. B* **44**, 7787 (1991).

Acknowledgments: This work was supported by the European Research Council, European Commision FP7, Engineering and Physical Research Council (UK), the Royal Society, U.S. Office of Naval Research, U.S. Air Force Office of Scientific Research, and the Körber Foundation. A.M. acknowledges support from the Swiss National Science Foundation.

Supporting Online Material

www.sciencemag.org/cgi/content/full/science.1218461/DC1
Materials and Methods
SOM Text
Figs. S1 to S5
References (*31*–*35*)

27 December 2011; accepted 23 January 2012
Published online 2 February 2012;
10.1126/science.1218461

The Local Structure of Amorphous Silicon

M. M. J. Treacy[1]* and K. B. Borisenko[2,3]

It is widely believed that the continuous random network (CRN) model represents the structural topology of amorphous silicon. The key evidence is that the model can reproduce well experimental reduced density functions (RDFs) obtained by diffraction. By using a combination of electron diffraction and fluctuation electron microscopy (FEM) variance data as experimental constraints in a structural relaxation procedure, we show that the CRN is not unique in matching the experimental RDF. We find that inhomogeneous paracrystalline structures containing local cubic ordering at the 10 to 20 angstrom length scale are also fully consistent with the RDF data. Crucially, they also matched the FEM variance data, unlike the CRN model. The paracrystalline model has implications for understanding phase transformation processes in various materials that extend beyond amorphous silicon.

Amorphous silicon (a-Si) can be regarded as a classic example of a disordered four-coordinated covalent material. Understanding its structure has implications for understanding structures and structure-properties correlations not only for similar covalently bonded networks but also for a wider range of other amorphous materials. In general, having the correct structural model of an amorphous state is important in order to understand the structural origins of glass transitions and associated phenomena. Previous studies rely on spatially heterogeneous dynamics using either crystalline (*1*, *2*) or noncrystalline (*3*, *4*) inhomogeneities to explain kinetics of glass transitions and phenomena of glass-forming ability. Such knowledge is essential for a number of industrially important materials, such as phase-change memory materials for information storage (*5*, *6*). Accurate structural models are crucial for understanding mechanisms of deformation in metallic glasses (*7*). This knowledge is needed to ultimately build novel materials with the required properties. It is widely believed that the structure of a-Si is well represented by the continuous random network (CRN) model, which was first introduced by Zachariasen as a model for network glasses (*8*). The ideal CRN for a-Si is a fully four-coordinated, nonperiodic structure that is metastable with respect to crystalline silicon and is constructed primarily from five-, six- and seven-membered rings. Crystalline Si comprises six-membered rings only. High-quality CRN models, which reproduce the experimental density, have been developed by applying bond-swapping algorithms (*9*, *10*), in conjunction with framework relaxation using appropriate potentials (*11*, *12*). The models generate a reduced density function (RDF) that matches the essential features of experimental data obtained by high-energy x-ray and neutron diffraction (*13*), as well as electron diffraction (*14*). In addition, the models broadly reproduce features observed in Raman spectra (*15*), as well as the vibrational density of states obtained by neutron diffraction (*12*, *16*).

Other models for a-Si have been proposed. The paracrystallite model of Hosemann and Baggchi (1962) (*17*) and the microcrystallite model of Turnbull and Polk (1972) (*18*) are generally discredited because they are thought to be inconsistent with RDF data. Both models describe materials containing small grains of ordered material that are just a few nanometers in extent, but in the paracrystallite model there are strain gradients throughout the grains. The width of the second peak in the RDF suggests a range of Si-Si-Si angles that is thought to be inconsistent with either type of crystalline order. However, it has been argued that fluctuation electron microscopy (FEM) data provide irrefutable evidence for the presence of substantial topological crystallinity in a-Si at the 10 to 20 Å length scale (*19*). Although the FEM evidence has been reproduced by several groups for various samples of a-Si that were amorphized by different methods (*20*–*22*), the presence of topologically crystalline ordering in a-Si is not widely accepted as it appears to contradict carefully conducted RDF experiments (*13*). It has been asserted that claims

[1]Department of Physics, Arizona State University, Tempe, AZ 85287, USA. [2]Department of Materials, University of Oxford, Parks Road, Oxford OX1 3PH, UK. [3]Research Complex at Harwell, Rutherford Appleton Laboratory, Harwell Oxford, Didcot OX11 0FA, UK.

*To whom correspondence should be addressed. E-mail: treacy@asu.edu

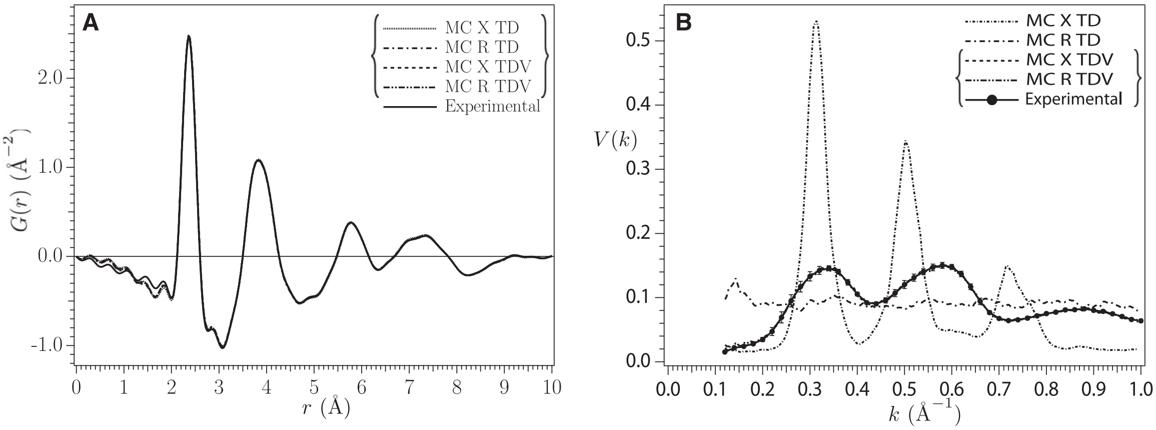

Fig. 1. (**A**) Reduced density functions, $G(r)$, obtained for an a-Si specimen and computed for four models by a Monte Carlo (MC) procedure using the experimental diffraction (D) and variance (V) data as a constraint. Both crystalline (X) and random (R) starting structures were used. A Tersoff potential (T) was applied as an additional constraint. (**B**) Variance plots, $V(k)$, for the experiment and four models. The braces, {}, in the legend indicate those traces that overlap.

Table 1. Selected structural and energetic properties of the four a-Si models. See text for details.

Model	U (eV/Si)	$R_{3\%}$	$R_{6\%}$	N_C	N_2	N_p
MC X TD	−3.99	0.2	84.6	3.58	611	281
MC R TD	−3.65	6.6	23.1	3.67	111	0
MC X TDV	−3.95	0.3	82.6	3.59	419	94
MC R TDV	−3.73	5.8	61.8	3.74	367	82

of longer-range order in glasses are unjustified because the random models, such as the CRN, account for all the observed features (*23*). We point out that although matching diffraction data are a necessary criterion for any successful model, alone it is not sufficient to identify a unique model. There exist topologically distinct homometric structures that also match the RDF data.

Experimentally, a-Si typically has a density about 1 to 2% less than that of the cubic crystalline phase. The area under the first-nearest neighbor peak of the RDF, $G(r)$, shows that a-Si has a coordination number less than 4, typically about 3.8 (*13*), which would account for the reduced density. Transmission electron microscopy (TEM) evidence shows that voids can occur in a-Si (*24*). Further, an experimentally constrained molecular relaxation (ECMR) study by Biswas *et al.* (*25*), using both diffraction (RDF) and FEM diffraction variance data as constraints, was found to support the void model. The implication is that a-Si can be described satisfactorily by an interrupted CRN model, with no topological order necessary to explain the data. However, the topology of the Biswas void model was not examined. The voids were introduced artificially, and it can be argued that the free void surfaces provide nucleation sites for paracrystallinity, which would explain the match to the FEM data.

Here we use a procedure similar to ECMR, but with a Tersoff atomic potential applied as an additional constraint. We show that refinements, made without introducing additional bias, yield inhomogeneous models containing topological crystallinity at the 10 to 20 Å length scale, with no voids, that are fully consistent with both the RDF and FEM data.

A serious deficiency of the ideal CRN model is that it is inconsistent with the FEM data (*19*). FEM examines the variability in microdiffraction patterns from small volumes of the sample, typically with probes of width $R \approx 10$ to 20 Å. The RDF and FEM techniques are complementary; the RDF method informs us about the mean diffraction, and FEM informs us about the variability of that diffraction from subregions of the sample. The RDF, being a volume-averaging technique, is insensitive to details about sample inhomogeneities. FEM microdiffraction simulations across CRN models (with 10 to 60 Å probes) confirm that different regions are qualitatively similar, as revealed by the featureless normalized variance of the microdiffraction pattern intensities. The normalized variance is obtained from the set of microdiffraction pattern intensities, $I(\boldsymbol{r}_p, \boldsymbol{k}, R)$, via

$$V(\boldsymbol{k},R) = \frac{\langle I^2(\boldsymbol{r}_p,\boldsymbol{k},R)\rangle_{r_p}}{\langle I(\boldsymbol{r}_p,\boldsymbol{k},R)\rangle^2_{r_p}} - 1 \qquad (1)$$

$\boldsymbol{r}_p$ is the location of the probe of width R (spatial resolution), and the angular brackets represent the averaging over all probe locations. For probe widths $R \geq 10$ Å, the two-dimensional variance pattern $V(\boldsymbol{k}, R)$ computed for typical CRN models is essentially flat, confirming that there are no special structural periodicities corresponding to a scattering vector $\boldsymbol{k}$. However, experimental FEM variance patterns from many different a-Si samples always show peaks near the 111, 200, 220, and 311 locations of the cubic Si structure. This indicates that there is crystalline topology present at length scales $R = 10$ to 20 Å. For larger probes, $R > 30$ Å, the variance fades as the probed width exceeds the typical correlation length. A recent correlograph study of such patterns (*22*) confirms this interpretation of inhomogeneity in a-Si.

Large models containing N atoms, and therefore $3N$ coordinate degrees of freedom, are underconstrained by electron diffraction data, which typically comprise about 400 experimental points after radial averaging. This underconstraint creates a broad solution space of homometric structures—those that will reproduce the diffraction intensity—even when models are additionally constrained by appropriate potentials for a-Si. The CRN itself is not a unique structure; there are many topologically equivalent arrangements. Thus, the solution space will be amply populated with similar CRN structures. However, CRN models are not the only viable structural arrangement consistent with diffraction data. The solution space is further confined when FEM data are added as constraints. When this is done, we find that CRN structures are excluded as solutions.

We recently applied an experimentally constrained structural relaxation (ECSR) computational procedure (*26*), closely similar to the ECMR method of Biswas *et al.* (*27*, *28*), to search for structural solutions for four different types of a-Si using electron diffraction data and FEM variance data (*26*). For each structural configuration, the ECSR algorithm evaluates a cost function that contains three terms: (i) the Tersoff potential, U, for the silicon model (*29*); (ii) the integrated square difference of the experimental and computed reduced electron diffraction intensities $\varphi(k)$ in the range $0 \leq k \leq 2.5$ Å^{-1}; and (iii) the integrated square difference of the experimental and computed FEM variance $V(k)$ in the range $0.12 \leq k < 1.0$ Å^{-1}. Variance calculations assume a probe size (resolution) of 10 Å. The x,y,z coordinates of a randomly selected atom are adjusted by a small random amount, and the cost function is reevaluated. The move is accepted or rejected via the Metropolis algorithm (*30*). The diffraction and variance costs were weighted relative to the Tersoff potential so that the typical changes in all three terms, arising from random atom moves, were approximately equal. Details of our experimental and

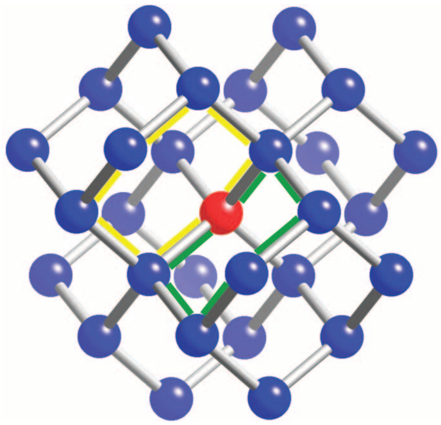

Fig. 2. The 29-atom local cluster for crystalline cubic silicon. The central atom (red) has four bonds and six possible intervertex angles. There are two six-membered rings spanning each intervertex angle (yellow and green paths), giving it a vertex symbol $6_2 \cdot 6_2 \cdot 6_2 \cdot 6_2 \cdot 6_2 \cdot 6_2$. This 9 Å diameter unit provides a convenient minimal topological description for a paracrystalline cluster. In real materials, strain may deform it from this idealization without altering the bonded topology. Local clusters for the CRN will contain some five-membered rings.

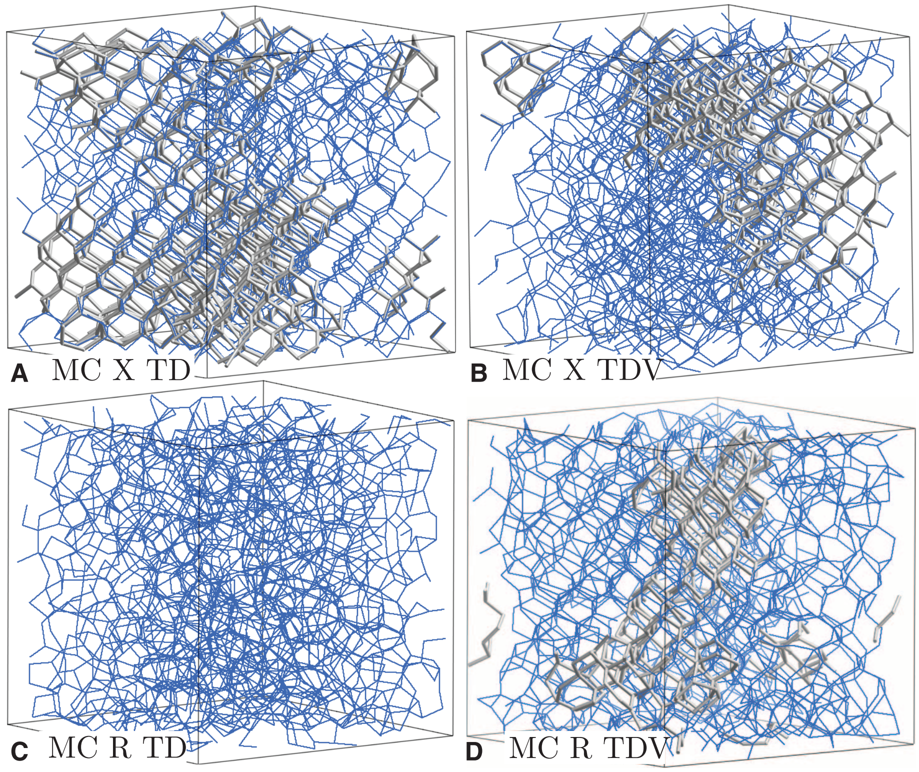

Fig. 3. (**A** to **D**) The four 1728-atom models, after structural relaxation, viewed as periodic networks. The atoms connected by gray bonds represent topologically cubic-Si regions. All four models give essentially identical *G*(*r*) plots (Fig. 1A).

computational methods are described elsewhere (*26*, *31*, *32*).

Results for an a-Si sample that was amorphized by implantation of high-energy Si ions are presented here. The experimental RDF, *G*(*r*), obtained from electron diffraction, is presented in Fig. 1A along with the simulated *G*(*r*) plots for four different ECSR runs. Both crystalline (X) and random (R) starting configurations were used. For each of these there were two runs: one with electron diffraction only as an experimental constraint (i.e., the variance weight was set to zero); the second with the experimental variance included. All four runs included the Tersoff potential. The notable feature of these five plots is that they are essentially identical. Yet, the structural topology of each model is substantially different, as revealed by the variance simulations for each model (Fig. 1B). For the two simulations that were not constrained by the variance (labeled "MC X TD" and "MC R TD"), the resulting variance plots are markedly different. For the crystalline starting configuration, strong variance peaks arise, indicating substantial inhomogeneity persisting in the final model. For the random starting configuration, the variance curve is essentially flat, indicating a homogeneous structure. It has a high density of three-membered rings, and so is appreciably different from an ideal CRN, which has mostly five-, six-, and seven-membered rings. Neither plot matches the variance data. The two plots for the models that were constrained by the variance data (labeled "MC X TDV" and "MC R TDV") match the experimental variance perfectly. Despite the dissimilarity of the starting structures, these two models are topologically similar. The model properties are summarized in Table 1.

Models that started from a crystalline configuration (X) have the lowest Tersoff energies *U* and retain the highest densities of six-membered rings, R_6. Conversely, the models that were seeded by a random, CRN-like structure have higher Tersoff energies, and substantially lower densities of six-membered and more three-membered rings, R_3. The average coordination numbers, N_C, were about the same for each model, ~3.6 for the crystal-seeded models and ~3.7 for the random-seeded models, assuming a maximum bond length of 2.7 Å. N_C rises to ~3.8 when estimated from the area under the first peak of *G*(*r*). A crude measure of latent crystalline coordination is obtained by examining the coordination sequences for each Si atom in the models. Cubic (and hexagonal) silicon has a coordination sequence that begins 1-4-12, out to the second shell. The parameter N_2 reports the number of Si atoms in the model that have this sequence. An atom with this sequence is not necessarily part of a topologically crystalline environment, but if it does not have this sequence, then it is clearly not in a topologically crystalline environment. A more reliable indicator of extensive crystalline topology, 10 Å and wider, is the atomic vertex symbol, which delineates a local cluster (*33*, *34*). This gives the size and number of rings at each of the six intervertex angles of a tetrahedrally coordinated silicon atom. Both cubic and hexagonal Si have vertex symbols $6_2 \cdot 6_2 \cdot 6_2 \cdot 6_2 \cdot 6_2 \cdot 6_2$, meaning that there are two distinct six-membered ring paths through each silicon atom and any two of its bonded neighbors. In crystalline cubic Si, there are 29 atoms involved in the local cluster that spans the vertex symbol, forming a unit that is ~9 Å in diameter (Fig. 2). The two models that were started as crystals both contain a substantial number of paracrystalline Si local clusters. In the table, N_p is the number of atoms that have the topologically cubic vertex symbol. Curiously, the model that was not constrained by the variance ("MC X TD") has approximately three times as much topological crystallinity as the variance-constrained model ("MC X TDV").

All four models are equally "diffraction amorphous." Both the "MC X TDV" (Fig. 3B) and the "MC R TDV" (Fig. 3D) models reproduce both the experimental *G*(*r*) and *V*(*k*) plots and converge to topologically similar structures. Because electron selected-area diffraction patterns are averaged over large areas, they show rotational homogeneity, whereas microdiffraction patterns show considerable spatial inhomogeneity. The inhomogeneous structures shown in Fig. 3, B and D, therefore appear to represent the real material better. The structure is not 100% ordered; only about 10 to 15% of the atoms must be associated with the topological ordering to reproduce the variance data. The remaining material is not topologically crystalline. Annealing reduces the amplitude of the variance peaks in this sample by about half, which reduces the extent of the paracrystalline ordering, but does not eliminate it (*26*).

An important difference between x-ray studies and FEM studies is the sample thickness. For FEM studies, the film should be less than about 300 Å, whereas in x-ray studies films can be substantially thicker, ~10 μm. As is true for all electron microscopy studies, structural artifacts at the film surfaces may affect results. Careful studies of a-Si samples in both plan view and cross-section view do not show any difference between surfaces and bulk. The thickness dependence of the variance signal from a-Si has been studied carefully, and it does not behave as a constant surface artifact (*21*, *35*). The FEM variance curves for a-Si have been consistently reproduced by several groups for a variety of a-Si samples prepared by different methods (*19*, *21*, *31*, *35*).

Amorphous silica, and some types of evaporated amorphous carbon, do show essentially flat variance curves that are consistent with a CRN (*36*, *37*). Recent evidence shows that ordered regions can persist in pressure- and temperature-amorphized silica glasses (*38*). Although the combination of the FEM variance data with the RDF data substantially narrows the available solution-space, the precise structural configuration of the inhomogeneity is still not established, although it appears most likely to be of paracrystalline type. More detailed models will require enhancements of the ECSR method as well as improved methods for modeling the scattering decoherence (related to inelastic scattering events), which affects the variance more strongly than the mean diffraction. Valuable additional information would be provided by application of variable-resolution FEM and correlograph analysis, where angular correlations in scattering are studied as a function of the probe size (*21*, *22*, *35*).

Because every a-Si sample studied by FEM to date, by several groups, shows distinctive variance peaks of the type associated with paracrystallinity, we conclude that they are all inhomogeneous at the 10 to 20 Å length scale, consistent with the paracrystallite model of Hosemann and Baggchi (*17*). Notwithstanding the RDF data, these samples do not agree with the ideal CRN model, which we conclude is a structural idealization that is not realized in practical a-Si thin films. Our conclusions regarding pervasive, heterogeneous, medium-range order in a-Si have implications for a wide variety of amorphous materials in general that have been studied by diffraction alone.

References and Notes

1. U. R. Pedersen, T. B. Schrøder, J. C. Dyre, P. Harrowell, *Phys. Rev. Lett.* **104**, 105701 (2010).
2. H. Tanaka, T. Kawasaki, H. Shintani, K. Watanabe, *Nat. Mater.* **9**, 324 (2010).
3. N. Jakse, A. Pasturel, *Appl. Phys. Lett.* **93**, 113104 (2008).
4. Y. Q. Cheng, H. W. Sheng, E. Ma, *Phys. Rev. B* **78**, 014207 (2008).
5. B.-S. Lee *et al.*, *Science* **326**, 980 (2009).
6. T. H. Lee, S. R. Elliott, *Phys. Rev. Lett.* **107**, 145702 (2011).
7. S. Pauly, S. Gorantla, G. Wang, U. Kühn, J. Eckert, *Nat. Mater.* **9**, 473 (2010).
8. W. H. Zachariasen, *J. Am. Chem. Soc.* **54**, 3841 (1932).
9. F. Wooten, K. Winer, D. Weaire, *Phys. Rev. Lett.* **54**, 1392 (1985).
10. G. T. Barkema, N. Mousseau, *Phys. Rev. B* **62**, 4985 (2000).
11. R. L. C. Vink, G. T. Barkema, W. F. van der Weg, N. Mousseau, *J. Non-Cryst. Solids* **282**, 248 (2001).
12. R. L. C. Vink, G. T. Barkema, M. A. Stijnman, R. H. Bisseling, *Phys. Rev. B* **64**, 245214 (2001).
13. K. Laaziri *et al.*, *Phys. Rev. B* **60**, 13520 (1999).
14. D. J. H. Cockayne, *Annu. Rev. Mater. Res.* **37**, 159 (2007).
15. R. L. C. Vink, G. T. Barkema, W. F. van der Weg, *Phys. Rev. B* **63**, 115210 (2001).
16. W. A. Kamitakahara, C. M. Soukoulis, H. R. Shanks, U. Buchenau, G. S. Grest, *Phys. Rev. B* **36**, 6539 (1987).
17. R. Hosemann, S. N. Baggchi, *Direct Analysis of Diffraction by Matter* (North-Holland, Amsterdam, 1962).
18. D. Turnbull, D. Polk, *J. Non-Cryst. Solids* **8-10**, 19 (1972).
19. M. M. J. Treacy, J. M. Gibson, P. J. Keblinski, *J. Non-Cryst. Solids* **231**, 99 (1998).
20. P. M. Voyles, J. E. Gerbi, M. M. J. Treacy, J. M. Gibson, J. R. Abelson, *Phys. Rev. Lett.* **86**, 5514 (2001).
21. S. N. Bogle, P. M. Voyles, S. V. Khare, J. R. Abelson, *J. Phys. Condens. Matter* **19**, 455204 (2007).
22. J. M. Gibson, M. M. J. Treacy, T. Sun, N. J. Zaluzec, *Phys. Rev. Lett.* **105**, 125504 (2010).
23. A. C. Wright, *Phys. Chem. Glasses Eur. J. Glass Sci. Technol. B* **49**, 103 (2008).
24. S. C. Moss, J. F. Graczyk, *Phys. Rev. Lett.* **23**, 1167 (1969).
25. P. Biswas, R. Atta-Fynn, D. A. Drabold, *Phys. Rev. B* **69**, 195207 (2004).
26. K. B. Borisenko *et al.*, *Acta Mater.* **60**, 359 (2012).
27. P. Biswas, D. Tafen, D. A. Drabold, *Phys. Rev. B* **71**, 054204 (2005).
28. J. Hwang, A. M. Clausen, H. Cao, P. M. Voyles, *J. Mater. Res.* **24**, 3121 (2009).
29. J. Tersoff, *Phys. Rev. B* **38**, 9902 (1988).
30. W. H. Press, S. A. Teukolsky, W. T. Vetterling, B. P. Flannery, *Numerical Recipes in C* (Cambridge Univ. Press, Cambridge, 1992).
31. B. Haberl *et al.*, *Phys. Rev. B* **79**, 155209 (2009).
32. See supporting material on *Science* Online.
33. C. S. Marians, L. W. Hobbs, *J. Non-Cryst. Solids* **124**, 242 (1990).
34. M. M. J. Treacy, P. M. Voyles, J. M. Gibson, *J. Non-Cryst. Solids* **266-269**, 150 (2000).
35. P. M. Voyles, D. A. Muller, *Ultramicroscopy* **93**, 147 (2002).
36. J. M. Gibson, J.-Y. Cheng, P. M. Voyles, M. M. J. Treacy, D. C. Jacobson, *Microstructural Processes in Irradiated Materials*, S. J. Zinkle, G. Lucas, R. Ewing, Eds. (Materials Research Society, Warrendale, PA, 1999), vol. 540, pp. 27–32.
37. G. Zhao, P. R. Buseck, A. Rougée, M. M. J. Treacy, *Ultramicroscopy* **109**, 177 (2009).
38. D. A. Keen, R. McGreevy, *Nature* **344**, 423 (1990).

Acknowledgments: M.M.J.T acknowledges support from the Leverhulme Trust and from the U.S. Department of Energy, Contract no. DE-PS02-09ER09-01. K.B.B. thanks the UK Engineering and Physical Sciences Research Council (grant EP/F048009/1) for support. We thank B. Haberl, J. S. Williams, J. E. Bradby, and A. C. Y. Liu for providing the data used in this report. The data used in this work have been presented previously in (*31*) and (*26*).

Supporting Online Material

www.sciencemag.org/cgi/content/full/335/6071/950/DC1
Materials and Methods
SOM Text
Tables S1 and S2
References (*39–44*)

3 October 2011; accepted 4 January 2012
10.1126/science.1214780

Satellite Estimates of Precipitation-Induced Dissipation in the Atmosphere

Olivier Pauluis[1,]* and Juliana Dias[2]

A substantial amount of frictional dissipation in the atmosphere occurs in the microphysical shear zones surrounding falling precipitation. The dissipation rate is computed here from recently available satellite retrieval from the Tropical Rainfall Measurement Missions and is found to average 1.8 watts per square meter between 30°S and 30°N. The geographical distribution of the precipitation-induced dissipation is closely tied to that of precipitation but also reveals a stronger dissipation rate for continental convection than for maritime convection. Because the precipitation-induced dissipation is of the same magnitude as the turbulent dissipation of the kinetic energy in the atmosphere, changes in the hydrological cycle could potentially have a direct impact on the amount of kinetic energy generated and dissipated by the atmospheric circulation.

Around each individual water droplet and ice crystal in the atmosphere, there is a microphysical flow that acts to slow down its fall. As a result, precipitation falls through the air at a terminal velocity determined by the balance between the gravitational acceleration and the aerodynamical drag exerted by the surrounding air. The effect of the drag is dramatic: The typical terminal velocity for a raindrop is about a few meters per second, which is two orders of magnitude smaller than the free-fall velocity it would attain in the absence of any drag force.

This drag also acts as damping mechanism that dissipates kinetic energy within the shear zones surrounding each individual hydrometeor (*1*). From a macroscopic perspective, a drag force $\mathbf{F}$ that acts on two different bodies moving at relative velocity $\mathbf{v_r}$ is associated with a net loss of mechanical energy equal to $\mathbf{F} \cdot \mathbf{v_r}$. For falling precipitation, the relative velocity is equal to the terminal velocity of the hydrometeors, v_T, where-

[1]Courant Institute of Mathematical Sciences, New York University, 251 Mercer Street, New York, NY 10012, USA. [2]Physical Sciences Division, Earth System Research Laboratory (ESRL)/National Oceanic and Atmospheric Administration (NOAA), Boulder, CO 80305, USA.

*To whom correspondence should be addressed. E-mail: pauluis@cims.nyu.edu

as the drag balances the gravitational acceleration on the droplets and is thus equal to $\rho q_p g$, with ρ the density of the air, q_p the specific humidity of the precipitation, and g the gravitational acceleration. The total amount of dissipation in an atmospheric column is given by the integral

$$D_P = \int_0^\infty g\rho q_p v_T dz \qquad (1)$$

The dissipation rate is thus equal to the rate at which precipitation water loses geopotential energy because of its downward velocity relative to the surrounding air.

The hydrological cycle has also a substantial impact on the maintenance of the atmospheric circulation. Because the atmosphere continuously exerts mechanical work in order to lift the water, which is then dissipated as precipitation falls, there is less kinetic energy available to sustain other atmospheric motions. The atmosphere as a whole can be viewed as acting as a heat engine that generates mechanical energy by transporting heat from the warm Earth's surface to the colder troposphere (*2*–*7*). The total work W generated by a heat engine can be written as

$$W = \eta Q \qquad (2)$$

with Q the thermal energy transported by atmospheric motions and η the mechanical efficiency. This mechanical efficiency of a heat engine is always smaller than the efficiency of a comparable Carnot cycle. For an average surface temperature of $T_{in} \approx 288$ K and emission temperature of $T_{out} = 255$ K, the corresponding Carnot efficiency is $[(T_{in} - T_{out})/(T_{in})]$, which is roughly equal to 0.1. For a typical value for atmospheric energy transport of $Q \approx 100$ W m^{-2}, the maximum work would thus be on the order of 10 W m^{-2}. However, because of its active hydrological cycle, the Earth's atmosphere does not behave like an idealized Carnot cycle. Rather, its mechanical efficiency is severely reduced because of the effect of diffusion of water vapor (*5*–*7*). Although the exact value of the mechanical efficiency for the atmospheric circulation is unknown, scaling arguments indicate that the atmospheric circulation might be about half as efficient as the corresponding Carnot cycle, that is, $\eta \sim 0.05$, so that the total mechanical work available to sustain all atmospheric motions would be on the order of $W \approx 5$ W m^{-2} (*8*, *9*).

Over long time scales, the amount of kinetic energy generated by atmospheric motions must be balanced by an equal amount of frictional dissipation, that is,

$$W = D_k + D_P \qquad (3)$$

Here, the dissipation is split between D_P, the precipitation-induced dissipation, and D_k, the dissipation of kinetic energy resulting from the turbulent energy cascade from the relevant scale of motion down to the Kolmogorov scale at which viscosity can act. Turbulent dissipation has received more attention than the precipitation-induced mechanism, and it is usually estimated to

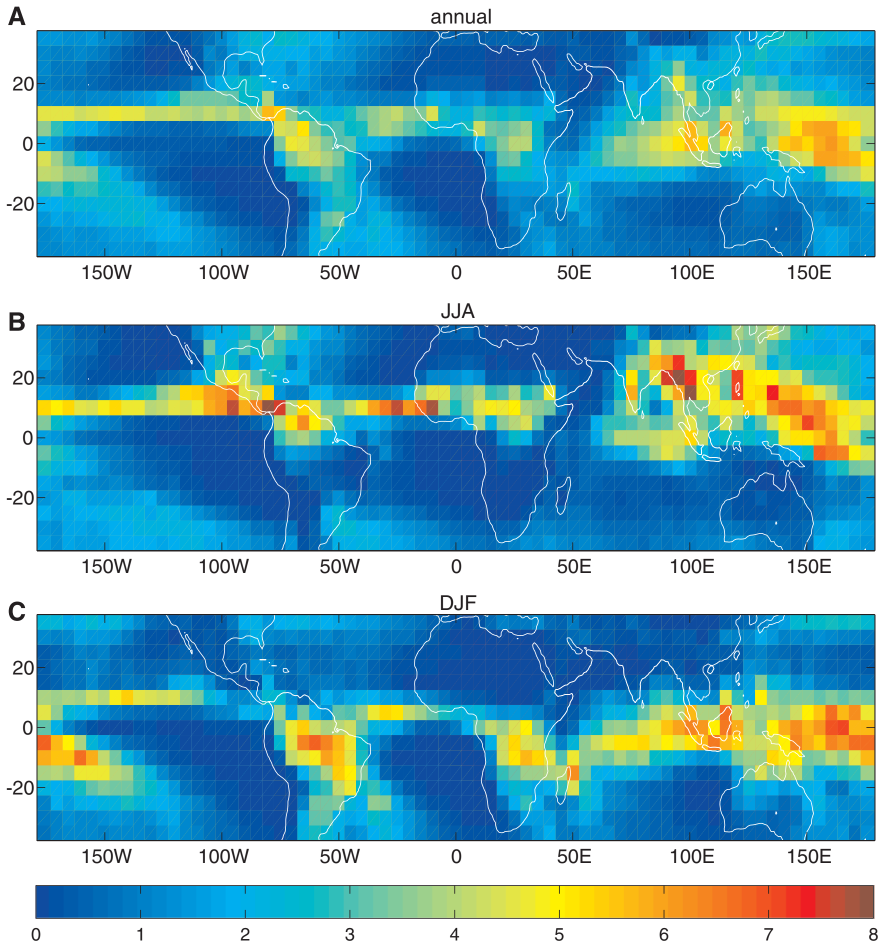

Fig. 1. Horizontal distribution of annual (**A**), JJA (**B**), and DJF (**C**) averages of D_P in W m^{-2}.

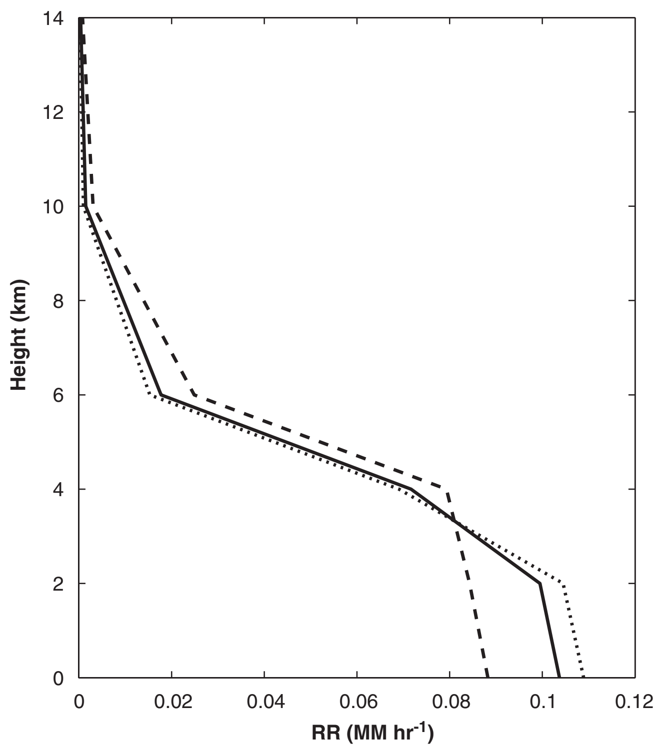

Fig. 2. Vertical profile of precipitation rate (RR) averaged in the tropics (solid), including only land (dashed) and only ocean (dotted).

be between 1 and 5 W m^{-2}, primarily on the basis of reanalysis data or general circulation models (*2*, *10*–*12*). The precipitation-induced dissipation D_P can be computed from the downward flux of precipitation water. Estimates based on both scaling arguments and numerical modeling (*1*, *6*) indicate that the averaged precipitation-induced dissipation in the tropics should be between 2 and 4 W m^{-2}. This indicates that the turbulent kinetic energy dissipation and the precipitation-induced dissipation are comparable, although the exact partitioning is unknown. The primary purpose of this paper is to obtain the precipitation-induced dissipation from statellite observations.

The data used in this study were derived from Tropical Rainfall Measuring Mission (TRMM) precipitation radar (PR) observations by the TRMM Science Data Information System, and the specific product we used is the 3A25. The 3A25 data set is an accumulation of the TRMM PR 2A25 retrieval algorithm, which uses backscattering radiation measurements from TRMM PR to obtain a vertical reflectivity profile. The precipitation rates are then recovered on the basis of the inversion technique by (*13*). The most unique characteristic of the TRMM PR is its capability to observe the three-dimensional structure of rain from space. Rain rates can be estimated at different heights because TRMM PR measures the intensity of backscattered energy from hydrometeors within fixed vertical layers. Although an improvement in the estimation of precipitation rate and latent heat release profiles over the globe is expected, TRMM PR is the most reliable precipitation data currently available on a global scale. We used 3A25 data to capture both the horizontal and seasonal characteristics of the distribution of kinetic energy dissipation resulting from precipitation. More specifically, the outputs we used include the monthly averaged precipitation rate from 1999 to 2007 on a grid of 5°-by-5° latitude-longitude, extending from 40°S to 40°N. There are six vertical levels: near the surface (i.e., the lowest level free from ground clutter) and at five fixed heights above the ellipsoid (2, 4, 6, 10, and 15 km).

The total amount of precipitation-related dissipation D_P is computed by using Eq. 1. A vertical integral is computed at each horizontal grid box, which yields an estimate for D_P in W m^{-2}. Figure 1 displays the time-averaged latitude-longitude plot of the precipitation-averaged dissipation D_P. The average dissipation rate around the globe and between 30°S to 30°N is D_P = 1.8 W m^{-2}. The dissipation rate increases to D_P = 2.5 W m^{-2}, when computing the average only between 15°S and 15°N, which is in good agreement with numerical simulations (*1*). The mean surface precipitation rate in the tropics in the TRMM data is 2.5 mm day^{-1}. There are a number of issues with the satellite retrieval that likely lead to underestimation of precipitation rates (*14*, *15*). In particular, the study by (*16*) shows evidence of an underestimation of about 25% of TRMM PR surface rain rate in comparison to rain gauge data from ocean buoys. Although detailed validations of the vertical structure of the rain rate are still lacking, the computed value for D_P is likely to underestimate the actual dissipation rate.

The geographical distribution of the dissipation is closely tied to the distribution of precipitation. In the annual mean (Fig. 1A), dissipation is large within the Intertropical Convergence Zone (ITCZ) over the Eastern Pacific and Atlantic Ocean as well as within the warm pool in the Western Pacific, where the average dissipation rate is D_P = 3.5 W m^{-2}. Above-average dissipation rates are also observed along the equatorial Indian Ocean, Southeast Asia, Amazon Basin, and Central Africa. During the northern summer (Fig. 1B), more dissipation occurs at about 10°N, over the coast of Africa and Caribbean regions, associated with the African easterly waves and tropical cyclones. Similarly, enhanced dissipation occurs during the southwestern Asian monsoons, where the dissipation rate peaks to $D_P \approx 10$ W m^{-2} in the period of June, July, and August (JJA). During the northern winter (Fig. 1C), enhanced precipitation-induced dissipation is found over the Subtropical Convergence Zone in both the South Pacific and the South Atlantic Oceans.

Although regions of high dissipation correspond to regions of high precipitation, the amount of dissipation is not simply proportional to the precipitation rate at the surface but depends on its vertical profile through the entire atmospheric column. Figure 2 displays the long-term mean vertical profile of the precipitation rate averaged from 40°S to 40°N, as well as the corresponding profiles over land and oceans. Precipitation over oceans (dotted line) is characterized by heavy rainfall rate in the lowest 4 km in comparison to over continents (dashed line). To disentangle the relationship between precipitation rate and dissipation, we introduce the precipitation scale height, H_P, defined as

$$H_P = \frac{D_P}{gP_{surf}} \qquad (4)$$

with P_{surf} the precipitation rate at the surface. Figure 3 shows that H_P is larger not only in

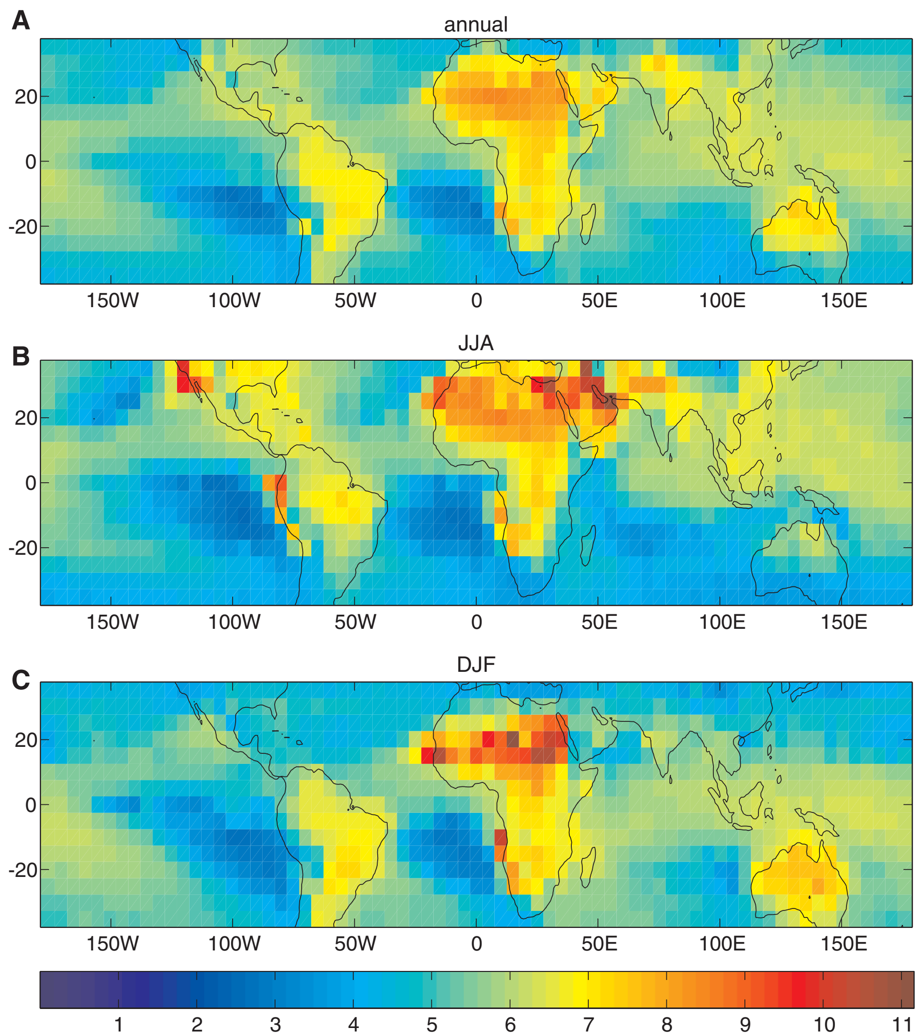

Fig. 3. Horizontal distribution of annual (**A**), JJA (**B**), and DJF (**C**) average precipitation scale-height H_P in km.

regions (such as Amazon Basin and Western Pacific) of enhanced D_P, but it is also larger over land, where it averages H_P = 6.9 km, than over the ocean, with H_P = 5.1 km. Both numbers fall within the range of H_P = 5 to 10 km estimated in (*1*) and are consistent with the fact that convective motions tend to be more intense over land over the ocean. In addition to the land-sea contrast, other geographic variations of H_P can be noted in Fig. 3, including high values over semiarid regions (Australia and Northern Africa) and over high-altitude regions (Himalaya and Andes). High values of H_P are also found over Southwest Mexico and Peru during JJA and over northern Africa during December, January, and February (DJF), corresponding to the dry season in these locations. These high values of H_P are associated with intermittent deep convection in an otherwise dry atmosphere. In such conditions, a large fraction of the precipitation reevaporates before reaching the ground. And although such reevaporating precipitation does not contribute to the rainfall at the surface, it does increase the amount of frictional dissipation within the atmospheric column, leading to higher value of the precipitation scale height in these regions. Conversely, the lowest H_P values occur along the eastern coast of South America and Africa, in regions characterized by shallow convection.

Our analysis of precipitation profiles from satellite measurements confirms that precipitation-induced dissipation is a major dissipative mechanism in Earth's atmosphere, with an average dissipation rate of 1.8 W m^{-2} for the tropical regions for the period of 1999 to 2007. Because it has been argued (*14*, *16*) that the TRMM PR instrument on which this study is based tends to underestimate the amount of precipitation, the actual value of the dissipation is likely to be somewhat larger than that reported here. Additional observations, either space-born or ground-based radars, could provide additional data to refine this estimate. Newly available retrievals from CloudSat Cloud Profiling Radar (*17*, *18*) should make it possible to extend the current analysis to include the extratropics. As Earth warms as a result of increased greenhouse gas concentration, both the amount of precipitation and the average height at which condensation occurs should increase. Both of these changes imply an increase in the precipitation-induced dissipation. A better understanding of the hydrological cycle and of the dissipation associated with it, in particular how these may be affected by natural or anthropogenic climate change, would provide new insights on how the intensity of the atmospheric circulation may vary.

References and Notes

1. O. Pauluis, V. Balaji, I. M. Held, *J. Atmos. Sci.* **57**, 989 (2000).
2. E. N. Lorenz, *The Nature and Theory of the General Circulation of the Atmosphere* (World Meteorological Organization, Geneva, 1967).
3. K. A. Emanuel, M. Bister, *J. Atmos. Sci.* **53**, 3276 (1996).
4. N. O. Rennó, A. P. Ingersoll, *J. Atmos. Sci.* **53**, 572 (1996).
5. R. Goody, *J. Atmos. Sci.* **60**, 2827 (2003).
6. O. Pauluis, I. M. Held, *J. Atmos. Sci.* **59**, 125 (2002).
7. O. Pauluis, *J. Atmos. Sci.* **68**, 91 (2011).
8. O. Pauluis, I. M. Held, *J. Atmos. Sci.* **59**, 140 (2002).
9. O. Pauluis, in *Non-Equilibrium Thermodynamics and the Production of Entropy*, A. Kleidon, R. D. Lorenz, Eds. (Springer-Verlag, Berlin, 2005), pp. 107–119.
10. J. P. Peixoto, A. H. Oort, M. de Almeida, A. Tomé, *J. Geophys. Res.* **96**, 10981 (1991).
11. J. P. Peixoto, A. H. Oort, *Physics of Climate* (American Institute of Physics, New York, 1992).
12. E. Becker, *Mon. Weather Rev.* **131**, 508 (2003).
13. T. Iguchi, T. Kozu, R. Meneghini, J. Awaka, A. K. Okamoto, *J. Appl. Meteorol.* **39**, 2038 (2000).
14. T. Bellerby, M. Todd, D. Kniveton, C. Kidd, *J. Appl. Meteorol.* **39**, 2115 (2000).
15. T. Iguchi *et al.*, *J. Meteorol. Soc. Jpn.* **87A**, 1 (2009).
16. K. P. Bowman, *J. Clim.* **18**, 178 (2005).
17. G. L. Stephens *et al.*, *Bull. Am. Meteorol. Soc.* **83**, 1771 (2002).
18. C. Mitrescu, T. L'Ecuyer, J. Haynes, S. Miller, J. Turk, *J. Appl. Meteorol. Climatol.* **49**, 991 (2010).

Acknowledgments: The TRMM 3A25 data were obtained from the TRMM Science Data and Information System (TSDIS) at Goddard Space Flight Center, NASA. The authors are thankful to A. Ackerman, A. Del Genio, G. Tselioudis, and A. Fridlind for their comments on a previous version of this manuscript. This work has been supported by NSF grants ATM-0545047 and AGS-0944058.

27 October 2011; accepted 25 January 2012
10.1126/science.1215869

Collapse of Classic Maya Civilization Related to Modest Reduction in Precipitation

Martín Medina-Elizalde and Eelco J. Rohling*

The disintegration of the Classic Maya civilization in the Yucatán Peninsula and Central America was a complex process that occurred over an approximately 200-year interval and involved a catastrophic depopulation of the region. Although it is well established that the civilization collapse coincided with widespread episodes of drought, their nature and severity remain enigmatic. We present a quantitative analysis that offers a coherent interpretation of four of the most detailed paleoclimate records of the event. We conclude that the droughts occurring during the disintegration of the Maya civilization represented up to a 40% reduction in annual precipitation, probably due to a reduction in summer season tropical storm frequency and intensity.

Ever since the discovery of the ancient Maya civilization, climate change has been invoked as a causal factor to explain its collapse centuries before the first arrival of Europeans on the American continent (*1*, *2*). It has since become well established that the disintegration of the Classic Maya Civilization was a complex process occurring from around 800 to 1000 A.D. [known as the Terminal Classic Period (TCP)] (*1*–*7*). Despite evidence suggesting that climate change does not fully explain the complex geographic and sociopolitical events of the TCP (*2*, *8*), paleoclimate records and archaeological evidence suggest that the TCP was punctuated by a series of drought events (*9*–*15*) that probably triggered significant societal disruptions at this time (*16*, *17*). Unfortunately, paleoclimate records have been interpreted largely in qualitative terms, and no coherent interpretative framework of these records exists. The TCP drought signals suggested by paleoclimate records are not far outside the amplitude of those preceding this time interval, when the Maya civilization flourished. Perhaps the magnitude of these droughts was rather modest despite the large associated environmental and societal disruptions.

Here we develop the first coherent, quantitative view of the four best-dated and best-resolved paleoclimate records from the Yucatán Peninsula (YP) (Figs. 1 and 2). We evaluate YP lake responses to perturbations to the seasonal precipitation cycle using a straightforward isotope mass balance model, for comparison with environmental patterns suggested by these records. This approach provides a single consistent interpretative framework for all records considered and thus for a quantitative cross-validation of the environmental signals.

The key YP paleoclimate records that we consider (Fig. 2) show similar environmental patterns over the TCP, which are near to synchronous within chronological uncertainties. The high-resolution U-Th–dated stalagmite (named Chaac after the Maya god of rain) $\delta^{18}O$ record represents variability in the annual mean $\delta^{18}O$ of precipitation and reveals a succession of extended drought periods interrupted by brief recoveries (*14*) (Fig. 2A). The Lake Chichancanab gastropod and Punta Laguna ostracod $\delta^{18}O$ records show

National Oceanography Centre, University of Southampton, Southampton, UK.

*Present address: Centro de Investigación Científica de Yucatán, UCIA, Cancún, México.

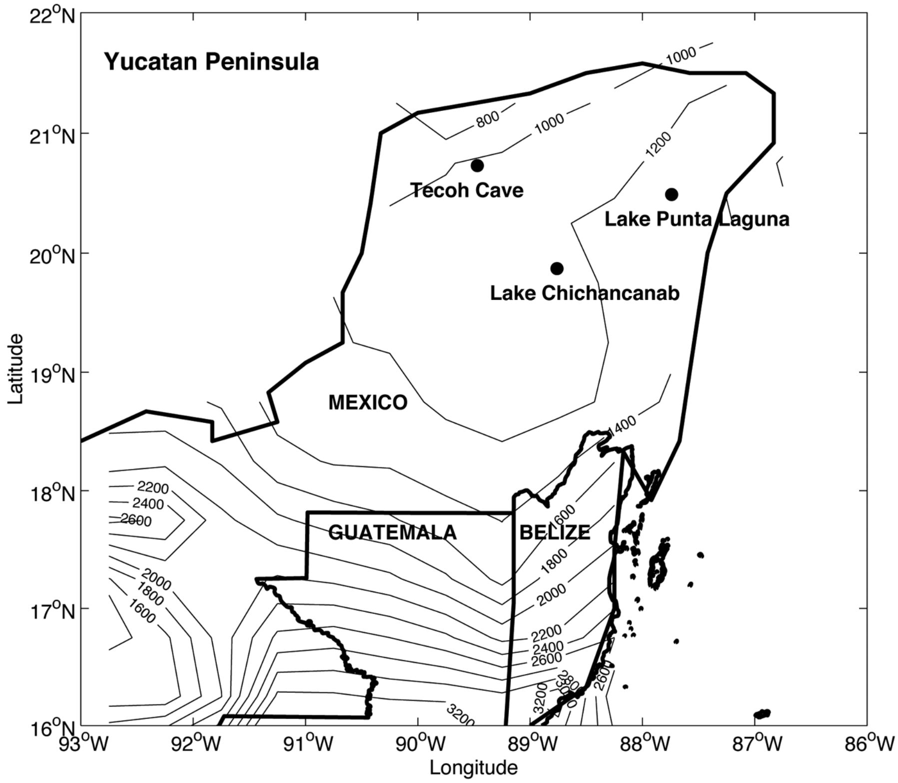

Fig. 1. Map of the YP, including the countries of México, Belize, and Guatemala. Contours represent total annual precipitation isolines (in millimeters per year). The locations of the stalagmite Chaac, the town of Tecoh (20°45′N, 89°28′W, 20 m above sea level); Lake Chichancanab (19°52′N, 88°46′W); and Lake Punta Laguna (20°38′N, 87°37′W, 18 m above sea level) are indicated (black circles).

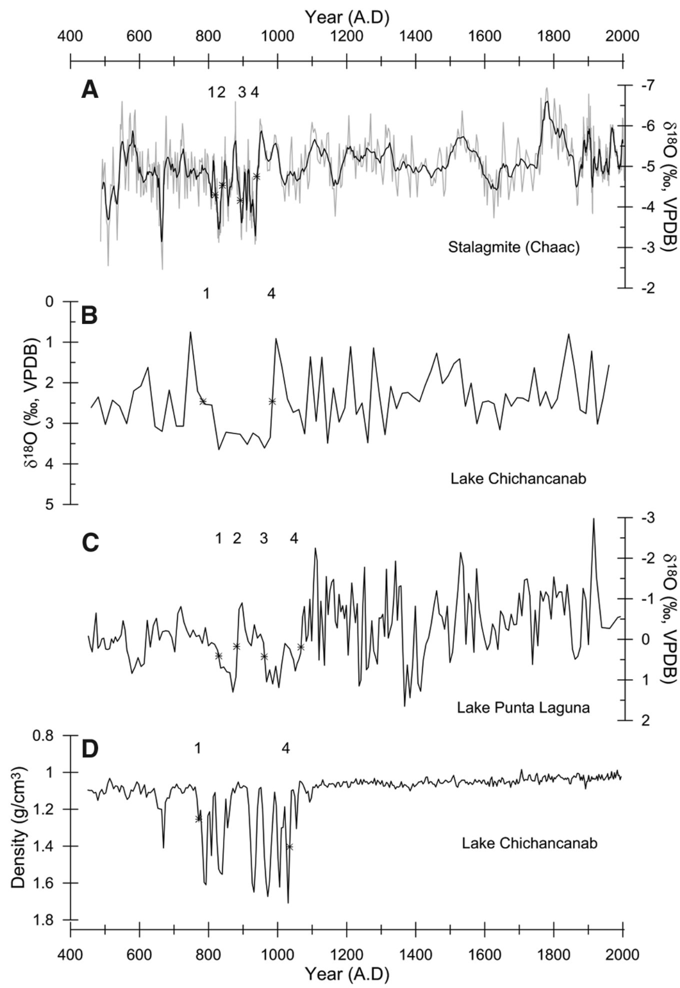

Fig. 2. YP climate records spanning the past 1500 years. (**A**) Stalagmite Chaac δ^{18}O record of changes in the δ^{18}O composition of rainfall (*14*). VPDB, Vienna Pee Dee belemnite standard. (**B**) Lake Chichancanab *Pyrgophorus coronatus* δ^{18}O record, reflecting changes in the evaporation/precipitation isotope balance (*9*). (**C**) Lake Punta Laguna ostracod *Cytheridella ilosvayi* δ^{18}O record, also reflecting this isotope balance (*10*). (**D**) Lake Chichancanab sediment density record, reflecting gypsum precipitation and lake drawdown (*15*). In (A) to (D), symbols and numbers (1 to 4) represent tiepoints used in graphic tuning of the lake records to the Chaac δ^{18}O record (*18*) (Fig. 3) The TCP isotopic anomalies do not significantly exceed those bounding the TCP, suggesting modest changes in the balance of evaporation and precipitation.

changes in the balance between the supply of light isotopes by precipitation and their removal by evaporation (*9*, *10*) (Fig. 2, B and C). Last, the Lake Chichancanab sediment density record (Fig. 2D) reflects gypsum supersaturation due to evaporative drawdown and concentration of the lake, which even today is at gypsum saturation (*15*). The Lake Chichancanab gastropod δ^{18}O record lacks resolution relative to all the other records, which explains why the brief drought recoveries inside the TCP are not visible (*10*, *14*) (Fig. 2).

The underlying processes driving the patterns and amplitudes of the YP environmental records during the TCP are evaluated with an isotope mass balance model set up for Lake Chichancanab (*18*). Our model successfully reproduces: (i) a steady modern annual mean lake level, with superimposed seasonal variability; (ii) mass-balanced isotope fluxes; and (iii) an equilibrium lake water δ^{18}O of 3.9 per mil (‰) that agrees with observed δ^{18}O values for Lake Chichancanab (*9*, *19*, *20*). Thus, our straightforward isotope model offers a realistic approximation for the assessment of lake sensitivity to perturbations of the precipitation cycle.

Modeled lake variability through the TCP needs to meet the following conditions indicated by the paleoclimate records shown in Fig. 2: (i) significant lake drawdown but not fully desiccated, as evidenced by the uninterrupted organic calcite sequences; and (ii) a total lake δ^{18}O amplitude fluctuation of ~ ±2.5‰. This platform is used to evaluate the implication for YP lake mass and isotope balance of two different scenarios of perturbation of the seasonal precipitation cycle and δ^{18}O of precipitation (δ_P). In these scenarios,

precipitation (P) is perturbed by a constant fraction for every month of the wet season, which we take to be the 5 months (June to October) during which P today exceeds 100 mm (*21*). Every time we impose a perturbation of P, we impose proportional changes in δ_P, in accordance with the amount effect relationship between modern P and δ_P values [$\delta_P/\Delta P = -0.0234$‰/mm; regression coefficient (R^2) = 0.80] (*18*).

The first scenario that we test is that the TCP droughts reflect a persistent summer season shift of the convective activity away from the YP (*13*). In this scenario, we reduce monthly summer precipitation to values where the mean summer precipitation becomes equal to the mean winter precipitation, which effectively means that the area is "locked" in a winter precipitation mode. Using the amount effect relationship, δ_P is then adjusted proportionally. As a result of such a perturbation of summer precipitation, Lake Chichancanab fully desiccates in 14 years, which is within the time span of the two longest TCP droughts (*14*) (Fig. 2A). This is in conflict with evidence of the continuous existence of Lakes Chichancanab and Punta Laguna throughout the TCP. Furthermore, modeled lake isotope values become extremely positive, in excess of 10‰, far exceeding recorded isotope anomalies (Fig. 2, B and C). Finally, this scenario would imply a mean isotope shift of 2.5‰ in the Chaac $\delta^{18}O$ record as opposed to the observed 1‰ (Fig. 2A).

In the second scenario, we use our isotope mass balance model to simulate the development of Lake Chichancanab as a function of weaker perturbations in summer precipitation (Fig. 3). We maintain the modern annual rainfall cycle but shift the summer precipitation amount and therefore mean summer season δ_P so that the annual mean δ_P changes in accordance to the interannual $\delta^{18}O$ precipitation anomalies reflected by Chaac (*18*) (Fig. 3A). Modeled annual mean lake $\delta^{18}O$ anomalies that result from these changes in P and δ_P are in close agreement with observations from Lake Chichancanab and especially Lake Punta Laguna, thus validating the imposed precipitation shifts (*18*) (Fig. 3, B and C).

Calculated summer precipitation reductions associated with the Chaac $\delta^{18}O$ anomalies range from 30 to 50%, which equate to annual mean P reductions of 25 to 40% (*18*) (Fig. 3A). Modeled Lake Chichancanab water level is reduced by 30% during the two longest and most severe droughts centered at 830 and 928 C.E. (*14*) (Fig. 3C). Given that the lake today is close to gypsum saturation already (*15*), these water level reductions are consistent with supersaturation and precipitation of gypsum, in agreement with the Lake Chichancanab density record (*15*) (Fig. 3C). The equal magnitude of all gypsum precipitation events during the TCP contrasts with more subtle variations in modeled lake depth, although the timing of these events is very similar between the two records. We thus infer that gypsum precipitation represents a nonlinear threshold response to lake level (Fig. 3D).

We find that available paleoclimate records support a coherent and consistent interpretation of considerable reductions in precipitation during the TCP, but not as severe as would be implied by previously proposed mechanisms (*13*). If these repeated episodes of drier climate had a significant role in the fate of the Classic Maya civilization, as suggested by archaeological evidence (*16*, *17*), then this would imply that the ecological carrying capacity of the YP is highly sensitive to precipitation reductions. Indeed, such sensitivity to relatively minor changes in precipitation would agree with observations that variations in interannual precipitation today, mainly associated with the frequencies of tropical storms and depressions, significantly affect the groundwater table in the YP (*20*). Our estimated TCP rainfall reductions are within the range of rainfall deficits over the YP as projected by climate models for the end of this century (*22*, *23*).

Finally, we note that the TCP drought episodes are predominantly characterized by the absence of light (summer) isotope values (*14*). Today, the lightest isotope excursions are associated with the large precipitation fluxes of tropical storms and hurricanes (*20*, *24*, *25*), and the region depends on tropical depressions, storms, and hurricanes to maintain a positive net water balance and avoid desiccation (*24*, *26*, *27*). We suggest, therefore, that the droughts associated with the disintegration of the Maya civilization may have been triggered by a reduced frequency and intensity of cyclones over the YP. The inferred P reductions during the TCP are within the range associated with one to three tropical storms (*26*, *28*, *29*). Our interpretation of the TCP droughts may be validated by future research focused on detailed dating of storm deposits around the Yucatán and/or monthly resolved paleotempest records [such as those from speleothems (*25*)].

The modest reductions in precipitation associated with the end of the Classic Maya civilization highlight the critical sensitivity of the ecological carrying capacity of the YP to even small shifts in the region's hydrological budget, such as those projected for the near future (*22*, *23*). This study shows that it is possible to reconstruct the geographical pattern of precipitation evolution in México and Central America by increasing the coverage of stalagmite and lake records. Given the now apparent temporal complexity in the record of precipitation change (*14*) (Fig. 3A), we expect spatial complexities also.

This study advances the debate from one centered around qualitative interpretations of intense droughts to one around quantitative estimations

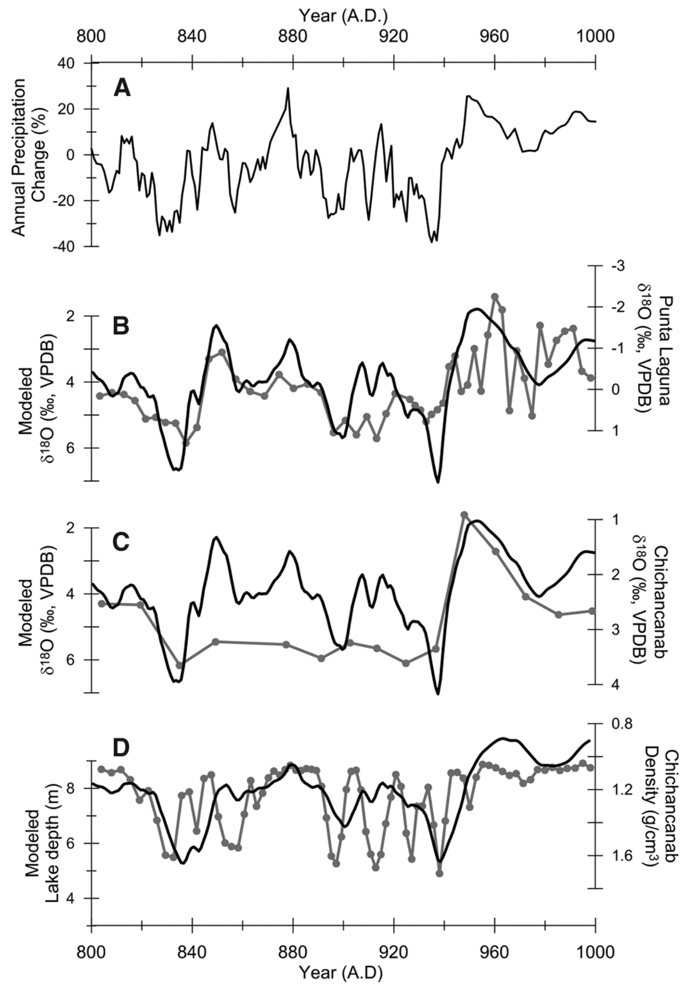

Fig. 3. (**A**) TCP annual precipitation percent changes, reflecting Chaac $\delta^{18}O$ anomalies, used in the isotope mass balance model for Lake Chichancanab. (**B** and **C**) Comparison of lake $\delta^{18}O$ evolutions during the TCP suggested by modeled (black) and paleoclimate (gray line with symbols) records, from Lake Chichancanab (B) and Punta Laguna (C). (**D**) Comparison between modeled lake level (black) and Lake Chichancanab sediment density record (gray with symbols), reflecting gypsum precipitation and lake drawdown. The lake paleoclimate records were graphically tuned to the stalagmite Chaac $\delta^{18}O$ record (*18*). Tuning tiepoints are shown in Fig. 2.

that support the scenario of drought of subtle variability with high impact. In addition, the data and modeling support an interpretation of decreased rainfall during the summer, associated with a reduction in the severity and frequency of tropical storms. This study suggests that there is substantial potential for establishing a relationship between the actual climatic variability over the region and the spatially complex historical events (*30*) that shaped the demise of the Maya civilization.

References and Notes

1. L. Schele, M. E. Miller, in *The Blood of Kings: Dynasty and Ritual in Maya Art*, G. I. Braziller, Ed. (George Braziller, New York, and Kimbell Art Museum, Fort Worth, TX, 1986), p. 335.
2. A. A. Demarest, P. M. Rice, D. S. Rice, in *The Terminal Classic in the Maya Lowlands: Collapse, Termination, and Transformation*, A. A. Demarest, P. M. Rice, D. S. Rice, Eds. (Univ. Press of Colorado, Boulder, CO, 2004), pp. 1–11.
3. T. P. Culbert, in *Precolumbian Population History in the Maya Lowlands*, T. P. Culbert, D. S. Rice, Eds. (Univ. of New Mexico Press, Albuquerque, NM, 1990), p. 395.
4. W. J. Folan, *Información Universidad Autónoma Ciudad de México (UACM)* **13**, 122 (1988).
5. B. L. Turner, in *Population Reconstruction for the Central Maya Lowlands: 1000 B.C. to A.D. 1500*, T. P. Culbert, D. S. Rice, Eds. (Univ. of New Mexico Press, Albuquerque, NM, 1990), pp. 301–324.
6. T. P. Culbert, L. J. Kosakowsky, R. E. Fry, W. A. Haviland, in *Precolumbian Population History in the Maya Lowlands*, T. P. Culbert, D. S. Rice, Eds. (Univ. of New Mexico Press, Albuquerque, NM, 1990), pp. 103–121.
7. P. A. Andrews, E. W. Andrews, F. R. Castellanos, *Ancient Mesoam.* **14**, 151 (2003).
8. J. Aimers, D. A. Hodell, *Nature* **479**, 44 (2011).
9. D. A. Hodell, J. H. Curtis, M. Brenner, *Nature* **375**, 391 (1995).
10. J. H. Curtis, D. A. Hodell, M. Brenner, *Quat. Res.* **46**, 37 (1996).
11. J. H. Curtis *et al.*, *J. Paleolimnol.* **19**, 139 (1998).
12. M. F. Rosenmeier, D. A. Hodell, M. Brenner, J. H. Curtis, T. P. Guilderson, *Quat. Res.* **57**, 183 (2002).
13. G. H. Haug *et al.*, *Science* **299**, 1731 (2003).
14. M. Medina-Elizalde *et al.*, *Earth Planet. Sci. Lett.* **298**, 255 (2010).
15. D. A. Hodell, M. Brenner, J. H. Curtis, *Quat. Sci. Rev.* **24**, 1413 (2005).
16. G. E. Braswell *et al.*, in *The Terminal Classic in the Maya Lowlands: Collapse, Transition, and Transformation*, A. A. Demarest, P. M. Rice, D. S. Rice, Eds. (Univ. Press of Colorado, Boulder, CO, 2004), pp. 162–194.
17. K. Carmean, N. Dunning, J. K. Kowalski, in *The Terminal Classic in the Maya Lowlands: Collapse, Transition, and Transformation*, A. A. Demarest, P. M. Rice, D. S. Rice, Eds. (Univ. Press of Colorado, Boulder, CO, 2004), pp. 424–449.
18. Materials and methods are available as supporting material on *Science* Online.
19. A. Covich, M. Stuiver, *Limnol. Oceanogr.* **19**, 683 (1974).
20. E. Perry, G. Velazquez-Oliman, A. R. Socki, *Hydrogeology of the Yucatán Peninsula*, 21st Symposium on Plant Biology, Arturo Gomez Pompa, Scott Fedick, Eds. (Haworth Press, Binghamton, NY, 2003), pp. 115–138.
21. CONAGUA, Servicio meteorológico nacional, México; available at http://smn.cna.gob.mx/ (2011).
22. J. H. Christensen *et al.*, *Regional Climate Projections. Climate Change 2007: The Physical Science Basis* (Cambridge Univ. Press, Cambridge, 2007).
23. A. V. Karmalkar, R. S. Bradley, H. F. Diaz, *Clim. Dyn.* **37**, 605 (2011).
24. R. J. Lawrence, D. S. Gedzelman, *Geophys. Res. Lett.* **23**, 527 (1996).
25. A. B. Frappier, D. Sahagian, S. J. Carpenter, L. A. Gonzalez, B. R. Frappier, *Geology* **35**, 111 (2007).
26. W. K. Michener, E. R. Blood, K. L. Bildstein, M. M. Brinson, L. R. Gardener, *Agric. Appl.* **7**, 770 (1997).
27. H. Jiang, E. J. Zipser, *J. Clim.* **23**, 1526 (2010).
28. F. N. Scatena, M. C. Larsen, *Biotropica* **23**, 317 (1991).
29. NOAA, National Weather Service/National Hurricane Center; available at: www.nhc.noaa.gov/ (2011).
30. R. B. Gill, *The Great Maya Droughts: Water, Life, and Death* (Univ. of New Mexico Press, Albuquerque, NM, 2000).

Acknowledgments: This paper contributes to UK Natural Environment Research Council projects NE/C003152/1, NE/I009906/1, and NE/H004424/1. We thank two anonymous reviewers for their valuable comments and suggestions.

Supporting Online Material

www.sciencemag.org/cgi/content/full/335/6071/956/DC1
Materials and Methods
SOM Text
Table S1
References (*31*–*34*)

14 November 2011; accepted 23 January 2012
10.1126/science.1216629

Evolution of the Earliest Horses Driven by Climate Change in the Paleocene-Eocene Thermal Maximum

Ross Secord,[1,2]* Jonathan I. Bloch,[2] Stephen G. B. Chester,[3] Doug M. Boyer,[4] Aaron R. Wood,[5,2] Scott L. Wing,[6] Mary J. Kraus,[7] Francesca A. McInerney,[8] John Krigbaum[9]

Body size plays a critical role in mammalian ecology and physiology. Previous research has shown that many mammals became smaller during the Paleocene-Eocene Thermal Maximum (PETM), but the timing and magnitude of that change relative to climate change have been unclear. A high-resolution record of continental climate and equid body size change shows a directional size decrease of ~30% over the first ~130,000 years of the PETM, followed by a ~76% increase in the recovery phase of the PETM. These size changes are negatively correlated with temperature inferred from oxygen isotopes in mammal teeth and were probably driven by shifts in temperature and possibly high atmospheric CO_2 concentrations. These findings could be important for understanding mammalian evolutionary responses to future global warming.

Interest in how organisms respond to climate change has intensified in recent years with projected warming of ~2° to 4°C over the next century (*1*). Although models can be developed to predict evolutionary responses to warming of this magnitude, empirical examples must be drawn from fossil or historical records. Here we report a dramatic example of shifts in body size in the earliest known horses (family Equidae) during the Paleocene-Eocene Thermal Maximum (PETM) (~56 million years ago). The PETM is recognized in marine and continental records by an abrupt negative carbon isotope excursion (CIE) that lasted ~175 thousand years (ky), caused by the release of thousands of gigatons of carbon to the ocean-atmosphere system (*2*, *3*). Some marine records suggest that although $\delta^{13}C$ values shifted rapidly at the onset of the CIE in 21 ky or less (*2*), temperature increase was slower, peaking 60 ky or more into the CIE (*4*) at ~5° to 10°C above pre-CIE levels (*5*, *6*). We use oxygen isotope values in mammal teeth as a proxy for local temperature change in the continental interior of North America, and we show that equid body size during the PETM was negatively correlated with temperature.

In extant mammals and birds (endotherms), closely related species or populations within a species are generally smaller-bodied at lower latitudes, where ambient temperature is greater (*7*). This relationship, known as Bergmann's rule, is followed by ~65 to 75% of studied extant mammals (*8*, *9*). The cause of Bergmann's rule is usually attributed to thermoregulation and the optimization of body size (*10*) and/or the availability of food resources related to primary productivity (*11*). Bergmann's rule predicts that average mammalian body size should decrease with warming climate, and smaller size in endotherms has even been suggested as a third "universal" response to warming, along with changes in phenology and species distribution (*10*). Declining body size has been attributed to warming over decadal and millennial scales in some living endotherms (*12*, *13*), but many counterexamples also exist (*10*). Furthermore, it is difficult to distinguish natural selection (genetic change) from ecophenotypic plasticity (morphological response

[1]Department of Earth and Atmospheric Sciences, University of Nebraska, Lincoln, NE 68588, USA. [2]Florida Museum of Natural History, University of Florida, Gainesville, FL 32611–7800, USA. [3]Department of Anthropology, Yale University, New Haven, CT, 06520, USA. [4]Department of Anthropology and Archaeology, Brooklyn College, City University of New York, New York, NY 11210, USA. [5]Department of Geology and Geological Engineering, South Dakota School of Mines and Technology, Rapid City, SD 57701, USA. [6]Department of Paleobiology, Smithsonian Museum of Natural History, Washington, DC 20560, USA. [7]Department of Geological Sciences, University of Colorado, Boulder, CO 80309, USA. [8]Department of Earth and Planetary Sciences, Northwestern University, Evanston, IL 60208, USA. [9]Department of Anthropology, University of Florida, Gainesville, FL 32611–7305, USA.

*To whom correspondence should be addressed. E-mail: rsecord2@unl.edu

not genetically fixed) over such short time scales. The size change documented here was, however, sustained over thousands of generations, strongly suggesting that natural selection was the cause.

Previous studies lacked the stratigraphic resolution to recognize patterns in body size change within the PETM but demonstrated gross changes in size in several mammal lineages, based on first molar tooth area (*14*, *15*). Size changes occurred in herbivorous ungulates (Perissodactyla, Artiodactyla, Condylarthra, and Tillodontia), Primates, and faunivores and omnivores (Creodonta, Carnivoramorpha, and Palaeanodonta), affecting both immigrant and endemic taxa (Fig. 1). These changes conform well to Bergmann's rule in terms of the expected direction of size change. Quantifying published results, size reduction occurred in 10 Paleocene genera that ranged into the PETM, representing 38% of the range-through genera. This was followed by post-PETM size increases in eight of these genera, indicating that body size response was strongly taxon-specific (Fig. 1 and table S7). Post-PETM size increases also occurred in an additional eight genera, seven of which first appeared in the PETM (Fig. 1). Together these 16 genera represent a size increase in 40% of PETM genera that ranged into post-PETM biozone Wa-1 (Fig. 2).

Sifrhippus [formerly *Hyracotherium* (*16*)] first appeared in North America and Europe during the PETM. Because of the lack of a plausible ancestor on these continents, it is widely thought to be an immigrant that crossed high-latitude dispersal routes opened by PETM warming (*17*). We use *Sifrhippus* to document mammalian body size change within the PETM. *Sifrhippus* is the most abundantly represented genus in new collections from the Cabin Fork area (~10 km^2) of the southern Bighorn Basin, Wyoming, and the only one for which detailed stratigraphic and quantitative morphological data are available. We also isotopically sampled *Sifrhippus*, *Coryphodon* (Pantodonta; large archaic herbivorous ungulates), and *Ectocion* and *Copecion* (phenacodontid condylarths; herbivorous ungulates of uncertain affinities). The PETM at Cabin Fork is represented by a ~35-m-thick sequence of fluvial mudstones, floodplain soils (paleosols), and fluvial sandstones. We constructed an age model that assumes varying rates of sediment accumulation: Avulsion deposits (mudstones and thin sandstones) represent fast rates, and paleosols represent much slower rates [see the supporting online material (SOM)]. Local sections were correlated to a composite section (Fig. 2) using marker beds traced with a differential Global Positioning System unit (SOM).

The CIE at Cabin Fork is recorded in the carbonate component of mammalian tooth enamel ($\delta^{13}C_E$) (Fig. 2, A and B) and in bulk organics and leaf wax *n*-alkanes (*6*, *18*). $\delta^{13}C_E$ in mammalian herbivores reflects the $\delta^{13}C$ value of the vegetation they consume, with predictable enrichment (*19*). Plants in turn track the $\delta^{13}C$ value of atmospheric CO_2, with influences from environmental factors such as humidity and vegetation density (*20*, *21*). At Cabin Fork, phenacodontids (*Ectocion* and *Copecion*) record a negative shift of ~4.6 per mil (‰) in $\delta^{13}C_E$ at the onset of the CIE (Fig. 2A). This is consistent with estimates of atmospheric change of ~4.6‰ during the PETM from a leaf discrimination model (*20*) and ~4.0‰ from modeling of marine carbonate dissolution (*2*), indicating that phenacodontid $\delta^{13}C_E$ is primarily tracking atmospheric $\delta^{13}C$ values, rather than environmental change.

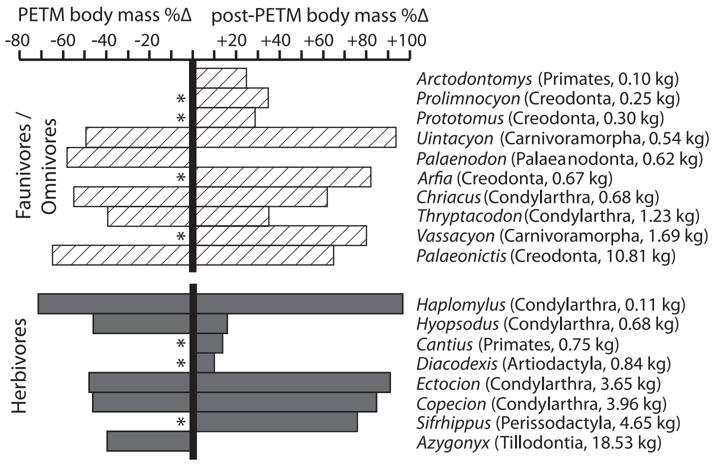

Fig. 1. Summary of percent mean body size change in genera that exhibit change from the latest Paleocene to the PETM (left), and from the PETM to the post-PETM (right). No genus exhibits a size increase in the PETM or a decrease after the PETM. Compiled from published sources, except for *Sifrhippus* from this study. Asterisks indicate genera that first appear in the PETM. See table S7 for a summary of all PETM taxa and sources.

Sifrhippus sandrae first appears at Cabin Fork near the base of the lowest intermittent red bed (LIRB) at 14.5 m (Fig. 2). The onset of the CIE in most mammal teeth also begins at the base of the LIRB (Fig. 2, A and B) but is recorded slightly lower (13.75 m) in dispersed bulk organics. The oldest specimens of *S. sandrae* had an average body size of ~5.6 kg, based on first lower molar area (SOM). Body size in *S. sandrae* progressively decreased from its first appearance at 14.5 m to the 41-m level, with a total reduction of ~30% over ~130 ky ($P < 0.001$) (Fig. 2D and SOM). Individuals at 41 m had an average body weight of ~3.9 kg and are among the smallest known horses. The dwarfing of *S. sandrae* was followed by a ~76% increase in body size during the recovery phase of the CIE, to an average size of ~7.0 kg (Fig. 2D).

The mode of evolution (random, static, or directional) for *Sifrhippus* body size change was determined using a moving window log rate interval (mwLRI) analysis, which is a modification of the standard LRI analysis (*22*) (SOM). Both methods assume that rates of change in a time series variable are inversely proportional to the interval of time over which rates are measured, because of the occurrence of small reversals in the variable. The relationship between rates of change and the lengths of intervals over which they are observed is used to determine evolutionary mode (*22*). Our mwLRI results indicate with 95% confidence that *Sifrhippus* body size directionally decreased from its first appearance to the 41-m level, after which stratigraphic resolution and sample sizes are insufficient to distinguish between directional and random evolutionary change. Thus, *Sifrhippus* experienced sustained selection for diminutive body size for ~130 ky.

To test whether body size change in *Sifrhippus* is significantly correlated with temperature, as predicted by Bergmann's rule, we used $\delta^{18}O$ values in *Coryphodon* enamel ($\delta^{18}O_E$) as a proxy for change in mean annual temperature (MAT). *Coryphodon* was a large water-dependent or semiaquatic mammal (*21*, *23*). Studies of ecologically similar living mammals have shown that their $\delta^{18}O_E$ faithfully records the $\delta^{18}O$ of surface water (*24*, *25*), which in turn is strongly correlated with air temperature at mid- to high latitudes (*26*). *Sifrhippus* first lower molar area is negatively correlated with *Coryphodon* $\delta^{18}O_E$ values ($P \leq 0.05$, SOM), suggesting that *Sifrhippus* body size decreased as ambient air temperature increased.

Greater aridity in the PETM could also have contributed to diminished body size by lowering primary productivity. Both floras and paleosols in the Bighorn Basin suggest increased aridity during at least parts of the PETM (*6*, *20*, *27*). To test this, we used two aridity proxies. The first is based on the difference between mean $\delta^{18}O_E$ values in aridity-sensitive and aridity-insensitive mammals (*24*). *Coryphodon* should be aridity-insensitive because of its probable water dependence (*21*, *23*), whereas *Sifrhippus* is the taxon most likely to be aridity-sensitive, because it has the highest average mammalian $\delta^{18}O_E$ value, suggesting that it consumed leaves in open areas where leaf water was evaporatively ^{18}O-enriched. Increased aridity should result in higher *Sifrhippus* $\delta^{18}O_E$ values and greater separation between it and *Coryphodon* $\delta^{18}O_E$ (Fig. 3A). Our second aridity proxy estimates mean annual precipitation (MAP) based on paleosol major oxides (Fig. 3C and SOM).

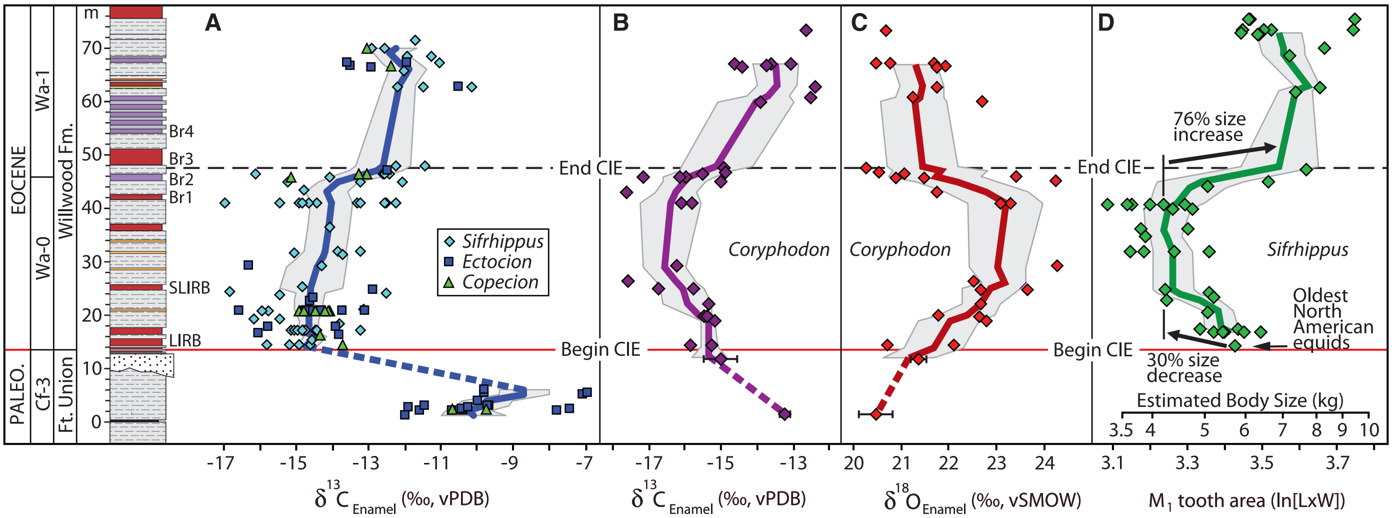

Fig. 2. Comparison of PETM Cabin Fork records. (**A**) From left to right, epochs, mammalian biozones, formations, meter levels, marker beds, and $\delta^{13}C_E$ values for three common mammal genera. vPDB, Vienna Pee Dee belemnite standard. (**B** and **C**) $\delta^{13}C_E$ and $\delta^{18}O_E$ values for *Coryphodon*. vSMOW, Vienna standard mean ocean water standard. (**D**) Log-transformed measurements of first lower molar area (length × width) for *Sifrhippus*. Data points represent single individuals except where error bars (indicating 95% confidence of the mean for multiple samples from one individual) are shown. Solid colored lines show five-point moving averages; the gray area is the 95% envelope of uncertainty for each line. PALEO, Paleocene; Cf, Clarkforkian; Wa, Wasatchian. LIRB, SLIRB, and Br denote key marker beds.

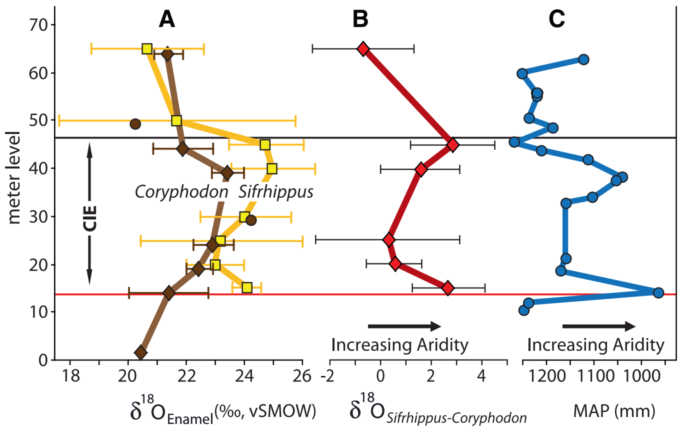

Fig. 3. Aridity and precipitation proxies. (**A**) Comparison of mean $\delta^{18}O_E$ values for aridity-insensitive *Coryphodon* (brown diamonds) and aridity-sensitive *Sifrhippus* (gold squares). Data are in 5-m bins. Brown circles are singletons of *Coryphodon*. (**B**) Aridity proxy curve based on (A), showing mean differences between *Sifrhippus* and *Coryphodon* $\delta^{18}O_E$. Greater difference implies greater aridity. Error bars show 95% confidence of the mean, offset in (A) by 1 m to avoid overlap. (**C**) MAP proxy based on paleosol major oxides from a nearby correlative section (HW16 section, SOM).

Both proxies suggest drier conditions at the beginning of the CIE, followed by wetter conditions starting at ~20 m (~68 ky into the PETM), with a return to drier conditions by ~38 m (~108 ky into the PETM). Overall, there is poor agreement between *Sifrhippus* body size change and the aridity proxies. Both proxies indicate a shift to wetter conditions while body size in *Sifrhippus* is decreasing, which is counter to expectations if the primary cause of dwarfing was lowered productivity caused by increased aridity.

Our results are consistent with mammalian dwarfing driven by warming, but temperature alone may be an insufficient explanation. Although body mass in living mammals is highly correlated with MAT in the Nearctic [coefficient of determination (R^2) = –0.75], this relationship weakens above ~11°C and reverses at higher temperatures in the Neotropics (*9*). MAT was well above ~11°C in the latest Paleocene and PETM of the Bighorn Basin (*6*). Furthermore, ~25 to 35% of living mammals deviate from Bergmann's rule (*8*, *9*), and it is likely that at least some mammal lineages would have gotten larger during the PETM if MAT were the only controlling factor.

Another possible cause for body size decrease in the PETM is elevated atmospheric partial pressure of CO_2 (P_{CO_2}) (*28*), which might covary with temperature. In many extant plants, elevated CO_2 increases biomass but reduces nitrogen and protein content in leaves and can elevate phenol levels, yielding cellulose-rich vegetation that is less nutritious and harder for herbivores to digest (*29*). Ultimately, this should result in slower growth and reproductive rates in herbivorous mammals (*30*), conceivably resulting in selection for smaller body size. Although this mechanism could have reduced body size in herbivores, size also decreased among PETM carnivores (Fig. 1), which must be explained by an indirect response, such as selection for smaller predators because of smaller prey (*31*). Recent modeling of rates of carbon release during the PETM shows the largest increase in P_{CO_2} at the onset of the CIE, followed by lower concentrations later in the event (*2*). This is inconsistent with a P_{CO_2}-driven decrease in body size, because *Sifrhippus* was smallest near the end of the main phase of the PETM. Although elevated P_{CO_2} could have been a contributing factor, our results favor temperature as the primary driver of dwarfing in *Sifrhippus*.

PETM warming was similar in magnitude to that predicted by some global models over the next century (*1*) but occurred at a much slower rate and began from a warmer late Paleocene baseline. Nevertheless, some generalizations applicable to future warming may still be relevant. Diminished body size in some mammal species, along with changes in ecology and physiology, might be expected in response to warming. The pattern of dwarfing seen in the PETM mirrors recent reductions in body size in endotherms that have been attributed to anthropogenic warming (*10*, *12*). Although the rate of present warming is much faster than during the PETM, and mammals may not respond in exactly the same manner, the dramatic response to warming observed in PETM equids provides a measure of possible responses to future warming in modern mammals.

References and Notes

1. Intergovernmental Panel on Climate Change (IPCC), *Climate Change 2007 Synthesis Report* (IPCC, Geneva, 2007).
2. Y. Cui *et al.*, *Nat. Geosci.* **4**, 481 (2011).
3. F. A. McInerney, S. L. Wing, *Annu. Rev. Earth Planet. Sci.* **39**, 489 (2011).
4. G. J. Bowen, D. J. Beerling, P. L. Koch, J. C. Zachos, T. Quattlebaum, *Nature* **432**, 495 (2004).
5. R. Secord, P. D. Gingerich, K. C. Lohmann, K. G. Macleod, *Nature* **467**, 955 (2010).
6. S. L. Wing *et al.*, *Science* **310**, 993 (2005).

7. E. Mayr, *Animal Species and Evolution* (Harvard Univ. Press, Cambridge, MA, 1963).
8. K. G. Ashton, M. C. Tracy, A. de Queiroz, *Am. Nat.* **156**, 390 (2000).
9. M. Á. Rodríguez, M. Á. Olalla-Tárraga, B. A. Hawkins, *Glob. Ecol. Biogeogr.* **17**, 274 (2008).
10. J. L. Gardner, A. Peters, M. R. Kearney, L. Joseph, R. Heinsohn, *Trends Ecol. Evol.* **26**, 285 (2011).
11. B. K. McNab, *Oecologia* **164**, 13 (2010).
12. V. Millien *et al.*, *Ecol. Lett.* **9**, 853 (2006).
13. F. A. Smith *et al.*, *Global Planet. Change* **65**, 122 (2009).
14. P. D. Gingerich, *Univ. Mich. Pap. Paleontol.* **28**, 1 (1989).
15. W. C. Clyde, P. D. Gingerich, *Geology* **26**, 1011 (1998).
16. Numerous authors have shown the use of "*Hyracotherium*" to be invalid for North American equids. Thus, the species "*Hyracotherium*" *sandrae* (PETM) and "*H.*" *grangeri* (post-PETM) were assigned to the new genera *Sifrhippus* Froelich 2002 and *Arenahippus* Froelich 2002, respectively. We found, however, that characters used to separate *Sifrhippus* from *Arenahippus* are highly variable and not useful for generic identification. Thus, we refer both species to *Sifrhippus* pending formal revision.
17. P. L. Koch, J. C. Zachos, P. D. Gingerich, *Nature* **358**, 319 (1992).
18. F. A. Smith, S. L. Wing, K. H. Freeman, *Earth Planet. Sci. Lett.* **262**, 50 (2007).
19. B. H. Passey *et al.*, *J. Archaeol. Sci.* **32**, 1459 (2005).
20. A. F. Diefendorf, K. E. Mueller, S. L. Wing, P. L. Koch, K. H. Freeman, *Proc. Natl. Acad. Sci. U.S.A.* **107**, 5738 (2010).
21. R. Secord, S. L. Wing, A. Chew, *Paleobiology* **34**, 282 (2008).
22. P. D. Gingerich, *Genetica* **112–113**, 127 (2001).
23. M. T. Clementz, P. A. Holroyd, P. L. Koch, *Palaios* **23**, 574 (2008).
24. N. E. Levin, T. E. Cerling, B. H. Passey, J. M. Harris, J. R. Ehleringer, *Proc. Natl. Acad. Sci. U.S.A.* **103**, 11201 (2006).
25. J. D. Bryant, P. N. Froelich, *Geochim. Cosmochim. Acta* **59**, 4523 (1995).
26. W. Dansgaard, *Tellus* **16**, 436 (1964).
27. M. J. Kraus, S. Riggins, *Palaeogeogr. Palaeoclimatol. Palaeoecol.* **245**, 444 (2007).
28. P. D. Gingerich, *Trends Ecol. Evol.* **21**, 246 (2006).
29. P. Stiling, T. Cornelissen, *Glob. Change Biol.* **13**, 1823 (2007).
30. C. E. Owensby, R. C. Cochran, L. M. Auen, in *Carbon Dioxide, Populations, and Communities,* C. Koerner, F. Bazzaz, Eds. (Academic Press, San Diego, CA, 1996), pp. 363–371.
31. S. G. B. Chester, J. I. Bloch, R. Secord, D. M. Boyer, *J. Mamm. Evol.* **17**, 227 (2010).

Acknowledgments: We thank T. Bown, P. Gingerich, B. MacFadden, K. Rose, E. Sargis, and S. Strait for helpful discussions and advice; J. Curtis, B. Tucker, and A. Baczynski for help with isotope lab work; J. Bourque and A. Hastings for specimen preparation; and P. Koch and two anonymous reviewers for helpful comments. Supported by NSF grants EAR-0640076 (J.I.B., J.K., R.S.), EAR-0719941 (J.I.B.), EAR-0717892 (S.L.W.), EAR-0718740 (M.J.K.), and EAR-0720268 (F.A.M.). Data used in this paper are available in the SOM.

Supporting Online Material
www.sciencemag.org/cgi/content/full/335/6071/959/DC1
Materials and Methods
SOM Text
Figs. S1 to S4
Tables S1 to S9
References

12 September 2011; accepted 13 January 2012
10.1126/science.1213859

One-Time Transfers of Cash or Capital Have Long-Lasting Effects on Microenterprises in Sri Lanka

Suresh de Mel,[1] David McKenzie,[2]* Christopher Woodruff[3]

Standard economic theory suggests that one-time business grants can have at most temporary effects, and accordingly, policies to increase incomes of the self-employed in developing countries typically rely on sustained engagement. In contrast, we found long-lasting impacts from one-time grants given in a randomized experiment to subsistence firms. Five years after we gave $100 or $200 to 115 of 197 male and 100 of 190 female Sri Lankan microenterprise owners, we found 10-percentage-point-higher enterprise survival rates, and $8-to-$12-per-month-higher profits for male-owned businesses that received the grants. Female-owned businesses showed no long-term (or short-term) impacts. Our follow-up investigation interviewed 94% of the original sample and collected survivorship data from the remaining 6%, demonstrating that tracking long-term outcomes is both feasible and worthwhile. The results suggest that one-off grants may have lasting impacts on some types of subsistence firms, challenging the view that sustained engagement is always required.

Self-employment is one of the major sources of income for the urban poor across the world, with between 47 and 69% of poor (per capita income less than $2 per day) households in urban areas in Indonesia, Pakistan, Peru, and Nicaragua running a business (*1*), most often without paid employees. Typical policies to improve the incomes of these households and their businesses are based on sustained provision of services. Three such programs are (i) microfinance, which is often based on the expectation of a succession of loans, and in many cases regular follow-up meetings with clients in groups (*2*–*4*); (ii) conditional cash transfer programs, which typically give households regular transfers over a period of years (*5*, *6*); and (iii) business training programs, which are based on the idea that capital alone is not enough—as in the ancient proverb "give a man a fish and he eats for a day, teach a man to fish and he can feed himself for life"—with some evidence suggesting that training works best when accompanied by one-on-one follow-up visits (*7*).

But can just giving a fish feed a man for life? That is, does the much simpler policy of giving a one-time grant to small business owners have any long-term effect? Traditional economic models of firm investment such as the Ramsey model predict that there is an efficient size for a business, conditional on the owner's ability level. Any shock to capital in this model will have only temporary effects, and the firm will quickly return to the steady state. In such a model, an extra infusion of capital in the business can speed up convergence to this steady-state efficient size but cannot have any long-term effect (*8*).

In contrast, a one-off infusion of capital can have a permanent impact on business investment if there are poverty traps or under-investment caused by production nonconvexities (in which the only profitable investments are lumpy ones, such as buying a large machine, and where it may be not be possible to operate a business if capital falls below some threshold level) (*9*); if there are self-control problems and time-inconsistent preferences (for example, in which today an individual prefers that tomorrow he or she reinvests profits in the business, but when tomorrow comes prefers to spend the money) (*8*, *10*); or if there are intra-household inefficiencies (for example, owners may underinvest when they expect proceeds to be taken by a spouse or other family members) (*8*, *11*). Knowing whether the traditional models or these alternatives best describe

Table 1. Impact of the grants on business survival rates and reporting profits. Data are ordinary least squares results of the impact of the grant on (i) whether the business was closed in 2010, as measured in the June 2010 and December 2010 survey rounds and by observation and proxy reports for firms not interviewed, and (ii) whether it reports profits in either survey round. Robustness to excluding proxy reporting is shown in table S2. Sample size is 197 for male-owned firms and 190 for female-owned firms. Huber-White SE are shown in parentheses. *, **, and *** denote impact is significantly different from zero at the 10, 5, and 1% levels, respectively.

	Males		Females	
	Closed	Reports profits	Closed	Reports profits
Treatment amount (in 10,000s of LKR)	−0.109***	0.0876**	0.0252	−0.0176
	(0.0401)	(0.0378)	(0.0558)	(0.0546)
Control group mean	0.29	0.77	0.26	0.77

[1]Department of Economics, University of Peradeniya, Peradeniya 20400, Sri Lanka. [2]Development Research Group, The World Bank, Washington, DC 20433, USA. [3]Department of Economics, University of Warwick, Coventry CV4 7AL, UK.

*To whom correspondence should be addressed. E-mail: dmckenzie@worldbank.org.

the world is crucial for designing policies to help poor entrepreneurs as well as for charitable giving decisions. However, to date there is no long-term evidence on the effect of one-time injections of capital into these small businesses.

Does it matter whether the "fish" is given to a man or a woman? Microfinance has traditionally focused on women, with the belief that their businesses are smaller and more credit-constrained and thus in more need of access to capital (*12*). For example, 96% of the clients of the Grameen Bank, which is probably the most famous microfinance organization, are female. Grameen's founder, Nobel laureate Muhammad Yunus, has famously argued that capital, not skills, is the constraint on these businesses, stating that "giving the poor access to credit allows them to immediately put into practice the skills they already know" (*13*). Yet in many societies, women face social constraints and additional demands on their time from household responsibilities. These may limit the types of business they operate, and thus the ability of capital alone to generate expansion of their subsistence-level enterprises.

In April 2005, we began a randomized experiment among 408 microenterprises with no paid employees in urban Sri Lanka, in which grants of 10,000 or 20,000 Sri Lankan Rupees (LKR) (approximately US$100 to $200 at the time) were given to just over half of these firms. Half of those grants were given as cash, the other half as in-kind purchases of equipment or materials for their business. In the short term (within 2.5 years of receiving the grants), we have found that these grants led to relatively large increases in business profits for male owners but no change in business profits for female business owners (*11*, *14*). Here, we report on the results of reinterviewing the same firms in June and December 2010, between 4.5 and 5.5 years after the one-time grants were given, enabling measurement of the long-run impacts on business survival and profitability.

This Report's main contribution is in providing evidence that one-off grants can have longer-term effects on microenterprises. One critique of randomized experiments in development economics is that they tend to focus only on short-term impacts (*15*, *16*). There are a few recent studies that track long-term outcomes in health and education (*17*–*21*); a further contribution of this Report is being the first to track outcomes over a longer period for firms. Tracking firms over longer periods is important in order to be able to distinguish between the standard Ramsey model, in which any impacts of additional capital are temporary, and other models of firm behavior in which effects may persist. It also is important for measuring impacts on firm survival that may take several years to materialize. Yet, there are questions about the incentives of researchers to continue monitoring impacts over longer periods, as well as the feasibility of doing so because of sample attrition. This Report illustrates that it is both feasible and beneficial to track impact trajectories for a firm intervention over longer periods of time.

Our baseline sample was obtained via a door-to-door screening survey of households in selected administrative units of urban areas in the Kalutara, Galle, and Matara districts of Sri Lanka. The target population was microenterprise owners aged 20 to 65 who worked at least 30 hours per

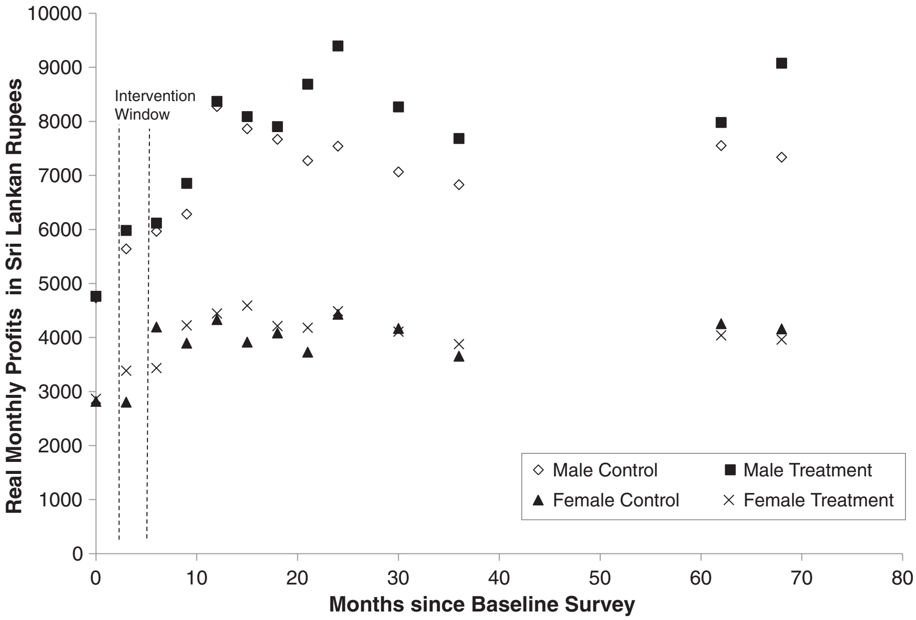

Fig. 1. Mean monthly real profits by survey round for treatment and control firms by gender. Data are from the 13 rounds of the Sri Lanka Microenterprise Survey. Intervention window shows the time period during which the one-time grants were given. The data for males are also shown in fig. S3, with pointwise 95% confidence intervals.

Table 2. Test of equality of treatment and control means in sample of firms that survive to report profits in 2010. Columns show means of baseline or time-invariant variables by treatment status for the 161 male-owned firms and 151 female-owned firms surviving to report profits in either or both the June 2010 and December 2010 survey rounds. *P* values are from *t* tests of equality of means. An *F* test of joint orthogonality of these characteristics to treatment status has a *P* value of 0.410 for males and 0.211 for females.

	Males			Females		
	Control	Treatment	*P* value	Control	Treatment	*P* value
Business characteristics						
Age of business (years)	10.37	12.54	0.240	9.25	11.22	0.232
Real profits in month of March 2005 (LKR)	4748	4919	0.778	2883	2669	0.578
Real revenue in month of March 2005 (LKR)	16098	14554	0.583	8818	7455	0.453
Total invested capital stock excluding land and buildings March 2005 (LKR)	32231	30290	0.649	21038	21278	0.951
Firm is in trade sector	0.51	0.50	0.922	0.43	0.44	0.958
Hours in the business worked by the owner in March 2005	59.27	55.70	0.282	51.84	44.73	0.065
Owner characteristics						
Age of owner	44.06	42.05	0.280	39.65	42.77	0.073
Years of education of owner	7.97	8.89	0.059	10.03	9.04	0.050
Number of digits recalled in digit-span recall test	5.91	5.97	0.778	5.73	5.71	0.915
Household asset index	0.18	0.07	0.656	0.77	0.33	0.053
Implied coefficient of relative risk aversion from lottery game	0.27	0.49	0.421	–0.29	–0.09	0.363

week in their business, had no paid employees, and had less than 100,000 LKR (~US$1000) in capital, excluding land and buildings. These criteria were intended to restrict our focus to the types of subsistence microenterprises that are most prevalent among the poor in developing countries (*22*). The baseline interviews were carried out in April 2005.

The resulting sample consists of 408 microenterprises, of which 197 are male-owned, 190 female-owned, and the remaining 21 jointly run by husband and wife. We dropped the last group given its small size and the important differences in effects by gender, but show in table S1 pooled results that include these jointly owned firms. The sample then contains a diverse group of the types of subsistence businesses typical in urban areas in most developing countries: small grocery stores, bicycle repairmen, food preparation (such as string hoppers and lunch packets), sewing clothing, and small-scale manufacture.

At baseline, in April 2005 the average male-owned firm had monthly profits of 4,700 LKR and a median capital stock, excluding land and buildings of 25,000 LKR, and the average female-owned firm had monthly profits of 2,800 LKR and a median capital stock, excluding land and buildings of 10,000 LKR. At an exchange rate of US$1 = 100 LKR, monthly profits were thus in the range of $1 to $2 per day for many firms. The median owner was in his or her early 40s, had been running the firm for 5 to 7 years, with male owners having a median of 9 years and female owners a median of 11 years schooling. Differences between male and female owners in the types of businesses they run and background of the owners are discussed in supporting online material (SOM) text 3.

In June 2010, we re-surveyed 348 of the 387 baseline firms (90%). In a second long-term follow-up round in December 2010, we surveyed 356 firms (92%). Only 24 of the 387 (6.2%) male- or female-owned firms could not be contacted in either survey because of being deceased (two people), migrating abroad (six people), migrating internally outside of the study areas (seven people), refusals (three people), or being unable to be found (six people). This high follow-up survey rate shows the possibility of doing long-term follow-ups with low attrition. Through physical observation and discussions with neighbors, we were able to verify whether the business had closed or not by the end of 2010, even for those firm owners not interviewed.

We began by testing whether the one-time grants affected the likelihood of a firm surviving until the last round of our survey, and the related question of whether the grants affected the proportion of the original firms who reported profits in either of the 2010 round of surveys (which requires both the firms not to have closed and the owners not to have refused to answer this question). Profits were collected for existing firms, and owners of firms that had closed were asked for details of their profits before closure and any current wage income. More detail on the measurement of these quantities and the estimation methodology are in the SOM text 4.

In addition to knowing whether the grants affected survival, we wished to know whether they affected the long-run profitability of the firm. Mean monthly real profits by survey round, treatment and control group status, and gender are plotted in Fig. 1. Two patterns emerge. First, after the intervention the male treatment group always had higher mean profits than those of the male control group, with the gap between the two not noticeably growing or shrinking systematically over time. Second, there was no such systematic pattern for females, with treatment and control groups typically having similar profits. The methodology used to test whether these differences are significant is presented in SOM text 4.

We examined whether one-off grants have long-term effects by testing three hypotheses:

Hypothesis 1 was, "One-time grants have no long-term effect on firm survival." If a one-time grant merely speeds convergence to a firm's optimal steady-state size as predicted by neoclassical theory, any effect should be temporary, and we should see no effect on firm survival. Results testing this hypothesis are shown in Table 1. We rejected the hypothesis for males: A one-time grant of approximately $100 lowered the likelihood of closure over the 5.75-year time period by 10.9 percentage points and, as a result, increased the likelihood the firm survived to report profits in the 2010 surveys by 8.8 percentage points. Given that 29% of the control firms close down over this time period, these are sizeable impacts, but as discussed in the SOM, they are plausible given the size of the grants and the estimated monthly return on the grants. In contrast, we cannot reject this hypothesis for females.

Table 3. Short- and Long-run impacts of grants on business profits. Data are from the 13 survey rounds of the Sri Lanka Microenterprise Survey, from April 2005 through December 2010, and are for 197 male-owned and 190 female-owned firms. The unbalanced panel is used so that firms do not appear in survey waves in which they do not report profits. Truncated profits truncates (caps) profits at the 99th percentile, reducing the influence of outliers. Log real profits uses log of profits instead of levels as the dependent variable. Total labor income is the sum of truncated profits and wage earnings. All regressions include firm fixed effects and survey wave dummies. Huber-White SEs are shown in parentheses, clustered at the firm level. *, **, and *** denote impact is significantly different from zero at the 10, 5, and 1% levels, respectively.

	Males				Females			
	Monthly real profits (LKR)	Truncated real profits (LKR)	Log real profits	Total labor income (LKR)	Monthly real profits (LKR)	Truncated real profits (LKR)	Log real profits	Total labor income (LKR)
Amount × first year since grant	648.2** (285.6)	685.3** (272.5)	0.142*** (0.0486)	799.7*** (278.9)	94.79 (265.1)	107.0 (249.1)	0.0500 (0.0639)	66.18 (254.0)
Amount × second year since grant	625.3 (406.4)	576.4 (384.3)	0.0927 (0.0563)	768.3* (391.6)	206.5 (450.3)	54.30 (371.8)	0.0288 (0.0785)	27.90 (376.3)
Amount × third year since grant	749.6* (411.5)	703.8* (392.8)	0.114* (0.0634)	867.9** (405.7)	3.994 (432.3)	−51.73 (391.3)	−0.0659 (0.105)	−36.33 (398.9)
Amount × five to six years since grant	1218* (622.3)	789.3 (499.6)	0.136** (0.0637)	875.8* (506.5)	−284.9 (450.8)	−258.9 (396.1)	−0.0914 (0.101)	−148.7 (447.6)
Mean for control group	6864	6806	8.55	6455	3855	3724	7.77	3587
P value for testing constant effect over time	0.816	0.965	0.629	0.991	0.489	0.651	0.241	0.914
Observations	2212	2212	2201	2329	2148	2148	2140	2233

The point estimate is actually positive (suggesting slightly more firms who received the grant closed) but small and statistically insignificant. These results are shown to be robust to concerns about survey attrition in SOM text 5.

Hypothesis 2 was, "One-time grants don't affect which firms survive." If the grants only prop up failing firms, we should see the characteristics of survivors in the treatment group differ substantially from those in the control group. As shown in Table 2, this is not the case for either male or female firms. Despite the lower failure rate, surviving male-owned treatment firms have similar initial profitability, revenues, and capital stock, and operate in similar sectors, to the surviving male-owned control firms. The only difference appears in owner education, which is higher in the surviving treated firms. However, an F test of joint orthogonality of these characteristics to treatment status fails to show any relationship between treatment and characteristics of surviving firms. Among females, there were more marginally apparent differences in owner characteristics, but again we cannot reject overall balance. As further shown in SOM text 5, the entire distributions of baseline profits are similar for surviving treatment and control, so that the grants are not differentially affecting smaller or larger firms within our sample.

Hypothesis 3 was, "One-off grants have at most temporary effects on business profitability." Traditional economic models predict that any impact on profits should be short-lived, merely speeding up the transition to an equilibrium steady-state. The results of estimating the treatment effect on profits are reported in Table 3. Consistent with Fig. 1, we found the one-time grants had lasting impacts on firm profitability for males but no impact in either the short or the long run for females. For males, a 10,000 LKR grant increased monthly profits by 600 to 1200 LKR, a 6 to 12% monthly real return. This persists throughout the time period and does not narrow dramatically (as would be the case with a temporary effect) or increase dramatically (as would be the case if returns compounded). This effect is robust, and strengthened, when we look at labor income and include the labor income for those businesses which have closed, and are shown in SOM text 5 to be robust to any selective attrition.

Conditional cash transfers in health and education typically tie payments to irreversible actions, such as children attending school or getting vaccinated. It is thus no surprise to find lasting impacts of such programs. In contrast, half of our grants were unconditional cash, and even the conditional grants typically took the form of inventories or raw materials that could easily have been taken out of the business if desired. Traditional economic theory would predict that such one-time grants would have at most temporary effects. However, we found enduring effects for male-owned microenterprises, with respect to both business survival and business profitability. This raises two questions: Why do we see these effects, and why don't female-owned microenterprises also benefit?

Economic theory suggests at least three categories of reasons why a one-time grant may have lasting effects. The first is that the extra funding provided by the grants may have played an insurance role, providing liquidity-constrained firms with the ability to keep the business open when faced with a temporary shock to the business that might otherwise force them to close down. As shown in SOM text 5, the main reason for business closure in our firms was business failure. However, the data also show that impacts are not much greater for poorer owners or firms with initially lower profitability within our sample. Because shocks are an important reason for business failure, smoothing against shocks may still help explain the lasting impacts if the frequency of shocks that cause businesses to fail are independent of business size within our sample.

A second potential explanation offered by theory is that the grants allowed liquidity-constrained firm-owners to make lumpy investment with high returns and that, in the absence of the grant, firm owners would not be able to save enough to make these investments themselves, getting stuck in a poverty trap (*9*). However, the majority of the grants were invested in inventories, materials, and other working capital rather than in lumpy equipment. The owners increased profits by selling larger quantities and a wider variety of products rather than dramatically changing their production technologies. Coupled with a lack of evidence for production poverty traps in other urban environments (*23*, *24*), this suggests production non-convexities are also not the main reason for the long-lasting effects.

The real returns to capital for these male firm-owners are around 11% per month (*11*). Faced with these returns, why does not the control group reinvest small amounts at a time, compounding and growing their profits to catch up to the treatment group? Recent behavioral theories of decision-making (*8*, *10*, *25*) are a third category of explanation and, in our view, offer the greatest potential for explaining why one-time grants have long-term effects. These theories also may help explain the differences in outcomes for males and females. For example, if firm owners lack self-control or have time-inconsistent preferences, they will keep putting off investment opportunities that are profitable in the long term. Because this leads to less capital invested in the firm, this may also make them more vulnerable to shocks. However, this raises the question of why this same behavior does not lead to an immediate decapitalization of the grants once they are received. Some friction in removing capital from the firm must be present. This could either be physical friction (it takes several days to liquidate stock, and this is enough to overcome immediate temptation) or mental accounting friction (once capital enters the business, it is treated differently from capital in the household).

Two factors seem to explain the lack of effect for female-owned microenterprises. First, much of the treatment does not get invested in the business but gets diverted to household uses. Second, a combination of household inefficiencies (*11*) and women working in industries with low efficient scale (*26*) means that the money these women do invest in their business has low returns. Capital alone thus does not appear to be enough to grow subsistence-level female-owned firms. Ongoing work is exploring the extent to which complementary interventions such as business training can help, or whether the other duties such as household production and child care constrain the extent to which women wish to grow their firms.

Overall, these results show that it is both feasible and of interest to track the outcomes of a microenterprise intervention over a substantial period of time, and that a one-off grant can have a lasting influence. Sometimes, giving a fish may be enough. As with any experiment, there are limits to the extent to how much one can generalize to other settings, but there is at least evidence from Ghana and Mexico that male-owned microenterprises have substantial short-term gains from one-time grants (*8*, *27*). Replicating these long-run results across a number of other settings therefore offers the potential to provide a basis for rethinking theories of microenterprise growth and the policy actions that can be used to aid subsistence entrepreneurs.

References and Notes

1. A. V. Banerjee, E. Duflo, *J. Econ. Perspect.* **21**, 141 (2007).
2. B. Armendáriz, J. Morduch, *The Economics of Microfinance* (MIT Press, Cambridge, MA, 2007).
3. D. Karlan, J. Zinman, *Science* **332**, 1278 (2011).
4. A. Banerjee, E. Duflo, R. Glennester, C. Kinnan, "The miracle of microfinance? Evidence from a randomized evaluation", BREAD Working Paper no. 278, 2010; available at: http://ipl.econ.duke.edu/bread/abstract.php?paper=278.
5. J. Hanlon, A. Barrientos, D. Hulme, *Just Give Money to the Poor: The Development Revolution from the Global South* (Kumarian Press, West Hartford, CT, 2011).
6. A. Fiszbein, N. Schady, "Conditional Cash Transfers: Reducing Present and Future Poverty," *World Bank Policy Research Report* (World Bank, Washington, DC, 2009).
7. M. Valdivia, "Training or technical assistance? A field experiment to learn what works to increase managerial capital for female microentrepreneurs"; available at http://siteresources.worldbank.org/INTGENDER/Resources/336003-1303333954789/final_report_bustraining_BM_march31.pdf, 2011.
8. M. Fafchamps, D. McKenzie, S. Quinn, C. Woodruff, "When is capital enough to get female microenterprises growing? Evidence from a randomized experiment in Ghana," World Bank Policy Research Working Paper no. 5706 (World Bank, Washington, DC, 2011); available at http://go.worldbank.org/84EOCSG1I0.
9. A. Banerjee, A. Newman, *J. Polit. Econ.* **101**, 274 (1993).
10. A. Banerjee, S. Mullainathan, "Climbing out of poverty: Long term decisions under income stress" (Centre for Economic Policy Research, London, 2007); available at www.cepr.org/meets/wkcn/7/770/papers/Banerjee.pdf.
11. S. de Mel, D. McKenzie, C. Woodruff, *Amer. Econ. J. Appl. Econ.* **1**, 1 (2009).
12. Socio-economic and Gender Analysis Programme, "A guide to gender sensitive microfinance" (Food and Agriculture Organization of the United Nations, 2002); available at http://www.fao.org/docrep/012/ak208e/ak208e00.pdf.
13. M. Yunus, *Banker to the Poor: Micro-Lending and the Battle Against World Poverty* (Public Affairs, New York, 1999).

14. S. de Mel, D. McKenzie, C. Woodruff, *Q. J. Econ.* **123**, 1329 (2008).
15. M. Ravallion, *Economists Voice* **6**, 1 (2009).
16. M. Woolcock, *J. Develop. Effective.* **1**, 1 (2009).
17. S. Baird, J. Haomry Hicks, M. Kremer, E. Miguel, "Worms at work: Long-run impacts of child-health gains" (Poverty Action Lab, 2011); available at http://www.povertyactionlab.org/publication/worms-work-long-run-impacts-child-health-gains.
18. SOM.1. summarizes the tracking of (*17*) and other health and education papers.
19. O. Ozier, "The impact of secondary schooling in Kenya: a regression discontinuity analysis" (2011); available at http://economics.ozier.com/owen/papers/ozier_JMP_20110117.pdf.
20. W. Friedman, M. Kremer, E. Miguel, R. Thornton, "Education as Liberation?" *NBER Working Papers 16939*, 2011; available at www.nber.org/papers/w16939.
21. R. Jensen, *Q. J. Econ.* **125**, 515 (2010).
22. SOM text 2 provides greater detail on the sampling methodology.
23. D. McKenzie, C. Woodruff, *Econ. Dev. Cult. Change* **55**, 3 (2006).
24. M. Lokshin, M. Ravallion, *Stud. Nonlinear Dynam. Econometrics* **8**, 1 (2004).
25. E. Duflo, M. Kremer, J. Robinson, *Am. Econ. Rev.* **101**, 2350 (2011).
26. M. S. Emran, A. K. M. M. Morshed, J. Stiglitz, "Microfinance and Missing Markets" (Mimeo, George Washington University, Washington, DC, 2007); available at http://papers.ssrn.com/sol3/papers.cfm?abstract_id=1001309.
27. D. McKenzie, C. Woodruff, *World Bank Econ. Rev.* **22**, 457 (2008).

Acknowledgments: We thank M. Groh for excellent research assistance and two anonymous reviewers and the editors for helpful comments. Financial support from NSF grants SES-0523167 and SES-0617424, the World Bank's Gender Action Plan, and the World Bank's Research Support Budget is gratefully acknowledged. The data are available at http://www2.warwick.ac.uk/fac/soc/economics/staff/academic/woodruff/data, and replication files are provided in the SOM.

Supporting Online Material
www.sciencemag.org/cgi/content/full/335/6071/962/DC1
SOM Text
Figs. S1 to S3
Tables S1 to S5
References (*28–32*)

22 August 2011; accepted 26 January 2012
10.1126/science.1212973

Evolutionarily Assembled cis-Regulatory Module at a Human Ciliopathy Locus

Jeong Ho Lee,[1] Jennifer L. Silhavy,[1] Ji Eun Lee,[1] Lihadh Al-Gazali,[2] Sophie Thomas,[3] Erica E. Davis,[4] Stephanie L. Bielas,[1] Kiley J. Hill,[1] Miriam Iannicelli,[6] Francesco Brancati,[6] Stacey B. Gabriel,[7] Carsten Russ,[7] Clare V. Logan,[8] Saghira Malik Sharif,[8] Christopher P. Bennett,[8] Masumi Abe,[9] Friedhelm Hildebrandt,[10] Bill H. Diplas,[11] Tania Attié-Bitach,[3] Nicholas Katsanis,[4,5] Anna Rajab,[12] Roshan Koul,[13] Laszlo Sztriha,[14] Elizabeth R. Waters,[15] Susan Ferro-Novick,[16] C. Geoffrey Woods,[17] Colin A. Johnson,[8] Enza Maria Valente,[6] Maha S. Zaki,[18] Joseph G. Gleeson[1]*

Neighboring genes are often coordinately expressed within cis-regulatory modules, but evidence that nonparalogous genes share functions in mammals is lacking. Here, we report that mutation of either *TMEM138* or *TMEM216* causes a phenotypically indistinguishable human ciliopathy, Joubert syndrome. Despite a lack of sequence homology, the genes are aligned in a head-to-tail configuration and joined by chromosomal rearrangement at the amphibian-to-reptile evolutionary transition. Expression of the two genes is mediated by a conserved regulatory element in the noncoding intergenic region. Coordinated expression is important for their interdependent cellular role in vesicular transport to primary cilia. Hence, during vertebrate evolution of genes involved in ciliogenesis, nonparalogous genes were arranged to a functional gene cluster with shared regulatory elements.

Cis-regulatory modules (CRMs) provide binding sites for transcription factors that regulate the expression of neighboring genes (*1*). Relatively little is known about the evolution of these regulatory elements, such as how CRMs arise or how the regulated genes cofunction, other than the rare instance such as *Hox* gene clusters evolved by gene duplication and the addition of regulatory elements to regulate body patterning (*2*).

Joubert syndrome (JBTS) is the most common neurodevelopmental disorder among the ciliopathy spectrum, which is thought to encompass disorders of structure or function of cellular primary (nonmotile) cilia (*3*). Affected JBTS patients show hypotonia, ataxia, abnormal eye movement, and a distinct mid-hindbrain malformation presenting the "molar tooth" sign on brain magnetic resonance images (MTI) (fig. S1A) (*4*). Mounting evidence suggests that primary cilia as cellular antennae sense a wide variety of signals, including Shh signaling, and play a crucial role in vertebrate development (*5*).

Recently, we reported deleterious mutations of the *transmembrane protein* (*TMEM*) *216* gene, linking to the JBTS2 locus on chromosome 11, in about half of the 10 JBTS2-linked families (Fig. 1A) (*6–8*). However, the remaining half of the JBTS2 families (verified by the pathognomonic MTI) were phenotypically indistinguishable (displaying optic coloboma, retinal dysplasia, nephronophthisis, and occasional occipital encephalocele) but were negative for mutations in *TMEM216* (fig. S1, A and B, and table S1). Furthermore, fibroblasts from these latter patients contained intact TMEM216 mRNA and protein expression (fig. S2, A and B), thereby suggesting another JBTS causative gene at the JBTS2 locus.

We thus performed resequencing of all known and predicted exonic and promoter genetic elements within the minimal 17-Mb candidate interval defined by *TMEM216* mutation-negative families (*9*). From these data, we identified four missense mutations and one splicing homozygous deleterious mutation in evolutionarily conserved residues of the nearby *TMEM138* gene of unknown function, thus accounting for all JBTS2-linked families (Fig. 1A, fig. S2C, and table S1). All mutations segregated according to a single recessive disease mode and were not present in 400 ethnically matched chromosomes. Among missense mutations in transmembrane domains, TMEM138 p.H96R led to unstable protein when transfected into heterologous cells (fig. S2D), suggesting loss of function as the disease mechanism.

Although both *TMEM* genes encode transmembrane proteins (Fig. 1A), neither the genes nor the proteins demonstrated sequence homology or shared any functional domains. Phylogenetic analysis showed that they represented two distinct protein families, which have evolved separately from invertebrates (figs. S4 and S5), excluding a gene-duplication event. In all higher

[1]Neurogenetics Laboratory, Howard Hughes Medical Institute (HHMI), Department of Neurosciences, University of California, San Diego, CA, USA. [2]Departments of Pediatrics, Faculty of Medicine and Health Sciences, United Arab Emirates University, Al Ain, United Arab Emirates. [3]Département de Génétique, INSERM U781, Hôpital Necker-Enfants Malades, Université Paris Descartes, Paris, France. [4]Center for Human Disease Modeling, Duke University Medical Center, Durham, NC, USA. [5]Department of Cell Biology and Pediatrics, Duke University Medical Center, Durham, NC, USA. [6]Istituto di Ricovero e Cura a Carattere Scientifico Casa Sollievo della Sofferenza, Mendel Laboratory, San Giovanni Rotondo, Italy. [7]Broad Institute of Harvard and Massachusetts Institute of Technology, Cambridge, MA, USA. [8]Department of Clinical Genetics, Yorkshire Regional Genetics Service, St. James's University Hospital, Beckett, UK. [9]Transcriptome Research Center, National Institute of Radiological Sciences, Chiba-shi, Japan. [10]HHMI, Department of Pediatrics, University of Michigan, Ann Arbor, MI, USA. [11]McKusick-Nathans Institute of Genetic Medicine, Johns Hopkins University School of Medicine, Baltimore, MD, USA. [12]Genetic Unit, Directorate General of Health Affairs, Ministry of Health, Muscat, Sultanate of Oman. [13]Department of Child Health (Neurology), Sultan Qaboos University Hospital, College of Medicine and Health Sciences, Muscat, Oman. [14]Department of Pediatrics, Division B, University of Szeged, Szeged, Hungary. [15]Biology Department, San Diego State University, San Diego, CA, USA. [16]Department of Cellular and Molecular Medicine, HHMI, University of California at San Diego (UCSD), La Jolla, CA, USA. [17]Section of Ophthalmology and Neurosciences, Wellcome Trust Brenner Building, Leeds Institute of Molecular Medicine, St James's University Hospital, Leeds, UK. [18]Clinical Genetics Department, Human Genetics and Genome Research Division, National Research Centre, Dokki, Giza, Egypt.

*To whom correspondence should be addressed. E-mail: jogleeson@ucsd.edu

vertebrates, the two genes aligned in a head-to-tail configuration, with a conserved ~23–kilo–base pair noncoding intergenic interval (Fig. 1B). A synteny map of the genomic locus in a species with deposited reference sequence indicated that they were joined by an ancient chromosomal rearrangement at the amphibian-to-reptile evolutionary transition ~340 million years ago (Fig. 1B and fig. S3). Adjacent genes often exhibit correlated expression (*10*) and, thus, confer a selective advantage as a genetic module for a certain biological function (*11*). Therefore, the arrangement of two *TMEM* genes causing indistinguishable phenotypes prompted us to test whether these genes represent co-regulated and cofunctioning genes within a CRM.

To test for coordinated expression, we examined tissue-expression patterns of human *TMEM138* and *TMEM216* using the microarray database and in situ hybridization of human embryos. We found tight coexpression values of human *TMEM138* and *TMEM216* across the major tissues, including the brain and kidneys (fig. S6B), and similar expression patterns in various tissues, including the kidneys, cerebellar buds, and telencephalon, at 4 to 8 gestational weeks (gw) of human embryos (Fig. 2A and fig. S6C). To test whether this coordinated expression was due to the adjacent localization, we compared mRNA levels in zebrafish versus mice, representing species before and after the gene rearrangement event. Using quantitative polymerase chain reaction (qPCR), we detected tightly coordinated expression levels in mice compared with those in zebrafish (correlation coefficient $r = 0.984$ versus 0.386) (Fig. 2B and fig. S6D), which suggests that *TMEM138* and *TMEM216* might share regulatory elements

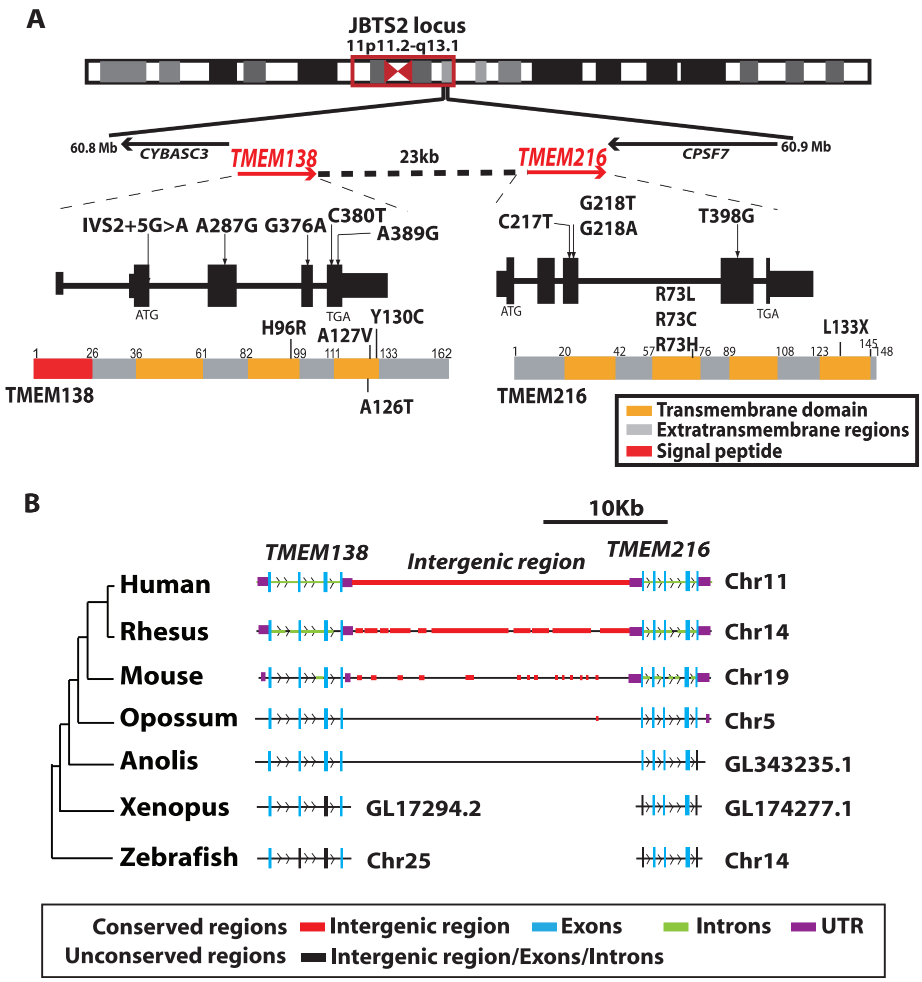

Fig. 1. Genetic heterogeneity at JBTS2 locus and the evolutionary location of the *TMEM138* and *TMEM216* genes mutated in JBTS2-linked families. (**A**) JBTS2 locus (red box) on chromosome 11. *TMEM138* encoding a trispan membrane protein is aligned in a head-to-tail configuration with *TMEM216* encoding a tetraspan membrane protein. All missense and splicing mutations of *TMEM138* and *TMEM216* found in JBTS2-linked families are indicated on the predicted transcript and protein. (**B**) Schematic synteny representation of *TMEM138*, *TMEM216*, and the intergenic region showing that the head-to-tail configuration of *TMEM138* and *TMEM216* on the same chromosome is conserved from reptiles to humans, but not in lower vertebrates, in which the two *TMEM*s are located on different chromosomes (table S2). Conserved regions have >50% sequence similarity to humans. UTR, untranslated region.

(REs) within the ~23-kb intergenic region. We further examined several experimental features and found that regulatory factor X 4, a transcription factor regulating ciliary genes, binds a RE conserved in the noncoding intergenic region to mediate coordinated expressions of *TMEM138* and *TMEM216* (see SOM text and fig. S7)

The coordinated expression and indistinguishable ciliopathy phenotype caused by either mutation of *TMEM138* and *TMEM216* suggests possible functional relations at the protein level, possibly co-regulating ciliogenesis. We noticed short cilia and failure of ciliogenesis in *TMEM138*- (p.A126T) and *TMEM216*- (p.R73L) mutated fibroblasts, respectively (Fig. 3A), as well as defects of ciliogenesis after knockdown of *TMEM138* and *TMEM216* in IMCD3 cells (fig. S8), suggesting that both TMEM138 and TMEM216 are required for ciliogenesis. Immunostaining of endogenous TMEM138 with a marker (Arl13b) of the ciliary axoneme and transition zone demonstrated closely adjacent localization with TMEM216 at the base of cilia (γ-tubulin), as reported previously (Fig. 3B and fig. S9C) (*6*). We also noted prominent TMEM138 and TMEM216 adjacent but nonoverlapping vesicular staining around the base of cilia (Fig. 3B and fig. S9, C and D).

Earlier electron-microscopic findings suggested that vesicles transporting to the cilium play a crucial role for targeted delivery of membrane proteins from the Golgi apparatus (*12*, *13*). It is noteworthy that TMEM216 localized to post-Golgi vesicles along microtubules, as well as the Golgi apparatus surrounding the base of cilium, whereas TMEM138 localized to adjacent but nonoverlapping distinct vesicles, shown by immunoelectron microscopic analysis (figs. S10, S11, and S12A). This observation suggests that both TMEM138 and TMEM216 might mark vesicles en route to the base of cilium, which is known to be crucial for ciliary assembly (*14*). Using time-lapse analysis with or without fluorescence recovery after photobleaching, we found that the net flux of TMEM216-tagged vesicular movements is toward the centrosome in dsRed-Centrin2 (centrosomal marker) expressing cells (fig. S12B and movies S1 and S2). TMEM138-tagged vesicles displayed tethered vesicular movement with TMEM216-tagged vesicles (fig. S12C and movie S3). This observation prompted us to ask whether the two distinct vesicles differentially carry known ciliary proteins essential for ciliary assembly. We further examined several experimental features showing that TMEM138 and TMEM216 mark two distinct but linked vesicle pools, each associated with unique cilia-targeted proteins, including CEP290 (see SOM text and fig S13).

To understand the adjacency of the two vesicular pools, we tested whether either was required to move vesicles containing the other. Although TMEM216 vesicular movement was not notably affected by disruption of *TMEM138* by small interfering RNA (siRNA), the knockdown of *TMEM216* disrupted the trafficking of

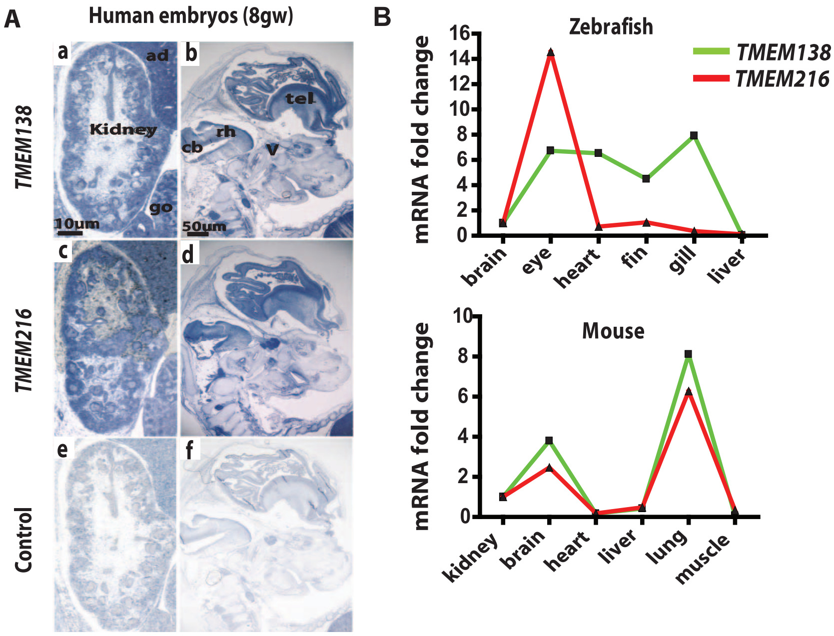

Fig. 2. Coordinated expression of adjacent *TMEM138* and *TMEM216* mediated by the noncoding intergenic region. (**A**) Similar expression patterns of *TMEM138* and *TMEM216* based on in situ hybridization at 8 gw in human embryonic tissues. *TMEM138* antisense (a and b), *TMEM216* antisense (c and d), and sense control probes (*TMEM138*) (e and f) are shown. *TMEM138* and *TMEM216* are strongly expressed in kidney, gonad (go), and adrenal gland (ad) as well as in the central nervous system, in particular in the cerebellar bud (cb), telencephalon (tel), rhombencephalon (rh), and cranial nerve ganglia such as trigeminal (V). (**B**) Real-time qPCR of *TMEM138* and *TMEM216* in selected tissues indicates tightly coordinated mRNA expressions in mouse tissues (having head-to-tail configuration), but not zebrafish (having two genes on different chromosomes). Housekeeping genes *36B4* (mouse) and *Rpl13a* (zebrafish) are used for normalization.

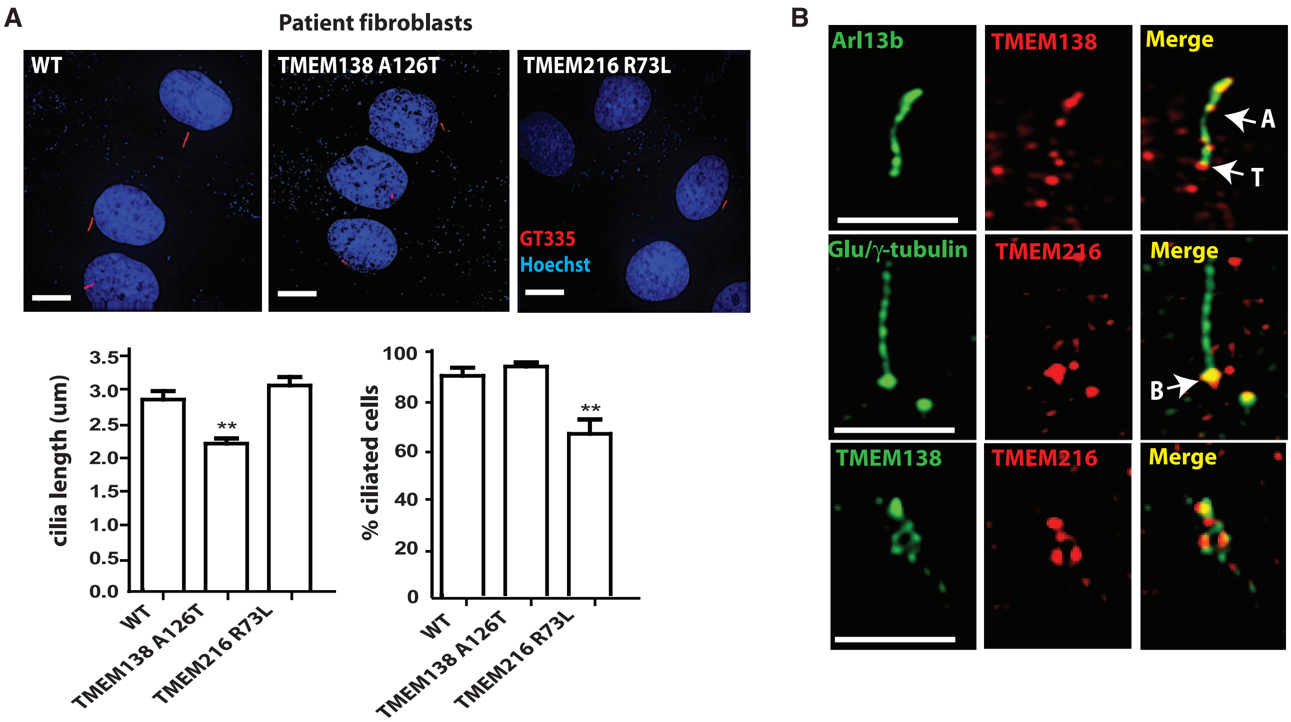

Fig. 3. Tethered vesicular trafficking of TMEM138 and TMEM216 to primary cilia is required for ciliogenesis. (**A**) In patient fibroblasts under 48-hour serum starvation, TMEM138 p.A126T (MTI-656) mutations caused short cilia, and TMEM216 p.R73L mutations disrupt ciliogenesis (defined as having cilia <1 μm long).$^*P < 0.05$, $^{**}P < 0.01$ [versus wild type (WT) by one-way analysis of variance (ANOVA) with Bonferroni posttest, $n = 40$ to 50 cells]. Error bars indicate SEM. (**B**) In IMCD3 cells, high-resolution images of endogenous TMEM138/216 staining show that TMEM138 localized to ciliary axonemes and the base of cilia, whereas TMEM216 localized primarily to basal bodies. Both TMEMs also show closely adjacent vesicular patterns around the base of cilia (also see fig. S9C). Anti-Arl13b (cilia), anti-Glu/γ tubulin (cilia plus centrosome), polyclonal mouse anti-TMEM138 (fig. S9, A and B), and rabbit anti-TMEM216 antibodies were used. A, ciliary axoneme; T, transition zone; B, basal body. Scale bars, 5 μm.

TMEM138, as well as CEP290 (figs. S13B and S14, A and B, and movies S5 and S6), suggesting functional dependence on TMEM216 for trafficking TMEM138 and associated proteins.

To determine the mechanism of this functional dependence, we considered the potential role of tethering proteins in linking these two distinct vesicular pools. Several vesicle tethering factors, including the transport protein particle (TRAPP) II complex, p115, and the conserved oligomeric Golgi complex are known to be involved in tethering Golgi vesicles (*15*). Among these potential tethering proteins, we found that TRAPPII mediated the tethering of TMEM138 and TMEM216 vesicles crucial for ciliary assembly (Fig. 4A, SOM text, figs. S14C to S16, and movies S7 and S8).

We questioned whether the protein localization or mutant phenotype of the two TMEMs in species that diverged before the coordinated gene regulation should be distinct. We found the

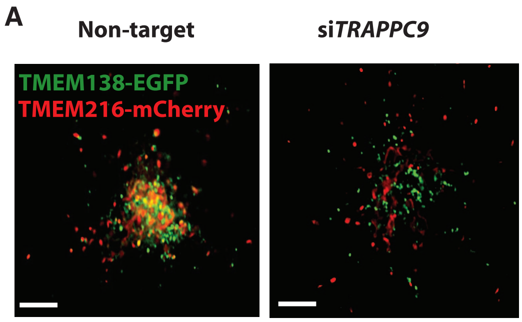

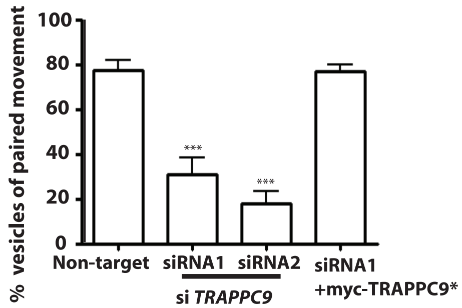

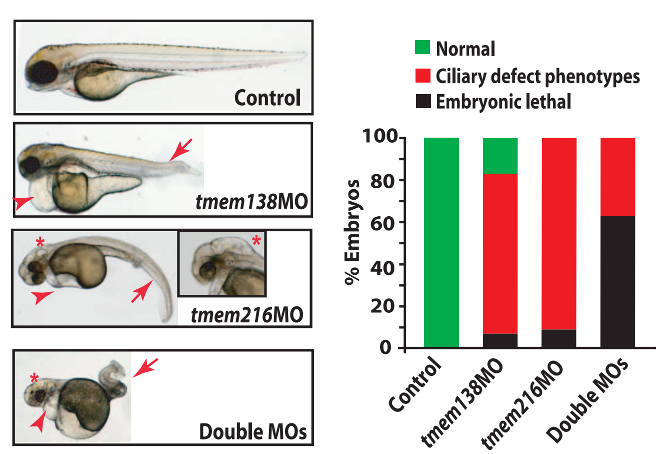

	%				No.
	Hydrocephalus	Pericardial effusion	Kinked tail	Lethal	Total
*tmem138*MO	0	63	29	4	269
*tmem216*MO	57	95	81	5	227
Double MOs	32	32	32	68	201

Fig. 4. Functional relatedness of TMEM138 and TMEM216. (**A**) Live-cell imaging shows that knockdown of TRAPPC9, a major subunit of the TRAPPII complex, detached the tethered TMEM138 and TMEM216 vesicles (movies S7 and S8). Defects in tethering were largely rescued by myc-*TRAPPC9** (*9*). ***$P <$ 0.001 (by one-way ANOVA with Bonferroni posttest, n = 90 to 110). Scale bars, 5 μm. Error bars indicate SEM. (**B**) Injection of translation-blocking antisense morpholinos (MOs) to *tmem138* (6 ng), *tmem216* (4 ng), or double MOs in WT (AB) zebrafish embryos leads to ciliary phenotypes of curved or kinked tail (arrows) and heart edema (arrowheads) at 3 days post-fertilization in a synergistic and dose-dependent manner (fig. S18A). Only *tmem216* morphants present hydrocephalus (*) (>50 embryos for each condition) (fig. S18B).

retention of the coordinated vesicular movement in a zebrafish cell line (ZF4) expressing the tagged version of the two TMEMs zebrafish orthologs, suggesting that the coordinated localization of proteins evolutionarily preceded the coordinated gene expression (movie S11). We next tested for conserved genetic function in zebrafish by comparing the morpholino knockdown phenotypes of each. Both knockdowns shared some typical ciliary phenotypes such as pericardial effusion, a curved or kinked tail (*16*) in a synergistic and dose-dependent manner, as well as gastrulation defects (Fig. 4B and fig. S18, A to D). However, only *tmem216* morphants presented hydrocephalic brains [ciliary phenotype (*17*)] and more severe defects of the left/right heart axis (Fig. 4B and figs. S17 and S18A). Together, the data indicate that before their adjacent genomic localization, the proteins' organismal functions were not completely congruent and were associated with distinguishable phenotypes, unlike JBTS2-linked Joubert patients.

Our findings suggest that nonparalogous genes not only can be chromosomally rearranged into a functional gene cluster during vertebrate evolution, but also can be assembled into a new CRM by evolving regulatory elements, which correlate with their coordinated expression. We are aware of few other examples in which mutations in adjacent genes lead to indistinguishable or similar human phenotypes: mutations in *EVC* or *EVC2* cause another ciliopathy, Ellis–van Creveld Syndrome; mutations in *ABCG5* and *ABCG8* cause sitosterolemia; and disruptions of *PKD1* and *TSC2* cause renal cysts (*18*–*20*). Our results provide insight into the evolved coordinated expression and functional relatedness of adjacent nonparalogous genes as a pathogenesis of phenotypically indistinguishable genetic disorders caused by mutations at a single locus.

References and Notes

1. D. M. Jeziorska, K. W. Jordan, K. W. Vance, *Semin. Cell Dev. Biol.* **20**, 856 (2009).
2. M. Manzanares *et al.*, *Nature* **408**, 854 (2000).
3. J. L. Tobin, P. L. Beales, *Genet. Med.* **11**, 386 (2009).
4. D. Doherty, *Semin. Pediatr. Neurol.* **16**, 143 (2009).
5. V. Singla, J. F. Reiter, *Science* **313**, 629 (2006).
6. E. M. Valente *et al.*, *Nat. Genet.* **42**, 619 (2010).
7. L. C. Keeler *et al.*, *Am. J. Hum. Genet.* **73**, 656 (2003).
8. E. M. Valente *et al.*, *Am. J. Hum. Genet.* **73**, 663 (2003).
9. Materials and methods are available as supporting material on *Science* Online.
10. L. D. Hurst, C. Pál, M. J. Lercher, *Nat. Rev. Genet.* **5**, 299 (2004).
11. J. M. Stuart, E. Segal, D. Koller, S. K. Kim, *Science* **302**, 249 (2003).
12. S. Sorokin, *J. Cell Biol.* **15**, 363 (1962).
13. D. S. Papermaster, B. G. Schneider, J. C. Besharse, *Invest. Ophthalmol. Vis. Sci.* **26**, 1386 (1985).
14. M. V. Nachury, E. S. Seeley, H. Jin, *Annu. Rev. Cell Dev. Biol.* **26**, 59 (2010).
15. H. Cai, K. Reinisch, S. Ferro-Novick, *Dev. Cell* **12**, 671 (2007).
16. H. Khanna *et al.*, *Nat. Genet.* **41**, 739 (2009).
17. N. Pathak, T. Obara, S. Mangos, Y. Liu, I. A. Drummond, *Mol. Biol. Cell* **18**, 4353 (2007).
18. V. L. Ruiz-Perez *et al.*, *Am. J. Hum. Genet.* **72**, 728 (2003).
19. K. E. Berge *et al.*, *Science* **290**, 1771 (2000).
20. E. Kleymenova *et al.*, *Mol. Cell* **7**, 823 (2001).

Acknowledgments: We thank the patients and families for invaluable contributions; the Broad Sequencing Plaform, the UCSD Neuroscience Core (grant P30NS047101), and T. Meerloo at the UCSD ImmunoEM Core; M. G. Rosenfeld, B. Ren, P. Novick, K. Frazer, and S. Rifkin for discussion; and C. Janke (Centre de Recherche de Biochimie Macromoléculaire, Montpellier, France, GT335 antibody), T. Caspary (Emory Arl13b antibody), P. Aza-Blanc (Sanford-Burnham Institute, siRNAs), and D. Traver (UCSD) for ZF4 cells. This work was supported by the Daland Fellowship from the American Philosophical Society (J.H.L.), the Italian Ministry of Health (RC2010, Ricerca Finalizzata 2006), Telethon Foundation Italy (GGP08145, E.M.V.), the Pierfranco and Luisa Mariani Foundation (E.M.V.), l'Agence National pour la Recherche (grant ANR-2010-BLAN-1122 01- Foetocilpath, T.A.-B.), the American Heart Association (grant 09POST2250641, J.E.L.), Newlife Foundation for Disabled Children, the Medical Research Council (grant G0700073), the Sir Jules Thorn Charitable Trust (09/JTA, C.A.J.), European Community's Seventh Framework Programme FP7/2009 (241955), SYSCILIA (E.E.D., N.K., C.A.J.), Distinguished George W. Brumley Professorship (N.K.), the NIH (grants NS052455 and NS04843, J.G.G.; DK068306 and DK090917, F.H.; U54 HG003067, E.S. Lander; EY021872, E.E.D.; HD042601, DK075972, DK072301, N.K.), Simons Foundation Autism Research Initiative (J.G.G.), and HHMI (F.H., S.F.-N., J.G.G.).

Supporting Online Material

www.sciencemag.org/cgi/content/full/science.1213506/DC1
Materials and Methods
SOM Text
Figs. S1 to S19
Tables S1 to S7
References
Movies S1 to S11

2 September 2011; accepted 23 December 2011
Published online 26 January 2012;
10.1126/science.1213506

Control of Nonapoptotic Developmental Cell Death in *Caenorhabditis elegans* by a Polyglutamine-Repeat Protein

Elyse S. Blum, Mary C. Abraham, Satoshi Yoshimura, Yun Lu, Shai Shaham*

Death is a vital developmental cell fate. In *Caenorhabditis elegans*, programmed death of the linker cell, which leads gonadal elongation, proceeds independently of caspases and apoptotic effectors. To identify genes promoting linker-cell death, we performed a genome-wide RNA interference screen. We show that linker-cell death requires the gene *pqn-41*, encoding an endogenous polyglutamine-repeat protein. *pqn-41* functions cell-autonomously and is expressed at the onset of linker-cell death. *pqn-41* expression is controlled by the mitogen-activated protein kinase kinase SEK-1, which functions in parallel to the zinc-finger protein LIN-29 to promote cellular demise. Linker-cell death is morphologically similar to cell death associated with normal vertebrate development and polyglutamine-induced neurodegeneration. Our results may therefore provide molecular inroads to understanding nonapoptotic cell death in metazoan development and disease.

Programmed cell death is essential for metazoan development and is required to sculpt organs, eliminate harmful cells, and counter cell division (*1*, *2*). Apoptosis, an extensively studied cell death process, requires caspase activation and is accompanied by a stereotypical morphological signature that includes chromatin compaction, cytoplasmic shrinkage, and no gross disruption of organelles (*3*). Mice lacking key apoptotic effectors such as caspase-3, caspase-9, Apaf-1, or Bax and Bak have mild defects and can survive to adulthood (*4*). Given the prevalence of cell death during mouse development (*5*), these observations raise the possibility that a nonapoptotic cell death pathway plays key roles in animal development. Although genes promoting necrotic cell death have been identified (*6*), they are not required for normal development (*7*). Indeed, genes dedicated to nonapoptotic developmental cell death have not been described.

We previously described the programmed death of the *Caenorhabditis elegans* linker cell during male reproductive system development (*8*). The linker cell leads the migration of the male gonad and dies between the fourth larval stage (L4) and adulthood (*9*). Linker cell demise is orchestrated by a cell-autonomous process independent of all *C. elegans* caspases and other known cell death genes (*8*, *10*). Electron microscopy (EM) of the dying linker cell reveals nonapoptotic features, including crenellation (indentation) of the nuclear envelope, uncondensed chromatin, and organelle swelling (Fig. 1C) (*8*). However, linker cell death does not require the unfolded protein response or other stress responses (tables S1 and S2). Similar morphological features are seen during normal developmental death of neurons in the vertebrate spinal cord and ciliary ganglion (*11*–*13*), suggesting that linker cell–type death is morphologically conserved.

To uncover the molecular mechanisms leading to linker cell death, we performed a genome-wide RNA interference (RNAi) screen to identify genes whose inactivation prevents linker cell death. We fed 18,132 bacterial clones, expressing double-stranded RNA (dsRNA) corresponding to 89% of predicted protein-coding *C. elegans* genes, individually to RNAi-sensitized males expressing a *lag-2* promoter::green fluorescent protein (GFP) linker cell reporter (*14*). The screen strategy was validated by recovery of the *lin-29* gene, previously identified as required for linker cell death (*8*). We recovered five additional RNAi clones leading to linker cell survival. Three clones also affect linker cell migration and may thus affect multiple aspects of linker cell fate. One of the remaining clones, derived from the gene *pqn-41* (Fig. 2A), caused linker cell survival in 20% of animals (Fig. 1A) with no obvious pleiotropic effects (fig. S1) and was further studied.

To confirm that the clone we identified inactivates *pqn-41*, we generated a deletion allele, *ns294*, in the gene. *pqn-41*(*ns294*) animals lack 337 nucleotides, removing portions of intron 17 and exon 18 of the predicted genomic structure (Fig. 2A). Consistent with our RNAi results, *pqn-41*(*ns294*) adult males possess an inappropriately surviving linker cell (Fig. 1, A and B). Furthermore, in *pqn-41*(*ns294*) mutants the linker cell persists at least 24 hours after the L4-adult transition (19% survival, n = 79 animals), suggesting that reducing *pqn-41* function not only delays but may block linker cell death. RNAi against *pqn-41* in *pqn-41*(*ns294*) animals does not increase linker cell survival (16% survival, n = 108 animals), suggesting that *ns294* may be a strong loss-of-function allele. To test whether *pqn-41*(*ns294*) mutants have defects in developmental apoptosis, we scored for surviving pharyngeal cells that normally die apoptotically (*15*) and observed none (n = 10 animals). Thus, the nonapoptotic nature of linker cell death may reflect distinct molecular machineries.

None of the *pqn-41*(*ns294*) surviving cells exhibit nuclear crenellation (n = 19 animals),

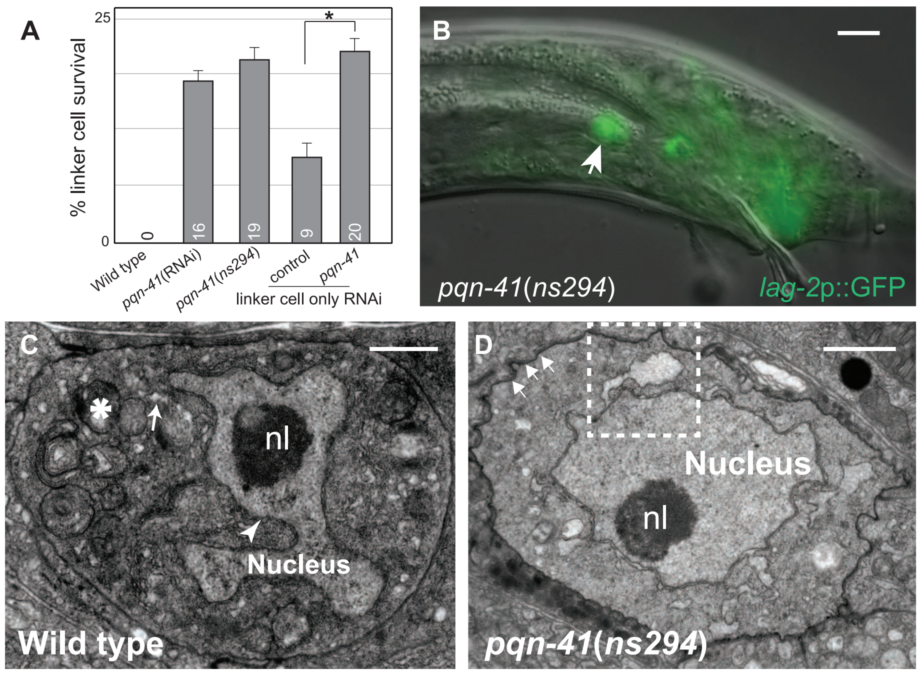

Fig. 1. PQN-41 is required for linker cell death. (**A**) Linker cell survival 2 to 4 hours after the L4 molt. Numbers, percentages. Error bars indicate SEM. *$P < 0.04$; $n \geq 50$ animals. Increased survival in *rde-1* may reflect reduced *let-7* miRNA function (*8*). (**B**) Adult *pqn-41*(*ns294*) male with surviving linker cell (arrow). Scale bar, 10 μm. (**C**) Electron micrograph of dying linker cell in a wild-type animal. nl, nucleolus. Arrow indictaes swollen ER, asterisk indicates mitochondria, and arrowhead indicates nuclear envelope crenellation. (**D**) Electron micrograph of linker cell in (B). Arrows indicate adhesion junctions. Dashed box is enlarged in fig. S2A. Scale bars in (C) and (D), 2 μm.

Laboratory of Developmental Genetics, The Rockefeller University, 1230 York Avenue, New York, NY 10065 USA.

*To whom correspondence should be addressed. E-mail shaham@rockefeller.edu

as observed with light microscopy. To examine surviving linker cell morphology at higher resolution, we performed serial-section EM. We found that the cell forms adherens junctions to surrounding epithelia (*8*) and that nuclear envelope crenellation is mild (n = 2 animals) (Fig. 1D). In both animals, however, organelle swelling was evident (Fig. 1D and fig. S2, A and B), suggesting that *pqn-41* may be required for nuclear crenellation but not organelle swelling.

To determine whether *pqn-41* functions cell-autonomously, we examined *rde-1*(*ne219*) RNAi–deficient mutants (*16*), containing a *mig-24* promoter::*rde-1* cDNA transgene restoring RNAi only in the linker cell (*17*). Feeding *pqn-41* RNAi bacteria to these mutants resulted in linker cell death defects similar to systemic RNAi (Fig. 1A), suggesting that *pqn-41* functions cell-autonomously. To further examine this issue, we assessed whether expression of *pqn-41* within the linker cell can restore linker cell death to *pqn-41*(*ns294*) mutants. The *pqn-41* locus encodes at least three alternate transcripts, which we designated *pqn-41*A, -B, and -C (Fig. 2). *pqn-41*A/B span the locus, differing by alternative in-frame exon b. *pqn-41*C mRNA initiates immediately upstream of exon b (Fig. 2B). We found that expression of *pqn-41*C is sufficient to promote linker cell demise in *pqn-41*(*ns294*) mutants (Fig. 2D), strongly suggesting that *pqn-41* functions cell autonomously to promote linker cell death.

*pqn-41*C encodes a protein composed of runs of glutamine residues with one to eight residues per run (Fig. 2C and fig. S3A). Of the 427 *pqn-41*C codons, 151 encode glutamine. The average number of nonglutamine amino acids interrupting adjacent glutamine residues in PQN-41C is 1.8 and is the second smallest in the *C. elegans* proteome (fig. S4). Glutamine-rich domains are hallmarks of some neurodegenerative disease (ND) proteins and of Q/N-rich prions (*18*). Both domain classes can adopt coiled-coil structures (*18*). Similarly, PQN-41C is predicted to contain six coiled-coil motifs demarcated by flanking prolines (CC1-6) (fig. S5). Three sequences outside the coiled-coil motifs are conserved among nematodes (CD1-3) (fig. S3B), as is the overall proportion of glutamines (38, 37, and 37% in *C. remanei*, *C. brenneri*, and *C. briggsae*, respectively).

ND and Q/N-rich polyglutamine proteins tend to aggregate in cells (*18*). Similarly, we found that a PQN-41C::GFP protein forms cytoplasmic aggregates in the linker cell (Fig. 3G), suggesting that PQN-41C shares structural features with these proteins. To understand the importance of the coiled-coil and conserved regions to PQN-41C function, we examined the effects of protein truncations on the ability of PQN-41C to rescue *pqn-41*(*ns294*) mutants (fig. S6A). Truncation of consecutive pairs of coiled-coil domains abolishes PQN-41C rescuing activity. Coil-breaking prolines in coiled-coil domains 2, 4, and 6 also reduce rescue efficiency. Thus, sequences encoding the coiled-coil regions are

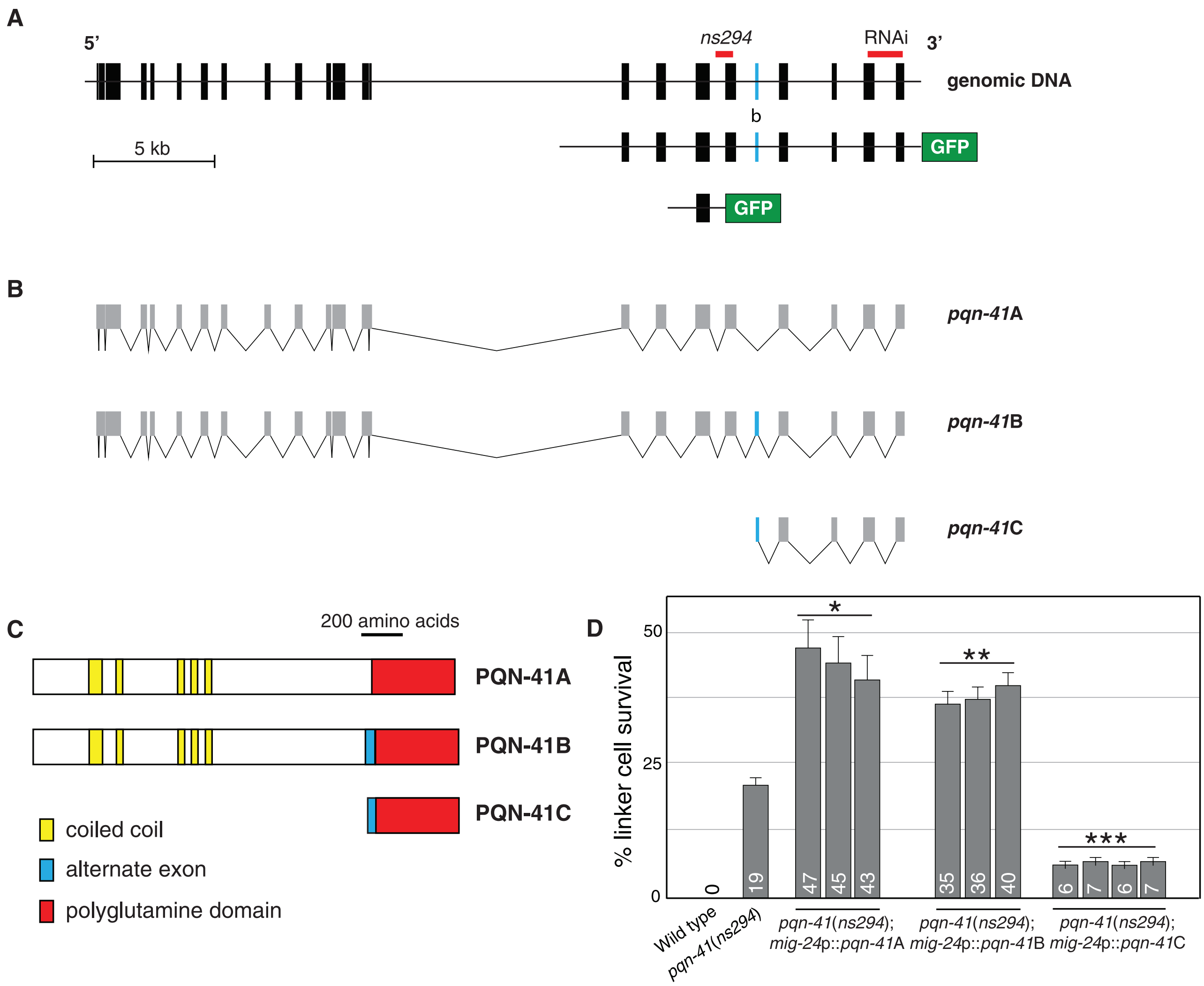

Fig. 2. PQN-41C promotes linker cell death. (**A**) *pqn-41* genomic region. Alternative exon b is labeled with the letter "b." GFP not to scale. (**B**) Three mRNAs generated by the *pqn-41* region. (**C**) Predicted protein structures for mRNAs in (B). (**D**) Linker cell survival in *pqn-41*(*ns294*) mutants expressing the indicated cDNAs. Numbers are percentages. Error bars indicate SEM. Asterisks signify different from *pqn-41*(*ns294*): *P < 0.0009, n = 138 animals; **P < 0.0007, n = 236 animals; ***P < 0.004, n = 229 animals.

important for PQN-41C function. Truncation of conserved domain CD3 also abolishes rescue, whereas deletion of the CD1/2 domains has only modest effects.

Expression of polyglutamine repeats is often toxic. However, PQN-41C does not exhibit nonspecific cellular toxicity. Expression of PQN-41C in the linker cell of *pqn-41*(*ns294*) males starting in L2 larvae did not cause precocious cell death (*n* = 227 animals). Rather, cell death was initiated appropriately at the L4-adult transition. Likewise, expression of PQN-41C in the hermaphrodite distal tip cells or the anchor cell did not kill these cells (*n* > 38 animals for each). Thus, PQN-41C requires the appropriate cellular context to promote death.

To investigate the functions of the *pqn-41*A/B transcripts, we tested whether they could restore linker cell death to *pqn-41*(*ns294*) mutants. We found that both transcripts enhance linker cell survival in *pqn-41*(*ns294*) (Fig. 2D) and wild-type animals (fig. S6B). Although other polyglutamine proteins can protect cells from polyglutamine toxicity (*19*), it is puzzling that PQN-41A/B protect the linker cell, given that both proteins contain the glutamine-rich sequences of PQN-41C. It is possible that the N terminus of PQN-41A/B overrides the cell death–promoting activity of the glutamine-rich domain. Supporting this idea, the N terminus is sufficient to block linker cell death (fig. S6B). Furthermore, PQN-41A/B::GFP proteins expressed in the linker cell fail to aggregate (Fig. 3, E and F).

ND and Q/N-rich proteins often contain coiled-coil motifs outside the glutamine-rich domain or associate with proteins containing such domains (*18*). Similarly, PQN-41A and -B N-termini are predicted to contain at least five coiled-coil motifs (fig. S7). We found, however, that deletion of sequences encoding different coiled-coil domains did not abolish ectopic survival induced by *pqn-41*B (fig. S6B).

We next sought to characterize *pqn-41* expression. A 13-kb DNA fragment derived from the *pqn-41* locus and fused to *gfp* sequences is broadly expressed in transgenic animals in most cells starting in the embryo (Figs. 2A and 3). However, expression is only switched on in the linker cell as the cell begins to die (Fig. 3, A to D). A 2.5-kb DNA subfragment derived from this reporter promotes *gfp* expression nearly exclusively in the linker cell, and only upon cell death initiation (Fig. 2A and fig. S8). The sequences driving linker cell expression of *pqn-41* overlap with those deleted in *pqn-41*(*ns294*) mutants and lie upstream of the *pqn-41*C start (Fig. 2A), suggesting that they may control *pqn-41*C expression.

We previously demonstrated a role for the LIN-29 zinc-finger transcription factor in linker cell death (fig. S9B) (*8*). *lin-29* is expressed in the linker cell before the cell begins to die, suggesting that *lin-29* might control *pqn-41* expression. However, *pqn-41* expression is only modestly disturbed in *lin-29*(RNAi) males (Fig. 4B and fig. S10A). To identify strong regulators of *pqn-41* expression, we tested clones identified in our RNAi screen. A clone directed against the gene *tir-1*—encoding a p38 mitogen-activated protein kinase (MAPK) scaffolding protein important for *C. elegans* innate immunity, neuronal differentiation, and stress responses (*20*, *21*)—blocks linker cell death, as does the *tir-1*(*qd4*) genetic lesion (fig. S9B). We tested whether other genes involved in innate immunity and stress affect linker cell death. Two independent alleles of the p38 cascade MAPKK gene *sek-1* strongly block linker cell death (Fig. 4A, fig. S9, and table S2); however, none of the other genes we tested had an effect (table S2). Thus, *sek-1* promotes linker cell death independently of innate immunity, stress response, and neuronal differentiation pathways. Unlike in *lin-29*(RNAi) animals, *pqn-41* expression is often not detected in *sek-1* mutants (Fig. 4B), suggesting that *sek-1* functions upstream of *pqn-41*. Consistent with this idea, double mutants carrying a strong loss-of-function lesion in *sek-1* and the *pqn-41*(*ns294*) allele have a survival defect similar to that of *sek-1* mutants alone (fig. S9B). Furthermore, EM of surviving linker cells in *sek-1*(*ag1*) mutants reveals no nuclear crenellation, but some endoplasmic reticulum (ER) swelling (*n* = 2 animals) (Fig. 4C), which is consistent with regulation of *pqn-41* by *sek-1*. The differential effects of *lin-29* and *sek-1* on *pqn-41* expression suggest that these genes function independently. Indeed, we found that *sek-1* expression does not require *lin-29* function, and vice versa (fig. S10, B and C). Furthermore, *lin-29* mutants do not exhibit the extent of ER swelling of *sek-1* mutants (*n* = 3 animals) (fig. S11). Last, strong loss-of-function mutations in *lin-29* and *sek-1* interact additively (fig. S9B), suggesting that these genes may indeed function in parallel.

To determine where *sek-1* functions, we examined its expression using a *sek-1* genomic region::GFP reporter. This transgene was expressed in the linker cell throughout the cell's development (Fig. 4D). Expression of a *sek-1* cDNA using the *mig-24* linker cell–specific promoter restored cell death in *sek-1* mutants to a greater extent than did expression of *sek-1* using the *lin-48* promoter, which is active in surrounding cells (Fig. 4A) (*22*). These results support a cell-autonomous role for *sek-1* in linker cell death.

The studies described here—as well as the morphological similarities between linker cell death and vertebrate developmental cell death—raise the possibility that PQN-41–like proteins might mediate nonapoptotic developmental cell death in vertebrates. The vertebrate proteins MED12

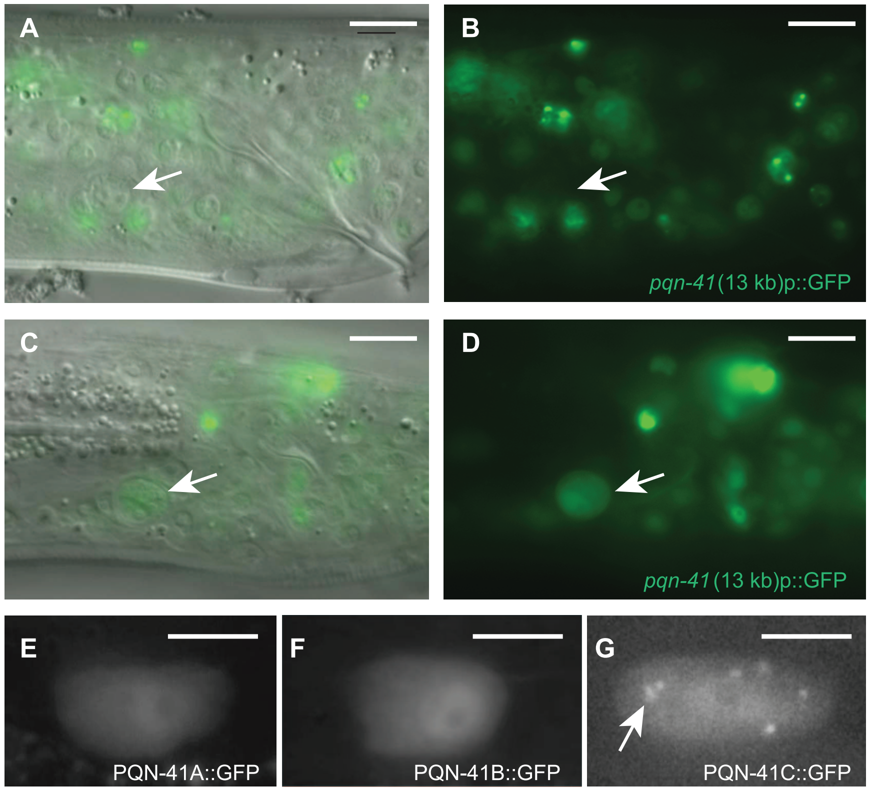

Fig. 3. PQN-41 is expressed as the linker cell dies. (**A**) Differential interference contrast and fluorescence image of late L4 male expressing the 13 kb *pqn-41*::GFP reporter in Fig. 2A. Arrow indicates linker cell. (**B**) Fluorescence image only. (**C**) Same as (A) except in an older L4 animal. (**D**) Fluorescence image only. (**E** to **G**) Expression of *mig-24* promoter::*pqn-41*A, -B, and -C cDNA GFP translational fusions, respectively. Arrow indicates cytoplasmic puncta. Scale bars, 10 μm [(A) to (D)], 5 μm [(E) to (G)].

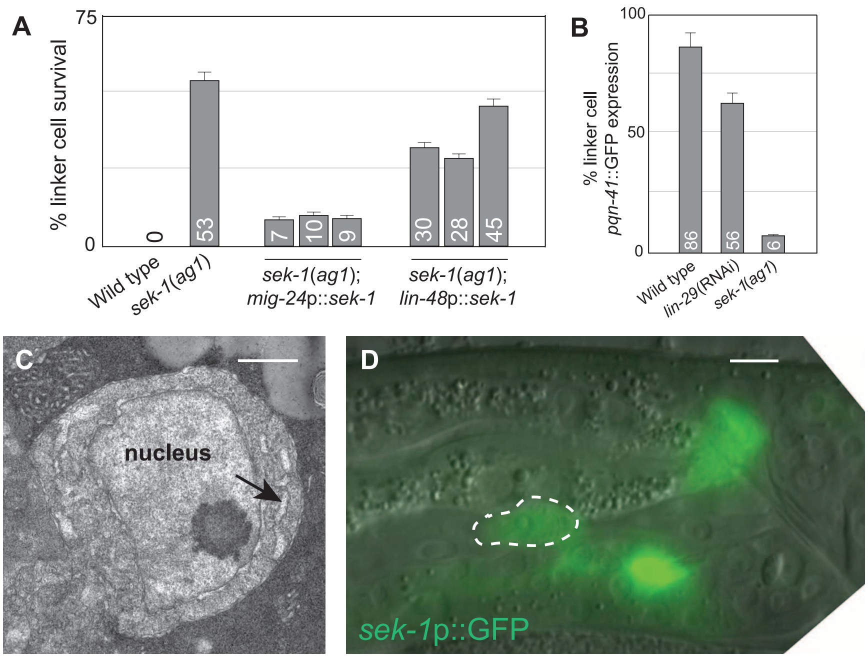

Fig. 4. SEK-1 MAPKK is required for linker cell death. (**A**) Linker cell survival in *sek-1*(*ag1*) mutants expressing the indicated promoter::cDNA constructs. Numbers are percentages. Error bars indicate SEM; $n \geq 70$ animals. (**B**) Expression of the 2.5 kb *pqn-41*::GFP reporter in late L4 (wild-type) or young adult (*lin-29*, *sek-1*) animals ($n \geq 50$ animals). (**C**) Electron micrograph of linker cell in fig. S9A. Arrow indicates swollen ER. Scale bar, 2 μm. (**D**) Late L4 male expressing a *sek-1* promoter::GFP reporter. Dashed line, linker cell. Scale bar, 5 μm.

and p400 may be good candidates for such proteins. They are the most similar in primary sequence structure to PQN-41, contain glutamine-rich C termini (fig. S12), are nuclearly localized, and are important in tumor formation (*23*, *24*). Intriguingly, EM studies reveal that nuclear envelope crenellation is strongly associated with several polyQ expansion diseases (fig. S13). Our studies thus raise the possibility that these disease proteins might promote neurodegeneration by inappropriately activating a linker cell death–type process.

References and Notes

1. M. C. Abraham, S. Shaham, *Trends Cell Biol.* **14**, 184 (2004).
2. Y. Fuchs, H. Steller, *Cell* **147**, 742 (2011).
3. J. F. Kerr, A. H. Wyllie, A. R. Currie, *Br. J. Cancer* **26**, 239 (1972).
4. N. Honarpour *et al.*, *Dev. Biol.* **218**, 248 (2000).
5. E. Coucouvanis, G. R. Martin, *Cell* **83**, 279 (1995).
6. W. Declercq, T. Vanden Berghe, P. Vandenabeele, *Cell* **138**, 229 (2009).
7. K. Newton, X. Sun, V. M. Dixit, *Mol. Cell. Biol.* **24**, 1464 (2004).
8. M. C. Abraham, Y. Lu, S. Shaham, *Dev. Cell* **12**, 73 (2007).
9. J. E. Sulston, D. G. Albertson, J. N. Thomson, *Dev. Biol.* **78**, 542 (1980).
10. H. M. Ellis, H. R. Horvitz, *Cell* **44**, 817 (1986).
11. G. Pilar, L. Landmesser, *J. Cell Biol.* **68**, 339 (1976).
12. R. W. Oppenheim *et al.*, *J. Neurosci.* **21**, 4752 (2001).
13. T. Borsello, V. Mottier, V. Castagné, P. G. Clarke, *J. Comp. Neurol.* **453**, 361 (2002).
14. F. Simmer *et al.*, *Curr. Biol.* **12**, 1317 (2002).
15. R. E. Ellis, H. R. Horvitz, *Development* **112**, 591 (1991).
16. H. Tabara *et al.*, *Cell* **99**, 123 (1999).
17. K. K. Tamai, K. Nishiwaki, *Dev. Biol.* **308**, 562 (2007).
18. F. Fiumara, L. Fioriti, E. R. Kandel, W. A. Hendrickson, *Cell* **143**, 1121 (2010).
19. P. W. Faber, C. Voisine, D. C. King, E. A. Bates, A. C. Hart, *Proc. Natl. Acad. Sci. U.S.A.* **99**, 17131 (2002).
20. N. T. Liberati *et al.*, *Proc. Natl. Acad. Sci. U.S.A.* **101**, 6593 (2004).
21. C. F. Chuang, C. I. Bargmann, *Genes Dev.* **19**, 270 (2005).
22. A. D. Johnson, D. Fitzsimmons, J. Hagman, H. M. Chamberlin, *Development* **128**, 2857 (2001).
23. M. Fuchs *et al.*, *Cell* **106**, 297 (2001).
24. N. Mäkinen *et al.*, *Science* **334**, 252 (2011).

Acknowledgments: We thank J. Darnell and Shaham lab members for discussions; N. Tishbi for technical assistance; and D. Kim, C. Bargmann, M. Kinet, M. Kato, P. Sternberg, K. Nishiwaki, and K. Matsumoto for reagents. Some nematode strains used in this work were provided by the *Caenorhabditis* Genetics Center, funded by the National Center for Research Resources. E.S.B. is supported in part by the Rockefeller Women & Science Fellowship Program and NIH training grant CA09673. S.S. is supported by NIH grant R01HD042680.

Supporting Online Material

www.sciencemag.org/cgi/content/full/335/6071/970/DC1
Materials and Methods
Figs. S1 to S13
Tables S1 and S2
References (*25*–*65*)

11 October 2011; accepted 4 January 2012
10.1126/science.1215156

The Robustness and Restoration of a Network of Ecological Networks

Michael J. O. Pocock,*† Darren M. Evans,‡ Jane Memmott

Understanding species' interactions and the robustness of interaction networks to species loss is essential to understand the effects of species' declines and extinctions. In most studies, different types of networks (such as food webs, parasitoid webs, seed dispersal networks, and pollination networks) have been studied separately. We sampled such multiple networks simultaneously in an agroecosystem. We show that the networks varied in their robustness; networks including pollinators appeared to be particularly fragile. We show that, overall, networks did not strongly covary in their robustness, which suggests that ecological restoration (for example, through agri-environment schemes) benefitting one functional group will not inevitably benefit others. Some individual plant species were disproportionately well linked to many other species. This type of information can be used in restoration management, because it identifies the plant taxa that can potentially lead to disproportionate gains in biodiversity.

All species are embedded in complex networks of interactions (*1*). Modeling food webs, and more generally, species' interaction networks, has advanced the understanding of the robustness of ecosystems in the face of species loss (*1*, *2*). A key question, of applied relevance, is how the robustness of different species' interaction networks varies and whether it covaries. This is particularly important given the current rate of species' declines and extinctions (*3*) and its consequent impact on ecosystem function. Currently, understanding of species' interaction networks is mostly limited to partial subsets of whole ecosystems [but see (*4*, *5*)]. However, studying the interdependence of different networks is important (*6*) and can alter our perspective on network fragility, a fact already shown with nonecological examples (*7*). Moreover, this approach can be used to identify keystone species in the overall network; if these species are made

School of Biological Sciences, University of Bristol, Woodland Road, Bristol BS8 1UG, UK.

*To whom correspondence should be addressed. E-mail: michael.pocock@ceh.ac.uk
†Present address: NERC Centre for Ecology & Hydrology, Crowmarsh Gifford, Wallingford, Oxfordshire OX10 8BB, UK.
‡Present address: Department of Biological Sciences, Hardy Building, University of Hull, Cottingham Road, Hull HU6 7RX, UK.

the focus of restoration efforts, then disproportionate gains for biodiversity are a real possibility.

In our study, we overcame the logistical constraints of studying multiple species' interaction networks in order to more fully test for variation in their robustness and fragility. Our networks comprised 1501 quantified unique interactions between a total of 560 taxa, comprising plants and 11 groups of animals: those feeding on plants (butterflies and other flower visitors, aphids, seed-feeding insects, and granivorous birds and mammals) and their dependants (primary and secondary aphid parasitoids, leaf-miner parasitoids, parasitoids of seed-feeding insects, and rodent ectoparasites) (Fig. 1). We selected these groups because sampling their interactions is tractable in the field; they encompass a wide taxonomic and functional range; and they include animals regarded as bioindicators, such as birds and butterflies (*8*, *9*), and as ecosystem service providers, such as pollinators and parasitoids (*10*, *11*) (table S1). The networks thus included trophic (*12*), mutualistic (*13*), and parasitic (*4*) interactions. Previously, these networks have only been studied in isolation because they are logistically difficult to sample and because most terrestrial ecologists focus on only a taxonomic subset of species (such as birds, butterflies, or bumblebees).

We worked at the whole-farm scale on a 125-ha farm (Norwood Farm, Somerset, UK) and undertook replicated sampling in all habitats, both cropped and noncropped, over 2 years (*14*). The abundance of each of the 560 taxa was quantified from field surveys. Interaction frequencies in most networks were quantified directly from field sampling (and thus represent a sample of each taxon's realized niche). Logistical constraints stopped us from identifying leaf-mining insects, so leaf-miner parasitoids were treated as if they were linked directly to host plants [thus assuming them to be generalist on leaf-miners that were host-specific; an approach justified in (*14*)]. For birds, mammals, and butterflies, their interactions with plants were based on prior knowledge of their interactions (from the literature) and were quantified with models of foraging behavior [details in (*14*); and thus approximated the taxon's realized niche]. Intensive study of a single site, as in many other food web studies [such as (*15*, *16*)], provided us with spatiotemporal replication across habitats and seasons and with detailed data that we could not have obtained from extensive surveys of multiple farms. We sampled this particular farm because we expected it to be relatively biodiverse (it was managed organically at relatively low intensity and was subject to an agri-environment scheme). This allowed us to simulate species loss from a biodiverse site, which provided stronger inference than if we had simulated the gain of (by definition, unrecorded) species from a low-diversity site.

We evaluated the robustness of 11 groups of animals, comprising each trophic level in the

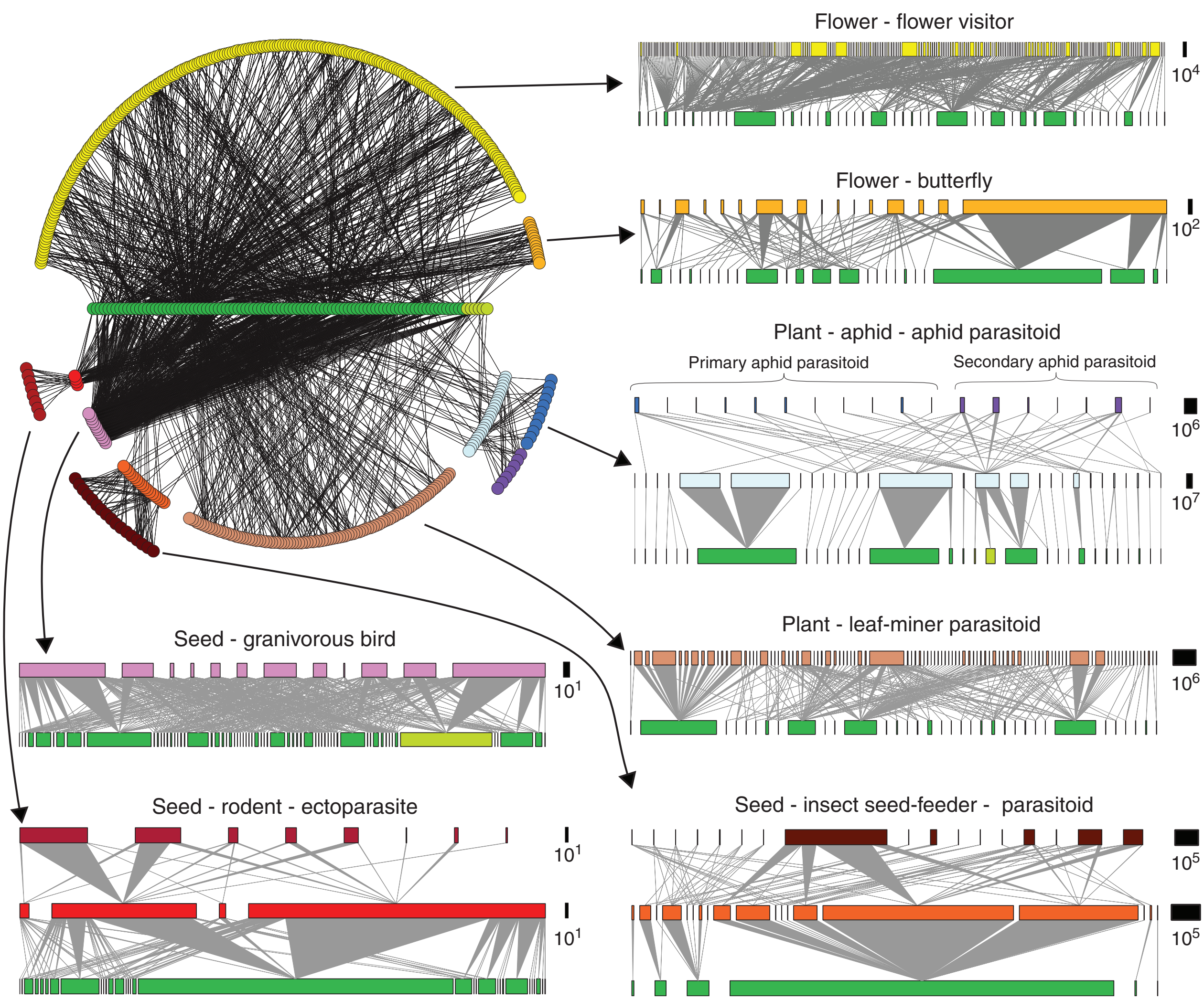

Fig. 1. Species' interaction networks at Norwood Farm, Somerset, UK. The entire network of networks is shown at top left (in which each circle represents one species), and quantitative visualizations are shown for each of the seven quantified individual networks (in which each block is a species, and the width of blocks of each color represents relative abundance). Details of the networks are given in table S1 and (*14*). Dark green and light green circles and blocks indicate noncrop and crop plants, respectively, whereas other colors indicate animal groups. Scale bars indicate the abundance of animal taxa. Plants are scaled in proportion to their interactions with animals in each network.

seven linked networks, by simulating the sequential removal of plant taxa 20,000 times (*14*). In our model, animal taxa became disconnected (a "secondary extinction") when all their food species became extinct; depending on the animal group, this was either plants or the animals they preyed on. In simulating the loss of plants, we used an established method (*12*, *17*) and assumed bottom-up rather than top-down regulation of the animals, as justified by (*18*). This ecologically informed approach has practical application, because plants can be managed more directly [such as through field rotations or via agri-environment schemes (*19*)] than can putative animal bioindicators. We considered two complementary models of robustness: (i) where all taxa were weighted equally (R_S) (*17*) and (ii) the quantitative equivalent, where taxa were weighted by their abundance (R_Q) (*20*), calculating $\overline{R}$ as the average area under the curve of the secondary extinctions against primary extinctions across the 20,000 simulations (*21*). Given this approach, our models can be interpreted equally as representing the cascading negative effects of plant loss and the cascading positive effects of plant restoration.

We found that under randomized sequences of loss of plant taxa, the bird seed-feeder, rodent seed-feeder, rodent ectoparasite, and secondary aphid parasitoid networks were most robust ($\overline{R}\rightarrow 1$; Fig. 2). The robustness of the first two networks was derived from literature-based interactions, so they represent the entire realized niche rather than a sample of the realized niche, whereas the third depended on a network derived from literature-based interactions. However, all of our reported conclusions are robust to the exclusion of literature-derived networks and to variation in sampling efficiency [supporting online material (SOM) part 5 and tables S4 and S7]. Aphid,

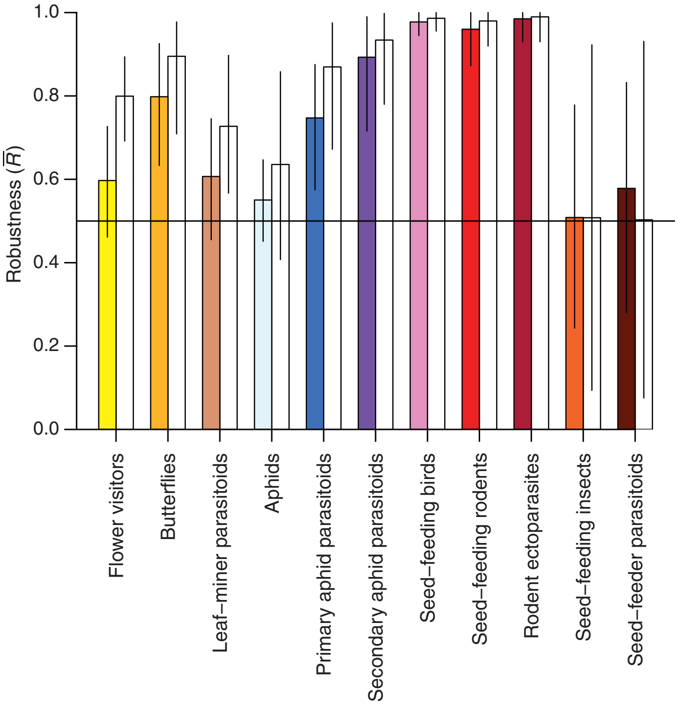

Fig. 2. The average robustness of the 11 animal groups (median $R \pm 90\%$ confidence interval). The colored bars, matching the colors in Fig. 1, show R_S and the adjoining white bars show R_Q. As $\overline{R}\rightarrow 1$, animal groups are increasingly robust to the simulated sequential loss of plant taxa, whereas for animal groups with low robustness, $\overline{R}\rightarrow 0.5$.

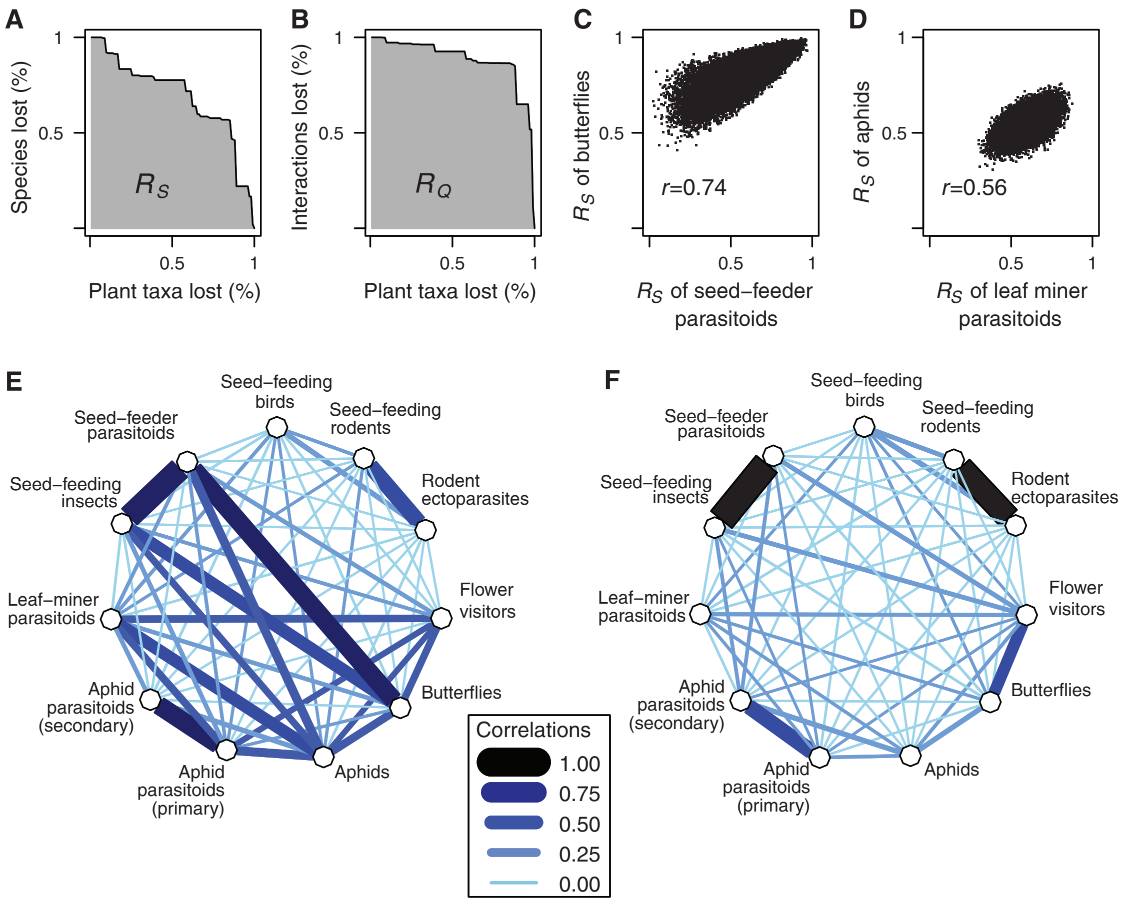

Fig. 3. Correlations between the robustness of animal groups and the simulated loss of plant taxa in networks of the farmland species' interaction network. The robustness of flower visitors to one random sequence of plant loss is the area under the curve for (**A**) the qualitative case and (**B**) the quantitative case. The pairwise correlations in robustness varied in the 20,000 simulations of the sequential loss of plant taxa, as two examples (**C** and **D**) show. These pairwise correlations were summarized to show the connectivity between all animal groups, considering (**E**) R_S and (**F**) R_Q.

insect seed feeder, and pollinator networks appeared more fragile ($\overline{R}$→0.5; Fig. 2). We tested whether robustness was related to other network metrics (table S4). We found that network robustness was related to network generalization [the relationship of H_2', a measure of niche differentiation (*22*, *23*), to R_S: $\beta = -0.903$, $t_9 = -2.316$, $P = 0.046$, and to R_Q: $\beta = -0.545$, $t_9 = -6.131$, $P < 0.001$]. We also found that network robustness was not related to network complexity [the relationship of e^{H_2}, a measure of interaction diversity (*22*, *23*), to R_S: $\beta = 0.018$, $t_9 = 0.231$, $P = 0.823$, and to R_Q: $\beta = 0.099$, $t_9 = 1.769$, $P = 0.111$]. Our findings provide no positive support for the long-debated relationship between complexity and stability, in common with other empirical studies (*24*). The relationship of robustness to generalization is probably to be explained through the nestedness that is characteristic of many ecological networks and which confers robustness on networks (*24*, *25*).

Although the animals in the networks all depended (directly or indirectly) on plant taxa, we found that the robustness of some networks covaried, but overall the covariance was less than expected as compared to a null model (Fig. 3 and SOM part 3). None of the correlations was substantially negative (minimum $r = -0.05$; table S5), so sequences of plant loss that were relatively benign for one animal group were never consistently unfavorable for another group. Although some individual pairwise correlations were strongly positive (Fig. 3, E and F), these correlations were between animal groups that were linked either trophically (such as fleas and rodents) or through shared resources (such as butterflies and seed-feeding insects that shared plant hosts).

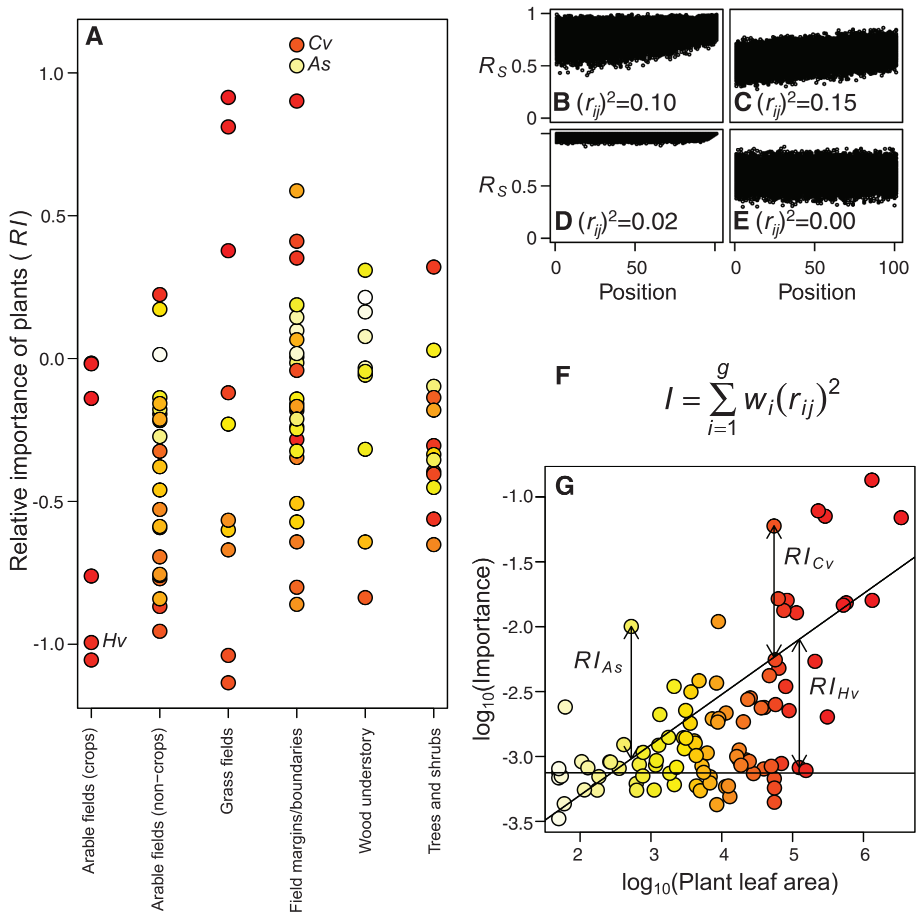

Fig. 4. The relative importance of the plants in the Norwood Farm network of quantified networks. (**A**) The relative importance of the plants varied by habitat with colors from white to red representing increasing abundance, as shown in (G), and was calculated as shown in this workflow (**B** to **G**). The importance of each species of plant (j) for each animal group (i) was the coefficient of determination (r_{ij}^2); that is, the square of the correlation coefficient, between the calculated robustness with plants removed in random order and the position of the plant in that order, as exemplifed for (B) *Rubus fruticosus* and butterflies, (C) *Anthriscus sylvestris* and flower visitors, (D) *Persicaria* spp. and birds, and (E) *Anthriscus sylvestris* and leaf-miner parasitoids. (F) The weighted sums of these coefficients of determination across groups (g) gave the importance (I) of each plant taxon; in this case, the groups were weighted according to their uniqueness (SOM part 4). (G) Abundance [assessed as leaf area of the plants (*14*, *31*)] was strongly related to importance for a subset of plant taxa, so the relative importance of each plant taxon (RI) was calculated as the residual from the steeper regression line (determined by a two-component mixture regression model), exemplifed by *Cirsium vulgare* (*Cv*), *Anthriscus sylvestris* (*As*), and *Hordeum vulgare* (*Hv*).

The practical implication of these findings for our agroecosystem is that agri-environmental management of plants that is targeted to produce cascading positive effects for one animal group (such as farmland insect pollinators) will have varying (but not systematically negative) effects on other animal groups. Such results have indeed been found with empirical assessments of agri-environment scheme success more generally (*26*).

Our approach, considering the robustness of the linked networks, provides information on the network of networks. To reveal the varying importance of individual species within these linked networks, we identified the most important plants within the networks: keystone (*27*) plant taxa that have substantial and disproportionate cascading effects across the multiple networks (Fig. 4). In practical terms, this information could be used to focus restoration management on plant taxa with the greatest potential to achieve efficient and positive results for biodiversity and the resultant ecosystem services. We found that the taxa that were most important relative to their abundance [that had the most influence on modeled robustness across the networks (*14*)] tended to (i) be nonwoody taxa, (ii) occur in noncropped ground, and (iii) be members of the Apiaceae and Asteraceae families (Fig. 4, table S6, and fig. S3). Agri-environmental policies encouraging plants with high relative importance could provide benefits for biodiversity and so potentially support ecosystem service provision, but because some of these plants are typically regarded as farmland weeds, this could be controversial. Any such policies would need to consider how these relationships are affected by the local farming system and landscape context (*28*), and would need to consider the balance of practicality (how these plants are affected by agricultural practice, including arable crop rotations), cost (impacts on crop yield/profitability and detrimental effects on rare farmland plants of conservation concern), and benefits (cascading effects on biodiversity and, potentially, ecosystem services).

Agricultural change has been one of the main drivers of biodiversity loss in recent times (*29*), and yet during this period the importance of ecosystem services provided by biodiversity, even in intensive agricultural systems, has become well recognized (*30*). Our approach, which included empirically constructing multiple linked networks for cropped and seminatural habitat at a whole-farm extent and modeling their response to environmental change, could become increasingly important for research on biodiversity and ecosystem services. The optimist's scenario, of management targeted to benefit one animal group and inevitably resulting in multiple benefits for many different groups, was not supported by our modeling of empirical species' interaction data from this site. Therefore, in order to bring benefits to a wide range of taxa, it is essential to have focused and ecologically informed management, such as the targeted management of specific plant taxa based on their cascading effects within a network of networks.

References and Notes

1. J. M. Montoya, S. L. Pimm, R. V. Solé, *Nature* **442**, 259 (2006).
2. E. Thébault, C. Fontaine, *Science* **329**, 853 (2010).
3. S. H. M. Butchart *et al.*, *Science* **328**, 1164 (2010).
4. K. D. Lafferty, A. P. Dobson, A. M. Kuris, *Proc. Natl. Acad. Sci. U.S.A.* **103**, 11211 (2006).
5. C. J. Melián, J. Bascompte, P. Jordano, V. Krivan, *Oikos* **118**, 122 (2009).
6. C. Fontaine *et al.*, *Ecol. Lett.* **14**, 1170 (2011).
7. S. V. Buldyrev, R. Parshani, G. Paul, H. E. Stanley, S. Havlin, *Nature* **464**, 1025 (2010).
8. M. A. McGeogh, *Biol. Rev. Camb. Philos. Soc.* **73**, 181 (1998).
9. European Environment Agency, *Assessing Biodiversity in Europe: The 2010 Report* (European Environment Agency, Copenhagen, 2010).
10. J. E. Losey, M. Vaughan, *Bioscience* **56**, 311 (2006).
11. H. S. Sandhu, S. D. Wratten, R. Cullen, B. Case, *Ecol. Econ.* **64**, 835 (2008).
12. J. A. Dunne, R. J. Williams, N. D. Martinez, *Ecol. Lett.* **5**, 558 (2002).
13. J. Bascompte, P. Jordano, C. J. Melián, J. M. Olesen, *Proc. Natl. Acad. Sci. U.S.A.* **100**, 9383 (2003).
14. Materials and methods are available as supporting material on *Science* Online.
15. S. J. Hall, D. Raffaelli, *J. Anim. Ecol.* **60**, 823 (1991).
16. F. J. F. Van Veen, C. B. Müller, J. K. Pell, H. C. J. Godfray, *J. Anim. Ecol.* **77**, 191 (2008).
17. J. Memmott, N. M. Waser, M. V. Price, *Proc. Biol. Sci.* **271**, 2605 (2004).
18. C. Scherber *et al.*, *Nature* **468**, 553 (2010).
19. M. R. Wade, G. M. Gurr, S. D. Wratten, *Philos. Trans. R. Soc. London Ser. B* **363**, 831 (2008).
20. C. N. Kaiser-Bunbury, S. Muff, J. Memmott, C. B. Müller, A. Caflisch, *Ecol. Lett.* **13**, 442 (2010).
21. E. Burgos *et al.*, *J. Theor. Biol.* **249**, 307 (2007).
22. N. Blüthgen, *Basic Appl. Ecol.* **11**, 185 (2010).
23. N. Blüthgen, F. Menzel, N. Blüthgen, *BMC Ecol.* **6**, 9 (2006).
24. J. M. Tylianakis, E. Laliberté, A. Nielsen, J. Bascompte, *Biol. Conserv.* **143**, 2270 (2010).
25. J. Bascompte, P. Jordano, J. M. Olesen, *Science* **312**, 431 (2006).
26. D. Kleijn *et al.*, *Ecol. Lett.* **9**, 243, discussion 254 (2006).
27. L. S. Mills, M. E. Soulé, D. F. Doak, *Bioscience* **43**, 219 (1993).
28. D. Gabriel *et al.*, *Ecol. Lett.* **13**, 858 (2010).
29. J. R. Krebs, J. D. Wilson, R. B. Bradbury, G. M. Siriwardena, *Nature* **400**, 611 (1999).
30. Millennium Ecosystem Assessment, *Ecosystems and Human Well-being: Biodiversity Synthesis* (World Resources Institute, Washington, DC, 2005).
31. M. J. O. Pocock, D. M. Evans, J. Memmott, *Agric. Ecosyst. Environ.* **135**, 279 (2010).

Acknowledgments: J. Brooks helped throughout the project, and 14 field assistants helped with field and laboratory work; 15 taxonomists (listed in SOM text) assisted with species' identification; and Cate Le Grice-Mack (the landowner) gave full support throughout the project. The authors declare no competing interests. The interaction data are available from the Dryad Digital Repository, doi:10.5061/dryad.3s36r118. The project was supported by the Biotechnology and Biological Sciences Research Council (grant no. BBD0156341) and the Department for Environment, Food and Rural Affairs (grant no. BD2303).

Supporting Online Material
www.sciencemag.org/cgi/content/full/335/6071/973/DC1
Materials and Methods
SOM Text
Figs. S1 to S4
Tables S1 to S7
References (*32–80*)

6 October 2011; accepted 19 December 2011
10.1126/science.1214915

Botulinum Neurotoxin Is Shielded by NTNHA in an Interlocked Complex

Shenyan Gu,[1] Sophie Rumpel,[2] Jie Zhou,[1] Jasmin Strotmeier,[2] Hans Bigalke,[2] Kay Perry,[3] Charles B. Shoemaker,[4] Andreas Rummel,[2] Rongsheng Jin[1]*

Botulinum neurotoxins (BoNTs) are highly poisonous substances that are also effective medicines. Accidental BoNT poisoning often occurs through ingestion of *Clostridium botulinum*–contaminated food. Here, we present the crystal structure of a BoNT in complex with a clostridial nontoxic nonhemagglutinin (NTNHA) protein at 2.7 angstroms. Biochemical and functional studies show that NTNHA provides large and multivalent binding interfaces to protect BoNT from gastrointestinal degradation. Moreover, the structure highlights key residues in BoNT that regulate complex assembly in a pH-dependent manner. Collectively, our findings define the molecular mechanisms by which NTNHA shields BoNT in the hostile gastrointestinal environment and releases it upon entry into the circulation. These results will assist in the design of small molecules for inhibiting oral BoNT intoxication and of delivery vehicles for oral administration of biologics.

The seven serotypes of botulinum neurotoxin (BoNT) (named A to G) are sequence-specific endopeptidases. They invade nerve cells at neuromuscular junctions, where they inhibit the release of the neurotransmitter acetylcholine by cleaving SNAREs (soluble *N*-ethylmaleimide–sensitive factor attachment protein receptors), and subsequently paralyze the affected muscles (*1*). Although BoNT poisoning often occurs through oral ingestion of tainted food products, the molecular mechanism by which BoNTs avoid destruction in the hostile environment of the gastrointestinal (GI) tract is unknown.

Naturally occurring BoNTs are protected within progenitor toxin complexes (PTCs), which are high molecular weight multiprotein complexes composed of the BoNT and several nontoxic neurotoxin-associated proteins (NAPs) (*2*). The NAPs include the 140-kD NTNHA (nontoxic nonhemagglutinin), which together with BoNT forms the minimally functional PTC (M-PTC), and three hemagglutinin (HA) proteins, which assemble with the M-PTC and have been suggested to facilitate BoNT transcytosis across the intestinal barrier (*1*, *3*). The protecting function of the M-PTC is sufficiently effective that it reduces the oral median lethal dose (LD_{50}) of BoNT 10- to 20-fold compared with free BoNT (*4*, *5*). Intriguingly, the protected BoNT is released from the PTC upon transition from acidic to neutral pH, as occurs during absorption from the intestine into the bloodstream (*6*). Once in the circulation, free BoNT travels to neuromuscular junctions, where it invades neurons. The molecular architecture of PTC is largely unknown, with the exception of two low-resolution structures revealed by electron crystallography (30 Å) and electron microscopy (*7*, *8*).

We focused our study on the M-PTC of serotype BoNT/A1 (referred to as BoNT/A) because it is a major cause of human botulism and is a concern for bioterrorism (*9*). We established a robust recombinant system in *Escherichia coli* to produce a genetically modified, catalytically inactive BoNT/A (~150 kD) that carries three mutations [Glu^{224}→Gln^{224}, Arg^{363}→Ala^{363}, and Tyr^{366}→Phe^{366} (E224Q/R363A/Y366F)] in the catalytic site (*10*) and the corresponding full-length NTNHA-A1 (~140 kD, referred to as NTNHA-A) (*11*). $BoNT/A^{E224Q/R363A/Y366F}$ adopts a structure essentially identical to that of wild-type BoNT/A (*12*) and is referred to here as BoNT/Ai (fig. S1 and table S2). The free forms of BoNT/Ai and NTNHA-A are monomeric at pH = 6.0 and 7.5 (fig. S2) and assemble into a monomeric M-PTC at pH = 6.0 with a dissociation constant (K_d) of ~30.8 nM and 1:1 stoichiometry, as analyzed by analytic ultracentrifugation (AUC) and isothermal titration calorimetry (ITC) (fig. S2 and table S1). By contrast, no assembly occurs at pH = 7.5.

Free BoNT/Ai and NTNHA-A are inherently fragile, as shown by in vitro cleavage by digestive proteases such as trypsin and pepsin (Fig. 1A). Free wild-type BoNT/A is inactivated by trypsin or by incubation at pH = 3 or less, on the basis of ex vivo mice phrenic nerve hemidiaphragm (MPN) assays (Fig. 1B). In contrast, the structural integrity and activity of BoNT/A is protected in the in vitro–reconstituted M-PTC at low pH, but not at neutral or alkaline pH (Fig. 1, A and B). Thus, the recombinant M-PTC faithfully mimics the behavior of native M-PTC.

To understand the molecular mechanism underlying BoNT/A protection and the pH-dependent assembly of the M-PTC, we determined a 2.7 Å

[1]Center for Neuroscience, Aging and Stem Cell Research, Sanford-Burnham Medical Research Institute, 10901 North Torrey Pines Road, La Jolla, CA 92037, USA. [2]Institut für Toxikologie, Medizinische Hochschule Hannover, Carl-Neuberg-Straße 1, 30625 Hannover, Germany. [3]Northeastern Collaborative Access Team (NE-CAT) and Department of Chemistry and Chemical Biology, Cornell University, Building 436E, Argonne National Laboratory, 9700 South Cass Avenue, Argonne, IL 60439, USA. [4]Division of Infectious Disease, Department of Biomedical Science, Tufts Cummings School of Veterinary Medicine, 200 Westboro Road, North Grafton, MA 01536, USA.

*To whom correspondence should be addressed. E-mail: rjin@sanfordburnham.org

resolution crystal structure of the M-PTC facilitated by a BoNT/A-specific nanobody (*13*), as well as the structure of a nanobody-free M-PTC at 3.9 Å resolution (Fig. 1, C and D; figs. S3 and S4; and table S2). Nanobodies are the smallest antigen-binding fragments (~12 to 15 kD) of naturally occurring heavy-chain–only antibodies (VHH) present in camelids and have been exploited as inhibitors of BoNTs (*13*). The VHH binds on the surface of BoNT/Ai far from the NTNHA-A–interacting sites. It facilitates a more compact crystal packing and thus improves the diffraction quality of the crystals (fig. S5 and table S3). The two independently solved crystal structures of the M-PTC are indistinguishable, demonstrating that the structure presented here represents the physiological conformation of the M-PTC, independent of VHH or crystal packing (fig. S3B).

BoNT/Ai and NTNHA-A form an interlocked compact complex and bury an unusually large solvent-accessible area (~3600 Å^2 per molecule) through multivalent interfaces (Fig. 1). BoNT/Ai is composed of a 50-kD light chain (LC, a Zn^{2+}-endoprotease) and a 100-kD heavy chain (HC), which has two domains: The N-terminal domain (H_N) mediates LC translocation across the endosomal membrane, whereas the C-terminal domain (H_C) is the receptor-binding domain (*1*). Unexpectedly, the protective component NTNHA-A has a structure highly similar to BoNT/Ai despite a low sequence identity (~20%). NTNHA-A also displays three domains that, when compared pairwise with LC, H_N, or H_C, yield root mean square deviations of 2.2 Å (314 Cα pairs), 2.3 Å (300), and 1.9 Å (319), respectively, and thus are termed nLC, nH_N, and nH_C ("n" indicates NTNHA) (Fig. 1, C and D, and fig. S6). At the center of the complex is the H_C fragment that is surrounded by all three domains of NTNHA-A (table S4). Notably, H_C rotates about 140° around a linker connecting H_N and H_C, resulting in a distinct conformation in comparison to the free form of BoNT/A (Fig. 2) (*12*). Complementing this, H_N also forms many polar interactions with nH_N and nH_C (Fig. 3, D and E). In contrast, LC does not bind NTNHA-A.

Despite their similarities, a structural comparison between NTNHA-A and BoNT/Ai revealed several features specific to NTNHA-A (fig. S6). NTNHA-A does not possess most of the characteristic structural features of BoNT/A that are crucial to its functions: (i) nLC does not have the catalytic zinc-binding HExxH+E (H and x indicate His and any amino acid, respectively) signature motif that is conserved among all BoNT serotypes; (ii) NTNHA-A does not have the homologous long loop (Val^{431} to Leu^{453}) that in BoNT/A connects LC and HC and is cleaved posttranslationally to activate BoNT/A; (iii) a functionally essential disulfide bond (Cys^{430}–Cys^{454} in BoNT/A) that is involved in translocation of LC and is conserved in all BoNTs is not present in NTNHA-A (*14*); (iv) nH_C maintains the core structure of H_C but has deletions in many surface areas that are not directly involved in BoNT/Ai binding; and (v) none of the ganglioside-binding residues of H_C, including the highly conserved ganglioside-binding motif (E+H+SxWY) (S and W indicate Ser and Trp, respectively) found in many BoNT serotypes, is conserved in NTNHA-A (*15*, *16*).

NTNHA-A has a large insert in nLC (nGly^{116} to nAla^{148}, termed the nLoop) that is not present in LC. Furthermore, the nLoop is conserved in NTNHA-A1, B, C, D, and G but is missing in NTNHA-A2, E, and F (fig. S7). Notably, many of the known spontaneous nicking sites in NTNHA are located in the nLoop (*17*), and, consistent with this, we observed that recombinant NTNHA-A was nicked between nLys^{133} and nLys^{134} during long-term storage. The nicking sites in NTNHA are masked in the HA-bound PTC, and the M-PTC that contains the nicked NTNHA can no longer assemble with HAs (*17*, *18*). Moreover, NTNHA-A2, E, and F, which lack the nLoop, do not have accompanying HA proteins and only form the HA-negative M-PTC (*19*–*21*). The crystal structure reveals that the nLoop is fully exposed on the M-PTC surface and has no visible electron density, presumably because of its high flexibility (Fig. 1C). Collectively, these data suggest that the nLoop could participate in the interaction with HAs to assemble the larger PTCs.

The conformation of BoNT/Ai in the M-PTC brings the receptor-binding site located in the C-terminal subdomain of H_C close to the C-terminal boundary of the long rodlike H_N (Fig. 2). This conformation contrasts with crystal structures of the free BoNT/Ai (fig. S1), free BoNT/A, and free BoNT/B serotype, where the receptor-binding site in H_C points to the N-terminal boundary of H_N (*12*, *22*–*24*). The H_C reorientation is mediated by a linker between H_N and H_C (Leu^{845} to Thr^{876} in BoNT/A, referred to as the H_N-H_C linker), which adopts an essentially identical structure in free BoNT/A and BoNT/B but changes its conformation in the M-PTC (Fig. 2 and fig. S8). The conformational change is likely induced by NTNHA-A rather than pH because the same conformation is adopted by all structures of free BoNT/A or BoNT/B crystallized at pHs ranging from 5.0 to 7.0 (*12*, *22*–*24*).

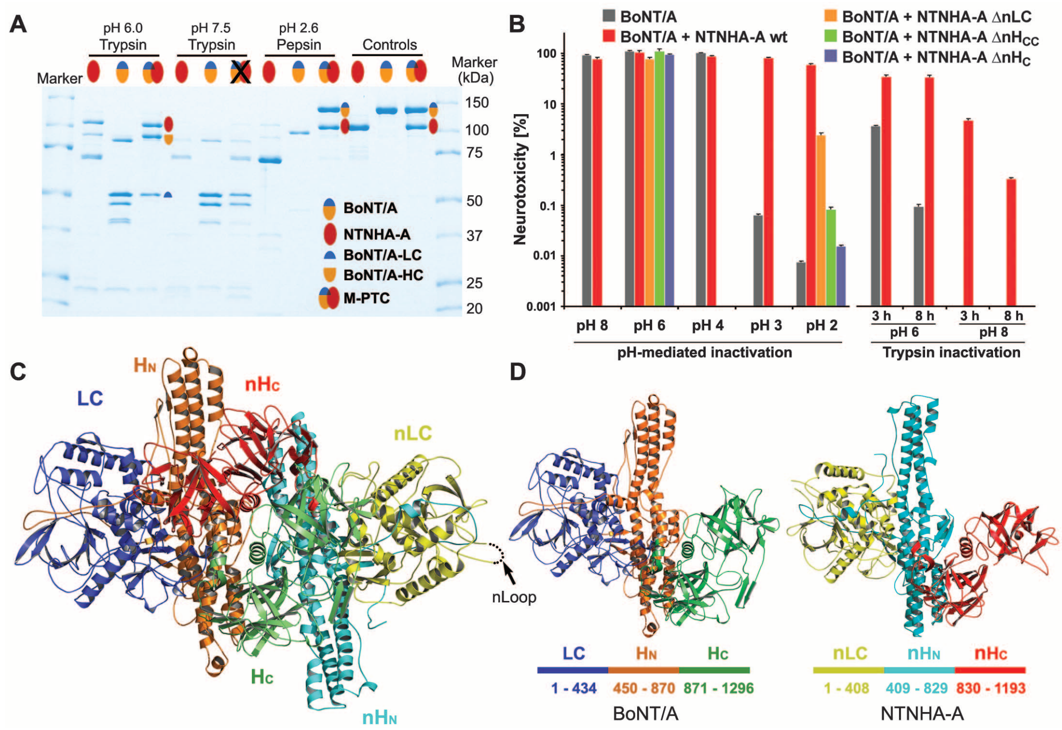

Fig. 1. The architecture of the M-PTC. (**A**) NTNHA-A protects BoNT/Ai against trypsin and pepsin digestion when they assemble into M-PTC in an acidic environment. (**B**) NTNHA-A protects active BoNT/A against low pH–mediated inactivation. It also protects BoNT/A against trypsin inactivation at pH = 6.0 but not at pH = 8.0. wt, wild type. (**C**) Cartoon presentation of the M-PTC. BoNT/Ai domains are blue (LC), orange (H_N), and green (H_C). NTNHA-A domains are yellow (nLC), cyan (nH_N), and red (nH_C). (**D**) Individual structures of BoNT/Ai and NTNHA-A in the M-PTC.

We speculated that the flexible H_N-H_C linker may play a role in coordinating H_C-mediated receptor binding and H_N-mediated translocation, given that the membrane-anchored receptors impose some geometric restrictions on the position of H_C with respect to the membrane surface (*24*, *25*) and that the long helical H_N needs to strategically orientate on the membrane to achieve efficient translocation of LC to the cytosol (*26*–*28*). To test this, we produced two mutants of BoNT/A in which the structure of the H_N-H_C linker was altered by point mutations. BoNT/A$^{R861A/E868P/K871P}$, containing the helix breaker proline (P) and where K indicates Lys, is expected to destabilize the helical linker, whereas BoNT/A$^{L862K/L863E/T867K}$, with extra ion pairs and T indicating Thr, will likely stabilize the helical structure. The two BoNT/A mutants showed wild-type–like characteristics with respect to protein folding, receptor binding capability, Zn^{2+}-endoprotease activity, and NTNHA-A binding (fig. S9). However, the toxicity of both mutants was significantly decreased by ~sixfold in the MPN assay. Although the exact conformations of the two mutants are not known, we conclude that the observed decrease in toxicity is due to the disrupted coordination between H_N and H_C, leading to decreased efficiency of LC translocation. These data further suggest that any disturbance in the structural integrity of the H_N-H_C linker may affect the optimal positioning of H_C and H_N during BoNT intoxication. Thus, the structural features of the H_N-H_C linker might represent a serotype-specific signature for the various BoNTs. For example, BoNT/E serotype has a more rapid LC translocation, which has been suggested to result from its intrinsically more flexible linker (fig. S8) (*27*, *29*).

To validate the physiological relevance of the M-PTC structure, we performed systematic truncation studies. The isolated H_C fragment bound to NTNHA-A with high affinity at pH = 6.0 (K_d ~ 48.3 nM) but not at pH = 7.5 and thus largely replicated the binding behavior of full-length BoNT/Ai. Consistent with this, the H_C-deleted BoNT/Ai (LH_N) no longer bound NTNHA-A (fig. S10). BoNT/Ai has a larger unfavorable bind-

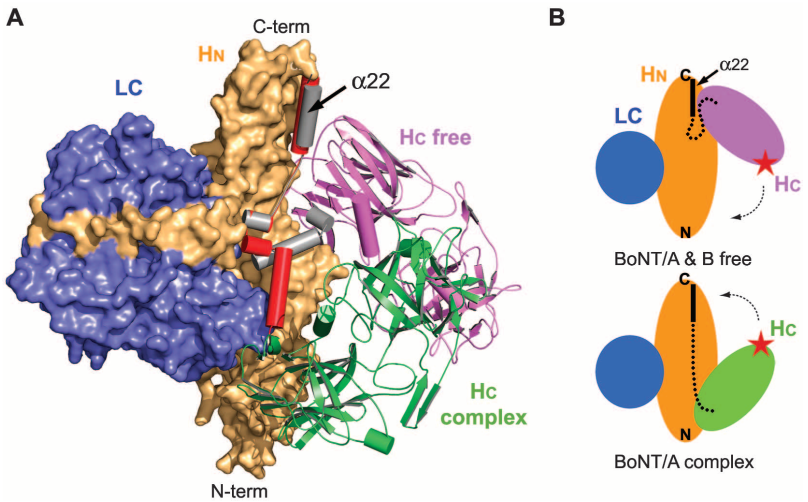

Fig. 2. The H_C fragment of BoNT/A can rotate around a linker connecting H_N and H_C. (**A**) Superposition of the free and complex forms of BoNT/A based on Cα atoms in LC and H_N. H_C of free BoNT/A is violet; LC and H_N are omitted for clarity. Linkers in the free and complex forms of BoNT/A are gray and red, respectively. (**B**) Cartoon model showing two distinct conformations of BoNT/A that bring the receptor-binding site in H_C (red star) close to the opposite tip of the long helical H_N.

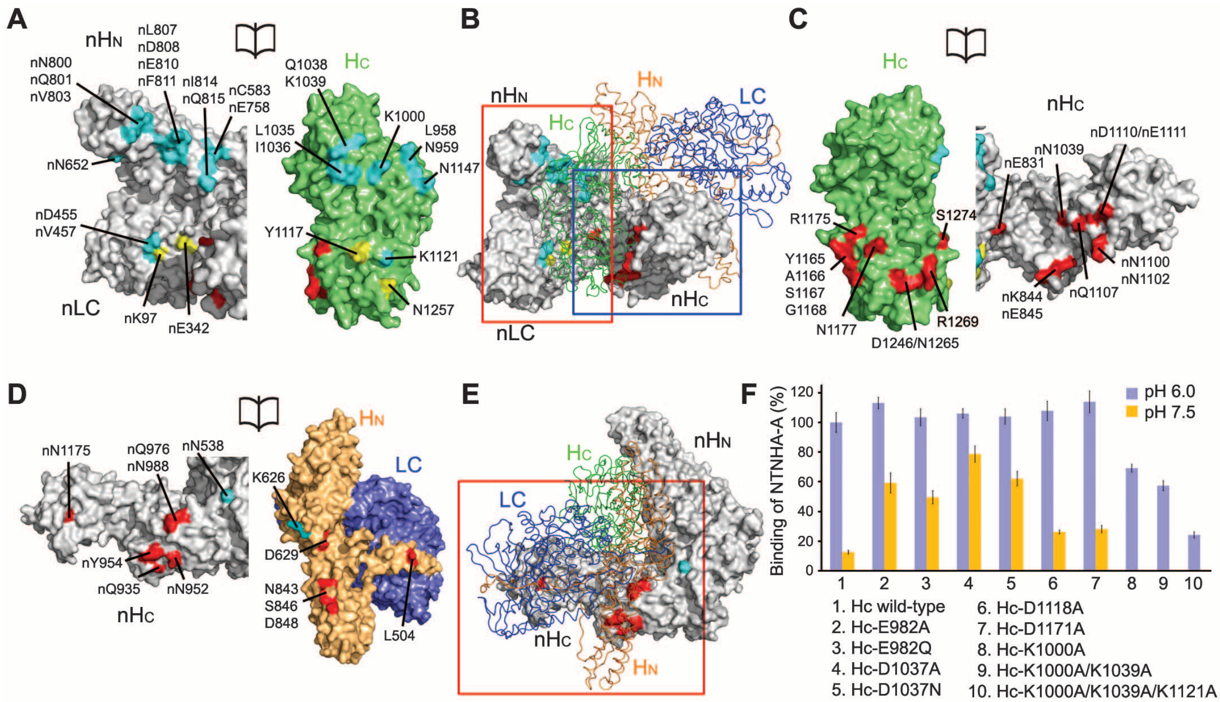

Fig. 3. M-PTC is stabilized by extensive intermolecular interactions. (**A** to **C**) H_C interacts with all three domains of NTNHA-A. The overall structure of the M-PTC is shown in (B), where NTNHA-A is in surface representation (gray) and BoNT/Ai is blue, orange, and green for LC, H_N, and H_C, respectively. Open-book views of the interfaces highlighted in the red and blue boxes are shown in (A) and (C), respectively. Residues in H_C that form hydrogen bonds or salt bridges with nLC, nH_N, or nH_C are yellow, cyan, and red, respectively. C, Cys; I, Ile; V, Val. (**D**) Open-book view of the interface highlighted in the red box of (**E**). H_N directly contacts nH_C (interacting residues shown in red) and nH_N (cyan), but not nLC. (**F**) Precipitation assays between full-length NTNHA-A (prey) and H_C variants (baits). Bar graph shows mean ± SD, n = 3 (n is the number of assays). Binding of samples 8 to 10 at pH = 7.5 was not detectable.

ing entropy than H_C ($\Delta\Delta S \sim -16.8$ cal mol^{-1} K^{-1}) (table S1), which could be due to a loss of conformational entropy of BoNT/Ai upon NTNHA-A binding and may be related to the reorientation of H_C. Truncating nH_C or the C-terminal subdomain of nH_C (nH_{CC}) in NTNHA-A abolished the protective function of NTNHA-A at pH = 2, suggesting that nH_C is crucial for shielding the sensitive H_C of BoNT/A (Fig. 1B).

Additional support for the M-PTC structure is provided by structure-based mutagenesis studies. Interactions between H_C and NTNHA-A were gradually weakened as more intra-PTC charge-charge interactions were disrupted: The binding affinity at pH = 6.0 decreased in the order of H_C-K1000A > H_C-K1000A/K1039A > H_C-K1000A/K1039A/K1121A (Fig. 3F and fig. S10). Even a single point mutation, H_C-K1000A, significantly decreased the binding affinity by ~sevenfold ($K_d \sim 337.5$ nM). The H_C-centered protection by NTNHA-A is biologically relevant. Although the integrity of H_C is crucial to enrich BoNT/A on the neuron surface at the early stage of intoxication, it is much more sensitive to proteolysis than LC and H_N in the free BoNT/A (*30*, *31*).

To understand how a pH change can trigger the disassembly of the PTC, we focused on H_C because it largely replicates the binding features of full-length BoNT/Ai. We specifically concentrated on residues located in the complex interface that are titratable in an acidic environment (e.g., His, Glu, and Asp). We found four acidic residues in H_C, each of which is located in the vicinity of an intra-PTC salt bridge or a long-range electrostatic interaction: Glu^{982} is near Lys^{1000}–nAsp^{808}; Asp^{1037}, Lys^{1039}–nGlu^{810}; Asp^{1118}, Lys^{1121}–nAsp^{455}; and Asp^{1171}, Arg^{1175}–nAsp^{1110} (Fig. 4 and fig. S11). Our mutagenesis studies show that these charge-charge interactions are crucial for the assembly of the M-PTC (Fig. 3F). Analyzing the surface electrostatic potentials shows that BoNT/Ai is generally positively charged around these acidic residues, whereas the opposing NTNHA-A surface is largely negatively charged (fig. S11). Therefore, negatively charged BoNT/Ai residues in these areas pose an unfavorable force, which could potentially weaken the local electrostatic interactions in a pH-dependent manner.

To address the potential roles of these acidic residues in pH sensing, we mutated them individually to nontitratable residues. Single point mutants of the H_C fragment (E982A, D1037A, D1118A, or D1171A, where D indicates Asp) all folded correctly (fig. S12) and bound NTNHA-A at pH = 6.0 to a similar extent as the wild-type H_C. H_C-E982A and H_C-D1037A showed significant binding to NTNHA-A at pH = 7.5 (Fig. 3F and fig. S10). Thermodynamic studies showed that H_C-E982A binds to NTNHA-A at pH = 6.0 similarly to the way the wild-type H_C does, predominantly driven by enthalpy ($K_d \sim 39.4$ nM); it also binds to NTNHA-A at pH = 7.5, driven by both enthalpy and entropy ($K_d \sim 279.5$ nM) (table S1). Furthermore, a single mutation of E982A significantly increased binding between the full-length BoNT/Ai and NTNHA-A at pH = 7.5, as measured in a precipitation assay (~20% binding by mutant versus <5% by the wild-type protein). These data suggest that Glu^{982} and Asp^{1037} are important pH-sensing residues that modulate the pH-dependent assembly of the M-PTC.

The pK_a (where K_a is the acid dissociation constant) of the ionizable groups in proteins may be substantially shifted from the intrinsic pK_a depending on the microenvironment surrounding these groups (*32*). Glu^{982} and Asp^{1037} of BoNT/A are predicted (*33*) to have clearly increased pK_a values upon binding to NTNHA-A, partly because of desolvation effect when they are buried in the context of the M-PTC. Thus, Glu^{982} and Asp^{1037} are likely protonated at pH = 6.0 as their pK_a values increase during the BoNT/A–NTNHA-A interaction, leading to a stable M-PTC. In contrast, these residues are deprotonated in a neutral or alkaline environment, generating repulsive charge interactions with NTNHA-A to destabilize the M-PTC assembly. We replaced Glu^{982} and Asp^{1037} with the isosteric, nontitratable residues Gln and Asn (N), respectively, to mimic their protonated state. Both H_C-E982Q and H_C-D1037N showed significant binding with NTNHA-A at pH = 7.5, further supporting the pH-sensing role of these two residues (Fig. 3F and fig. S10). At the same time, thermodynamic studies revealed a loss of enthalpy on binding of H_C-E982A to NTNHA-A at pH = 7.5 compared to pH = 6.0 ($\Delta\Delta H \sim 6.3$ kcal mol^{-1}) (table S1), suggesting that the protein-protein interaction network between H_C and NTNHA-A is partly impaired at pH = 7.5. Thus, additional pH-sensing components might exist in H_C that become fully engaged in binding with NTNHA-A only at pH = 6.0.

Collectively, these data suggest that the assembly of the M-PTC is dynamically regulated by key pH-sensing residues that switch protonation states in response to the environmental pH. These interaction sites would likely be the most malleable parts of the PTC and could be specifically targeted for the development of small-molecule inhibitors to break up the PTC in the acidic GI tract. A pharmacological approach such as this, which focuses on preventive countermeasures at the earliest stage of BoNT intoxication, would complement current efforts to design inhibitors that block the subsequent neuronal action of BoNT. Our results also suggest mechanisms for the development of an oral drug delivery system in which proteinaceous drugs could be conjugated to a BoNT fragment and protected from degradation with NTNHA.

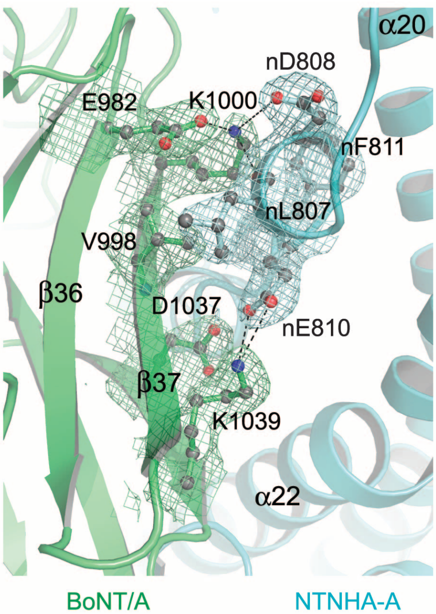

Fig. 4. A pH-sensing mechanism. A close-up view of pH-sensing residues Glu^{982} and Asp^{1037}, which are buried in the M-PTC in the vicinity of intra-PTC charge-charge interactions. Key residues in the interface are shown as ball-and-stick models. Hydrogen bonds and charge-charge interactions are indicated by dotted lines. A simulated-annealing omit map of the M-PTC contoured at 1 σ was overlaid with the final refined model.

References and Notes

1. C. Montecucco, G. Schiavo, *Q. Rev. Biophys.* **28**, 423 (1995).
2. M. D. Collins, A. K. East, *J. Appl. Microbiol.* **84**, 5 (1998).
3. H. Ito *et al.*, *FEMS Immunol. Med. Microbiol.* **61**, 323 (2011).
4. I. Ohishi, S. Sugii, G. Sakaguchi, *Infect. Immun.* **16**, 107 (1977).
5. L. W. Cheng *et al.*, *Toxicology* **249**, 123 (2008).
6. K. H. Eisele, K. Fink, M. Vey, H. V. Taylor, *Toxicon* **57**, 555 (2011).
7. F. Burkard, F. Chen, G. M. Kuziemko, R. C. Stevens, *J. Struct. Biol.* **120**, 78 (1997).
8. K. Hasegawa *et al.*, *J. Biol. Chem.* **282**, 24777 (2007).
9. S. S. Arnon *et al.*, *JAMA* **285**, 1059 (2001).
10. T. Binz, S. Bade, A. Rummel, A. Kollewe, J. Alves, *Biochemistry* **41**, 1717 (2002).
11. Materials and methods are available as supporting material on *Science* Online.
12. D. B. Lacy, W. Tepp, A. C. Cohen, B. R. DasGupta, R. C. Stevens, *Nat. Struct. Biol.* **5**, 898 (1998).
13. J. Mukherjee *et al.*, *PLoS ONE* **7**, e29941 (2012).
14. A. de Paiva *et al.*, *J. Biol. Chem.* **268**, 20838 (1993).
15. A. Rummel, S. Mahrhold, H. Bigalke, T. Binz, *Mol. Microbiol.* **51**, 631 (2004).
16. P. Stenmark, J. Dupuy, A. Imamura, M. Kiso, R. C. Stevens, *PLoS Pathog.* **4**, e1000129 (2008).
17. Y. Sagane *et al.*, *Biochem. Biophys. Res. Commun.* **292**, 434 (2002).
18. H. Kouguchi, T. Watanabe, Y. Sagane, H. Sunagawa, T. Ohyama, *J. Biol. Chem.* **277**, 2650 (2002).
19. N. Fujii *et al.*, *J. Gen. Microbiol.* **139**, 79 (1993).
20. A. K. East, M. D. Collins, *Curr. Microbiol.* **29**, 69 (1994).
21. G. Lin, W. H. Tepp, C. L. Pier, M. J. Jacobson, E. A. Johnson, *Appl. Environ. Microbiol.* **76**, 40 (2010).
22. S. Swaminathan, S. Eswaramoorthy, *Nat. Struct. Biol.* **7**, 693 (2000).
23. S. Eswaramoorthy, D. Kumaran, J. Keller, S. Swaminathan, *Biochemistry* **43**, 2209 (2004).
24. Q. Chai *et al.*, *Nature* **444**, 1096 (2006).
25. R. Jin, A. Rummel, T. Binz, A. T. Brunger, *Nature* **444**, 1092 (2006).
26. M. R. Baldwin, J. J. Kim, J. T. Barbieri, *Nat. Struct. Mol. Biol.* **14**, 9 (2007).
27. D. Kumaran *et al.*, *J. Mol. Biol.* **386**, 233 (2009).
28. M. Montal, *Annu. Rev. Biochem.* **79**, 591 (2010).
29. J. Wang *et al.*, *J. Biol. Chem.* **283**, 16993 (2008).
30. C. C. Shone, P. Hambleton, J. Melling, *Eur. J. Biochem.* **151**, 75 (1985).

31. F. Chen *et al.*, *Infect. Immun.* **65**, 1626 (1997).
32. C. N. Pace, G. R. Grimsley, J. M. Scholtz, *J. Biol. Chem.* **284**, 13285 (2009).
33. H. Li, A. D. Robertson, J. H. Jensen, *Proteins* **61**, 704 (2005).

Acknowledgments: We thank A. Brunger and T. Binz for critical reading of the manuscript; the staff of beamline 9-2 at the Stanford Synchrotron Radiation Lightsource (SSRL) and the NE-CAT staff of the Advanced Photon Source (APS), particularly K. Rajashankar, for assistance in data collection; G. Yao, N. Krez, A. M. Kruel, and J. Tremblay for excellent technical assistance; and R. Liddington and A. Bobkov for assistance with ITC and AUC. This work was partly supported by an Alfred P. Sloan Research Fellowship (R.J.), by the Deutsche Forschungsgemeinschaft (DFG Exzellenzinitiative GSC 108 to S.R.), by the Robert-Koch-Institut (1362/I-979 to A.R.), and by grants from the National Institute of Allergy and Infectious Diseases (NIAID), NIH, Department of Health and Human Services (HHS), under award number U54 AI057159 (C.B.S.). Atomic coordinates and structure factors for the VHH-bound M-PTC, M-PTC, and BoNT/Ai have been deposited with the Protein Data Bank under accession codes 3V0A, 3V0B, and 3V0C, respectively. Sanford-Burnham Medical Research Institute has a pending patent application, titled "Botulinum neurotoxin protective complex delivery compositions," that was filed in November of 2011. BoNT availability is subject to the restrictions that apply to HHS select agents and NIAID Category A pathogens.

Supporting Online Material
www.sciencemag.org/cgi/content/full/335/6071/977/DC1
Materials and Methods
Figs. S1 to S13
Tables S1 to S4
References (*34–51*)

21 September 2011; accepted 12 January 2012
10.1126/science.1214270

Single-Molecule Fluorescence Experiments Determine Protein Folding Transition Path Times

Hoi Sung Chung,* Kevin McHale, John M. Louis, William A. Eaton*

The transition path is the tiny fraction of an equilibrium molecular trajectory when a transition occurs as the free-energy barrier between two states is crossed. It is a single-molecule property that contains all the mechanistic information on how a process occurs. As a step toward observing transition paths in protein folding, we determined the average transition-path time for a fast- and a slow-folding protein from a photon-by-photon analysis of fluorescence trajectories in single-molecule Förster resonance energy transfer experiments. Whereas the folding rate coefficients differ by a factor of 10,000, the transition-path times differ by a factor of less than 5, which shows that a fast- and a slow-folding protein take almost the same time to fold when folding actually happens. A very simple model based on energy landscape theory can explain this result.

Theory predicts that folding mechanisms are heterogeneous, so that an individual unfolded molecule can self-assemble to form its biologically active, folded structure by means of many different sequences of conformational changes (*1*). The distribution of these folding pathways can now be calculated from atomistic molecular dynamics simulations (*2–6*). Information on pathway distributions from experiments must come from measurements on single molecules, because only average properties are obtained in experiments on the large ensemble of molecules in bulk experiments. A single-molecule, equilibrium protein folding-unfolding trajectory is illustrated in Fig. 1, as monitored by Förster resonance energy transfer (FRET) spectroscopy, and its relation to the free-energy barrier as it crosses between the folded and unfolded states is shown. The most interesting part of the trajectory is contained in what appears to be an instantaneous jump between the two states, called the transition path, which contains all of the information on the mechanism of folding and unfolding. The first step toward observing transition paths in protein folding, which we report here, is the determination of its average duration (transition-path time) for a fast-folding, all-β protein [39-residue formin-binding protein (FBP) WW domain] shown to be two-state in ensemble studies (*7*, *8*), as well as a markedly reduced upper bound compared with our previous study for the 56-residue, α/β protein GB1 (the B1 immunoglobulin-binding domain of protein G from *Streptococcus*) (*9*). In contrast to a rate coefficient, which measures the frequency of a transition, the transition-path time is the duration of a successful barrier-crossing event (Fig. 1).

Laboratory of Chemical Physics, National Institute of Diabetes and Digestive and Kidney Diseases, National Institutes of Health (NIH), Bethesda, MD, 20892–0520, USA.

*To whom correspondence should be addressed. E-mail: chunghoi@niddk.nih.gov (H.S.C.); eaton@helix.nih.gov (W.A.E.)

The strategy used in this study is to illuminate dye-labeled protein molecules at very high intensities to increase the number of detected photons per transition path, to discard the majority of photons from the less-interesting segments of the trajectories between transitions, and to analyze the transition region with a maximum likelihood method by using simple models for the transition path.

Photon trajectories were measured for immobilized WW domain and protein GB1 molecules with donor and acceptor fluorophores attached to cysteines incorporated into the proteins (Fig. 2). In these trajectories, two properties of each photon were recorded—the color, either donor green or acceptor red, and the absolute time of arrival to within ~0.5 ns. As shown in Fig. 3, A and B, transitions between states are clearly resolved in the binned fluorescence and photon trajectories, and the FRET efficiency distributions (Fig. 3, C and D) are bimodal, which indicates the presence of two states. The photon trajectories were extracted from the region near the transitions and analyzed using the Gopich-Szabo maximum likelihood method (*10*).

For a given model, the Gopich-Szabo method calculates the parameters of the model that can most accurately reproduce the photon trajectories (Fig. 3). We adopt a one-step model for the transition path, which may be viewed as the simplest discrete representation of how the FRET efficiency changes along the path. This picture can be represented in a kinetic model for a two-state system with a finite transition path by introducing a third virtual state, S, for which the FRET efficiency is midway between the folded and unfolded states [$E_S = (E_F + E_U)/2$]. In this model, the lifetime of S (τ_S) corresponds to the average transition-path time, $\langle t_{TP} \rangle$ (Fig. 4A). S has the property of a transition state, because the rate coefficients from S to F and S to U (k_S) are the same, and therefore, the $p_{fold} = ½$.

The likelihood function for the *j*th photon trajectory is (*10*):

$$L_j = \mathbf{v}_{fin}{}^{T} \prod_{i=2}^{N} \{\mathbf{nF}(c_i)\exp[(\mathbf{K}-\mathbf{n})\tau_i]\}\,\mathbf{nF}(c_1)\mathbf{v}_{ini} \quad (1)$$

Here, **K** is the rate matrix [equation S6 (*11*)] containing the three rate coefficients ($k_{F'}$, $k_{U'}$, and k_S), N is the number of photons in the *j*th trajectory, c_i is the color of the *i*th photon (donor or acceptor), and τ_i is a time interval between the *i*th and (i – 1)th photons as shown in fig. S4B (*11*). The photon color matrix **F** depends on the color of a photon as **F**(*acceptor*) = ***E*** and **F**(*donor*) = **I** – ***E***, where ***E*** is a diagonal matrix with elements that are FRET efficiencies of the three states (F, S, and U), and **I** is the unit matrix. **n** is a diagonal matrix with elements that are photon count rates of the three states. $\mathbf{v}_{ini}$ and $\mathbf{v}_{fin}$ are vectors that describe the state (folded or unfolded) at the beginning and the end of the trajectory. Practically, log-likelihood functions were calculated, and the total log likelihood function of all trajectories was calculated by summing the log-likelihood functions ($\ln L = \sum_j \ln L_j$) of individual trajectories that contain a transition between folded and unfolded states. In the likelihood function L, τ_S is the only variable parameter (*11*).

The difference of the log-likelihood functions, $\Delta\ln L = \ln L(\tau_S) - \ln L(0)$, as a function of τ_S, is plotted in Fig. 4B for the WW domain. This function was calculated from 527 transitions between the folded and unfolded states. In this plot, the likelihood at $\tau_S = 0$, $L(0) = \lim_{\tau_S \to 0} L(\tau_S)$ is the value for a two-state model where every transition between folded and unfolded states is instantaneous, i.e., it occurs faster than the shortest photon interval. Therefore, the plot displays how much better (or worse) a two-state model with a finite transition-path time describes the photon trajectories than a two-state model with an instantaneous transition. There is a highly significant peak in the likelihood function in Fig. 4B at 16 (±3) μs. (The error is the standard deviation obtained from the curvature of the peak.) Simulations of photon trajectories show that, if $\Delta\ln L$ at the peak is higher than a certain confidence level, the value of τ_S at the peak corresponds to the assumed τ_S and does not arise from statistical fluctuations (fig. S6) (*11*). We used a confidence level that satisfies a condition $L(\tau_S)/[L(\tau_S) + L(0)] = 0.95$, which assures 95% confidence in the significance of the maximum and corresponds to $\Delta\ln L \approx 3$ (the dashed horizontal lines in Fig. 4). The value of 16 μs at $\Delta\ln L = 7.8$ is therefore a well-determined quantity and corresponds, in our model (Fig. 4A), to the average transition-path time $\langle t_{TP} \rangle$. That $\langle t_{TP} \rangle$ is the same for folding and unfolding transitions is shown in fig. S5 (*11*), which is consistent with the requirement of microscopic reversibility that $\langle t_{TP} \rangle$ for a barrier crossing be the same in both directions (*12*).

To extrapolate the value of $\langle t_{TP} \rangle$ to the viscosity in the absence of glycerol, we determined the rate coefficients at different viscosities (table S1) (*11*). Using a linear free-energy relation to account for the change in stability resulting from the addition of glycerol and guanidinium chloride (GdmCl), we find that the rate coefficients for folding and unfolding depend inversely on the first power of the viscosity (*11*), so $\langle t_{TP} \rangle$ should scale the same way (see Eqs. 2 and 3 below). Because the viscosity of 3 M GdmCl in 50% glycerol solution is found to be 10 times that of 2 M GdmCl (*11*), our best estimate of $\langle t_{TP} \rangle$ in the absence of a viscogen at 293 K is ~2 μs.

We have used the simplest possible model for determining $\langle t_{TP} \rangle$. However, more realistic models that depict a more gradual change in the FRET efficiency along a transition path—with two and three steps in the FRET efficiency in the transition path between states instead of just one (Fig. 4A)—yield very similar values for $\langle t_{TP} \rangle$ (fig. S9) (*11*). We also found that the value of $\langle t_{TP} \rangle$ is not sensitive to the choice of the FRET efficiency for S, as long as the value is between the two FRET efficiencies of the folded and unfolded states ($0.6 \leq E_S \leq 0.7$) (fig. S7) (*11*).

For proteins with very low free-energy barriers, it may be possible to estimate $\langle t_{TP} \rangle$ from ensemble measurements. Gruebele and co-workers have studied the kinetics of the ultrafast-folding, 33-residue FiP35 WW domain, which has a very similar fold to that of our WW domain (FBP28) and ~30% sequence identity (*13*). Prior to the ~10-μs folding-unfolding relaxation at the melting temperature of ~350 K, a ~1.5-μs relaxation was observed, which was called a "molecular phase" and attributed to a change in the small population of molecules at the top of a low free-energy barrier in response to the temperature jump. No molecular phase was observed for the FBP WW domain (*7*), presumably because it is a slower folder owing to a higher barrier, and there is therefore no detectable amplitude from the change in the barrier top population. In this interpretation, Gruebele's ~1.5-μs relaxation corresponds to the lifetime, τ_S, of our kinetic model for the transition path (Fig. 4).

Shaw and co-workers have simulated equilibrium trajectories of the FiP35 WW domain using all-atom molecular dynamics calculations (*4*). They found $\langle t_{TP} \rangle$ to be 0.5 (±0.1) μs at 360 K using the TIP3P explicit water model (*6*). After rescaling for the difference in viscosity compared with real water, the simulated $\langle t_{TP} \rangle$ becomes ~1.5 μs (*14*). Although the sequences for the two WW domains are different, the finding of similar values for $\langle t_{TP} \rangle$ from the simulations and both ensemble and single-molecule experiments provides support for the accuracy of the simulations, for Gruebele's interpretation of the molecular phase, and for our interpretation of the single-molecule photon trajectories.

The folding time of protein GB1 in 4 M urea is ~1 s. This time is far too long to observe folding transitions in trajectories simulated by atomistic equilibrium molecular dynamics, which makes even an upper bound for the transition-path time an interesting quantity. In previous work (*9*), we were able to determine an upper bound of ~200 μs, based on an analysis of individual trajectories. The photon count rate in those experiments was only 50 ms^{-1}, and the average time before photobleaching was ~100 ms. In the present experiments, the much higher count rate of 350 ms^{-1} from the increased illumination intensity, together with the collective analysis using the maximum likelihood method, has allowed us to determine a much more accurate upper bound. The penalty for the higher photon count rate is that the lifetime of the trajectories is shortened to ~10 ms by the more intense illumination, and transitions, albeit clearly resolved (Fig. 3B), are only observed in a very small fraction of the trajectories. Measurement at 4 M urea (with no added glycerol) of trajectories for ~47,000 molecules yielded just 114 transitions.

These 114 transitions were analyzed with the same model as for the WW domain. No peak is observed in the $\Delta\ln L$ versus τ_S plot (Fig. 4C), so $\langle t_{TP} \rangle$ is too short to measure. Nevertheless, the analysis permits a determination of an upper bound for $\langle t_{TP} \rangle$. By analogy to the significance of the peak for the WW domain, we can set a confidence level for the answer to the question: How long can $\langle t_{TP} \rangle$ be before it becomes inconsistent with the data? The 95% confidence level that τ_S in a two-state model with a finite transition path is less consistent with the photon trajectories than a two-state model with an instantaneous transition path is given by its value at $\Delta\ln L \approx -3$. In other words, $\langle t_{TP} \rangle$ cannot be longer than τ_S at $\Delta\ln L = -3$ and is therefore an upper bound on $\langle t_{TP} \rangle$. As shown in Fig. 4C, this upper bound is ~10 μs.

The major result of our experiments is that, whereas the folding rate coefficients for the WW domain and protein GB1 differ by four orders of magnitude, $10^4\ s^{-1}$ and $1\ s^{-1}$, the transition-path times differ by less than fivefold (~2 μs and <10 μs), which shows that a fast- and a slow-folding protein take almost the same time to fold when folding actually happens.

It is interesting that a simple model by A. Szabo, based on describing the kinetics of folding for a two-state system as diffusion over a barrier on a one-dimensional free-energy surface

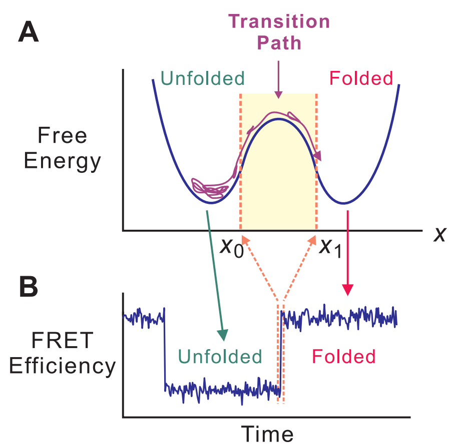

Fig. 1. Schematic of a folding transition path for a two-state protein. (**A**) The kinetics of protein folding is described by energy landscape theory as diffusion on a one-dimensional free-energy surface with an order parameter (x) as a reaction coordinate (*1*, *15*, *25*, *26*). The unfolded molecule spends the vast majority of time visiting a large number of conformations in the free-energy well of the unfolded state. A transition path is the part of the trajectory that crosses the reaction coordinate x at x_0 and reaches x_1 on the other side of the barrier without recrossing x_0 (*12*). The duration of this part is the transition-path time. (**B**) FRET efficiency trajectory. In the typical experiment, the donor and acceptor FRET fluorophores are attached to cysteine residues, which are closer on average in the folded state (higher FRET efficiency) than in the unfolded state (lower FRET efficiency). The duration of the jump in the FRET efficiency trajectory is the transition-path time. The FRET efficiency monitors reconfiguration of the polypeptide backbone to form the native fold but is most probably blind to the annealing of side chains. Consequently, the transition path measured by FRET is expected to be shorter than the transition path monitored by side-chain contacts, for example, in a molecular dynamics simulation (*6*).

as in the energy landscape theory of Wolynes, Onuchic, and co-workers (*1*, *15*), can explain this result. According to Kramers' theory for such a barrier crossing (Fig. 1A), the folding time ($\tau_F = 1/k_F$) is given by:

$$\tau_F = \frac{2\pi}{D^*\beta\omega\omega^*}\exp\left(\beta\Delta G_F^*\right) \equiv \tau_0 \exp\left(\beta\Delta G_F^*\right) \qquad (2)$$

where D^* is the diffusion coefficient at the barrier top, ω^2 is the curvature of the unfolded well (near x_0 in Fig. 1A), $-(\omega^*)^2$ is the curvature at the barrier top, $\beta = 1/k_BT$ (where k_B is Boltzmann's constant and T is temperature), and ΔG_F^* is the height of the folding free-energy barrier (*16*–*20*). For $\omega = \omega^*$, $\langle t_{TP}\rangle$ is approximately given by (*9*, *12*):

$$\langle t_{TP}\rangle \approx \frac{\ln\left(3\beta\Delta G_F^*\right)}{D^*\beta(\omega^*)^2} \approx \frac{\tau_0}{2\pi}\ln\ln\left(\frac{\tau_F}{\tau_0}\right)^3 \qquad (3)$$

The model predicts that $\langle t_{TP}\rangle$ is insensitive to the barrier height and that fast- and slow-folding proteins will have similar transition-path times as long as there are only small differences in the curvatures and the diffusion coefficients (i.e., small difference in τ_0). The diffusion coefficient depends on the roughness of the underlying energy landscape and could therefore differ substantially among proteins (*21*–*23*). The best current estimate for τ_0 of fast-folding proteins is ~1 µs (*24*), which predicts a ratio of $\langle t_{TP}\rangle$ for protein GB1 and the WW domain of 1.4, compared with the experimental ratio of <5, if we assume the same τ_0 for the two proteins. This ratio varies from 1.3 to 1.8 for τ_0 between 0.1 and 10 µs.

Our determination of an average transition-path time is a first step toward the goal of obtaining information on the distribution of folding pathways from measurements of interdye distance versus time trajectories during transition paths. However, the result of this first step by itself has turned out to be extremely interesting. Folding involves a complex and intricate rearrangement of a polypeptide chain to form a unique structure, yet the time for this nontrivial self-assembly process

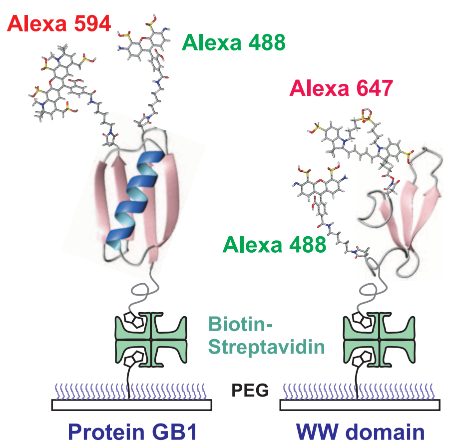

Fig. 2. Schematic of immobilized folded proteins showing donor (green-emitting) and acceptor (red-emitting) fluorophores. The proteins are attached to a polyethyleneglycol (PEG)–coated glass surface via a biotin-streptavidin-biotin linkage (*11*).

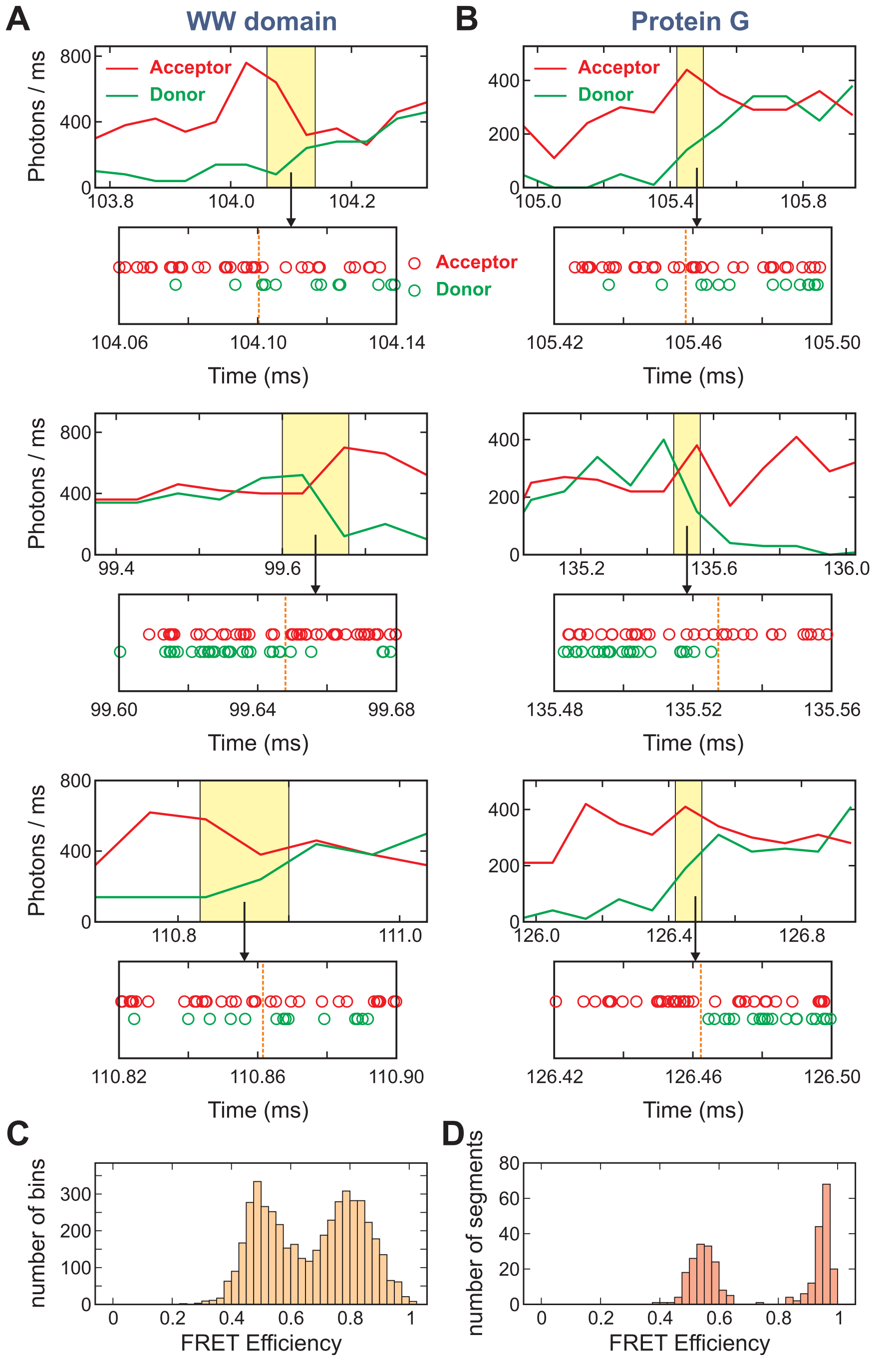

Fig. 3. Representative fluorescence and photon trajectories and FRET efficiency histograms of WW domain and protein GB1. (**A** and **B**) For the fluorescence trajectories—donor (green) and acceptor (red)—photons were collected in 50-µs bins for the WW domain and in 100-µs bins for protein GB1. Measurements were made at 293 K at high illumination intensity (A) in 3 M GdmCl in 50% glycerol for the WW domain (20 kW/cm^2, ~650 photons/ms) and (B) in 4 M urea for protein GB1 (10 kW/cm^2, ~350 photons/ms). Strings of arrival times and colors of donor and acceptor photons (photon trajectories) in the transition region (the 80-µs yellow-shaded regions) are displayed below the binned fluorescence trajectories. Dashed vertical lines in the photon trajectories indicate the most probable transition interval found by the Viterbi algorithm (*11*). The absolute times refer to the start of data collection, ~100 ms before the laser was turned on. (**C** and **D**) FRET efficiency histograms. The mean FRET efficiencies for the WW domain were calculated (C) for each of the 50-µs bins for the trajectories with the mean photon count rate >400 ms^{-1} and (D) for folded and unfolded segments of protein GB1 containing ~2500 photons.

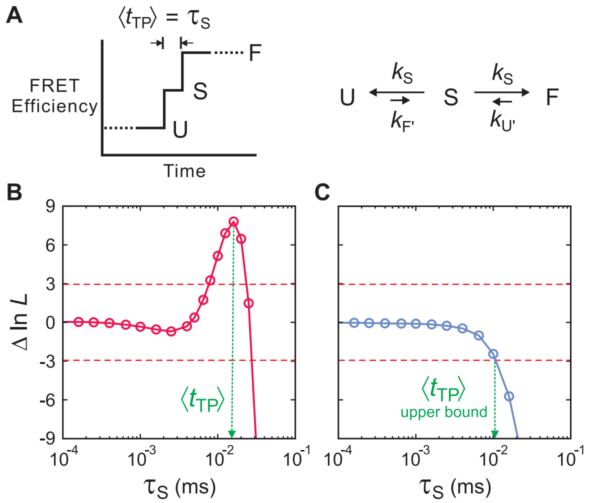

Fig. 4. Determination of average transition-path times in a kinetic model. (**A**) Schematic of a FRET efficiency trajectory using a one-step model to describe the transition path from unfolded (U) to folded (F) states for a protein exhibiting two-state kinetics and thermodynamics. The average transition-path time, $\langle t_{TP} \rangle$, is equal to the lifetime of a virtual intermediate state S [$\tau_S = (2k_S)^{-1}$]. (**B** and **C**) The difference of the log likelihood, $\Delta \ln L = \ln L(\tau_S) - \ln L(0)$, between the two-state model with a finite transition-path time and a two-state model with an instantaneous transition-path time is plotted as a function of τ_S (B) for the WW domain in 3 M GdmCl in 50% glycerol and (C) for protein GB1 in 4 M urea. The horizontal dashed line at $\Delta \ln L = +3$ represents the 95% confidence limit for the significance of the peak in (B), and the intersection of the likelihood function with the horizontal dashed line at $\Delta \ln L = -3$ in (C) yields the 95% confidence limit for the upper bound of τ_S.

is almost the same for two proteins with different topologies and vastly different folding rates.

References and Notes

1. J. D. Bryngelson, J. N. Onuchic, N. D. Socci, P. G. Wolynes, *Proteins* **21**, 167 (1995).
2. F. Noé, C. Schütte, E. Vanden-Eijnden, L. Reich, T. R. Weikl, *Proc. Natl. Acad. Sci. U.S.A.* **106**, 19011 (2009).
3. G. R. Bowman, V. S. Pande, *Proc. Natl. Acad. Sci. U.S.A.* **107**, 10890 (2010).
4. D. E. Shaw *et al.*, *Science* **330**, 341 (2010).
5. S. Piana, K. Lindorff-Larsen, D. E. Shaw, *Biophys. J.* **100**, L47 (2011).
6. K. Lindorff-Larsen, S. Piana, R. O. Dror, D. E. Shaw, *Science* **334**, 517 (2011).
7. H. Nguyen, M. Jager, A. Moretto, M. Gruebele, J. W. Kelly, *Proc. Natl. Acad. Sci. U.S.A.* **100**, 3948 (2003).
8. M. Petrovich, A. L. Jonsson, N. Ferguson, V. Daggett, A. R. Fersht, *J. Mol. Biol.* **360**, 865 (2006).
9. H. S. Chung, J. M. Louis, W. A. Eaton, *Proc. Natl. Acad. Sci. U.S.A.* **106**, 11837 (2009).
10. I. V. Gopich, A. Szabo, *J. Phys. Chem. B* **113**, 10965 (2009).
11. Materials and methods are available as supporting online material on *Science* Online.
12. G. Hummer, *J. Chem. Phys.* **120**, 516 (2004).
13. F. Liu, M. Nakaema, M. Gruebele, *J. Chem. Phys.* **131**, 195101 (2009).
14. I. C. Yeh, G. Hummer, *J. Phys. Chem. B* **108**, 15873 (2004).
15. N. D. Socci, J. N. Onuchic, P. G. Wolynes, *J. Chem. Phys.* **104**, 5860 (1996).
16. In the case of protein GB1, there is the possibility of a sparsely populated intermediate between the folded and unfolded states (*17–20*). In this study, we have implicitly defined the transition-path time for both the WW domain and protein GB1 in terms of just the two deep minima of the folded and unfolded states.
17. S. H. Park, M. C. R. Shastry, H. Roder, *Nat. Struct. Biol.* **6**, 943 (1999).
18. E. L. McCallister, E. Alm, D. Baker, *Nat. Struct. Biol.* **7**, 669 (2000).
19. A. Morrone *et al.*, *Biophys. J.* **101**, 2053 (2011).
20. B. A. Krantz, L. Mayne, J. Rumbley, S. W. Englander, T. R. Sosnick, *J. Mol. Biol.* **324**, 359 (2002).
21. Clarke and co-workers (*22*) have found, for example, domains with similar structures and stability that have folding rates that differ by ~3000-fold. The slower-folding domains show very little dependence on solvent viscosity, which suggests a large internal friction and, therefore, a much smaller D^* (*22*, *23*).
22. B. G. Wensley *et al.*, *Nature* **463**, 685 (2010).
23. T. Cellmer, E. R. Henry, J. Hofrichter, W. A. Eaton, *Proc. Natl. Acad. Sci. U.S.A.* **105**, 18320 (2008).
24. J. Kubelka, J. Hofrichter, W. A. Eaton, *Curr. Opin. Struct. Biol.* **14**, 76 (2004).
25. R. B. Best, G. Hummer, *Proc. Natl. Acad. Sci. U.S.A.* **102**, 6732 (2005).
26. J. Kubelka, E. R. Henry, T. Cellmer, J. Hofrichter, W. A. Eaton, *Proc. Natl. Acad. Sci. U.S.A.* **105**, 18655 (2008).

Acknowledgments: We thank I. Gopich, A. Szabo, and G. Hummer for numerous helpful discussions and A. Aniana for technical assistance in the expression and purification of proteins. This work was supported by the Intramural Research Program of the National Institute of Diabetes and Digestive and Kidney Diseases, NIH.

Supporting Online Material

www.sciencemag.org/cgi/content/full/335/6071/981/DC1
Materials and Methods
Figs. S1 to S9
Table S1
References (*27–37*)

25 October 2011; accepted 25 January 2012
10.1126/science.1215768

The Alarmin Interleukin-33 Drives Protective Antiviral CD8+ T Cell Responses

Weldy V. Bonilla,[1,2]* Anja Fröhlich,[3,4]* Karin Senn,[5]* Sandra Kallert,[1,2] Marylise Fernandez,[1,2] Susan Johnson,[1,2] Mario Kreutzfeldt,[1,6] Ahmed N. Hegazy,[3,4,7] Christina Schrick,[1,6] Padraic G. Fallon,[8] Roman Klemenz,[5] Susumu Nakae,[9] Heiko Adler,[10] Doron Merkler,[1,6,11] Max Löhning,[3,4]† Daniel D. Pinschewer[1,2]†

Pathogen-associated molecular patterns decisively influence antiviral immune responses, whereas the contribution of endogenous signals of tissue damage, also known as damage-associated molecular patterns or alarmins, remains ill defined. We show that interleukin-33 (IL-33), an alarmin released from necrotic cells, is necessary for potent CD8+ T cell (CTL) responses to replicating, prototypic RNA and DNA viruses in mice. IL-33 signaled through its receptor on activated CTLs, enhanced clonal expansion in a CTL-intrinsic fashion, determined plurifunctional effector cell differentiation, and was necessary for virus control. Moreover, recombinant IL-33 augmented vaccine-induced CTL responses. Radio-resistant cells of the splenic T cell zone produced IL-33, and efficient CTL responses required IL-33 from radio-resistant cells but not from hematopoietic cells. Thus, alarmin release by radio-resistant cells orchestrates protective antiviral CTL responses.

Pathogen-associated molecular patterns (PAMPs) characterize intruding microorganisms and are important for adaptive immune responses to viral infection (*1*). Conversely, endogenous molecular patterns, which indicate tissue injury, are referred to as alarmins and form a second class of damage-associated molecular patterns (DAMPs) (*2*). Unlike PAMPs, the potential contribution of alarmins to antiviral immune defense remains largely elusive.

Many viruses are excellent inducers of cytotoxic CD8+ T lymphocytes (CTLs) (*3*), the basis of which is incompletely understood. To screen

[1]Department of Pathology and Immunology, University of Geneva, 1 rue Michel Servet, 1211 Geneva 4, Switzerland. [2]World Health Organization Collaborating Center for Vaccine Immunology, University of Geneva, Switzerland. [3]Experimental Immunology, Department of Rheumatology and Clinical Immunology, Charité–University Medicine Berlin, Berlin, Germany. [4]German Rheumatism Research Center (DRFZ), a Leibniz Institute, Charitéplatz 1, 10117 Berlin, Germany. [5]Institute for Cancer Research, Department of Pathology, University Hospital of Zurich, Schmelzbergstrasse 12, 8091 Zurich, Switzerland. [6]Division of Clinical Pathology, Geneva University Hospital, 1 rue Michel Servet, 1211 Geneva 4, Switzerland. [7]Department of Gastroenterology, Hepatology and Endocrinology, Campus Charité Mitte, Charité–University Medicine Berlin, Berlin, Germany. [8]Institute of Molecular Medicine, St. James's Hospital, Trinity College Dublin, Dublin 8, Ireland. [9]The Institute of Medical Science, The University of Tokyo, 4-6-1 Shirokanedai, Minato-ku, Tokyo 108-8639, and Japan Science and Technology Agency, Precursory Research for Embryonic Science and Technology (PRESTO), 4-1-8 Hncho, Kawaguchi, Saitama 332-0012, Japan. [10]Helmholtz Zentrum München, Institute of Molecular Immunology and Clinical Cooperation Group Hematopoietic Cell Transplantation (CCG HCT), Marchioninistraße 25, 81377 München, Germany. [11]Department of Neuropathology, University Medical Center, Georg August University, Göttingen, Germany.

*These authors contributed equally to this work.
†These authors contributed equally to this work. To whom correspondence should be addressed. E-mail: loehning@drfz.de (M.L.); daniel.pinschewer@gmx.ch (D.P.P.)

for inflammatory signals augmenting antiviral CTL responses, we used lymphocytic choriomeningitis virus (LCMV) infection of mice. We performed a genome-wide cDNA expression analysis of total spleen tissue from LCMV-infected mice and compared it to an analysis of uninfected controls. From a large panel of interleukins and pro-inflammatory cytokines, interferon-γ (IFN-γ) and IL-33 were most up-regulated (table S1). The IL-33 receptor ST2, an IL-1 receptor family member also known as T1 and IL1RL1, was also up-regulated.

IL-33 is expressed in the nucleus of non-hematopoietic cells, such as fibroblasts and epithelial and endothelial cells of various tissues (*4*), but its role in antiviral CTL responses is unknown. Its bioactive pro-inflammatory form is released as a result of necrosis but not apoptosis, classifying IL-33 as an alarmin (*5*–*7*). IL-33 mRNA expression peaked at 3 to 5 days after infection and grossly paralleled the kinetics of LCMV RNA (Fig. 1A). To test whether IL-33 was important for CTL responses to LCMV, we performed infection experiments in IL-33–deficient ($Il33^{-/-}$) mice (*8*). Absence of IL-33 reduced the absolute number of CTLs responding to the immunodominant LCMV epitope GP33 by >90%. The frequency of epitope-specific CTLs was reduced by >75% (Fig. 1B). When expressed as a nuclear factor in healthy cells, IL-33 is complexed with chromatin and modulates gene expression (*9*). Upon release from necrotic cells, however, IL-33 binds and signals through ST2 (*10*, *11*). To assess which one of these roles of IL-33 accounted for defective CTL responses in $Il33^{-/-}$ mice, we used transgenic mice expressing a soluble decoy receptor for IL-33 [*Il1rl1-Fc* mice (*12*)]. *Il1rl1-Fc* mice displayed defective CTL expansion analogously to $Il33^{-/-}$ mice (fig. S1A). Mice lacking the IL-33 receptor ST2 [$Il1rl1^{-/-}$ (*13*)] also mounted similarly reduced responses to all three LCMV epitopes tested (Fig. 1C and fig. S1, B and C). This indicated that

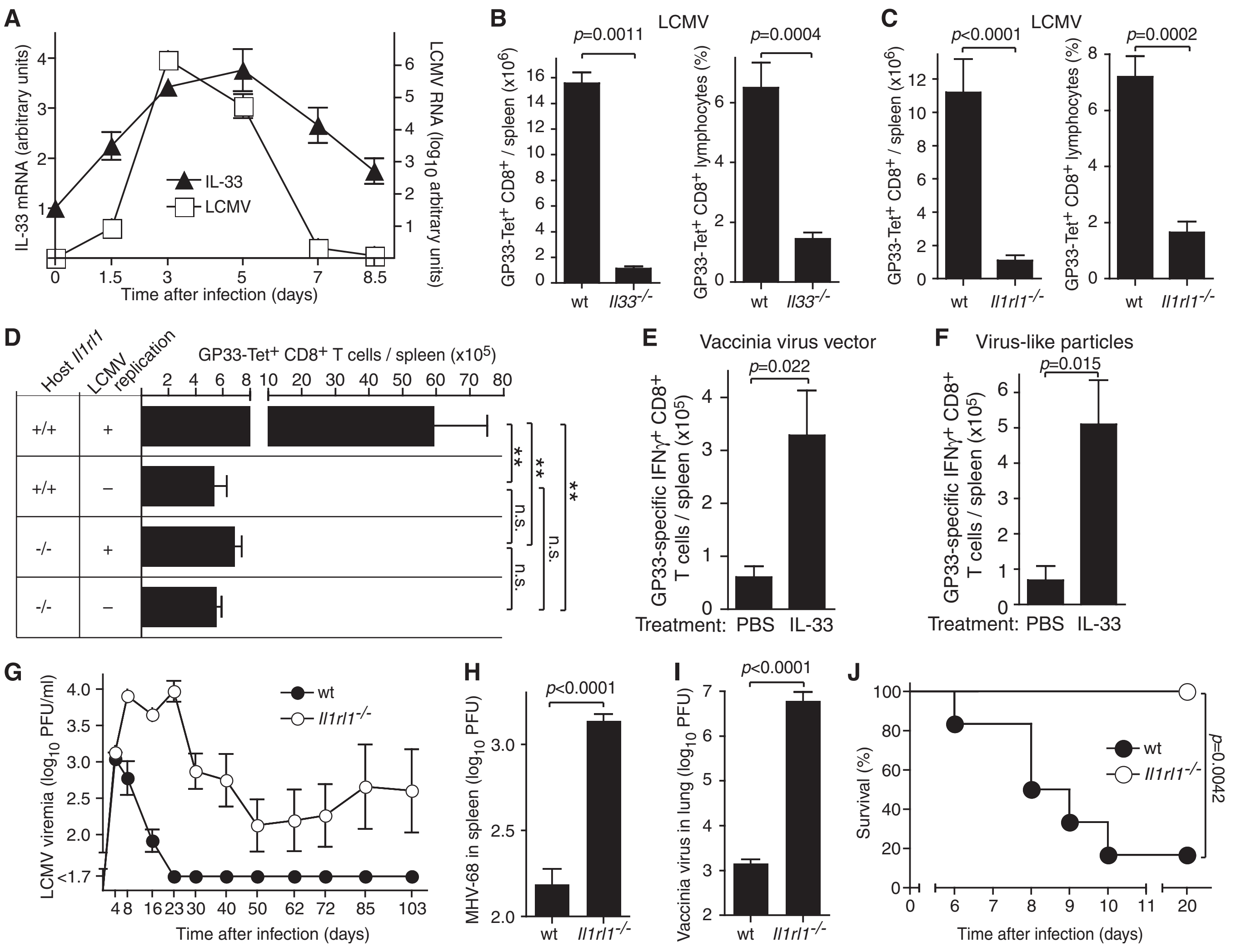

Fig. 1. The IL-33–ST2 pathway drives protective CTL responses to replicating viral infection. (**A**) Kinetic analysis of IL-33 and LCMV RNA expression in the spleen after LCMV infection. Symbols represent the mean ± SEM of four mice. *N* = 1 (*N* refers to the number of times an experiment was performed). (**B** and **C**) The number of GP33-specific CTLs in the spleen, as detected by peptide–major histocompatibility complex (MHC) tetramer staining, on day 8 after LCMV infection. Bars represent mean ± SEM of five mice. *N* = 1 (B) or 3 (C). (**D**) Epitope-specific CTLs of WT and $Il1rl1^{-/-}$ mice responding to replicating WT LCMV infection or to replication-deficient rLCMV vectors. Bars represent the mean ± SEM of five mice. *N* = 2. $P < 0.0001$ by one-way analysis of variance (ANOVA). Results of Bonferroni's posttest are indicated. n.s., not significant; $*P < 0.05$; $**P < 0.01$. (**E** and **F**) WT mice were vaccinated with recombinant VV vector expressing LCMV-GP (E) or with GP33-carrying VLPs (F) on day 0 and were treated with IL-33 or diluent [phosphate-buffered saline (PBS)] daily from day 1 to 7, and CTL responses were determined on day 8. Bars represent the mean ± SEM of four to five mice. *N* = 2 (E) or 1 (F). (**G**) Viremia after infection with 2×10^6 plaque-forming units (PFU) of LCMV-WE. Symbols represent the mean ± SEM of five mice. *N* = 2. (**H**) Splenic MHV-68 titers on day 10 after infection. Bars represent the mean ± SEM of five mice. *N* = 1. (**I**) Pulmonary VV titers on day 8 after infection. Bars represent the mean ± SEM of four to five mice. *N* = 1. (**J**) Incidence of choriomeningitis after intracerebral LCMV infection. Terminally diseased animals were killed in accordance with Swiss law. Survival was compared by using the log rank test. Groups of six mice were used. One of two similar experiments is shown. Unpaired two-tailed student's *t* test was used for statistical analysis in (B), (C), (E), (F), (H), and (I).

IL-33 was released to the extracellular compartment and signaled through ST2 to amplify antiviral CTL responses.

Analogous to the responses against LCMV, an RNA virus, *Il1rl1*$^{-/-}$ mice also exhibited significantly reduced CTL responses against murine γ-herpesvirus 68 [MHV-68 (*14*)], a DNA virus (fig. S1D). In further analogy to LCMV, MHV-68 induced IL-33 mRNA up-regulation (fig. S1E). The differences in CTL responses to LCMV and MHV-68 were also reflected in reduced antigen-specific cytotoxicity (fig. S1, F and G). However, CTL responses to a nonreplicating adenovirus-based vaccine vector were similar in *Il1rl1*$^{-/-}$ and wild-type (WT) mice (fig. S1H).

Given IL-33 can act as an alarmin, we hypothesized that productive viral replication may represent a unifying characteristic of LCMV and MHV-68 infection, differentiating them from adenoviral vectors. Indeed, the CTL responses of WT and *Il1rl1*$^{-/-}$ mice to replication-deficient LCMV-based vaccine vector (*15*) were indistinguishable, and the magnitude of these responses was comparable to the magnitude of responses observed in WT LCMV-infected *Il1rl1*$^{-/-}$ mice (Fig. 1D). Further, *Il1rl1*$^{-/-}$ mice mounted defective CTL responses against WT vaccinia virus (VV), whereas attenuated [thymidine kinase–deficient (*16*)] VV-based vectors induced comparable responses in *Il1rl1*$^{-/-}$ and WT controls (fig. S1I). Thus, we hypothesized that exogenously administered IL-33 could mimic viral replication to enhance vaccine-induced CTL responses. Indeed, recombinant IL-33 significantly augmented CTL responses to VV-based vectors and viruslike particles (VLPs) (Fig. 1, E and F).

CTLs play a pivotal role in the resolution of primary viral infection (*14*, *17*). *Il1rl1*$^{-/-}$ mice controlled low-dose LCMV infection (fig. S1J) but displayed elevated viremia after high-dose LCMV infection and often progressed to viral persistence, whereas WT control mice eliminated the virus (Fig. 1G and fig. S1K). ST2-deficient mice also displayed a log increase in splenic MHV-68 titers and three logs increase in pulmonary VV titers (Fig. 1, H and I). LCMV-neutralizing antibody responses were comparable in *Il1rl1*$^{-/-}$ mice and WT controls (fig. S1L), suggesting that defective CTL responses of *Il1rl1*$^{-/-}$ mice were at the root of impaired LCMV control.

LCMV can cause lethal CTL-mediated immunopathologic disease of the central nervous system when administered intracranially (*17*). Five out of six WT mice developed terminal disease within 10 days, whereas all *Il1rl1*$^{-/-}$ mice survived without clinical signs of immunopathology (Fig. 1J).

The IL-33 receptor ST2 has predominantly been detected on mast cells and CD4^{+} T helper type 2 cells (*18*–*20*), reportedly exerting pleiotropic effects on helminth-specific immunity, allergy, anaphylaxis, autoimmune, and cardiovascular disease (*20*, *21*). Conversely, ST2 expression on human and mouse CTLs has only recently been found under select in vitro culture and differentiation conditions (*22*). Hence, we investigated which cells were sensing IL-33 for augmenting antiviral CTL responses. To this end, we reconstituted lethally irradiated mice with an approximately 1:1 mixture of WT (CD45.1^{+}) and ST2-deficient bone marrow (CD45.1^{-}) (Fig. 2A and fig. S2A). Compared with uninfected mice, WT cells were 10-fold overrepresented in the population of antigen-specific CTLs responding to LCMV infection (Fig. 2A). In contrast, the repartition of WT and *Il1rl1*$^{-/-}$ B cells remained unaltered (fig. S2A). These observations suggested that virus-reactive

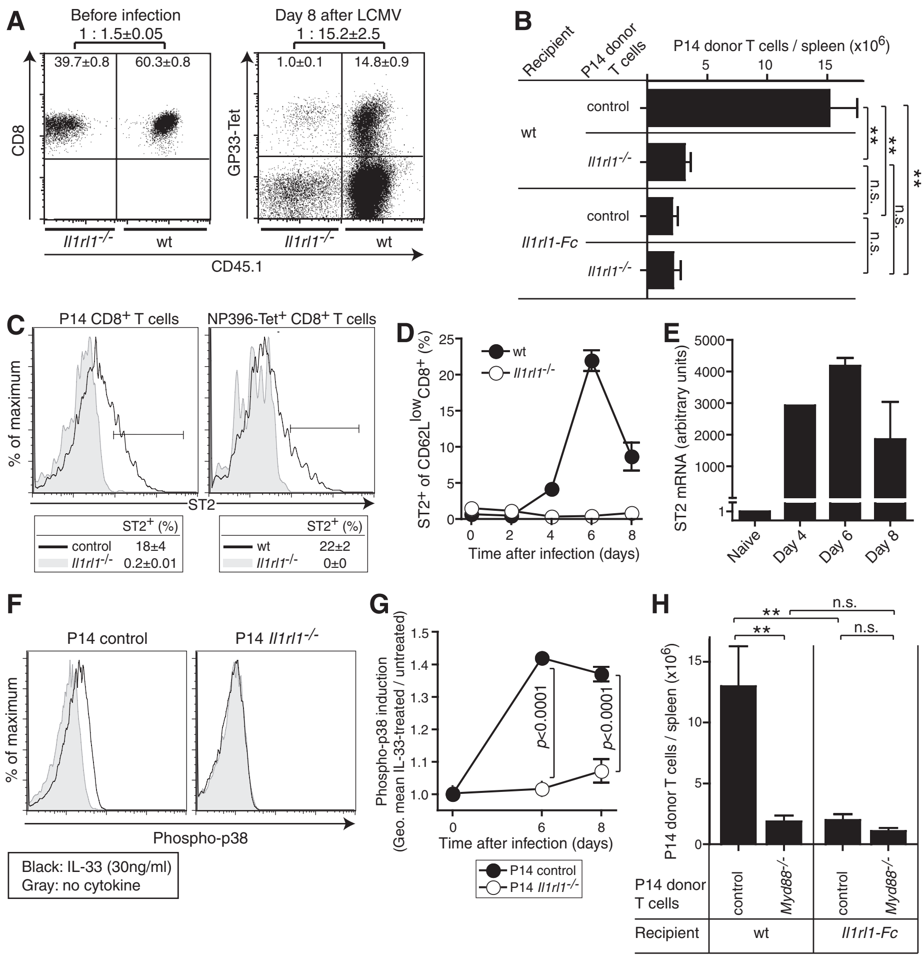

Fig. 2. CD8^{+} T cell–intrinsic signaling through ST2 and MyD88 augments antiviral CTL responses. (**A**) Irradiated recipients were reconstituted with WT (CD45.1^{+}) and *Il1rl1*$^{-/-}$ (CD45.1^{-}) bone marrow. Flow cytometric analysis of WT and *Il1rl1*$^{-/-}$ total CD8^{+} T cells before infection (left) and virus-specific CD8^{+} T cells 8 days after LCMV challenge (right). Values represent mean frequency ± SEM of three mice. $N = 2$. (**B**) Control (CD45.1^{+}CD45.2^{-}) and *Il1rl1*$^{-/-}$ (CD45.1^{+}CD45.2^{+}) P14 CD8^{+} T cells (10^4) were cotransferred into WT and *Il1rl1-Fc* recipient mice (CD45.1^{-}CD45.2^{+}) and were enumerated on day 8 after LCMV. Bars represent the mean ± SEM of four mice per group. $P < 0.0001$ by one-way ANOVA. Results of Bonferroni's posttest are indicated. One representative of three similar experiments is shown. (**C**) Control and *Il1rl1*$^{-/-}$ P14 cells (10^4) were individually transferred into WT recipients (left). Peptide-MHC tetramer–binding cells in WT and *Il1rl1*$^{-/-}$ mice were studied (right). On day 6 after LCMV infection, the indicated cell populations in spleen were analyzed for ST2 expression by flow cytometry. Values represent the mean ± SD of three mice. $N = 2$. (**D**) Flow cytometric analysis of splenic CD62L^{low}CD8^{+} T cells over time after LCMV infection. Symbols represent the mean ± SEM of three mice (WT days 2 to 8; *Il1rl1*$^{-/-}$ day 6) or the mean of two mice (other symbols). $N = 2$. (**E**) Quantitative reverse-transcription polymerase chain reaction (qRT-PCR) analysis of ST2 mRNA levels in P14 CD8^{+} T cells. Day 6 and 8 values represent the mean ± SEM of three mice. RNA samples from three donor mice were pooled for combined analysis on days 0 and 4. $N = 1$. (**F** and **G**) Flow cytometric analysis of intracellular phospho-p38 expression in control and *Il1rl1*$^{-/-}$ P14 cells isolated on day 6 (F) or over time after LCMV infection and treated ex vivo with recombinant IL-33. Symbols in (G) represent the mean ± SEM of three mice. Unpaired two-tailed student's *t* test was used for statistical analysis. One representative of two similar experiments is shown. (**H**) Control (CD45.1^{+}CD45.2^{-}) and *Myd88*$^{-/-}$ (CD45.1^{+}CD45.2^{+}) P14 cells were cotransferred to WT and *Il1rl1-Fc* recipient mice (CD45.1^{-}CD45.2^{+}). Expansion was assessed 8 days after LCMV infection. Bars represent the mean ± SEM of four mice per group. $P = 0.0008$ by one-way ANOVA. Results of Bonferroni's posttest are indicated. $N = 1$.

CTLs respond to IL-33 directly. Independent evidence was obtained when T cell receptor–transgenic GP33-specific CTLs (*23*) (P14 cells) were adoptively transferred, followed by LCMV challenge (Fig. 2B). Impaired expansion of ST2-deficient P14 cells in WT recipients corroborated CTL-intrinsic ST2 signaling. As expected, no such differences were seen between control and ST2-deficient P14 cells in the IL-33–depleted environment of *Il1rl1-Fc* mice (Fig. 2B). Primary CTL responses to LCMV are CD4 T cell independent (*24*), and the differences in CTL responses between WT and $Il1rl1^{-/-}$ mice persisted when $CD4^+$ T cells were depleted (fig. S2B). Altogether, these findings established a CTL-intrinsic role of ST2 signaling in the expansion of antiviral CTLs.

On day 6 after LCMV infection, we observed ST2 expression on up to 20% of virus-specific CTLs, representing the peak of expression as monitored on activated ($CD62L^{low}$) CTLs (Fig. 2, C and D, and fig. S2, C and D). In P14 cells, we detected a simultaneous peak of ST2 mRNA (Fig. 2E). IL-33 signaling through ST2 involves the adaptor protein MyD88 and downstream phosphorylation of p38 mitogen-activated protein kinase (*10*). Exposure of day 6 LCMV-infected splenocytes to IL-33 ex vivo increased phospho-p38 levels in control P14 cells but not in ST2-deficient ones (Fig. 2F). In concordance with induction of ST2 expression upon activation, IL-33 failed to trigger detectable phospho-p38 signals in naïve P14 cells but did so on day 6 and 8 after infection (Fig. 2G). MyD88 serves important CTL-intrinsic functions, but the upstream receptor(s) accounting for these effects had remained elusive (*25*). In agreement with previous reports, $Myd88^{-/-}$ P14 cells expanded significantly less than control P14 cells when adoptively transferred into WT recipients and challenged with LCMV (Fig. 2H). In the IL-33–depleted environment of *Il1rl1-Fc* recipients, however, control and $Myd88^{-/-}$ P14 cells responded equivalently, suggesting that defective expansion of $Myd88^{-/-}$ P14 cells was largely attributable to a lack of ST2 downstream signaling.

CTL functionality represents an important correlate of protective capacity (*26*). A substantial proportion of control P14 effector cells were plurifunctional, co-expressing IFN-γ, tumor necrosis factor (TNF)-α, IL-2, and the degranulation marker CD107a in various combinations (Fig. 3A). Conversely, about 95% of ST2-deficient P14 cells were monofunctional or lacked effector function (Fig. 3A). Reduced plurifunctionality was also observed in polyclonal antiviral CTL populations of ST2-deficient compared with WT mice (fig. S3A). Coexpression of granzyme B and CD107a indicates efficient cytotoxicity and was nearly undetectable in ST2-deficient P14 cells (Fig. 3B). Control P14 cells also contained significantly higher levels of the anti-apoptotic protein Bcl-2 than ST2-deficient cells (Fig. 3C).

We performed genome-wide cDNA expression profiling of control and ST2-deficient effector P14 cells, yielding 63 differentially expressed candidate genes (fig. S3B and table S2). We validated differential expression of *Klrb1c* (NK1.1) and *Clec2i*, which influence effector cell differentiation and proliferation (*27*, *28*); *Ifitm1* and *Ifitm3*, which mediate the antiproliferative effects of IFN-γ and pro-apoptotic signals (*29*); and *Tspan5*, which affects cell proliferation, migration, and adhesion (*30*); thus corroborating the broad and profound effects of ST2 signals on the $CD8^+$ effector T cell transcriptome (Fig. 3D). The gene that encodes KLRG-1, which is a marker of effector CTLs (*31*), was also among the gene array candidates. Indeed, ST2-deficient P14 cells and virus-specific CTLs of $Il1rl1^{-/-}$ mice exhibited a significant reduction in $KLRG\text{-}1^{high}CD127^{low}$ effector CTLs, failed to express NK1.1, and expressed somewhat higher levels of the inhibitory receptor PD-1 (Fig. 3, E and F, and fig. S3, C to E). With transition to the memory phase, however, the size of the LCMV-specific CTL pool and the cells' KLRG-1 expression became similar in WT and

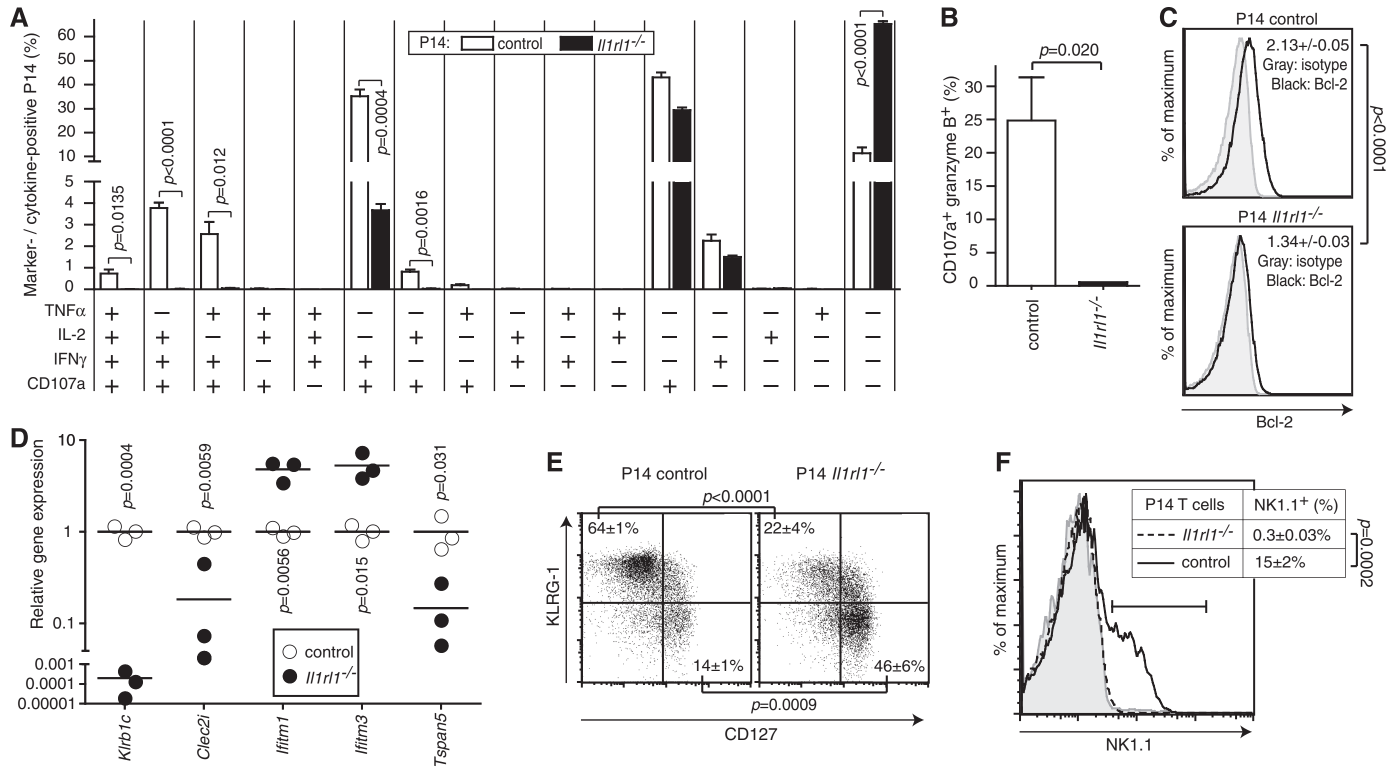

Fig. 3. Broad and profound influence of ST2 signaling on effector CTL differentiation and functionality. (**A** to **C**) $CD45.1^+$ control and ST2-deficient P14 $CD8^+$ T cells (10^4) were adoptively transferred into WT recipient mice, which were then challenged with LCMV. Cytokine profile (A), cytolytic phenotype (B), and Bcl-2 expression (C) were assessed on day 8 after LCMV infection. Bars represent mean ± SEM of three mice. Values in (C) represent geometric mean indices (mean ± SD of three mice per group). *N* = 1 [(A) and (B)] or 2 (C). (**D**) Gene expression profile of P14 cells from recipients as in (A) to (C). The full set of differentially expressed genes is displayed in fig. S3B (also listed in table S2). We validated select genes by qRT-PCR. Symbols show individual mice. *N* = 1. (**E** and **F**) Phenotypic analysis of splenic $Il1rl1^{-/-}$ and control P14 $CD8^+$ T cells from day 8 LCMV-infected WT recipients as in (A) to (C). Values indicate mean ± SD of three mice. Naïve control P14 T cells are shown as reference in (F) (gray shaded). *N* = 1. Unpaired two-tailed student's *t* test was used for statistical analysis.

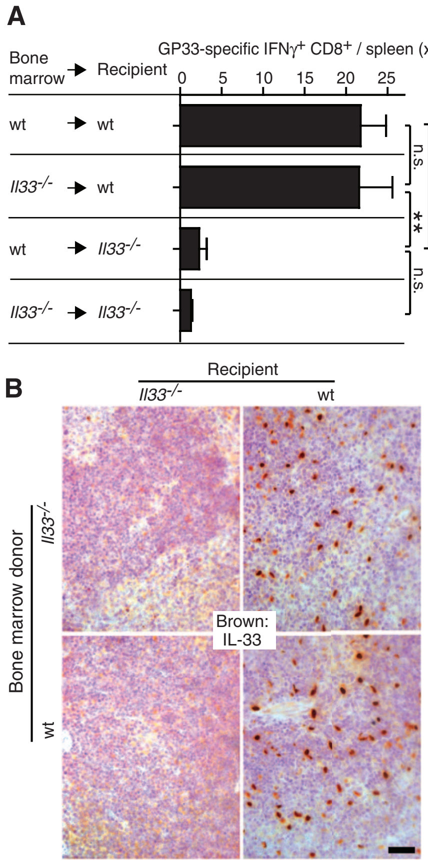

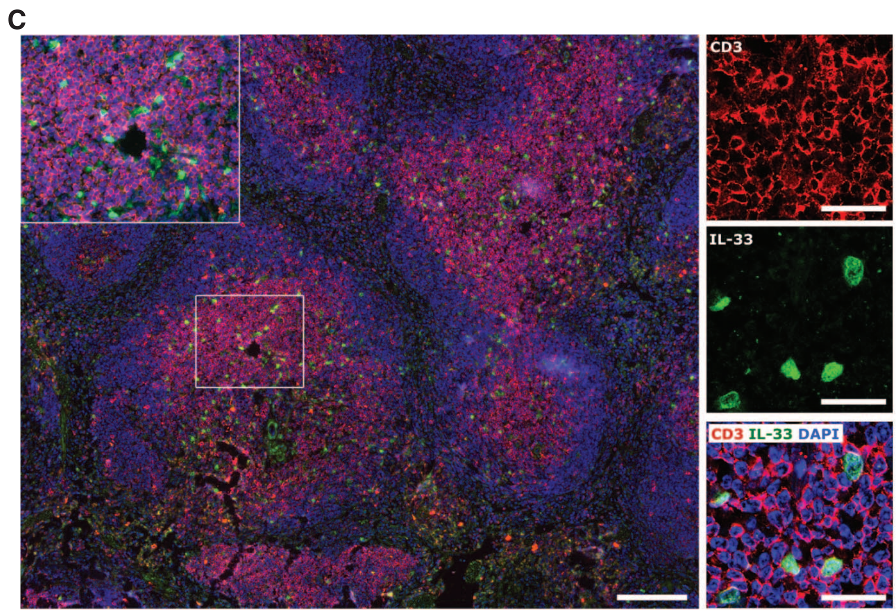

Fig. 4. Radio-resistant cells of the T cell zone produce IL-33 for efficient CTL induction. (**A**) Bone marrow chimeras were generated by using *Il33*$^{-/-}$ and WT recipients as indicated. Two months later, the CTL response to LCMV infection was determined (day 8 after infection). Bars represent the mean ± SEM of five mice. $P = 0.0038$ by one-way ANOVA. Results of Bonferroni's posttest are indicated. $N = 2$. (**B**) Spleens from chimeras as in (A) were analyzed for IL-33–expressing cells by immunohistochemistry. The scale bar indicates 50 μm. The image was acquired at 100-fold magnification. Representative pictures from one out of four animals are shown. (**C**) IL-33$^+$ cells (green) are predominantly found in the T cell zone (characterized by CD3$^+$ T cell clusters, red). DAPI (4′,6′-diamidino-2-phenylindole) was used to stain nuclei (blue). The central white rectangle is displayed at higher magnification in the top left corner of the large image. The small images at right show close vicinity of IL-33$^+$ cells and CD3$^+$ T cells. Scale bars indicate 200 μm (large image) or 50 μm (small images and inset). Images were acquired at 200-fold magnification by using a slide scanner (large image and inset) and at 400-fold magnification by confocal microscopy (small images). Representative pictures from one out of four mice are shown.

Il1rl1$^{-/-}$ mice, and vaccinated *Il1rl1*$^{-/-}$ mice controlled LCMV challenge infection as efficiently as WT controls (fig. S3, F and G). This supported the concept that inflammatory signals are more important for primary effector CTL responses than for memory formation (*25*, *32*).

To characterize the cellular source of IL-33 bolstering antiviral CTL responses, we generated reciprocal bone marrow chimeras by using WT or *Il33*$^{-/-}$ mice (Fig. 4A). WT recipient mice generated significantly more LCMV-specific CTLs than *Il33*$^{-/-}$ recipients, irrespective of the IL-33 competence of the bone marrow. These data suggested that radio-resistant, and thus nonhematopoietic, cells are the main source of IL-33. IL-33$^+$ cells were only detected in the spleen of chimeras generated from WT recipients, irrespective of the bone marrow received (WT or *Il33*$^{-/-}$, Fig. 4B). IL-33$^+$ cells colocalized predominantly with CD3$^+$ cells but only sparsely with B cells (Fig. 4C and fig. S4). This was compatible with IL-33 expression by fibroblastic reticular cells (*4*), a stromal cell population of the T cell zone and known target of LCMV infection (*33*).

In light of the evidence for IL-33 to act as an alarmin (*5*, *6*), our findings offer a previously unknown molecular link to understand how viral replication, commonly thought of as "danger" (*34*), can enhance CTL responses to infection. The nonredundancy with PAMPs is noteworthy, particularly in the context of viral replication, which provides abundant PAMP signals (*1*). The observed LCMV dose dependency suggests that the IL-33–ST2 axis is most relevant under conditions of high viral burden. We identified nonhematopoietic cells in the splenic T cell zone expressing IL-33. Depending on the site of initiation and expansion of T cell responses, other cell types expressing IL-33 may also supply this cytokine to CTLs (*35*), and potential regulation by the soluble form of ST2 remains to be investigated (*36*).

PAMPs act primarily on professional antigen-presenting cells and thereby are decisive for efficient priming of CTLs (*37*). IL-33 and possibly also other alarmins have complementary and nonredundant functions and, in the case of IL-33, act on antiviral CTLs directly. Taken together, this study establishes a paradigm for the role of nonhematopoietic cells providing alarmins to augment and differentiate protective CTL responses to viral infection.

References and Notes

1. D. Schenten, R. Medzhitov, *Adv. Immunol.* **109**, 87 (2011).
2. J. J. Oppenheim, D. Yang, *Curr. Opin. Immunol.* **17**, 359 (2005).
3. J. W. Yewdell, S. M. Haeryfar, *Annu. Rev. Immunol.* **23**, 651 (2005).
4. C. Moussion, N. Ortega, J. P. Girard, *PLoS ONE* **3**, e3331 (2008).
5. W. Zhao, Z. Hu, *Cell. Mol. Immunol.* **7**, 260 (2010).
6. G. Haraldsen, J. Balogh, J. Pollheimer, J. Sponheim, A. M. Küchler, *Trends Immunol.* **30**, 227 (2009).
7. C. Cayrol, J. P. Girard, *Proc. Natl. Acad. Sci. U.S.A.* **106**, 9021 (2009).
8. K. Oboki *et al.*, *Proc. Natl. Acad. Sci. U.S.A.* **107**, 18581 (2010).
9. V. Carriere *et al.*, *Proc. Natl. Acad. Sci. U.S.A.* **104**, 282 (2007).
10. J. Schmitz *et al.*, *Immunity* **23**, 479 (2005).
11. C. A. Dinarello, *Annu. Rev. Immunol.* **27**, 519 (2009).
12. K. A. Senn *et al.*, *Eur. J. Immunol.* **30**, 1929 (2000).
13. M. J. Townsend, P. G. Fallon, D. J. Matthews, H. E. Jolin, A. N. McKenzie, *J. Exp. Med.* **191**, 1069 (2000).
14. S. Ehtisham, N. P. Sunil-Chandra, A. A. Nash, *J. Virol.* **67**, 5247 (1993).
15. L. Flatz *et al.*, *Nat. Med.* **16**, 339 (2010).
16. R. M. Buller, G. L. Smith, K. Cremer, A. L. Notkins, B. Moss, *Nature* **317**, 813 (1985).
17. W. P. Fung-Leung, T. M. Kündig, R. M. Zinkernagel, T. W. Mak, *J. Exp. Med.* **174**, 1425 (1991).
18. M. Löhning *et al.*, *Proc. Natl. Acad. Sci. U.S.A.* **95**, 6930 (1998).
19. D. Xu *et al.*, *J. Exp. Med.* **187**, 787 (1998).
20. F. Y. Liew, N. I. Pitman, I. B. McInnes, *Nat. Rev. Immunol.* **10**, 103 (2010).
21. G. Palmer, C. Gabay, *Nat. Rev. Rheumatol.* **7**, 321 (2011).
22. Q. Yang *et al.*, *Eur. J. Immunol.* **41**, 3351 (2011).
23. H. Pircher, K. Bürki, R. Lang, H. Hengartner, R. M. Zinkernagel, *Nature* **342**, 559 (1989).
24. A. Rahemtulla *et al.*, *Nature* **353**, 180 (1991).
25. A. H. Rahman *et al.*, *J. Immunol.* **181**, 3804 (2008).
26. V. Appay, R. A. van Lier, F. Sallusto, M. Roederer, *Cytometry A* **73**, 975 (2008).
27. B. Ljutic *et al.*, *J. Immunol.* **174**, 4789 (2005).

28. W. Tian *et al.*, *Cell. Immunol.* **234**, 39 (2005).
29. M. J. Dobrzanski, J. B. Reome, J. A. Hollenbaugh, R. W. Dutton, *J. Immunol.* **172**, 1380 (2004).
30. L. A. Koopman *et al.*, *J. Exp. Med.* **198**, 1201 (2003).
31. N. S. Joshi *et al.*, *Immunity* **27**, 281 (2007).
32. A. H. Rahman *et al.*, *Blood* **117**, 3123 (2011).
33. S. N. Mueller *et al.*, *Proc. Natl. Acad. Sci. U.S.A.* **104**, 15430 (2007).
34. S. Gallucci, P. Matzinger, *Curr. Opin. Immunol.* **13**, 114 (2001).
35. R. Le Goffic *et al.*, *Am. J. Respir. Cell Mol. Biol.* **45**, 1125 (2011).
36. A. Becerra, R. V. Warke, N. de Bosch, A. L. Rothman, I. Bosch, *Cytokine* **41**, 114 (2008).
37. O. Joffre, M. A. Nolte, R. Spörri, C. Reis e Sousa, *Immunol. Rev.* **227**, 234 (2009).

Acknowledgments: This work was supported by Bundesministerium für Bildung und Forschung (BMBF)–FORSYS (A.F., M.L.), National Health and Medical Research Council (S.J.), German Research Foundation (GRK1121, A.N.H.), Science Foundation Ireland (P.G.F.), Program for Improvement of Research Environment for Young Researchers, the Special Coordination Funds for Promoting Science and Technology from the Japanese Ministry of Education, Culture, Sports, Science and Technology, Japan Science and Technology Agency, PRESTO (S.N.), BMBF (NGFNplus, FKZ PIM-01GS0802-3; H.A.), Wilhelm Sander-Stiftung (H.A.), German Research Foundation (SFB618 and SFB650, M.L.), Volkswagen Foundation (Lichtenberg Program, M.L.), Fondation Leenaards (D.D.P.), European Community (D.D.P.), and Swiss National Science Foundation (D.M., D.D.P.). We thank A. Bergthaler, G. R. Burmester, C. Gabay, M. Geuking, A. Kamath, P. H. Lambert, J. Luban, B. Marsland, G. Palmer, A. Radbruch, C. A. Siegrist, and R. M. Zinkernagel for discussions and advice; H. Saito, National Research Institute for Child Health and Development, for *Il33*$^{-/-}$ mice obtained under a materials transfer agreement (MTA) through the RIKEN Center for Developmental Biology, Laboratory for Animal Resources and Genetic Engineering; A. McKenzie (for *Il1rl1*$^{-/-}$ mice obtained under MTA); the University of Zurich (for rLCMV technology obtained under MTA) and G. Jennings [Cytos Biotechnology AG, Schlieren, Switzerland, holding patent rights on VLPs provided] for reagents; and J. Weber and B. Steer for technical assistance. The data presented in this paper are tabulated in the main paper and the supporting online material. Microarray data are deposited with National Center for Biotechnology Information Gene Expression Omnibus (GEO, accession number GSE34392) and ArrayExpress (accession number E-MTAB-901). D.D.P. is or has been a shareholder, board member, and consultant to ArenaVax AG, Switzerland, and to Hookipa Biotech GmbH, Austria, commercializing rLCMV vectors (patent application EP 07 025 099.8, coauthored by D.D.P.). The authors declare that they do not have other competing financial interests.

Supporting Online Material
www.sciencemag.org/cgi/content/full/science.1215418/DC1
Materials and Methods
Figs. S1 to S4
Tables S1 and S2
References (*38–40*)

18 October 2011; accepted 20 January 2012
Published online 9 February 2012;
10.1126/science.1215418

The Cellular Basis of $GABA_B$-Mediated Interhemispheric Inhibition

Lucy M. Palmer,[1] Jan M. Schulz,[1] Sean C. Murphy,[1] Debora Ledergerber,[1] Masanori Murayama,[2] Matthew E. Larkum[1,3]*

Interhemispheric inhibition is thought to mediate cortical rivalry between the two hemispheres through callosal input. The long-lasting form of this inhibition is believed to operate via γ-aminobutyric acid type B ($GABA_B$) receptors, but the process is poorly understood at the cellular level. We found that the firing of layer 5 pyramidal neurons in rat somatosensory cortex due to contralateral sensory stimulation was inhibited for hundreds of milliseconds when paired with ipsilateral stimulation. The inhibition acted directly on apical dendrites via layer 1 interneurons but was silent in the absence of pyramidal cell firing, relying on metabotropic inhibition of active dendritic currents recruited during neuronal activity. The results not only reveal the microcircuitry underlying interhemispheric inhibition but also demonstrate the importance of active dendritic properties for cortical output.

The connection between the two hemispheres of the cerebral cortex via the corpus callosum is one of the most studied and yet least understood pathways in the brain (*1*, *2*). An important function of transcallosal fibers is to mediate interhemispheric inhibition (*3*, *4*), which influences fine motor control (*5*, *6*), visuospatial attention (*7–9*), and somatosensory processing (*10*, *11*). To investigate the cellular mechanisms of interhemispheric inhibition, we performed in vivo patch-clamp recordings from layer 5 (L5) pyramidal neurons in the hindlimb area of the somatosensory cortex in urethane-anesthetized rats (Fig. 1A). Stimulation of the contralateral hindpaw (contralateral HS) (1-ms duration, 100 V) increased the baseline firing rate by a factor of about 3 (0.9 ± 0.2 to 2.9 ± 0.6 Hz; $P < 0.05$; $n = 19$) (Fig. 1, B to D, black). Ipsilateral hindpaw stimulation (ipsilateral HS), on the other hand, had little influence on the firing rate (1-ms duration, 100V; spontaneous, 1.1 ± 0.2 Hz and evoked, 1.2 ± 0.2 Hz; $n = 19$ (Fig. 1B, green). However, an inhibitory influence of ipsilateral HS could be uncovered by pairing it with contralateral HS (paired HS). Here, paired HS resulted in a significant decrease in evoked firing (evoked, 2.2 ± 0.5 Hz; $n = 19$; $P < 0.05$) when the ipsilateral hindpaw was stimulated 400 ms before the contralateral hindpaw (Fig. 1, B to D, blue). This influence of paired HS on action potential (AP) generation occurred throughout the entire evoked excitatory response, which lasted on average 513 ± 49 ms ($n = 19$) (Fig. 1C, gray area). Unexpectedly, paired HS had no discernible effect on the subthreshold responses (Fig. 1, B to D), which did not significantly decrease in average area (3.4 ± 0.6 versus 3.4 ± 0.6 mV•s; $n = 20$) nor variance (15.7 ± 1.9 versus 17.2 ± 02.1 mV^2; $n = 20$) (fig. S1).

The average $25 \pm 8\%$ decrease in the evoked firing during paired HS was somatotopically specific because stimulation of different regions of the body, or even different parts of the hindlimb, did not reduce the response to contralateral HS (fig. S2). Furthermore, the decrease in firing did not occur when the contralateral hindpaw was stimulated twice at an interval of 400 ms (fig. S3), and paired HS had no inhibitory effect on layer 2/3 (L2/3) pyramidal neurons (contralateral HS, 3.9 ± 0.6 Hz; paired HS, 3.6 ± 0.7 Hz; $t = 400$ ms; $n = 9$) (fig. S4). When the timing of the paired-HS interval was varied in 200-ms steps, L5 pyramidal neuron firing was only influenced when the ipsilateral hindpaw was stimulated either 200 or 400 ms before the contralateral hindpaw (Fig. 1E). The long-time course for this type of inhibition suggested the involvement of γ-aminobutyric acid type B ($GABA_B$) receptors, which can exert an effect for up to 500 ms in vitro (*12*). Indeed, application of the $GABA_B$-receptor antagonist, CGP52432 (1 μM) to the cortical surface blocked the decrease in firing generated by paired HS (contralateral HS, 1.9 ± 0.7 Hz; paired HS, 2.0 ± 0.9 Hz, $t = 400$ ms; $n = 8$) (Fig. 1E).

It has been suggested in humans that ipsilateral somatosensory stimulation leads to suppression of sensory responses due to transcallosal inhibition (*13*). We tested this hypothesis in rats using optogenetic stimulation of the transcallosal pathway in vivo. Deep-layer neurons infected with channelrhodopsin-2 (ChR2) conjugated with adenovirus (AAV) sent callosal fibers predominantly to the upper layers of the opposite hemisphere (Fig. 2A and fig. S5) [see supporting online material (SOM)]. Photostimulation (470 nm; trains of 10- by 10-ms pulses at 10 Hz, beginning 400 ms before the sensory stimulus) of callosal input decreased the evoked firing rate of L5 pyramidal neurons by $36 \pm 15\%$ when the light was focused above the hemisphere containing the recording electrode ($n = 9$; $P < 0.05$) (Fig. 2, B and C) and by $38\% \pm 14\%$ with photostimulation of the injected hemisphere ($n = 7$; $P < 0.05$) (fig. S6). Photoactivation of the callosal fibers alone did not influence spontaneous firing activity (0.6 ± 0.2 Hz prephotoactivation and 0.7 ± 0.3 Hz during photoactivation) (fig. S6), and there was

[1]Physiologisches Institut, Universität Bern, Bühlplatz 5, CH-3012 Bern, Switzerland. [2]Behavioral Neurophysiology Laboratory, Brain Science Institute, Riken, 2-1 Hirosawa, Wako, Saitama 351-0198, Japan. [3]Neurocure Cluster of Excellence, Department of Biology, Humboldt University, Charitéplatz 1, 10117, Berlin, Germany.

*To whom correspondence should be addressed. E-mail: matthew.larkum@gmail.com

no measurable influence of callosal fiber photoactivation on the underlying subthreshold envelope (contralateral HS alone, 2.1 ± 0.5 mV•s compared with contralateral HS + ChR2, 2.5 ± 0.5 mV•s; $P > 0.05$; $n = 13$) (fig. S6).

The corpus callosum consists almost entirely of excitatory fibers (*14*), which implies that interhemispheric inhibition arises from the activation of local interneurons. We tested this ex vivo with photostimulation of callosal fibers while recording from local interneurons in brain slices prepared from rats previously injected with ChR2/AAV (Fig. 2, A and D). To investigate monosynaptic callosal input, we added TTX (1 μM) and 4-AP (100 μM) (*15*) and activated callosal fibers using 460-nm light pulses over the field of view (10 by 10-ms pulses at 10 Hz, 60X objective). Interneurons were identified by their morphology and spiking characteristics (*16*) (fig. S7). The voltage response to monosynaptic callosal input in interneurons located in L1 (29.1 ± 6.6 mV; $n = 9$) and L2/3 (31.1 ± 4.6 mV; $n = 20$) was significantly larger than L5 interneurons (14.4 ± 3.5 mV; $n = 24$; $P < 0.05$) (Fig. 2, E and F). To further investigate the laminar specificity of callosal input on interhemispheric inhibition, we locally perfused the excitatory AMPA-receptor antagonist CNQX (100 μM) above the recorded cell in vivo. Interhemispheric inhibition evoked with paired HS was completely abolished by CNQX perfused into L1 (paired HS/contralateral HS 1.0 ± 0.1; $n = 6$) but not L2/3 (paired HS/contralateral HS, 0.6 ± 0.1; $n = 6$) (Fig. 2, G and H), suggesting that callosal input to L1 is crucial (see also fig. S8). (Local perfusion of CNQX did not in itself significantly change the AP firing rate of L5 pyramidal neurons in response to contralateral HS). In contrast to pyramidal neurons (Fig. 1B), ipsilateral HS alone evoked activity in L1 neurons. Two-photon calcium imaging from L1 neurons bulk-loaded with the calcium indicator Oregon Green 488 BAPTA-1-AM (OGB-1-AM) (Fig. 2I) revealed responses to ipsilateral HS in 41% of L1 neurons (Fig. 2J) ($n = 107$ neurons from seven rats). L1 contains a subpopulation of late-spiking, neurogliaform cells (~40% of cells) (*17*) that provide $GABA_B$-mediated inhibition (*18*) to the dendrites of pyramidal neurons (*19*).

The targeting of callosal input to L1 suggests that interhemispheric inhibition of L5 pyramidal neurons may act through a dendritically located mechanism (*12*, *19*, *20*). We therefore investigated the effects of ipsilateral HS on the calcium response in a population of L5 pyramidal neuron dendrites using a fiberoptic technique for recording dendritic activity (the "periscope" system) (*21*, *22*) (Fig. 3A) (see SOM). Contralateral HS evoked a biphasic Ca^{2+} signal in L5 pyramidal neuron dendrites (Fig. 3B, black trace) that was significantly reduced (31 ± 6%; $P < 0.05$) when paired with ipsilateral HS (t = 400 ms; $n = 13$) (blue trace, Fig. 3, B and C) (see fig. S9 for times all between $t = 0$ and $t = 800$ ms). This decrease in dendritic activity was abolished by application of the $GABA_B$-receptor antagonist CGP52432 (1 μM) to the cortical surface (Fig. 3C, right). The similar inhibitory influence of paired HS on firing rates and dendritic Ca^{2+} in L5 pyramidal neurons suggests a strong correlation between dendritic activity and somatic output in vivo.

Was the down-regulation of dendritic Ca^{2+} activity due to the pre- or postsynaptic activation of dendritic $GABA_B$ receptors (*12*) that are abundant in pyramidal apical dendrites (*23*)? We used three strategies to investigate this question. First, we recorded dendritic Ca^{2+} activity with the periscope while focally applying the $GABA_B$ agonist baclofen (50 μM) to the distal apical dendrites of L5 pyramidal neurons in vivo (Fig. 3D). We observed an even larger decrease in the area (55 ± 9%; $n = 8$) and amplitude (51 ± 6%; $n = 8$) of the evoked dendritic Ca^{2+} response (Fig. 3, E and F). Second, we performed whole-cell recordings from L5 dendrites identified by their distinctive complex AP waveforms (*24*) (fig. S10) and post hoc biocytin reconstructions (Fig. 3G) (see SOM). During baclofen applied either focally to the distal dendrite or on the cortical surface, the dendritic response to contralateral HS decreased by ~75% from 1.75 ± 0.3 Hz to 0.4 ± 0.2 Hz ($n = 5$; average dendritic patch distance, 943 ± 34 μm from the pia) (Fig. 3, H and I). Last, we recorded electrical activity at the soma in vivo (as in Fig. 1) in knockout mice that lacked $GABA_B$ receptor isoforms known to act presynaptically ($GABA_{B1a}{}^{-/-}$) and postsynaptically ($GABA_{B1b}{}^{-/-}$) in L5 pyramidal neurons (*12*, *25*) (Fig. 3J). In mice lacking the postsynaptically acting isoform ($GABA_{B1b}{}^{-/-}$), we recorded no interhemispheric inhibition using paired HS (7.6 ± 1.8 Hz versus 8.7 ± 1.9 Hz; t = 400 ms; $n = 7$) (Fig. 3K), whereas the inhibition remained in mice lacking the presynaptically acting isoform ($GABA_{B1a}{}^{-/-}$; 10.0 ± 4.9 Hz versus 6.1 ± 3.9 Hz; t = 400 ms; $n = 4$) (Fig. 3L). Furthermore, the inhibitory effect of focal application of baclofen to the dendrites was also occluded in $GABA_{B1b}{}^{-/-}$ mice (9.0 ± 2.3 versus 12.0 ± 4.5 Hz; $n = 5$) (Fig. 3, K and L). The specificity of the effect to $GABA_{B1b}$ receptors and the observed effects on dendritic Ca^{2+} strongly suggest that interhemispheric inhibition is mediated by dendritically located $GABA_B$ receptors.

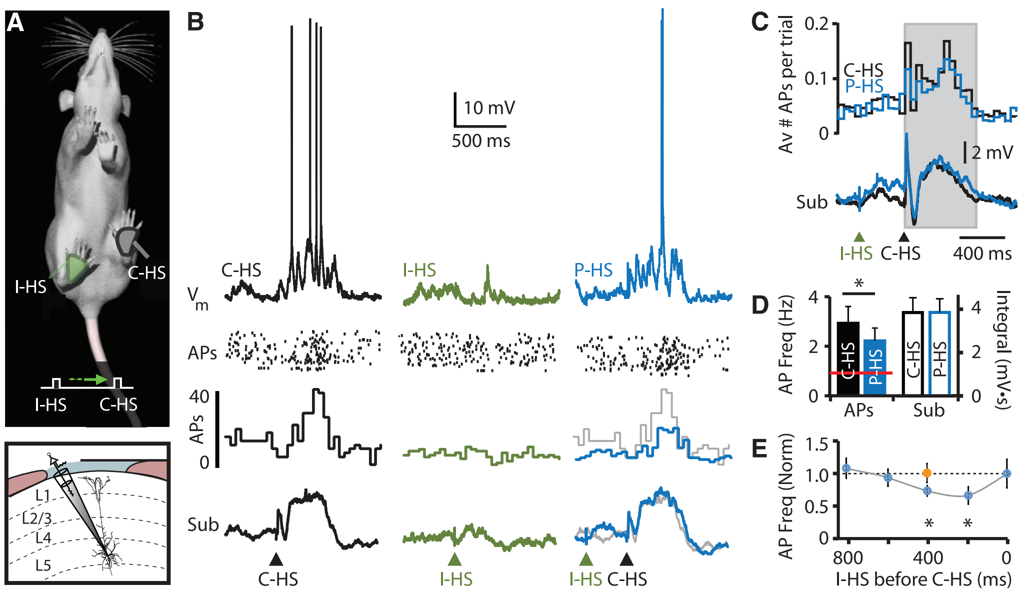

Fig. 1. Interhemispheric inhibition of sensory information. (**A**) Experimental design. (Top) Electrical stimulation (100 V, 1 ms), of contralateral and ipsilateral hindpaws during patch-clamp recordings from L5 pyramidal neurons (bottom). (**B**) (Top) Somatic response, (middle) raster plot and histogram of total AP firing over multiple trials, and (bottom) average subthreshold response in trials during contralateral HS (C-HS) (black; left), ipsilateral HS (I-HS) (green; middle), and paired HS (P-HS) (blue). I-HS 400 ms before C-HS (right). Gray traces, C-HS for comparison. (**C**) (Top) AP histogram for C-HS (black) and P-HS (t = 400 ms; blue) across all neurons (bin width = 50 ms; $n = 19$). (Bottom) Grand mean subthreshold responses to C-HS (black) and P-HS (blue; n = 20). Gray region used for statistics. (**D**) (Left) Average AP frequency during C-HS (black) and P-HS (blue; solid bars; n = 19). Red line, spontaneous firing rate. (Right) Average subthreshold response to C-HS (black) and P-HS (blue; n = 20; open bars). (**E**) Average normalized AP frequency during P-HS with I-HS 0, 200, 400, 600, and 800 ms before C-HS (blue dots). Orange dot, normalized average AP frequency during P-HS (t = 400 ms) with $GABA_B$ antagonist CGP52432 applied to cortical surface. *, $P < 0.05$.

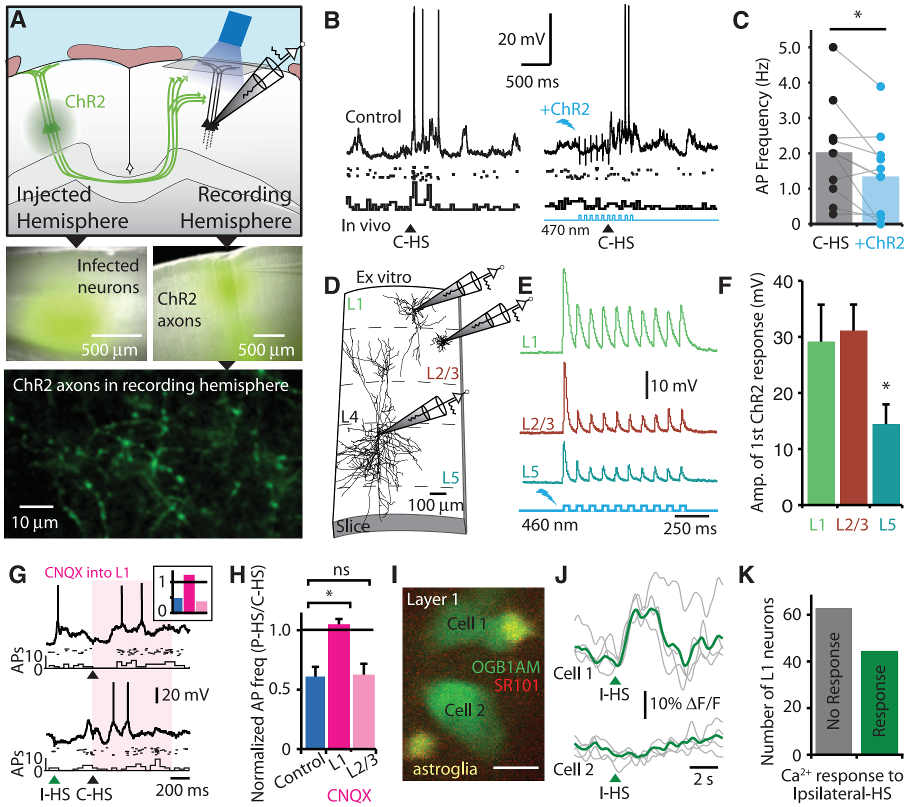

Fig. 2. Callosal fiber activation inhibits L5 pyramidal neuron firing and activates L1 neurons. (**A**) (Top) Experimental design. ChR2/AAV injected into hindlimb somatosensory cortex before patch recording in opposite hemisphere. (Middle) Overlays of bright-field images and ChR2 fluorescence from injected (left) and recording hemispheres (right) ex vivo. (Bottom) In vivo 2P image of ChR2 axons (green) in recording hemisphere at 100 µm below pia. (**B**) (Top) Somatic response, (middle) raster plot, and (bottom) histogram of APs during C-HS alone (left) and photostimulation with train of blue-light pulses above recording hemisphere (right). (**C**) Average firing frequency with C-HS (black) and during photostimulation of recording hemisphere (aqua; +ChR2). (**D**) Ex vivo recording from interneurons in L1, L2/3, and L5 in slices from ChR2/AAV-injected rats. (**E**) Voltage responses to local photostimulation in L1 (green), L2/3 (maroon), and L5 (turquoise). L1 and L5 interneurons recorded simultaneously; interneurons shown in (D). (**F**) Average voltage response to first photostimulation. (**G**) Example voltage response, raster plot, and AP histogram with (top) C-HS and (bottom) P-HS with focal application of CNQX into L1. (Inset) Normalized firing rates with P-HS during control (blue), CNQX in L1 (pink), and CNQX in L2/3 (salmon). Shaded region used for statistics. (**H**) Average AP frequency during P-HS with CNQX in L1 and L2/3. (**I**) In vivo 2P image of L1 (<200 µm below pia) counter-stained with OGB-1-AM and SR101. Neurons, green; astroglia, orange. (**J**) Individual (gray) and average (green) Ca^{2+} transients with I-HS for the cells in (I). (**K**) Number of cells in L1 that responded (green) and did not respond (gray) to I-HS. *, $P < 0.05$.

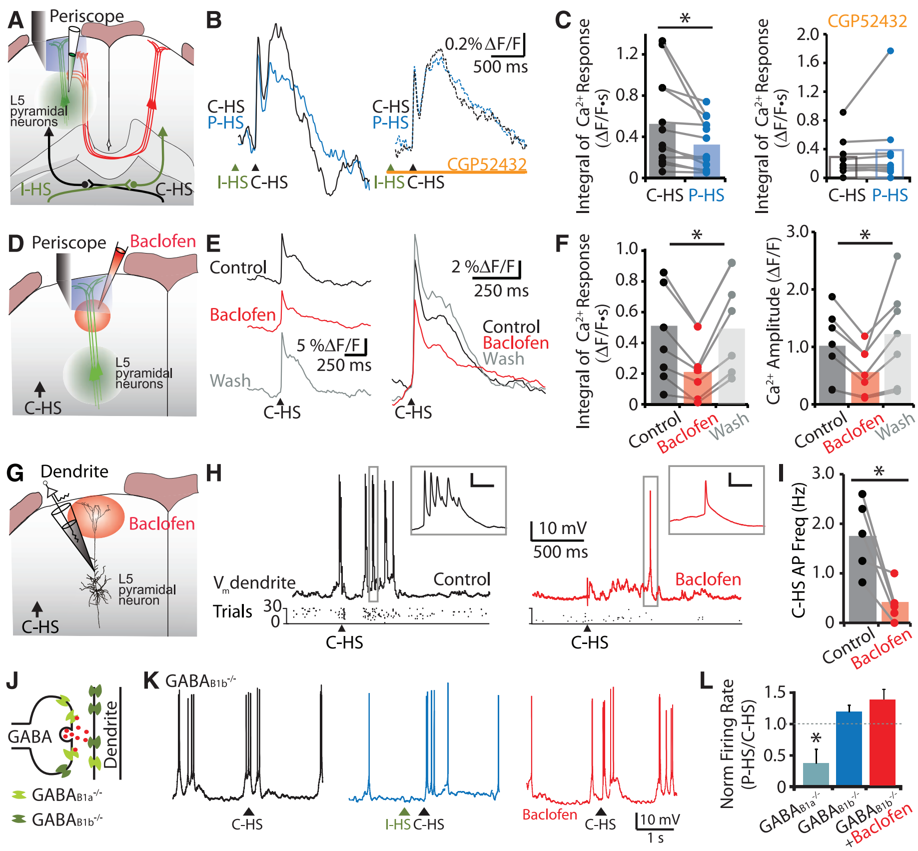

Fig. 3. Long-lasting interhemispheric inhibition is mediated by dendritic $GABA_B$ receptors. (**A**) Experimental design. L5 pyramidal neurons in the contralateral sensorimotor cortex bulk loaded with OGB-1-AM; dendritic Ca^{2+} responses recorded with periscope during C-HS and P-HS. (**B**) (Left) Average dendritic Ca^{2+} population response (fluorescence change, $\Delta F/F$; 15 trials) during C-HS (black) and P-HS (blue). (Right) Ca^{2+} response (10 trials) to C-HS (black) and P-HS (blue) during application of CGP52432 (1 µM) to cortical surface. (**C**) (Left) Integral of the Ca^{2+} response to C-HS (black) and P-HS (blue) in control conditions and (right) during CGP52432. (**D**) Experimental design. (**E**) Average dendritic Ca^{2+} population response with C-HS before (black), during (red), and after (gray) baclofen application. (**F**) (Left) Integral and (right) amplitude of Ca^{2+} response to C-HS. (**G**) Experimental design: L5 dendritic patch during baclofen application. (**H**) Dendritic patch-clamp responses to C-HS before (black) and during (red) baclofen. (Inset) Complex waveform from boxed region. Scale bar, 10 mV, 10 ms. (**I**) Normalized firing rate in the dendrite to C-HS before (black) and during (red) baclofen. (**J**) Distribution of $GABA_B$ subunits pre- and postsynaptically. (**K**) Somatic voltage responses to C-HS (black), P-HS (blue), and C-HS during focal baclofen (50 µM) application (red) in mice lacking postsynaptic $GABA_B$ receptors ($GABA_{B1b}{}^{-/-}$). (**L**) Normalized somatic firing rate during C-HS and P-HS in $GABA_{B1a}{}^{-/-}$ and $GABA_{B1b}{}^{-/-}$ mice. *, $P < 0.05$.

We next investigated how dendritic $GABA_B$ receptors influence cell spiking in vivo. We repeated the experiments with focal dendritic baclofen application during somatic recordings from L5 pyramidal neurons (Fig. 4A). Baclofen decreased the evoked firing response by a similar amount to dendritic Ca^{2+} activity (64 ± 10%; $n = 7$) (Fig. 4, B and C) (compare Figure 3F). Despite this, baclofen (like interhemispheric inhibition) had no significant effect on the subthreshold electrical response at the soma (control, 3.6 ± 0.7 mV•s; baclofen, 3.0 ± 0.5 mV•s; $n = 11$) (Fig. 4, C and D). How could such profound effects on dendritic activity and cell firing occur in the absence of any detectable effect on membrane potential at the cell body?

To investigate this, we performed the same experiments in vitro where we could isolate the causes and effects to the dendritic and/or somatic compartments of the neuron (Fig. 4E). Activating dendritic $GABA_B$ receptors continuously with baclofen resulted in an average hyperpolarizing response of only –1.2 ± 0.2 mV at the dendrite and –0.5 ± 0.2 mV at the soma ($n = 19$). Although this explained the negligible effect of dendritic $GABA_B$ inhibition on the somatic subthreshold responses reported throughout this study, it made the large effect on cell firing even more intriguing. We hypothesized that sufficiently large dendritic depolarization activates dendritic voltage-sensitive channels that causes further AP firing. At subthreshold levels, dendritic depolarization would not be expected to activate voltage-sensitive channels, and thus dendritic inhibition of these channels would not be detected (i.e., silent inhibition).

To test this hypothesis, we recorded responses to contralateral HS in vivo from the soma and dendrites of L5 pyramidal neurons and used these recorded waveforms as representative current input in our somatic and dendritic recordings in vitro. Current was injected at the soma in increasing steps of 100 pA and at the dendrite at a fixed amount of 600 to 800 pA (Fig. 4F). For low somatic current injection (0 to 100 pA), there was little or no AP firing in the neuron (Fig. 4, G and H), and baclofen had little effect on either the membrane potential at the soma (Fig. 4G) or the input resistance of the neuron (Fig. 4, K and L). Higher somatic current injection led to cell firing and back-propagating APs into the apical dendrite. In this case, baclofen caused a significant decrease in firing rate (Fig. 4, F and H) and a decrease in the gain of the frequency/current relationship (*26*) (Fig. 4H, top). Under these suprathreshold conditions, the membrane potential at the soma (measured from the voltage envelope with APs truncated) was hyperpolarized during the application of baclofen relative to control (Fig. 4H, bottom) indicating a loss of current transfer from the dendrite to the soma. These results show conclusively that dendritic $GABA_B$ inhibition alone can significantly reduce the firing output of L5 pyramidal neurons through a dendritically located mechanism that manifests only when the neuron is spiking.

To further investigate the importance of dendritic activity on somatic output, we restricted current injection to the soma while continuing to apply baclofen locally to the dendrite (Fig. 4I). Even with no dendritic input at all, activation of dendritic $GABA_B$ receptors still caused a significant decrease in AP firing rate (by 38 ± 5%, $n = 11$) (Fig. 4, J and L). Furthermore, the decrease in APs during $GABA_B$ receptor activation was not caused predominately by shunting inhibition

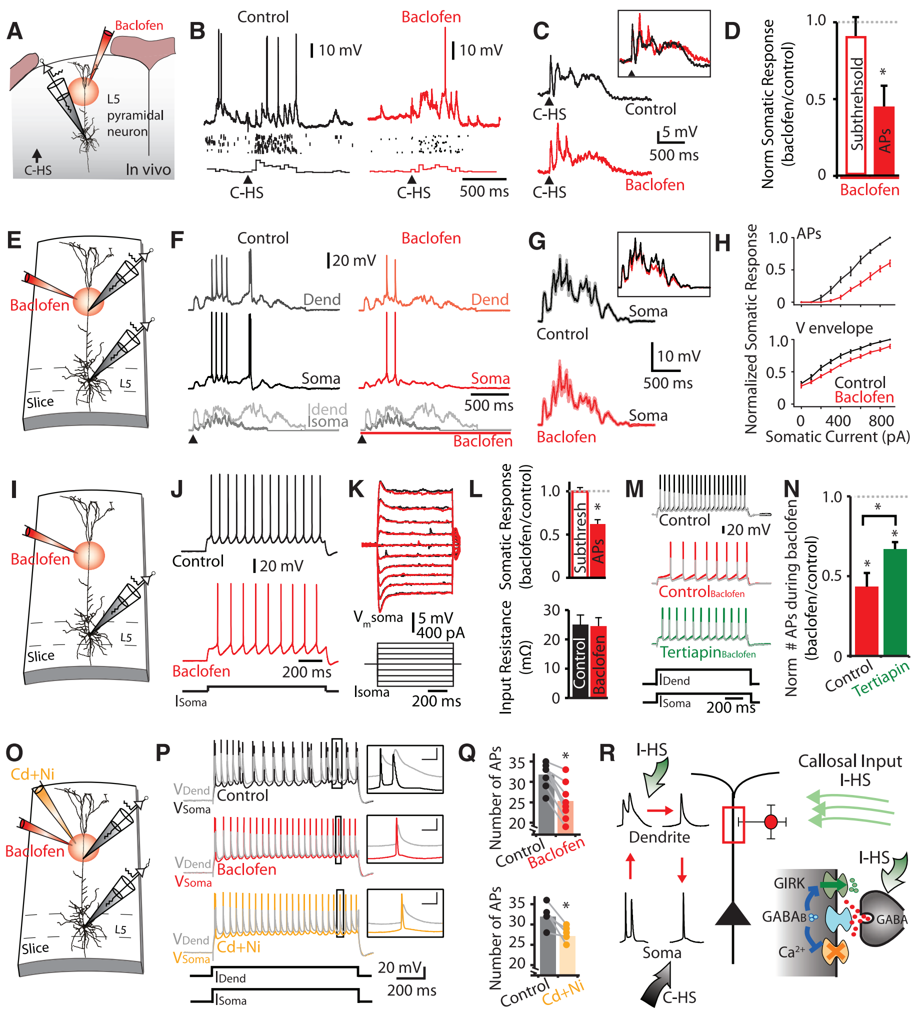

Fig. 4. The dendritic mechanisms of interhemispheric inhibition. (**A**) Experimental design. (**B**) Response to C-HS in control (black) and baclofen (red). (**C**) Average subthreshold response to C-HS. (Inset) Overlayed traces. (**D**) Average normalized response to C-HS during baclofen for the subthreshold voltage integral (open bar) and AP frequency (solid bar). (**E**) Experimental design. (**F**) (Top) Dendritic and somatic recordings in vivo with (bottom) waveforms injected into dendrite (light gray) and soma (dark gray). (**G**) Grand mean of the somatic subthreshold voltage responses to dual current injection shown in (F). (Inset) Overlayed traces. (**H**) Normalized somatic (top) firing rate and (bottom) voltage envelope integral evoked by constant dendritic and increasing somatic current injections during control (black) and baclofen (red). (**I**) Experimental design. (**J**) Somatic voltage response to suprathreshold current injection (400 pA) at soma. (**K**) Subthreshold voltage responses (top) to somatic current steps (bottom; 100 pA steps) before (black) and during (red) baclofen. (**L**) (Top) Normalized somatic subthreshold response (open bar) and number of APs (solid bar) during baclofen. (Bottom) Input resistance of the subthreshold somatic response during control (black) and baclofen (red). (**M**) Dual somatic (color) and dendritic (gray) voltage responses to current step injections (800 pA and 400 pA injected into the dendrite and soma, respectively) with (red) baclofen and (green) baclofen and tertiapin (0.5 μM) in the bath solution. (**N**) Normalized number of APs evoked for (M). (**O**) Experimental design. (**P**) Dual somatic/dendritic responses to current injections (800 pA and 1200 pA injected into the dendrite and soma, respectively) before (black) and during (red) baclofen or Cd + Ni (yellow). (Inset) Boxed region on left. Scale bar, 20 mV, 100 ms. (**Q**) Number of APs in (P). (**R**) Proposed cellular mechanism of interhemispheric inhibition. C-HS generates dendritic input and back-propagating Aps, which activate dendritic voltage-sensitive channels leading to more APs. I-HS activates $GABA_B$-mediating L1 interneurons that open GIRK and block Ca^{2+} channels (silent inhibition), which is only effective with dendritic depolarization from paired C-HS. *, $P < 0.05$ significance level.

because the same application of baclofen had no effect on the input resistance of the cell (Fig. 4, K and L).

What is the cellular basis of this $GABA_B$-mediated inhibition? Previous studies have shown that $GABA_B$ inhibition leads to activation of inward-rectifying K^+ channels (GIRK) (*27*) and inactivation of voltage-sensitive Ca^{2+} channels (*12*) in pyramidal neurons. Bath application of the GIRK antagonist tertiapin (0.5 μM) led to a 61 ± 11% decrease in the baclofen-induced hyperpolarization in the dendrite in vitro (n = 10) (fig. S11). Under these conditions, the inhibitory effect of baclofen on AP firing measured near threshold was partially occluded (control, 57 ± 9% versus tertiapin, 33 ± 5% reduction, respectively; average dendritic recording distance, 397 ± 2 μm) (Fig. 4, M and N). To determine the contribution of voltage-sensitive Ca^{2+} currents, we locally applied 50 μM Cd^{2+} and 100 μM Ni^{2+} to the apical dendrite at the same location as baclofen (Fig. 4O). Enough current was injected at the soma and dendrite to evoke firing well above threshold and maximize dendritic voltage-sensitive current activation. Ca^{2+} channel blockade accounted for 60 ± 18% (n = 5) of the reduction in AP firing induced by application of baclofen (average dendritic recording distance, 478 ± 36 μm) (Fig. 4, P and Q). In contrast to the GIRK channel antagonist, bath application of Ca^{2+} channel antagonists significantly reduced dendritic regenerative potentials and burst firing patterns (*28*) and occluded any further effect of baclofen on the spike waveform (fig. S12).

The dependence of dendritic $GABA_B$ inhibition on suprathreshold dendritic depolarization explains why this form of inhibition is normally silent. During contralateral HS, dendritic voltage-sensitive currents contribute to the overall depolarization of the neuron and, although blocked by $GABA_B$ receptor activation during ipsilateral HS, no inhibitory effect is measured because these currents are not activated without dendritic depolarization (e.g., due to dendritic input and/or back-propagating APs). Only with paired HS is the effect of regulating dendritic channel activity revealed (Fig. 4R). The magnitude of the effects observed in vitro would be sufficient to explain all of the effects seen in vivo. Although callosal inhibition could also affect pyramidal cell firing through network effects that alter synaptic input, we did not detect a change in subthreshold responses during interhemispheric inhibition (Fig. 1). We conclude, therefore, that interhemispheric inhibition is mediated predominantly through direct postsynaptic mechanisms in the apical dendritic shafts of pyramidal neurons.

It has been suggested that interhemispheric inhibition might regulate the gain of synaptic input (*29*) and thereby serve to enhance bimanual precision (*5*, *30*). Furthermore, loss of interhemispheric rivalry (through callosal inhibition) has been implicated in cases of lateralized impairment of attention (hemineglect) in human patients (*9*). Unraveling the mechanisms behind interhemispheric inhibition might therefore be critical to understanding these complex tasks. Our results reveal that long-lasting interhemispheric inhibition acts via a specific cortical microcircuitry mediated by dendritic $GABA_B$ receptors. This phenomenon of silent inhibition of dendritic channels, however, is likely to be a general phenomenon under many different conditions and may therefore represent a novel mechanism for explaining the anomalous decoupling of subthreshold and suprathreshold activity seen in other systems in vivo (*31–34*). The specific mechanisms of interhemispheric inhibition shown here, involving the underlying cortical microcircuitry, and dendritic $GABA_B$ receptors, offer new perspectives on fundamental and clinical studies involving interactions between the two cortical hemispheres.

References and Notes

1. M. S. Gazzaniga, *Nat. Rev. Neurosci.* **6**, 653 (2005).
2. J. S. Bloom, G. W. Hynd, *Neuropsychol. Rev.* **15**, 59 (2005).
3. H. Asanuma, O. Okuda, *J. Neurophysiol.* **25**, 198 (1962).
4. A. Ferbert *et al.*, *J. Physiol.* **453**, 525 (1992).
5. G. M. Geffen, D. L. Jones, L. B. Geffen, *Behav. Brain Res.* **64**, 131 (1994).
6. M. Kobayashi, S. Hutchinson, H. Théoret, G. Schlaug, A. Pascual-Leone, *Neurology* **62**, 91 (2004).
7. K. M. Heilman, E. Valenstein, *Neurology* **22**, 660 (1972).
8. C. C. Hilgetag, H. Théoret, A. Pascual-Leone, *Nat. Neurosci.* **4**, 953 (2001).
9. D. Cazzoli, P. Wurtz, R. M. Müri, C. W. Hess, T. Nyffeler, *Eur. J. Neurosci.* **29**, 1271 (2009).
10. M. Seyal, T. Ro, R. Rafal, *Ann. Neurol.* **38**, 264 (1995).
11. N. Forss, M. Hietanen, O. Salonen, R. Hari, *Brain* **122**, 1889 (1999).
12. E. Pérez-Garci, M. Gassmann, B. Bettler, M. E. Larkum, *Neuron* **50**, 603 (2006).
13. Y. Hlushchuk, R. Hari, *J. Neurosci.* **26**, 5819 (2006).
14. G. M. Innocenti, in *Cerebral Cortex*, E. G. Jones, A. Peters, Eds. (Plenum Press, New York, 1986), vol. 5, pp. 291–353.
15. L. Petreanu, D. Huber, A. Sobczyk, K. Svoboda, *Nat. Neurosci.* **10**, 663 (2007).
16. G. A. Ascoli *et al.*; Petilla Interneuron Nomenclature Group, *Nat. Rev. Neurosci.* **9**, 557 (2008).
17. Z. Chu, M. Galarreta, S. Hestrin, *J. Neurosci.* **23**, 96 (2003).
18. G. Tamás, A. Lörincz, A. Simon, J. Szabadics, *Science* **299**, 1902 (2003).
19. C. Wozny, S. R. Williams, *Cereb. Cortex* **21**, 1818 (2011).
20. H. G. Kim, M. Beierlein, B. W. Connors, *J. Neurophysiol.* **74**, 1810 (1995).
21. M. Murayama, E. Pérez-Garci, H. R. Lüscher, M. E. Larkum, *J. Neurophysiol.* **98**, 1791 (2007).
22. M. Murayama *et al.*, *Nature* **457**, 1137 (2009).
23. G. López-Bendito *et al.*, *Eur. J. Neurosci.* **15**, 1766 (2002).
24. F. Helmchen, K. Svoboda, W. Denk, D. W. Tank, *Nat. Neurosci.* **2**, 989 (1999).
25. B. Bettler, K. Kaupmann, J. Mosbacher, M. Gassmann, *Physiol. Rev.* **84**, 835 (2004).
26. M. E. Larkum, W. Senn, H. R. Lüscher, *Cereb. Cortex* **14**, 1059 (2004).
27. N. R. Newberry, R. A. Nicoll, *Nature* **308**, 450 (1984).
28. S. Williams, G. Stuart, *J. Physiol.* **521**, 161 (1999).
29. A. Schnitzler, K. R. Kessler, R. Benecke, *Exp. Brain Res.* **112**, 381 (1996).
30. C. Gerloff, F. G. Andres, *Acta Psychol. (Amst.)* **110**, 161 (2002).
31. V. Bringuier, F. Chavane, L. Glaeser, Y. Frégnac, *Science* **283**, 695 (1999).
32. M. Carandini, D. Ferster, *J. Neurosci.* **20**, 470 (2000).
33. M. Brecht, B. Sakmann, *J. Physiol.* **538**, 495 (2002).
34. H. Jia, N. L. Rochefort, X. Chen, A. Konnerth, *Nature* **464**, 1307 (2010).

Acknowledgments: We thank B. Bettler, J. Seibt, E. Pérez-Garci, T. Nyffeler, R. Müri and H. -R. Lüscher for their helpful comments on the manuscript. We also thank B. Bettler and M. Gassman for kindly providing the knockout mice ($GABA_{B1a}{}^{-/-}$ and $GABA_{B1b}{}^{-/-}$) and N. Nevian for technical assistance. This work was supported by SystemsX.ch (NeuroChoice) and the Swiss National Science Foundation (PP00A-102721 and 31003A_130694).

Supporting Online Material

www.sciencemag.org/cgi/content/full/335/6071/989/DC1
Materials and Methods
SOM Text
Figs. S1 to S12
References

30 November 2011; accepted 18 January 2012
10.1126/science.1217276

New Products: Genomics

PERSONAL UV-VIS SPECTROPHOTOMETER

The NanoDrop Lite is a compact ultraviolet-visible microvolume spectrophotometer. The new instrument is small enough to fit in a drawer, but powerful enough to help accelerate life science workflows related to sequencing, polymerase chain reaction (PCR)/real-time PCR, protein isolation, antibody production, HLA typing, and other applications. While NanoDrop Lite is designed with fewer features than the 2000 or 8000 series, it delivers where it counts: rapid, accurate, and reproducible microvolume measurements without the need for dilutions. It uses the same sample retention technology that has become a hallmark of NanoDrop instruments and surfaces can simply be wiped clean between samples. Features include local control and an optional docking printer that prints freezer-compatible, adhesive labels, offering even more convenience in the lab. The NanoDrop Lite can measure nucleic acid and protein concentration in sample sizes between 1.0 and 2.0 L and can measure 260/280 ratios for nucleic acids.

Thermo Fisher Scientific

For info: 877-724-7690 | www.thermoscientific.com/nanodrop

NEXT GENERATION SEQUENCING SYSTEM

The HiSeq 2500 is a next generation sequencing system that enables researchers and clinicians to sequence an entire genome in approximately 24 hours. The HiSeq 2500 offers: Unprecedented speed and flexibility with two modes allowing researchers to generate 120 gigabases (Gb) of data in 27 hours, or 600 Gb in a standard HiSeq run; high-quality data with a system that uses proven SBS chemistry that has made both the HiSeq 2000 and the MiSeq systems the most accurate next generation sequencers; expanded applications enabling researchers to sequence a human genome or 20 exomes in a day, or 30 RNA sequencing samples in as little as five hours; industry-leading simplicity and ease-of-use with an integrated cluster generation process that enables a simplified workflow; and a simple, field-based upgrade for the HiSeq 2000.

Illumina

For info: 800-809-4566 | www.illumina.com

NGS LIBRARY PREP MODULES

The NEXTflex DNA, ChIP-Seq, and PCR-Free Modules offer increased flexibility to next generation sequencing (NGS) library preparation. Modules are available for each step in the library preparation protocol including end repair, adenylation, ligation, and polymerase chain reaction (PCR). The modules are suitable for the library preparation from genomic or ChIP DNA for sequencing using Illumina's GAIIx, HiSeq, and MiSeq instruments. They provide substantial cost savings for scientists who will be preparing 100 or more samples for sequencing. The master mix modules streamline the workflow and in combination with up to 96 NEXTflex Barcodes, these modules are ideally suited for high throughput library preparation. The ligation modules feature the proprietary "Enhanced Adapter Ligation Technology" which results in library preps with a larger number of unique sequencing reads. Every NEXTflex Module passes rigorous enzymatic quality control and is functionally validated by sequencing on an Illumina platform.

Bioo Scientific

For info: 888-208-2246 | www.biooscientific.com

GENE FRAGMENTS

gBlocks Gene Fragments are double-stranded, sequence-verified genomic blocks up to 500 base pairs. Their high sequence fidelity and rapid delivery time makes gBlocks Gene Fragments ideal for a range of biology applications, including easy assembly of multiple gene fragments to reliably generate larger gene constructs. gBlocks Gene Fragments significantly reduce the cost for synthetic gene synthesis to less than US$0.20 per base pair. gBlocks Gene Fragments are provided as linear double-stranded DNA rather than already cloned into a vector, meaning that they can be easily and quickly utilized for a wide range of applications including custom protein synthesis, microRNA analysis, and in vitro transcription. For this reason, they are available with or without 5' phosphate modification depending on the required application. Each order is supplied as 200 ng of dried DNA, ensuring maximal stability prior to use, with most orders delivered within 3–4 business days.

Integrated DNA Technologies

For info: 800-328-2661 | www.idtdna.com

1-STEP RT-PCR KIT

The 1-Step RT-PCR Kit is designed for optimal convenience in carrying out highly sensitive and specific reverse transcription polymerase chain reactions (RT-PCR) in a single tube. 1-Step RT-PCR is a variation of the standard two-step RT-PCR, in which all components of the RT and PCR are mixed in one tube prior to starting the reactions so that RT and PCR can be carried out sequentially in one tube. The one-step method offers tremendous convenience when applied to analysis of single targets from multiple RNA samples and minimizes the possibility for introduction of contaminants into reactions between the RT and PCR steps. 1-Step RT-PCR Kit includes: AMV Reverse Transcriptase (from avian myeloblastosis virus), an optimized enzyme Taq DNA Polymerase (from *Thermus aquaticus*), a unique 10x concentrated RT-PCR buffer, our dNTP mixture, ribonuclease inhibitor, and DEPC-treated water.

G-Biosciences

For info: 800-628-7730 | www.gbiosciences.com

Electronically submit your new product description or product literature information! Go to **www.sciencemag.org/products/newproducts.dtl** for more information.

cell sciences®

Cytokine ELISA kits

www.cellsciences.com

These high quality research immunoassays are useful for the *in-vitro* quantitative and qualitative determination of cytokines from human serum, plasma and cell culture supernatant. Diaclone ELISA kits are ready-to-use, with pre-coated 12 x 8 strip plates, standards, buffers, detection antibody, conjugate and substrate. Do-it-yourself matched antibody pair kits for ELISA are also available. These ELI-PAIR kits offer the same quality, sensitivity and performance as Diaclone ELISA kits and are reasonably priced. ELI-PAIR kits include all necessary reagents for the immunoassay; capture antibody, biotinylated detection antibody, streptavidin - HRP, TMB, and enough lyophilized antigen to make one standard curve per plate. Visit our web site for complete information, pricing and protocols. Accuracy and reliability guaranteed; all reagents have been extensively validated according to the ISO 9001 quality system.

Human Cytokines & Growth Factors	Range
GM-CSF	8-500 pg/ml
IFN-α	8-500 pg/ml
IFN-γ	12.5-400 pg/ml
IFN-γ high sensitivity	0.78-25 pg/ml
IL-1α	31.2-1000 pg/ml
IL-1β	15.6-500 pg/ml
IL-2	31.2-1000 pg/ml
IL-2 high sensitivityy	1.87-60 pg/ml
IL-4	1.1-35 pg/ml
IL-4 high sensitivity	0.31-10 pg/ml
IL-5	7.8-250 pg/ml
IL-6	6.25-200 pg/ml
IL-6 high sensitivity	1.56-50 pg/ml
IL-7	6.25-200 pg/ml
IL-8	62.5-2000 pg/ml
IL-10	12.5-400 pg/ml
IL-10 high sensitivity	1.56-50 pg/ml
IL-12/p70	6.25-200 pg/ml
IL-12 high sensitivity	0.78-25 pg/ml
IL-12/p40 + p70	62.5-2000 pg/ml
IL-13	3.12-100 pg/ml
IL-17A	3.12-100 pg/ml
IL-17F	15.6-500 pg/ml
IL-23	78-5000 pg/ml
IL-27	31.25-1000 pg/ml
IP-10	6.25-200 pg/ml
MCP-1	16-1000 pg/ml
TGF-β1	0.5-30 ng/ml
TGF-β2	31.25-1000 pg/ml
TNF-α	25-800 pg/ml
VEGF-A Biolisa	16-1000 pg/ml
VEGF-A	31.25-2000 pg/ml
VEGF-R1	0.16-10 ng/ml

Human Cytokine Receptors	Range
CD25/IL-2R	68.75-2220 pg/ml
CD116/GM-CSF R	31.25-1000 pg/ml
CD117/c-KIT	0.31-10 ng/ml
CD124/IL-4R	31.25-1000 pg/ml
CD126/gp80	31.25-1000 pg/ml
CD130/gp130	56.25-1800 pg/ml
CD213a2/IL-13Rα2	156-5000 pg/ml
CD138/SYNDECAN-1	8-256 ng/ml

Mouse Cytokines	Range
GM-CSF	15.6-500 pg/ml
IFN-γ	31.25-1000 pg/ml
IL-1α	7.8-500 pg/ml
IL-2	15.6-500 pg/ml
IL-4	3.9-250 pg/ml
IL-5	7.8-500 pg/ml
IL-6	15.6-500 pg/ml
IL-10	31.25-1000 pg/ml
IL-12	31.25-2000 pg/ml
TGF-β1	0.5-30 ng/ml
TNF-α	31.25-1000 pg/ml

Rat Cytokines	Range
IFN-γ	31.25-1000 pg/ml
IL-1β	31.25-2000 pg/ml
IL-4	31.25-100 pg/ml
IL-6	31.25-2000 pg/ml
TGFβ1	0.5-30 ng/ml
TNF-α	31.25-1000 pg/ml

ELISA kits for human soluble antigens, adhesion markers and apoptosis markers are also available.

CELL SCIENCES INC • 480 NEPONSET STREET, BUILDING 12A, CANTON, MA 02021 • INFO@CELLSCIENCES.COM

TOLL FREE: (888) 769-1246 • TEL: (781) 828-0610 • FAX: (781) 828-0542 • WEB WWW.CELLSCIENCES.COM

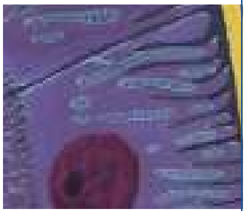

- Proteins
- Antibodies
- **ELISAs**
- Assay Services
- MultiAnalyte Profiling
- Activity Assays
- Stem Cells
- ELISpot Kits
- Flow Cytometry
- Cell Selection

R&D Systems Quantikine® ELISAs

The Most Referenced Immunoassays

A direct measure of product quality is the frequency of citations in the scientific literature. R&D Systems has more than 20 years of experience designing, testing, and optimizing the most cited ELISA kits in the world. Find out why scientists trust R&D Systems ELISAs more than any other brand.

R&D Systems is the Most Referenced ELISA Manufacturer

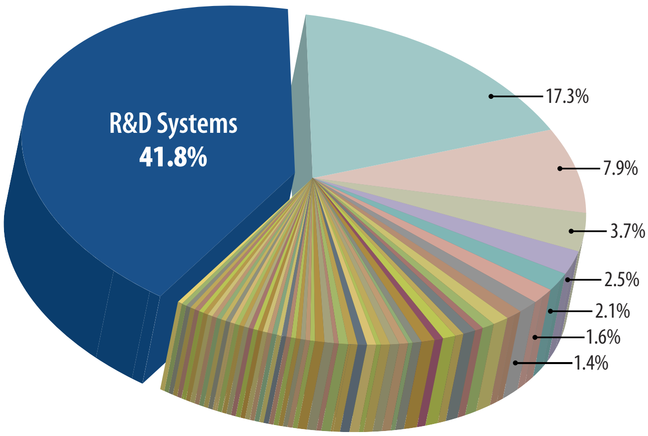

Approximately 42% of Referenced Immunoassays are Developed and Manufactured by R&D Systems. A survey of 860 manuscripts from 44 journals was conducted to compare the number of citations specifying the use of R&D Systems ELISAs to the number citing ELISAs from other commercial sources. A total of 433 ELISA citations referencing immunoassays from 66 different vendors were identified in the survey.

NEW Quantikine ELISA Kits

- α1-Acid Glycoprotein
- Angiopoietin-like 3
- Cathepsin V
- Clusterin
- Dkk-1
- EGF R/ErbB1
- EG-VEGF/PK1
- Fetuin A
- FGF-21
- Galectin-3
- Gas 6
- GDF-15
- IL-17A/F Heterodimer
- IL-19
- Lipocalin-2/NGAL
- MBL
- Proprotein Convertase 9/PCSK9
- Periostin/OSF-2
- Progranulin
- ST2/IL-1 R4
- Thrombomodulin/CD141
- Tie-1
- TIM-1/KIM-1

For more information visit our website at www.RnDSystems.com/go/ELISA

For research use only. Not for use in diagnostic procedures.

R&D Systems, Inc. www.RnDSystems.com

R&D Systems Europe, Ltd. www.RnDSystems.co.uk

R&D Systems China Co., Ltd. www.RnDSystemsChina.com.cn

Thermo
SCIENTIFIC

Quantify, verify,

In science there are always essential steps in any workflow. Accurate measurements of DNA, RNA and protein samples are critical for confidence in qPCR, sequencing, microarrays or bioproduction, but there's a better alternative to the time and complexity of conventional methods. Using minimal sample (0.5 – 2.0 µL), **Thermo Scientific NanoDrop** instruments make concentration and purity analysis so incredibly easy, and so much faster, you won't notice this step on the way to your ultimate discovery.

simplify

• Realize the difference.
Try any NanoDrop instrument for FREE.
www.thermoscientific.com/nanodrop

NanoDrop™ Lite
Basic microvolume measurements

NanoDrop™ 2000C
Full-spectrum microvolume and cuvette measurements in a single instrument

NanoDrop™ 2000
Full-spectrum microvolume measurements

NanoDrop 8000
Higher throughput, full-spectrum microvolume measurements

NanoDrop 3300
Full-spectrum microvolume fluorescence measurements

Produced by the *Science*/AAAS Custom Publishing Office

LIFE SCIENCE TECHNOLOGIES

Genomics

A New Era for Clinical Models

In This Issue

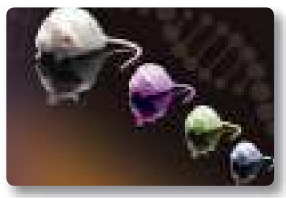

Not long ago, a clinically relevant and genomics-based model of disease meant an animal, but today's models also include cell lines and even computer-based simulations. Still, bioengineered mice and rats make up many of the models, and these genetically modified organisms provide increasingly accurate representations of how drugs treat human diseases. To get the most from genomics-based models for drug research, scientists can now combine information from bioengineered organisms, genomically modified cell lines, and computational models.

See full story on page 994.

Upcoming Features

Toxicology: Animal-Free Techniques—March 2
Polymer Science: Creating Synthetic Materials—March 16
Innovation in Japan—April 13


labeling & detection
molecular probes
cell culture
gibco
by life technologies
DNA
invitroge
by life technologies

INSPIRING INNOVATION
in more ways than one

The 3500 Series Genetic Analyzers

A key component in targeted disease research, the high-quality data of the 3500 Series Genetic Analyzers inspire greater confidence. The advanced consumables design and intuitive software interface keep you current and in control. Known for playing a key role in important genetic innovations using highly accurate and reliable Sanger sequencing, the 3500 Series technology does even more. Discover the system capable of performing more applications than any other sequencer.

Discover optimal sequencing quality and versatility at lifetechnologies.com/3500series

life technologies™

Genomics

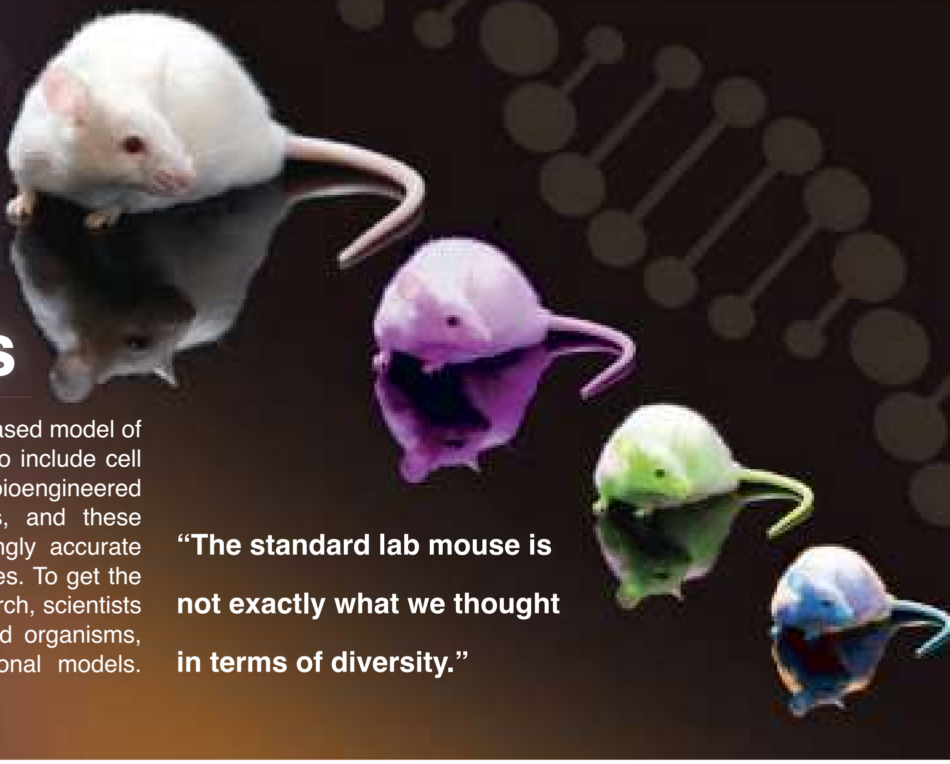

A New Era for Clinical Models

Not long ago, a clinically relevant and genomics-based model of disease meant an animal, but today's models also include cell lines and even computer-based simulations. Still, bioengineered mice and rats make up many of the models, and these genetically modified organisms provide increasingly accurate representations of how drugs treat human diseases. To get the most from genomics-based models for drug research, scientists can now combine information from bioengineered organisms, genomically modified cell lines, and computational models. **By Mike May**

"The standard lab mouse is not exactly what we thought in terms of diversity."

The lab mouse represents an icon of clinical research. A PubMed search of *mouse model* pulls up more than 150,000 articles, which indicates the pervasive use of this clinical tool in modeling diseases. Moreover, groups of scientists keep developing new ways to use mice in basic and medical research.

For example, two consortia—the International Knockout Mouse Consortium (IKMC) and the International Mouse Phenotyping Consortium (IMPC)—hope to improve bioengineered mouse models. First, the IKMC, based in laboratories in Europe and North America, is making individual mutant embryonic stem cell lines in which one of the mouse's roughly 20,000 protein-coding genes has been knocked out. So far, the IKMC has created more than three-quarters of these cell lines. As a next step, the IMPC—composed of 10 research institutions around the world—will produce knockout animals for each gene and analyze the phenotypic changes. Although the list of phenotypic tests remains under development, it will likely range from basic blood work to behavioral assessments. The IMPC plans to phenotype all 20,000 knockout mice by 2020.

To breed the cohorts of mice needed for this phenotyping project, the IMPC turned to some powerhouses in breeding, including **Charles River Laboratories** in Wilmington, Massachusetts. "The repository of knockout-mouse lines and the corresponding phenotypic data will lead to a global availability of novel mouse models across many areas of disease," says Iva Morse, corporate vice president, Charles River Genetically Engineered Models and Services. "Because of the IKMC and IMPC's efforts, researchers will be able to search for specific genes, examine the primary phenotype screens, and then get the animals for further testing."

Once all of the knockout mice are phenotyped, researchers will be able to use a database to review some of the fundamental anatomical, biochemical, and physiological impacts of each gene as well as possible disease-related factors. This phenotypic database should free researchers and resources to pursue more complex questions, such as how genes interact with environmental factors.

MAKING MOUSE MODELS MORE DIVERSE

Rather than only working with existing mouse strains, some researchers are developing new ones since many of the existing strains have little genomic variation. "The standard lab mouse is not exactly what we thought in terms of diversity," says John French, leader of the host susceptibility group at the **National Institute of Environmental Health Sciences** in Research Triangle Park, North Carolina. He explains that inbreeding has created some identical regions in the genomes of lab mice. For example, rather than having gene variants at a specific locus, inbred mice often all have the same allele in that spot. Consequently, mice from one line can be very similar to each other but extremely different from other mouse lines. For example, French describes using 18 strains of inbred mice to study the physiological impact of benzene exposure on biochemical processes that modify foreign compounds, such as drugs or poisons. Some characteristics—such as the amount of benzene in the blood after the same level of exposure—varied by as much as 36-fold between the strains. French notes that benzene exposure can

UPCOMING FEATURES

Toxicology: Animal-Free Techniques—March 2

Polymer Science: Creating Synthetic Materials—March 16

Innovation in Japan—April 13

lead to leukemia in both mice and humans, and this variance between inbred strains may be useful for risk assessment, because some strains may show higher incidence of disease than others.

Other experts also worry about the lack of diversity in traditional mouse lines. "The way rodent models have been used in drug development and toxicity testing only surveys a limited scope of the genetic diversity that's available," says Gary Churchill, a biostatistician at **The Jackson Laboratory** in Bar Harbor, Maine. "To assess if a drug will have dangerous side effects in a subset of the human population, we must sample broad genetic diversity in the model system."

To meet that need, Churchill and his colleagues created the Diversity Outbred (DO) Mouse population, which represents 45 million single nucleotide polymorphisms (SNPs) and 4 million copy number variations. As Churchill says, "We've captured mouse genetic diversity." In comparison, the most commonly used strains of mice—roughly 100 of them—only include about 12 million SNPs.

When studying a drug's impact, Churchill says, it will probably take 100–200 DO animals to explore the potential for diverse effects. Using this many animals should cover all of the SNPs and copy number variations, which will indicate how the drug would perform when encountering various genotypes.

During drug development, testing a new compound for toxicity is vital. However, Alison Harrill, a research investigator at **The Hamner Institutes for Health Sciences** in Research Triangle Park, North Carolina, says, "Drug safety is becoming a key bottleneck." When taking a new compound from the discovery stage through to regulatory approval, toxicity testing can take so much time and effort that it slows down the entire process. Moreover, some toxicity issues only emerge after a drug has gained regulatory approval. For instance, Harrill says, "Hepatotoxicity issues [have been found to] exist in about one-third of drugs pulled from the market."

In hopes of revealing toxicities at the research stage, Harrill works with DO mice because, she says, they provide a "better estimate of human responses and identify genetic variants that might increase the risk of an adverse drug reaction." She also notes that this strategy can be used to rescue drugs that have failed toxicity testing in previous clinical trials and allow researchers to develop screens that predict which patients would respond safely to the drugs and which ones would not.

MODELS OF METABOLISM

Mouse models of diseases can also help researchers find new drug targets. For diabetes, for instance, scientists at **Lexicon Pharmaceuticals** in The Woodlands, Texas, searched the company's collection of knockout mice for animals that have altered glucose control. According to Brian Zambrowicz, chief scientific officer, they found that knockout mice lacking the gene for either sodium-dependent glucose transporter 1 (SGLT1) or SGLT2 exhibited a "much improved oral glucose tolerance," or the ability to maintain balanced blood levels of glucose after eating. Because type II diabetes causes glucose levels to rise dangerously high in the blood, Zambrowicz and his colleagues hoped that a compound that blocks SGLT1 and 2 might treat the disease. The Lexicon scientists then developed cell-based assays to screen for compounds that inhibit these transport proteins and discovered LX4211, a compound that inhibits both transporters. One way this compound helps to maintain a balanced level of blood glucose is through its effects on SGLT2, which participates in the absorption of glucose by the kidney. Blocking this protein increases the amount of glucose that gets excreted in urine. In addition, LX4211 triggers the release of glucagon-like peptide-1 and peptide YY in the gastrointestinal track, and this mechanism provides further glucose regulation.

Genomic tools can also be used to reveal how a drug is metabolized. For example, Xavier de Mollerat, senior scientist at **Life Technologies** in Carlsbad, California, says that a scientist who suspects that a drug's metabolism depends on a specific receptor can use small interfering RNA (siRNA) to knock down, or inhibit, the receptor's expression and measure the drug's distribution before and after treatment. If the measurements differ, the receptor is involved. Researchers can also use this technique to make a transient animal model of a disease. If the lack of one or more genes is known to be involved in a disease, a researcher can use siRNA to knock down the gene(s). For example, Invivofectamine 2.0 from Life Technologies can simultaneously silence up to four genes with just one application of siRNA. As explained by de Mollerat, "This technology's lipid delivery system is designed to use siRNA in vivo. You inject the siRNA, and it knocks down its targets for weeks."

This technology also only requires a few steps. A scientist combines the desired siRNA with the Invivofectamine 2.0 reagent, performs a couple of simple processes, such as an incubation step, and then injects the mixture into the animal's blood stream or to a more specific location if desired. According to de Mollerat, the siRNA will knock down the gene's protein expression by 80–90 percent. "If you know the sequence, you can target it," de Mollerat says.

De Mollerat says that similar technology might work with messenger RNA (mRNA). Then, a researcher could compare knocking down a gene with siRNA to overexpressing it continued>

FEATURED PARTICIPANTS

Autism Speaks
www.autismspeaks.org

Broad Institute
www.broadinstitute.org

Charles River Laboratories
www.criver.com

GNS Healthcare
www.gnshealthcare.com

Lexicon Pharmaceuticals
www.lexgen.com

Life Technologies
www.lifetechnologies.com

Luminex
www.luminexcorp.com

National Cancer Institute
www.cancer.gov

National Institute of Environmental Health Sciences
www.niehs.nih.gov

Pfizer
www.pfizer.com

Sigma Life Sciences
www.sigmaaldrich.com/life-science.html

The Hamner Institute for Health
www.thehamner.org

The Jackson Laboratory
www.jax.org

Transposagen Biopharmaceuticals
www.transposagenbio.com

with mRNA. That would provide further information about a gene's function in general or how it participates in a disease.

RESEARCHING NEW DISEASES WITH RATS

Although mice have been the main bioengineered animal used for disease modeling in the past and will continue to be abundant in the future, genomically modified rats will also become an increasingly common tool. The numerous and extensive history of existing mouse lines provide good reasons to stick with this rodent, but the rat model offers upsides of its own. Just the larger size of rats can enhance certain aspects of drug research. For example, when scientists need a large amount of blood, such as for testing a compound's absorption, distribution, metabolism, and excretion (ADME), it is easier to obtain the necessary quantity from bigger animals. In addition, the physiology of liver metabolism in rats resembles that of humans more closely than mice do.

Consequently, bioengineered rat models will likely become more widely available in the next few years. For example, Charles River Laboratories arranged to distribute rat models of cancer related to the genes *p53* and *BCRP* from **Transposagen Biopharmaceuticals** in Lexington, Kentucky. As Morse explains: "New methods for manipulating the rat genome further advance functional genomics and allow us to make novel models of human disease." Even **Pfizer**, headquartered in New York, New York, is providing a genetically engineered rat model of diabetes to Charles River for distribution.

Scientists are continually expanding the catalog of diseases modeled in rats. One of the most exciting new advances arose from a collaboration between scientists at **Sigma Life Science** in St. Louis, Missouri, and **Autism Speaks,** an advocacy group. As Edward Weinstein, director of Sigma Advanced Genetic Engineering Labs, explains, "We thought that we could use rats to make some impact on autism." So he and his colleagues worked with Autism Speaks to help them "connect to the community and understand what the best models to make would be," Weinstein says.

Through this collaboration, Sigma scientists learned that a range of genes—including *MECP2*, *FMR1*, *NLGN3*, and others—contribute to autism. Consequently, Weinstein and his colleagues developed knockout rats for many of these genes.

"We hope that using a higher level organism—a rat instead of a mouse—will help unravel some of [the genomic complexity of autism]," explains Weinstein.

BEYOND THE ANIMAL MODEL

Creating models for clinical research does not solely depend on animal use these days. When conducting drug research, scientists often turn to cells for modeling as soon as possible, and Sigma Life Science offers a range of disease-model cell lines.

In particular, Sigma makes many cell lines for cancer research. Brad Keller, product manager at Sigma Life Science, says, "Genetically engineered cell lines for breast cancer are our biggest offering." He adds that they also have cell lines for colorectal and lung cancer. "Each cell line is specific," says Keller. For example, a cancer cell line will include a mutated gene discovered in patients with the disease. Moreover, these cell lines are created from human cells, which makes any experimental results more relevant to human disease.

Beyond cell lines, some projects involve computer simulations. For instance, the **Broad Institute** in Cambridge, Massachusetts, developed The Connectivity Map (cmap), which uses computer algorithms and genome-wide expression data to explore the connection between diseases, genes, and drugs. To expand cmap, researchers developed the L1000 assay, which runs on the FLEXMAP 3-D system from **Luminex** in Austin, Texas. This assay can screen about 1,000 genes per sample. "The assay makes genome-wide transcriptional profiling of compound treatments possible at library scale for the first time," says Matt Grow, Luminex's manager of strategic development.

In addition, Colin Hill, chief executive officer at **GNS Healthcare** in Cambridge, Massachusetts, points out that computer models "are being seen more and more as an important alternative to animal models." As an example, the **National Cancer Institute** of the U.S. National Institutes of Health came to Hill's company for the analysis of data from genetically modified mouse models of nonsmall cell lung cancer. In short, Hill's machine learning technology is searching the data—from imaging, genes, pathology, and more—for connections that could reveal mechanisms behind this cancer.

By combining animal models, cell lines, and simulations, researchers are now able to develop a wide ranging toolkit for modeling diseases. This breadth of models then allows for more in-depth testing of new drugs in a wider range of genomic variations.

Mike May is a freelance writer and editor for science and technology.

DOI: 10.1126/science.opms.p1200061

New Products: Genomics

PERSONAL UV-VIS SPECTROPHOTOMETER

The NanoDrop Lite is a compact ultraviolet-visible microvolume spectrophotometer. The new instrument is small enough to fit in a drawer, but powerful enough to help accelerate life science workflows related to sequencing, polymerase chain reaction (PCR)/real-time PCR, protein isolation, antibody production, HLA typing, and other applications. While NanoDrop Lite is designed with fewer features than the 2000 or 8000 series, it delivers where it counts: rapid, accurate, and reproducible microvolume measurements without the need for dilutions. It uses the same sample retention technology that has become a hallmark of NanoDrop instruments and surfaces can simply be wiped clean between samples. Features include local control and an optional docking printer that prints freezer-compatible, adhesive labels, offering even more convenience in the lab. The NanoDrop Lite can measure nucleic acid and protein concentration in sample sizes between 1.0 and 2.0 µL and can measure 260/280 ratios for nucleic acids.

Thermo Fisher Scientific
For info: 877-724-7690 | www.thermoscientific.com

NEXT GENERATION SEQUENCING SYSTEM

The HiSeq 2500 is a next generation sequencing system that enables researchers and clinicians to sequence an entire genome in approximately 24 hours. The HiSeq 2500 offers: Unprecedented speed and flexibility with two modes allowing researchers to generate 120 gigabases (Gb) of data in 27 hours, or 600 Gb in a standard HiSeq run; high-quality data with a system that uses proven SBS chemistry that has made both the HiSeq 2000 and the MiSeq systems the most accurate next generation sequencers; expanded applications enabling researchers to sequence a human genome or 20 exomes in a day, or 30 RNA sequencing samples in as little as five hours; industry-leading simplicity and ease-of-use with an integrated cluster generation process that enables a simplified workflow; and a simple, field-based upgrade for the HiSeq 2000.
Illumina
For info: 800-809-4566 | www.illumina.com

NGS LIBRARY PREP MODULES

The NEXTflex DNA, ChIP-Seq, and PCR-Free Modules offer increased flexibility to next generation sequencing (NGS) library preparation. Modules are available for each step in the library preparation protocol including end repair, adenylation, ligation, and polymerase chain reaction (PCR). The modules are suitable for the library preparation from genomic or ChIP DNA for sequencing using Illumina's GAIIx, HiSeq, and MiSeq instruments. They provide substantial cost savings for scientists who will be preparing 100 or more samples for sequencing. The master mix modules streamline the workflow and in combination with up to 96 NEXTflex Barcodes, these modules are ideally suited for high throughput library preparation. The ligation modules feature the proprietary "Enhanced Adapter Ligation Technology" which results in library preps with a larger number of unique sequencing reads. Every NEXTflex Module passes rigorous enzymatic quality control and is functionally validated by sequencing on an Illumina platform.
Bioo Scientific
For info: 888-208-2246 | www.biooscientific.com

GENE FRAGMENTS

gBlocks Gene Fragments are double-stranded, sequence-verified genomic blocks up to 500 base pairs. Their high sequence fidelity and rapid delivery time makes gBlocks Gene Fragments ideal for a range of biology applications, including easy assembly of multiple gene fragments to reliably generate larger gene constructs. gBlocks Gene Fragments significantly reduce the cost for synthetic gene synthesis to less than US$0.20 per base pair. gBlocks Gene Fragments are provided as linear double-stranded DNA rather than already cloned into a vector, meaning that they can be easily and quickly utilized for a wide range of applications including custom protein synthesis, microRNA analysis, and in vitro transcription. For this reason, they are available with or without 5' phosphate modification depending on the required application. Each order is supplied as 200 ng of dried DNA, ensuring maximal stability prior to use, with most orders delivered within 3–4 business days.
Integrated DNA Technologies
For info: 800-328-2661 | www.idtdna.com

1-STEP RT-PCR KIT

The 1-Step RT-PCR Kit is designed for optimal convenience in carrying out highly sensitive and specific reverse transcription polymerase chain reactions (RT-PCR) in a single tube. 1-Step RT-PCR is a variation of the standard two-step RT-PCR, in which all components of the RT and PCR are mixed in one tube prior to starting the reactions so that RT and PCR can be carried out sequentially in one tube. The one-step method offers tremendous convenience when applied to analysis of single targets from multiple RNA samples and minimizes the possibility for introduction of contaminants into reactions between the RT and PCR steps. 1-Step RT-PCR Kit includes: AMV Reverse Transcriptase (from avian myeloblastosis virus), an optimized enzyme Taq DNA Polymerase (from *Thermus aquaticus*), a unique 10x concentrated RT-PCR buffer, our dNTP mixture, ribonuclease inhibitor, and DEPC-treated water.
G-Biosciences
For info: 800-628-7730 | www.gbiosciences.com

Electronically submit your new product description or product literature information! Go to **www.sciencemag.org/products/newproducts.dtl** for more information.

UMDNJ ROBERT WOOD JOHNSON MEDICAL SCHOOL
University of Medicine & Dentistry of New Jersey

The Cancer Institute of New Jersey

NCI CCC A Comprehensive Cancer Center Designated by the National Cancer Institute

PATHOLOGY POSITION

Cancer Research Program

The Cancer Institute of New Jersey (CINJ), part of the University of Medicine & Dentistry of New Jersey (UMDNJ)-Robert Wood Johnson Medical School (RWJMS) seeks an active researcher with the skills and energy to integrate well with existing multidisciplinary Cancer Programs. An attractive component of the program is the access to translational laboratories for clinical investigators. The CINJ seeks to expand significantly the breadth and scope of existing research programs. We are looking to identify a Pathologist for this exciting and challenging position during this academic year.

Candidates must have an MD, MD/PhD or related degree. This position will include a role as Director of Pathology for CINJ and oversight for the Tissue Analytic Services core facility. It is anticipated that candidates will oversee a research program and be willing to collaborate with UMDNJ, RWJMS, CINJ, Rutgers University and Princeton University investigators with similar research interests. Primary academic appointment will be in the Department of Pathology and Laboratory Medicine, and resident member of CINJ. Rank will be commensurate with experience and there is an excellent benefits package.

CINJ, part of a comprehensive educational health science and hospital complex with convenient access to public transportation and major highways, is located in New Brunswick, New Jersey, approximately one hour from New York City and Philadelphia, and in the middle of the Washington-Boston corridor. Moreover, the majority of pharmaceutical companies are located near the CINJ complex. This proximity allows for collaborations at several levels, which is the norm for CINJ members.

Nominations, letters of interest, and CVs should be addressed to: **Robert DiPaola, MD, Director, The Cancer Institute of New Jersey, Chair, Search Committee, c/o Larissa Varela, 120 Albany Street, Tower 2, 5th Floor, New Brunswick, NJ 08901; E-mail: varelalc@umdnj.edu**.

The UMDNJ is an Affirmative Action/Equal Opportunity Employer M/F/D/V and a member of the University Health System of New Jersey.

Vienna University of Technology

TU WIEN

Vienna Doctoral Programme on Water Resource Systems

The Centre for Water Resource Systems at the Vienna University of Technology announces competition for the second intake of doctoral candidates for the Doctoral Programme on Water Resource Systems. The programme is anticipated to host a total of 70 doctoral students over a period of 12 years. This is a dedicated programme of the Austrian Science Fund (FWF) that promotes doctoral research and education at the highest standards and provides excellent opportunities for cross-disciplinary research. International networking is facilitated by a mobility programme with a spectrum of attractive international partner institutions and a comprehensive guest scientist programme.

Eight PhD student positions are available in the following research themes related to Water Resource Systems:

- Flood-hydrology
- Aquatic microbiology
- Diffuse water pollution
- Socio-hydrology and environmental economics
- Regional nutrient management
- Soil moisture remote sensing
- Mechanics of structures
- Micro-meteorology

Applicants for the PhD student positions must have a Master's degree (or equivalent) in a discipline related to water resource systems. The working language of the programme is English. Students are expected to work across disciplines and in cooperation with others. A capacity and willingness to integrate and collaborate is essential.

The Programme provides a salary according to the FWF scheme, together with a significant allowance for travel and research support. TU Wien is an equal opportunities employer. The contracts will be for three years and extension to a fourth year is possible. The preferred starting date is Oct. 1, 2012.

Candidates should send a letter of application, a statement of research interests, copies of education certificates and a Curriculum Vitae to office@waterresources.at (pdf format), or as a hard copy to The Centre of Water Resource Systems, c/o Dr. Gemma Carr, Vienna University of Technology, Karlsplatz 13/222-2, A-1040 Vienna, Austria. Please quote reference: DK-WRS.

Application deadline is April 30, 2012. Short listed candidates will be invited to a selection seminar. Financial support towards travel expenses is available on request. Information about the Doctoral Programme on Water Resource Systems may be viewed at http://waterresources.at

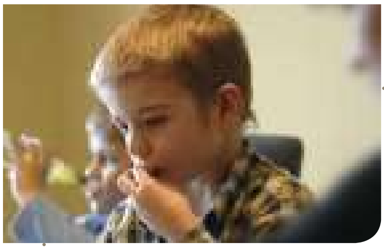

ucb newmedicines™
vital science, new ways

Post-Doctoral Fellowship Programme:
UCB seeking world-class post docs to lead pioneering research projects.

UCB, a global biopharmaceutical leader focusing on central nervous system and immunological disorders, is currently seeking industry leading scientists to join our post doctoral programme based at research centres in Belgium and the UK*.

UCB is a patient-centric biopharmaceutical company dedicated to the research, development and commercialisation of innovative medicines. Already the leader in epilepsy, UCB is committed to providing novel solutions for people with severe conditions such as Parkinson's disease, rheumatoid arthritis, and restless legs syndrome. Employing more than 8,500 people in over 40 countries, UCB produced revenues of € 3.2 billion in 2010. UCB NewMedicines is UCB's discovery research to clinical proof-of-concept organisation charged with building a prolific pipeline of differentiated molecules by channelling exquisite science for industry-beating performance.

Our research centres are home to a wealth of internal skills and experience in our chosen therapeutic areas, allied to unique and proprietary technology platforms. Our networks with leading global academic and industrial partners ensure access to novel technologies, targets and collaborative services. Our intellectual and scientific capability is evidenced not only by our record of proven delivery of drugs to patients but also by our scientists having published work in leading journals.

We are seeking post docs with expertise in one or more of the following:
immunology; neurobiology; Parkinson's Disease; immunohistochemistry; molecular and cell biology; computer and mathematical modelling; mass spectrometry; cell signalling; siRNA; synthetic organic chemistry.

Slough (UK)

Braine-l'Alleud (Belgium)

"There's a true focus on high quality fundamental scientific research. We have an excellent supportive mentor and the working environment is positive and dynamic, with ongoing opportunities to collaborate and swap new ideas with people from various departments."
Manuela, UCB post doc scientist

"Scientific challenges from my UCB colleagues enhanced my creative thinking, and I have amassed information on broad areas of expertise, including drug discovery and the clinical perspective of scientific research. My experience at UCB has certainly broadened my career options."
Gaurav, UCB post doc scientist

If you want to develop your career with an innovative biopharmaceutical company and contribute to our outstanding record of achievement please view the post-doctoral opportunities available through our 2012 programme. Further details on the specific projects for which we are recruiting and details of how to apply are available at: http://www.ucb.com/rd/post-doctoral-programme

*Brussels (BE) and Slough (UK)

UC RIVERSIDE
UNIVERSITY OF CALIFORNIA

Health ▪ Sustainability ▪ Policy ▪ Technology

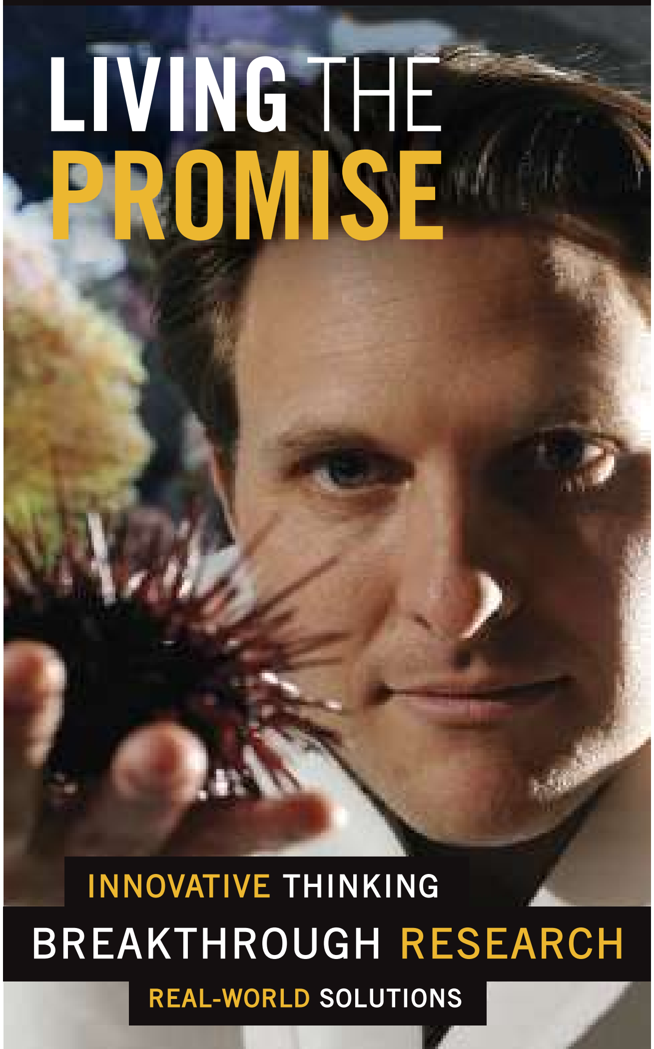

SUSTAINABILITY SOLUTIONS

Inspired by nature: By studying sea urchins, corals and snails, UCR engineers learn to synthesize new materials like lightweight armor and flexible ceramics.

- Protecting crops from disease while reducing pesticides
- Preserving fragile ecosystems impacted by climate change
- Improving air quality through cleaner emissions
- Combating costly, destructive invasive species

Explore more solutions:
promise.ucr.edu

Université Lille Nord de France

Université Lille 2
Droit et Santé

Lille 2 University recruits

A Top class professor in Toxicology

Join a University of Excellent, leader in Higher Education and Research.

Located at the very heart of a region opened on the world, Lille 2 University is member of the Research and Higher Education Cluster « Lille Nord de France University ».

www.univ-lille2.fr
> Section: Recrutement et concours

Contact : christelle.youmba@univ-lille2.fr

A tradition of Excellence

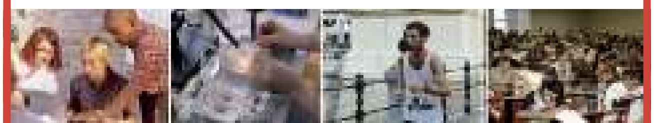

Law Healthcare Business administration Sport

www.univ-lille2.fr

Texas A&M
HEALTH SCIENCE CENTER
COLLEGE OF MEDICINE

Multiple Faculty Positions in Biomedical Sciences Research
Institute of Biosciences and Technology

The Texas A&M Health Science Center **Institute of Biosciences and Technology** (IBT), **http://ibt.tamhsc.edu/**, an internationally recognized leader in biomedical research located at the Texas Medical Center in Houston, TX, is recruiting multiple faculty members at all levels to develop outstanding research programs that complement existing strengths in Cancer Biology, Infectious Disease, Cardiovascular Physiology, and Environmental Health. As the new home for the **Gulf Coast Consortium for Chemical Genomics, http://gulfcoastconsortia.org/Research/John_S._Dunn_Gulf_Coast_Consortium_for_Chemical_Genomics.aspx**, and the joint Baylor/IBT Center for Advanced Imaging, candidates with research interests in high throughput screening technologies, drug discovery and translational research and/or programs that would be accelerated by access to high resolution, high content imaging capabilities are especially encouraged to apply.

Applicants should have M.D., Ph.D. or M.D./Ph.D. degree in biochemistry, molecular biology or a related science and an outstanding publication record; applicants at the Assistant Professor level should have at least 3 years post-doctoral experience. The IBT is entering an expansion phase and will be recruiting multiple new faculty who will receive **highly competitive packages for salary, start-up and support for graduate education, along with outstanding laboratory and office space** in the Texas A&M Health Science Center Alkek Building in the Texas Medical Center. Successful candidates will be expected to establish his/her independent research group, conduct highly meritorious research, establish collaborations with other investigators in the Texas Medical Center and components in the Texas A&M University System, and to obtain significant extramural funding. Applications will be received and evaluated on a rolling basis until **May 31, 2012**. To apply, please send a cover letter, curriculum vitae, statement of research interests, copies of key publications, and at least three references letter to: **Fen Wang, Ph. D., Chair of the Search Committee, Institute of Biosciences and Technology, 2121 W. Holcombe Blvd, Houston, TX 77030-3303; E-mail: fwang@ibt.tamhsc.edu**.

The Texas A&M Health Science Center is an Affirmative Action, Equal Opportunity Employer.

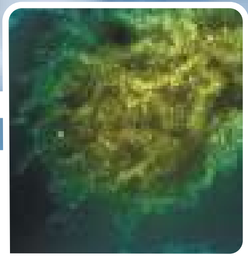

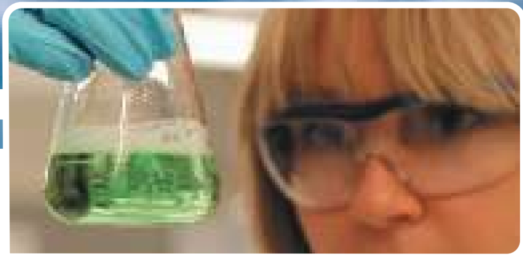

CHAIR POSITION IN POLYMER AND CATALYSIS IN THE KAUST CATALYSIS CENTER

جامعة الملك عبدالله
للعلوم والتقنية
King Abdullah University of
Science and Technology

The Catalysis Center at King Abdullah University of Science and Technology (KAUST) is launching a Professor Chair, sponsored by SABIC, in the field of **Polymer Sciences and Catalysis**.

KAUST is an international graduate-level, merit-based research university dedicated to advancing science and technology through innovative and collaborative research and to address challenges of regional and global significance. Located on the Red Sea coast of Saudi Arabia, KAUST offers superb research facilities, generous assured research funding, and internationally competitive salaries. Further information can be found at: *www.kaust.edu.sa.*

The KAUST Catalysis Center (KCC) is devoted to Catalysis by Design. The objectives of KCC areto develop new concepts in the fields of energy, environment, materials, and nanotechnologies. This center aims for excellence at the international level. To find out about KCC, visit *http://kcc.kaust.edu.sa*.

The theme of research associated with this Chair is "New Concept in Polymer Catalysis towards Major Breakthroughs." Considering the ambition of the topic, the profile of the candidate could vary from a young researcher to a more mature professor.

Applications should include a curriculum vitae, statements on research plans with brief research proposals as well as teaching philosophies. Please submit your application to the University's employment website at: *http://apptrkr.com/233725.*

BE AT THE FOREFRONT OF SCIENCE

General Manager Science and Policy

Opportunities of this calibre rarely become available – the chance to lead some of New Zealand's finest and most influential scientific talent and play an integral role in benefitting the environment. For a seasoned science leader, the level of influence on offer here will make this the defining move of your career.

This is a high level position with a key role in our senior leadership team and in New Zealand's science community. As Landcare Research's senior representative, you will operate at the science-policy interface working with decision-makers in central and local government and in other organisations. Critical to success in this role is your ability to interact closely and at high level with those who design, implement and review policies that have implications for our environment.

You will work in close collaboration with our GM Science and Industry, taking joint responsibility for much of our science output and impact. You will have responsibility for five of our ten Science Portfolios; these Portfolios are led by senior scientists with international reputations. You will also enjoy time to maintain your own scientific research and networks in the New Zealand and global science communities. You will be expected to develop well integrated portfolios of science that combine excellence and relevance, and attract science revenue to supplement the organisation's core funding.

To fully realise the potential of this role, it's vital you have considerable leadership expertise gained by driving large-scale science programmes and heading up a sizeable scientific team. Naturally you'll be PhD qualified, highly regarded in the scientific community and recognised as a leading figure in your related area. Ideally you will have a strong background in terrestrial ecosystems and/or biodiversity research, and have an interest in integrative science.

For the right person, there is also the opportunity to take a joint appointment as a Professor at the University of Auckland's School of Biological Sciences. This is an outstanding opportunity to leverage our collaboration with the University to promote the development of science capability among post graduates. In return, you can expect a competitive salary and benefits package, including personal development opportunities. Location is also negotiable, so you can be based at any of our major sites.

For further information please visit our website www.landcareresearch.co.nz/jobs where you will find a position description and an online application form. All applications must be received through the Landcare Research website.
For specific enquiries please contact General Manager People & Culture, Katrina Direen by email direenk@landcareresearch.co.nz

Applications close Friday, 16 March 2012.

EEO Employers Group

Landcare Research
Manaaki Whenua

Northeastern University
College *of* Science

Northeastern University is a center of use-inspired innovation, with multidisciplinary research teams focused on solving the complex problems of our society. We have initiated a search for a cluster of tenure or tenure-track faculty members (any level) to build on established strengths in Drug Discovery, Delivery, and Diagnostics with initial emphasis in the three areas of Antimicrobials, Neglected Tropical Diseases (NTDs), and Global Public Health. Applicants from both academia and industry are welcome to form the centerpiece of the new Global Health Initiative at Northeastern University.

Antimicrobial Research and Discovery
We are seeking an expert in basic research related to antimicrobial agents, and/or a specialist in antimicrobial discovery. Specific areas of interest include antimicrobial agents acting against bacterial or protozoan pathogens.

Medicinal Chemistry for Neglected Tropical Diseases
We invite applications from experts focused on medicinal chemistry and natural product approaches for anti-infective drug discovery, particularly pertaining to those diseases relevant to Global Health. Responsibilities will include establishment of an independent, externally funded research program, particularly in the context of a multi-disciplinary drug discovery team.

Public Health for Neglected Tropical Diseases
We seek proven experts in the area of public health practice and policy making who are interested in applying their skills toward strengthening health systems to respond to the high burden of NTDs in low- and mid-income countries. Experience in health practice, systems or policy related to major NTDs such as schistosomiasis, leishmaniasis, onchocerciasis, Human African trypanosomiasis, dracunculiasis and lymphatic filariasis, especially at the international level, is vital.

To view full job descriptions, visit Northeastern.edu/cos/pdfs/drugdiscoverypositions.pdf, or scan the QR code:

Although we are seeking applicants at the tenure and tenure-track level, applicants at all levels will be considered. Northeastern University is an Equal Opportunity, Affirmative Action Educational Institution and Employer, Title IX University. Northeastern University particularly welcomes applications from minorities, women and persons with disabilities. Northeastern University is an E-Verify Employer.

IIN Postdoctoral Fellowships in Nanotechnology

The International Institute for Nanotechnology (IIN) at Northwestern University is seeking extraordinary, young scientists and engineers who are pursuing leading-edge nanotechnology research for IIN Postdoctoral Fellowships. A global hub of excellence in the field, the IIN unites more than $550 million in nanotechnology research, infrastructure, and education under a single umbrella. Its collaborations with other universities, research institutions, and industry partners span 18 countries—and bridge the boundaries among science, engineering, and medicine.

Two-year IIN Postdoctoral Fellowships include a $65,000 stipend, as well as research and travel funds per annum.

Qualified candidates must be U.S. citizens and expect to earn a doctoral degree within the next year. They must have demonstrated innovation as well as outstanding achievement in their doctoral research and possess independent research abilities and ambitious scientific goals. Applicants must not hold any position, paid or unpaid, with Northwestern University throughout the nomination and award process.

Application Process:
Applicants must secure a postdoctoral appointment with an IIN faculty member (see faculty list at iinano.org)—and be nominated for an IIN Postdoctoral Fellowship by the sponsoring professor. The IIN is not accepting self-nominations and cannot respond to all queries. Please contact professors directly and mention your interest in the IIN Postdoctoral Fellowship. After candidates are nominated by sponsoring faculty, they will be evaluated by the IIN Executive Committee. Select nominees will be invited to apply.
www.iinano.org
nanotechnology@northwestern.edu

Deadline:
IIN Postdoctoral Fellowships are awarded on a rolling basis, up to six per year.

Northwestern University is an Affirmative Action, Equal Opportunity Employer.
Women and minorities are encouraged to apply.

NORTHWESTERN UNIVERSITY

INTERNATIONAL INSTITUTE FOR NANOTECHNOLOGY
Northwestern University

中国科学院北京基因组研究所

Junior and Senior Faculty positions in Computational Biology, Genomics and Systems Biology

Beijing Institute of Genomics, Chinese Academy of Sciences (CAS), Beijing, China

Beijing Institute of Genomics (BIG) invites applications for faculty positions in the following areas:

1. Computational biology that encompasses the development of computational tools and the applications of such tools to biological questions. Algorithm, software and database developments are encouraged.
2. Large-scale sequencing, assembly, annotation and analysis as well as sequencing technology and instrument R&D.
3. Systems biology, including the analysis of transcriptome, epigenome and proteome, that addresses fundamental biological questions.
4. Synthetic biology that focuses on the applications of genomics to questions of biosynthesis, and genomic engineering.

Candidates must have a doctoral degree, postdoctoral training and a proven record of high level publishing in order to qualify for the so-called "100 talent" or "1000 talent" programs. BIG has fully-equipped platforms for high throughput DNA sequencing, rapid genotyping, and high-performance computing. New faculty members will join an interactive, interdisciplinary community of scientists at CAS in Beijing Olympic Village. BIG offers a competitive start-up package that includes research funding, supporting staff, and personal benefits.

Inquiries in subfields of genomics not listed above are welcome. Candidates shall prepare an application package that includes Curriculum Vitae, description of past achievement and proposed future research (3-7 pages), copies of three representative publications, and a list of three referees with detailed contact information. All documents should be directed to **job@big.ac.cn**.

THE UNIVERSITY OF TEXAS
MD Anderson ~~Cancer~~ Center
Making Cancer History®

Assistant Professor in Bioinformatics

Department of Molecular Carcinogenesis

Sharon Y.R. Dent, Ph.D.
Professor and Chair
Molecular Carcinogenesis
The University of Texas
MD Anderson Cancer Center
Science Park
1808 Park Road 1C
Smithville, TX 78957

The Department of Molecular Carcinogenesis and The Center for Research on Environmental Disease at the University of Texas MD Anderson Cancer Center Science Park are seeking a non-tenure track assistant professor with expertise in bioinformatics.

We seek an individual with experience in carrying out complex functional and statistical analyses of biological data, including global gene expression analysis, ChIP-Seq, RNA-Seq and pathway analysis. This person will develop an interactive research program by collaborating with basic scientists on the biological interpretation and analysis of mouse and human "omics" data. We are particularly interested in individuals with experience in integrating various omics platforms and/or performing comparative analyses between species. Strong backgrounds in molecular biology, genetics, and statistics are essential.

Highly motivated and energetic candidates are encouraged to provide a current summary of their research goals and their CV via email to **mdaSciencePark@MDAnderson.Org**. Please include "MDACC Center Bioinformatics" in the subject line of the email.

MD Anderson Cancer Center is an equal opportunity employer and does not discriminate on the basis of race, color, national origin, gender, sexual orientation, age, religion, disability or veteran status except where such distinction is required by law. All positions at The University of Texas MD Anderson Cancer Center are security sensitive and subject to examination of criminal history record information. Smoke-free and drug-free facility.

Assistant Professor (Basic/Translational Researcher)

The University of Pittsburgh Department of Neurological Surgery is recruiting an experienced translational researcher at the rank of Assistant Professor in the tenure stream. Candidates should have a doctoral degree and at least five years of postdoctoral experience. Candidates must have an established record of receiving nationally competitive research support for his/her developing independent research program using pluripotent stem cell biology and directed differentiation to evaluate the effects of environmental exposures on development. In addition to his/her independent project, the successful candidate will participate in collaborative projects in neurological disease within the department, including the use of pluripotent stem cells for basic and translational studies. Additionally, this candidate will have responsibility for the overall coordination of the research efforts in the newly established Neuroapoptosis Laboratory, including the writing and editorial assistance of progress reports, manuscripts, and grant proposals. Thus, a background in the regulation and mechanisms of apoptosis is required. Salary is competitive and commensurate with training and experience.

In order to receive full consideration, applications must be received by **April 30, 2012**. Send inquiries to :

Robert Friedlander, M.D.
Chairman
Department of Neurological Surgery
Suite B-400 PUH, 200 Lothrop Street
Pittsburgh, PA 15213
(412) 647-6358
dudekgl@upmc.edu

The University of Pittsburgh is an Affirmative Action, Equal Opportunity Employer.

The Royal Society scientific meetings in 2012

2012 scientific discussion meetings at the Royal Society

Nuclear energy in the 21st Century
12 – 13 March
Organised by Professor Roger Cashmore FRS, Professor Robin Grimes and Dame Sue Ion FREng

Signal processing and inference for the physical sciences
26 – 27 March
Organised by Dr Nick Jones and Dr Thomas Maccarone

New windows on transients across the Universe
23 – 24 April
Organised by Professor Paul O'Brien, Professor Stephen Smartt, Professor Ralph Wijers and Professor Kenneth Pounds CBE FRS

Next-generation molecular and evolutionary epidemiology of infectious disease
14 – 15 May
Organised by Dr Oliver Pybus, Professor Christophe Fraser and Professor Andrew Rambaut

Photoactivatable metal complexes: from theory to therapy
18 – 19 June
Organised by Professor Peter Sadler FRS, Professor Akhil R Chakravarty and Dr Nicola J Farrer

Magnetoelectric phenomena and devices
24 – 25 September
Organised by Dr Neil Mathur and Professor James Scott FRS

Regulation from a distance: long-range control of gene expression in development and disease
22 – 23 October
Organised by Professor Wendy Bickmore and Professor Veronica van Heyningen FRS

Energy transduction and genome function – an evolutionary synthesis
12 – 13 November
Organised by Dr Nick Lane, Professor John F Allen, Professor John A Raven FRS and Professor William Martin

Achieving food and environmental security – new approaches to close the gap
3 – 4 December
Organised by Professor Guy Poppy, Professor Paul Jepson, Professor John Pickett CBE FRS and Dr Michael Birkett

Most of the above discussion meetings will be followed by a focused satellite meeting at the Kavli Royal Society International Centre – see meeting website listing for details.

2012 Theo Murphy meetings at the Kavli Royal Society International Centre

Rigidity of periodic and symmetric structures in nature and engineering
23 – 24 February
Organised by Dr Simon Guest, Professor Patrick Fowler and Professor Stephen Power

Nanolaboratories: physics and chemistry of small-molecule endofullerenes
15 – 16 March
Organised by Professor Malcolm Levitt FRS, Professor Tony Horsewill, Professor Nick Turro and Professor Yas Murata

Structure and dynamics of the thylakoid membrane
3 – 4 May
Organised by Professor James Barber FRS and Professor Peter Horton FRS

New frontiers in anisotropic fluid-particle composites
28 – 29 June
Organised by Professor John Sambles FRS, Professor Peter Raynes FRS and Dr Susanne Klein

Complex patterns in wave functions – drums, graphs and disorder
5 – 7 September
Organised by Dr Sven Gnutzmann and Professor Uzy Smilansky

Handling uncertainty in weather and climate prediction, with application to health, agronomy, hydrology, energy and economics
4 – 5 October
Organised by Professor Tim Palmer FRS

These meetings are free to attend, but pre-registration is essential.

For more details visit
royalsociety.org/events

EXCELLENCE IN SCIENCE

THE ROYAL SOCIETY

LSUHealth Shreveport

The Department of Cellular Biology and Anatomy at the LSU Health Sciences Center School of Medicine in Shreveport is currently recruiting faculty members with a Ph.D. or equivalent degree for tenure-track positions at the level of **Assistant and Associate Professor** in the areas of Cardiovascular Science or Neuroscience. These positions are being filled as part of a major expansion of the research program in the department. Recently renovated state-of-the-art laboratory space, competitive salaries and significant start-up packages will support the positions. The requirements for Assistant Professor include a minimum of two years of post-doctoral research experience and for Associate Professor a minimum of three years of experience at the level of Assistant Professor. The successful candidates are expected to have a distinguished record of scholarly activity including teaching experience in Cellular Biology and Anatomy, or related basic science areas. For the Associate Professor level, extramural funding (NIH R01 or equivalent) is expected.

This is an exciting opportunity for appropriate candidates to play a significant role in an invigorated department. Numerous outstanding research core facilities are available staffed by dedicated research associates. Opportunities to interact with investigators of similar interests are available.

Please submit your application with a curriculum vitae and names of three references via email to: **Dr. William G. Mayhan (wmayha@LSUHSC.edu), Professor and Chair, Department of Cellular Biology and Anatomy, LSU Health Sciences Center, School of Medicine in Shreveport, Shreveport, LA 71130**. In addition, please include a statement summarizing your research plans and teaching experience. Review of applications will begin immediately and will continue until the positions are filled.

LSUHSC-S is an Affirmative Action and Equal Opportunity Employer.

POSITIONS OPEN

BASIC SCIENCE INVESTIGATORS in The Area of HIV and/or HIV-Related Diseases

The Departments of Microbiology and Medicine at the University of Alabama at Birmingham (UAB), in conjunction with the Center for AIDS Research (CFAR), are seeking for outstanding basic science investigators in the area of human immunodeficiency virus (HIV) and/or HIV-related diseases (tenure and tenure-track at **ASSISTANT, ASSOCIATE,** and **FULL PROFESSOR** Positions). Areas of interest include, but are not limited to, HIV immunology, vaccinology, pathogenesis, structural biology, opportunistic infections, and diseases associated with HIV, such as hepatitis C virus and mycobacterium tuberculosis. Nationally competitive salaries, startup packages, and space allocations will be offered to successful candidates who will have the opportunity to interact with a core group of basic and clinical scientists at UAB with expertise in many different facets of HIV and HIV-related diseases. The University of Alabama at Birmingham is one of the top clinical and research institutions in the nation, located in a beautiful, livable, and affordable city with many cultural and outdoor attractions. Applicants should send curriculum vitae, a summary of research interests and the names of three references before April 30, 2012 to:

Dr. Paul Goepfert
Professor of Medicine and Microbiology
Director of the Alabama Vaccine Research Clinic
908 20th Street South, CCB 328
Birmingham, AL 35294-2050
E-mail: paulg@uab.edu

POSITIONS OPEN

Two **POSTDOCTORAL POSITIONS** are available at the Magee-Womens Research Institute to study the genomics of human ovarian failure, uterine anomalies, and tumors using cutting edge sequencing technologies. We also utilize transgenic animals to model pathologic human variants, study mechanisms, and identify therapies. The laboratory utilizes molecular and cellular biological techniques, whole exome and genome sequencing, chromosomal microarrays, mouse animal models, and targeted knockouts. Candidates must have a Ph.D. in biochemistry, molecular biology, genetics, or related fields; experience with reproductive tract preferred. Experience with transgenic mouse models and basic molecular biology techniques are desirable. Interested candidates should send a cover letter, their curriculum vitae, and the names and contact information of two references electronically to:

Aleksandar Rajkovic, M.D., Ph.D.
Director of Reproductive Genetics
University of Pittsburgh
Magee-Womens Research Institute
Department of OB/GYN and Reproductive Sciences
204 Craft Avenue - A224
Pittsburgh, PA 15213
Phone: 412-641-8635
E-mail: rajkovic@upmc.edu
Website: http://www.mwrif.org/205/rajkovic-lab

The University of Pittsburgh is an Affirmative Action/Equal Opportunity Employer.

POSTDOCTORAL POSITION
Germline Stem Cells

Studies include culture, differentiation and gene activity of male germline stem cells. See *Science* **316,** 404 (2007) & *PNAS* **106,** 21672 (2009). Send curriculum vitae, names of three references, and a letter describing research experience to: **R. L. Brinster, School of Veterinary Medicine, University of Pennsylvania. Email: cpope@vet.upenn.edu.**

POSITIONS OPEN

DEPARTMENT CHAIR
Pharmacological and Physiological Science

Saint Louis University, a Catholic Jesuit institution dedicated to education, research, service and health care, has initiated a national search for the next William Beaumont Professor and Chair of the Department of Pharmacological and Physiological Science (**website: http://medschool.slu.edu/pharmphys**). The successful applicant will have a Ph.D. or M.D. degree, a strong record of academic achievement in cellular and molecular mechanisms of biological processes, a sustained record of extramural research funding, administrative leadership, experience in both graduate student and medical student education, and enthusiasm for mentoring junior faculty. Interested candidates should submit a cover letter, curriculum vitae, and a description of their leadership vision to **website: http://jobs.slu.edu** (**Req. ID #20120062**). Letters of nomination may be sent electronically to **Enrico Di Cera,** M.D., Chair of the Search Committee (**e-mail: enrico@slu.edu**).

Saint Louis University is an Affirmative Action/Equal Opportunity Employer, and encourages nominations and applications of women and minorities.